On the design of Neutral Scanning Helium Atom Microscopes (SHeM)

Optimal configurations and evaluation of experimental findings

Adrià Salvador Palau

Thesis for the degree of Philosophiae Doctor (PhD)
University of Bergen, Norway
2021

UNIVERSITY OF BERGEN

On the design of Neutral Scanning Helium Atom Microscopes (SHeM)

Optimal configurations and evaluation of experimental findings

Adrià Salvador Palau

Thesis for the degree of Philosophiae Doctor (PhD)
at the University of Bergen

Date of defense: 09.11.2021

Year: 2021

Title: On the design of Neutral Scanning Helium Atom Microscopes (SHeM)

Name: Adrià Salvador Palau

Print: Skipnes Kommunikasjon / University of Bergen

Scientific environment

Research group

Department of Physics and Technology. Nanophysics Group.

Supervision

Supervisors: Bodil Holst (University of Bergen), Gianangelo Bracco (University of Genova).

Bodil Holst and Gianangelo Bracco supervised me in each step of this thesis. They are co-authors of all my papers and provided critical insight on the formulation of research problems and underlying physics of helium microscopes.

Funding

The research work presented in this thesis has been funded by the European Union: Theme NMP.2012.1.4-3 Grant no. 309672, project NEMI (Neutral Microscopy).

The Nanophysics group provided support for travelling, housing, and fees.

Due to, amongst others, the exceptional covid situation, most of the thesis writing and coursework were done from home and self-funded. Previous to the pandemic reaching Europe, stays in Bergen were arranged to do all the coursework that required the student's presence.

Acknowledgements

I would like to thank Bodil Holst and Gianangelo Bracco for their support and mentorship over the years. I would also like to thank my family, especially my parents for educating me on the values of rationality, scepticism and kindness. To my father: pare, espero que et recuperis plenament i puguem anar a nedar junts. Finally, I would also like to thank my girlfriend, Ashley Braunthal for her enormous patience and my friends for letting me annoy them about Physics. ...

Preface

This is the second Ph.D. thesis that I write. The reader might wonder: what brings somebody to study for two separate Ph.D.'s? I must say that I, myself, find it hard to answer this question. Perhaps the answer does not lay on why, but rather on why not. During the years, I have accumulated what I would like to think is a sizeable amount of knowledge in the field, and I have published the knowledge that I have generated in scientific papers. There was a point in which the amount of work reached a size that justified the compilation that I present here. I hope that in the future, when Scanning Helium Microscopes are a widespread tool, the findings outlined here are still useful, and that somewhere a physics student finds this thesis and uses it as a reference for his or her own work. ...

Abstract

Scanning Helium Microscopes (SHeMs) are novel microscopy tools using neutral helium atoms as the imaging probe. Helium atoms have several advantages compared to other probes such as electrons or helium ions. Helium atoms are neutral and inert and when compared to electrons their higher mass leads to a smaller de-Broglie wavelength for a given energy. Furthermore, helium atoms are strictly surface sensitive, scattering off the electron density distribution off the surface. These combined properties allow for non-destructive mapping of the surface of virtually any vacuum-compatible solid sample. Helium ions have a similar mass but they interact more strongly with the sample because they are not inert and require much higher energies to achieve electrostatic focusing. Charge neutrality makes helium a great imaging corpuscle, but also means that designing SHeMs is very difficult. Neutral helium atoms are very hard to manipulate, as electromagnetic fields cannot be used to focus and redirect the beam - instead, one needs to use diffraction optics and apertures. They are also hard to detect because helium has the highest ionisation potential of all atoms - hindering the task of ionisation based detectors. Therefore, to have a functioning microscope, one needs to form a highly intense atom beam. This thesis presents the work done over the last years to optimise the intensity of SHeMs, and more generally their atom-optics configuration. Amongst the papers included here are the first ones to show that SHeM optics have well-defined intensity maxima that give optimal designs. These papers show that existing designs were suboptimal and that the intensity could be increased several orders of magnitude. This thesis also features the first paper to present a design for a 3D imaging SHeM. A true nano-scale stereo microscope based on Heliometric stereo, a technique adapted from light. Besides these theoretical papers, two papers are included that focus on understanding the helium beam using experimental data. These papers are important as they provide the experimental foundations for the theoretical models used. Amongst other findings, the papers explore the importance of the Knudsen number at the skimmer, the validity of different intensity models, and the top-hat profile of the beam. The research presented here happened in parallel to a two order of magnitude improvement in detector efficiency. I believe that now we are in the position to build high-resolution SHeMs that have the potential to become an important tool for science and industry....

List of publications

All papers are published in peer reviewed journals listed in the Web of Science. Furthermore all journals are included included in the Norwegian list of point-giving journals. The list operates with two levels of which level 2 is the best. Physical Review A is a level 2 journal in that list. Review of Scientific Instruments and Journal of Vacuum Science and Technology B are level 1 journals.

First author papers

1. **Adrià Salvador Palau**, Gianangelo Bracco, Bodil Holst, *Theoretical model of the helium pinhole microscope*, Physical Review A **94**, 6, 2016. Citation: [85].

2. **Adrià Salvador Palau**, Gianangelo Bracco, Bodil Holst, *Theoretical model of the helium zone plate microscope* , Physical Review A **95**, 1, 2017. Citation: [95].

3. SD Eder, **Adrià Salvador Palau**[1], T. Kaltenbacher, Gianangelo Bracco, Bodil Holst, *Velocity distributions in microskimmer supersonic expansion helium beams: High precision measurements and modeling*, Review of Scientific Instruments **89**, 11, 2018. Citation: [39].

4. **Adrià Salvador Palau**, SD Eder, Truls Andersen, Anders Komr Ravn, Gianangelo Bracco, Bodil Holst, *Center-line intensity of a supersonic helium beam*, Physical Review A **98**, 6, 2018. Citation: [86].

5. Sam M Lambrick, **Adrià Salvador Palau**[1], Poul Erik Hansen, Gianangelo Bracco, John Ellis, Andrew P Jardine, Bodil Holst, *True-to-size surface mapping with neutral helium atoms*, Physical Review A **103**, 5, 2021. Citation: [73].

[1]Shared first authorship.

Non-first author papers

6. SD Eder, AK Ravn, B Samelin, G Bracco, **Adrià Salvador Palau**, T Reisinger, Erik Bergback Knudsen, K Lefmann, B Holst, *Zero-order filter for diffractive focusing of de Broglie matter waves*, Physical Review A **95**, 2, 2017. Citation: [37].

7. R. Flatabo, M. M Greve, SD Eder, M. Kallane, **Adrià Salvador Palau**, K. Berggren, B. Holst, *Atom sieve for nanometer resolution neutral helium microscopy*, Journal of Vacuum Science and Technology B **35**, 6, 2017. Citation: [47].

Contents

Chapter 1

Introduction

1.1 Thesis structure

This thesis is divided into four chapters. The first chapter, this introduction, provides the motivation and background for the thesis and the research questions. The second chapter (chapter 2) provides an in-depth review of existing literature by following the trajectory of a helium atom within a scanning helium microscope. It also places the papers included in this thesis in a broader research context. The third chapter presents the thesis conclusions. Finally, chapter 4 reprints all the papers included in the thesis.

1.2 Motivation and background

Skala Avdiron is today a minor sea resort in the Aegean sea where some Greeks like to spend the summer and drink away their sorrows. Once in a while, the owners of "Hotel Theoklitos" - the local tavern - receive some visitors that look different from the normal crowd: archaeologists, history geeks, and sometimes even physicists come there to see the ruins of ancient Abdera. They come to Abdera for one reason: two thousand five hundred years ago one of the most important philosophers in history was born here: Democritus. Democritus is the man that developed[1] the theory of atomism, and introduced the concept of atoms to mankind [15].

Today, atoms (in their modern understanding) are not only used to explain how matter is formed but as a tool to achieve other purposes. From the unbelievable destructive power of nuclear bombs [93], to the precise measure of time given by atom clocks [21],

[1] Together with his master, Leucippus.

atoms, as individual entities are the cornerstone of a variety of high-stakes applications. This thesis is about one of these applications, perhaps lesser-known: the possibility of using atoms to image microscopic samples.

The idea of using massive corpuscles as an imaging probe started with the electron microscope. This possibility was introduced by the realisation by De Broglie that every particle of matter propagates like a wave - with a wavelength proportional to the inverse of its momentum. Until then, only massless photons had been used - in optical microscopes. As it is well known, classical optical microscopes have a limited resolution given by the Abbe diffraction limit [101] [2]. For a given wavelength, massive particles carry significantly less energy than photons (see section 2.4), which opened the door for achieving much higher resolutions than with optical microscopes. By using a wavelength much smaller than the actual imaging resolution electrons also brought the possibility of imaging with a much higher depth of field than what can be achieved with optical microscopy [96].

Due to these advantages, and the possibility of manipulating electrons through electromagnetic fields, electron microscopes became a household tool in a vast range of scientific disciplines and industrial applications [40]. Amongst the uncountable achievements, it can be mentioned as a particularly timely result that Scanning Electron Microscopes have been able to provide detailed images of cells to the point where individual viruses attacking the cells could be appreciated [34]. For larger viruses, like the ebola virus [24], the entire virus structure could be imaged, something unthinkable in classical optical microscopes.

Scanning Electron Microscopes (SEM), however, have some drawbacks: electrons are charged. This means that biological samples, which are not conducting, cannot be easily imaged directly: they typically need to be coated by a conducting layer to avoid charging effects [108]. Similarly, electrons permeate into the samples, generating backscattered electrons in the process. This is generally a useful by-product but adds to the destructive power of this imaging technique and means that it is not strictly surface-sensitive [108]. Recently, helium ion microscopes have been added to the toolbox. They have the advantage of a lower penetration depth, but due to the high energy required for focusing, they still penetrate the sample and can lead to sample destruction [97].

This thesis presents a collection of theoretical and experimental studies of a technique specifically designed to address these drawbacks: imaging with neutral helium atoms. Neutral helium atoms are non-charged, exceptionally inert, and due to the much higher

[2] Since then this limit has been overcome in Scanning Near Field and Stimulated Emission Depletion microscopes [1, 55].

mass than electrons they carry a much smaller wavelength for a given energy [16]. This means that they bounce from the surface of the sample without penetrating it. The very low energy also means that delicate samples can be imaged without destruction.

The principle of imaging samples using helium atoms has been proven by several research groups. The first images were published by Holst et al. in 2008 [70]. The images were taken using MAGIE, which is one of the two helium microscopes developed by the Bergen group. This instrument uses a Fresnel zone plate to focus the beam and has been used to achieve a resolution of less than 1µm [35]. Alternative microscope designs, based on using a pinhole to collimate the beam soon emerged [42, 110]. These microscopes, albeit simpler and less powerful in principle, have provided the highest resolution images obtained with a helium microscope so far - $0.35\mu m$ [111].

One of the main learnings obtained from these initial designs is that neutrality and low-reactivity may be the main advantage but also the main drawback of using helium atoms as an imaging probe. The impossibility of focusing neutral particles using electromagnetic lenses leaves diffraction techniques, mirrors, and simple apertures as the only focusing device. On top of this, helium has the highest ionisation potential of all atoms, which makes helium detection a very difficult task [11]. Therefore, the design of neutral helium microscopes needs to be carefully optimised to obtain the maximum signal-to-noise ratio.

In recent years, the extreme sensitivity of helium atoms on the sample's surface has prompted the design of 3D imaging helium microscopes. These microscopes would be able to resolve the surface in 3D by using a variety of techniques in order to achieve nano-scale stereo imaging. This has recently been demonstrated on the micron scale through stereophotogrammetry [81], laying the experimental foundations to study the design of a true stereo neutral helium microscope.

Optimising the signal of helium microscopes and understanding how to build a stereo microscope capable of resolving the sample surface in 3D were two of the main problems in the field at the onset of this thesis work. This led to the two research questions formulated below.

1.3 Research questions

The research questions addressed in this thesis are:

1. What is the optimum configuration for helium microscopes that gives the highest signal-to-noise ratio possible for a given resolution?
2. Can helium microscopes be used as stereo-nanomicroscopes?

Chapter 2

Scanning Helium Microscopy: A historical review and state of the art

Neutral helium microscopy, also referred to as scanning helium atom microscopy and commonly abbreviated SHeM, is a novel imaging technique that uses a beam of neutral helium atoms as an imaging probe. The technique offers a number of advantages such as the very low energy of the incident probing atoms (less than 0.1 eV), unsurpassed surface sensitivity (no penetration into the sample bulk), a charge-neutral, inert probe and a high depth of field. This means that fragile and/or non-conducting samples can be imaged as well as samples with a high aspect ratio, with the possibility to obtain true-to-scale height information of 3D surface topography with nanometer resolution. However, for a full exploitation of this technique, a range of experimental and theoretical issues still needs to be resolved.

In this introduction, the main concepts needed to introduce the reader to the field are summarised, making an effort to set the articles that form the main contribution to this thesis work within a broader context. This is done by following the trajectory of the helium atoms step by step, from the initial acceleration in the supersonic expansion used to generate the beam over the interaction of the helium atoms with the sample to the final detection and post-processing. Note that the issues of contrast properties and detection/post-processing are addressed only very briefly. The contrast in a helium atom microscope is determined by the interaction of the helium beam with the samples to be investigated. The helium detection is determined by the detector properties. These are very complex topics in their own right and have not been the focus of this thesis work.

2.1 Introduction: Scanning Helium Microscopes

Neutral Helium Microscopes are surface characterisation tools that apply beams of neutral helium atoms as an imaging probe. The instruments use the supersonic expansion of helium gas into vacuum to generate a high-intensity beam with a narrow velocity distribution which is then collimated or focussed onto a sample. The scattered intensity signal is recorded "point by point" and used to create an image of the sample, in a manner similar to other beam probe microscopy techniques, such as scanning electron microscopy or helium ion microscopy, namely through Helmholtz reciprocity [49]. Neutral Helium Microscopes have, however, a crucial difference with respect to charged particle beams: due to the very low energy and strict surface sensitivity of the neutral helium beam, the image can only be formed by the backscattered neutral helium atoms. No photons or secondary electrons are generated during the scattering process.

Several abbreviations have been used for neutral helium microscopy over the years, i.e. NEMI for NEutral MIcroscope, HeM for Helium Microscope, and NAM for Neutral Atom Microscopy, however over the last few years the community seems to have converged to SHeM for Scanning Helium Microscope.

The research behind neutral helium microscopes includes four main areas, which can be mapped to the different stages of the imaging probe trajectory. Firstly fluid dynamics, which is used to model the supersonic expansion of helium gas into a vacuum and needed to establish the intensity and matter-wave properties of the helium beam. Secondly, de-Broglie matter-wave optics, which describes the interaction of the neutral helium atoms with the optical elements, such as zone plates, pinholes and mirrors, critical for the microscope resolution. Thirdly, helium atom surface scattering [16, 45, 57], modelling the interaction between the neutral helium atoms and the sample, thus determining the contrast properties and finally the helium atom detection, targeting the difficult problem of detecting hard-to-ionise neutral helium atoms. In addition to these three areas comes research specifically dedicated to the application of scanning helium microscopes. This includes problems such as optimisation of the overall configuration of the tool, advanced imaging techniques and signal processing, and practical applications.

2.2 A brief history of SHeM

In 1930, one year before the electron microscope was invented, Estermann and Stern scattered an effusive beam of neutral helium atoms off LiF(100) and saw diffraction peaks [41]. Their groundbreaking work had been made possible thanks to previous work

by Dunnoyer who established the first directed atom beam in 1911 [87].

The Estermann and Stern experiment did not instigate a new research field straight away, due to limitations in pumping technology which enabled only the production of effusive beams, which have low intensity and a broad velocity distribution (and therefore a broad de Broglie wavelength distribution). It took another twenty years for Kantrowitz and Grey to devise a helium source with a narrower velocity distribution [66]. This was achieved thanks to a supersonic expansion of helium gas into a lower-pressure chamber (see section 2.3.1). Notwithstanding the clear improvement that this brought, much narrower velocity distributions and higher intensities were imperative for the success of neutral helium atoms as a scattering probe.

Such beam properties were achieved in the early 1970s thanks to the improvement of vacuum techniques and the introduction of small nozzles, which allowed for supersonic expansion into ultra-high vacuum. The central part of the beam was selected using a conically shaped aperture, a so-called skimmer - until that point, slits had been preferred. By the 1980s, nozzle technology had advanced so much that the velocity distribution of the helium beams had become narrow enough that the small energy changes[1] resulting from the creation or annihilation of surface phonons could be measured [25]. This propelled helium atom scattering as a method suitable to study surface dynamics.

Eventually, physicists began to speculate on how the surface sensitivity of helium could also be used to construct an imaging instrument. It soon became clear that focusing optics was a particular challenge. Neutral, ground-state helium has the smallest polarisability of all atoms and molecules. Hence manipulation via electrostatic or electromagnetic field is essentially not possible. Furthermore, helium atoms at thermal energies do not penetrate solid materials. In practice, the only possible way to manipulate them is via their de-Broglie matter-wave properties. This leaves only three possibilities: simple collimation, focusing via mirror reflection or focusing via diffraction from free-standing structures. For example, Fresnel zone plates.

To the best of my knowledge, the first mentioning in the literature of the idea of a helium microscope was in the 1991 paper by Carnal et al [27]. This paper also presents the first experiment on focusing of neutral helium beams: The focusing of a beam of metastable helium atoms using a zone plate.

Other experiments quickly followed: The first focusing of a ground-state helium beam, and also the first focusing using a mirror was achieved in 1992, when Doak et al. obtained focusing in 1D by reflecting a helium beam off a mechanically bent, gold-coated piece

[1] meV range.

of mica. In 1997 Holst and Allison achieved astigmatic focusing in 2D by scattering a helium beam off a Si(111)-H(1x1) surface electrostatically bent to a parabolic shape [58]. The silicon wafer used had a thickness of 50 μm. The area of least confusion had a spot diameter of 210 μm. In [31] Grisenti et al obtained the first focusing of neutral, ground-state helium with a zone plate. They used a micro skimmer as a source.

In 1999 it was proposed that by changing the boundary conditions from round to an ellipsoidal mirror could be obtained by electrostatic bending [109], see also [76]. In [46] Fladisher et al achieved near stigmatic focusing of helium atoms using this method. One problem with the Si(111)-H(1x1) mirror is a considerable loss in intensity in the specular beam due to diffraction from the corrugated electron density distribution at the surface. In [9] Farias et al discovered that the reflectivity of an atom mirror could be dramatically improved by coating the silicon wafer surface with a 1-2 nm layer of lead. This so-called quantum stabilised mirror demonstrated a specular helium reflectivity of 67%. In a later work Anemone et al. explored the use of flexible thin metal crystals as focusing mirrors [4], following an early attempt from 1999 [59].

Despite these promising achievements in mirror focusing, it appears that to achieve focal spots at the nanometer range, near uniformly flat crystals without warp and bent are necessary. This technological requirement seems to have put an end to research on atom focusing mirrors, at least for the time being.

The first image obtained with neutral helium atom microscopy was made by Koch et al in 2008 [70] using a Fresnel zone plate, see Fig. 2.1. Koch et al obtained a 2D shadow image of a free-standing grating structure with a resolution of around 2 micron using a micro skimmer and a Fresnel zone plate to focus the helium beam onto the grating structure and scan the focussed beam across the structure - the helium zone plate microscope (see Fig. 2.8). The best resolution obtained with a zone plate up till now is slightly less than 1 micron [35]. This is very far from the theoretical resolution limits which are discussed in section 2.4. It should be mentioned that the zone plate has also been used to focus a beam of deuterium atoms, demonstrating the potential of making microscopes with other atomic and molecular beams [92].

Following Koch's work, other research groups focused on a simpler configuration: the pinhole microscope. This configuration uses a simple pinhole to collimate the beam instead of focusing optics. In this way, Philip Witham and Erik Sanchez managed to obtain the first scanning helium microscopy images in reflection mode [110], see Fig. 2.6. The initial resolution was 1.5 μm and later 0.35 μm [111], which remains the highest resolution obtained so far with a neutral helium atom microscope. Witham and Sanchez also demonstrated microscopy with an ^{84}Kr-beam [112]. Around the same time

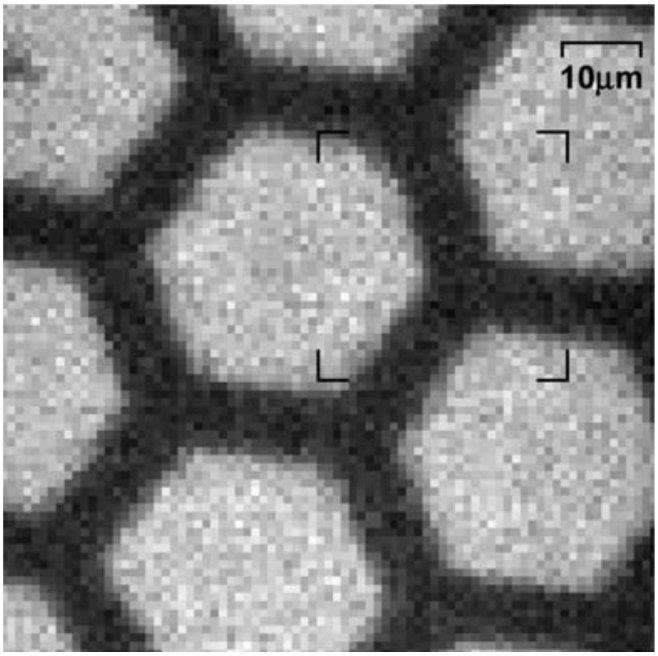

Figure 2.1: First image taken with a neutral helium microscope. The sample is a hexagonal copper grating with a period of 36 μm and a rod thickness of 8 μm. Image from [70].

as Witham and Sanchez, another group had worked on a pinhole microscope with a slightly different source design and using a skimmer [42] (see Fig. 2.7). The first images from this instrument were published in 2015 [42] (see Fig. 2.2). To this day the pinhole setup remains the most widespread neutral helium microscopy design, despite the fact that higher resolution can theoretically be achieved with the zone plate configuration as will be discussed in section 2.6.

As previously discussed the neutral helium probe is unique because it does not penetrate into the sample - thus providing the possibility of true-to-height 3D imaging of the surface. This was demonstrated experimentally on the microscale for the first time in [43]. The technique was then used for taxonomy in [81] see Fig. 2.3. See section 2.7 for further discussion, and **the fifth paper in this thesis for a theoretical discussion**. Finally, diffraction imaging was demonstrated for the first time in [13]. Diffraction imaging enables the detection of nano-crystalline patches on the sample surface.

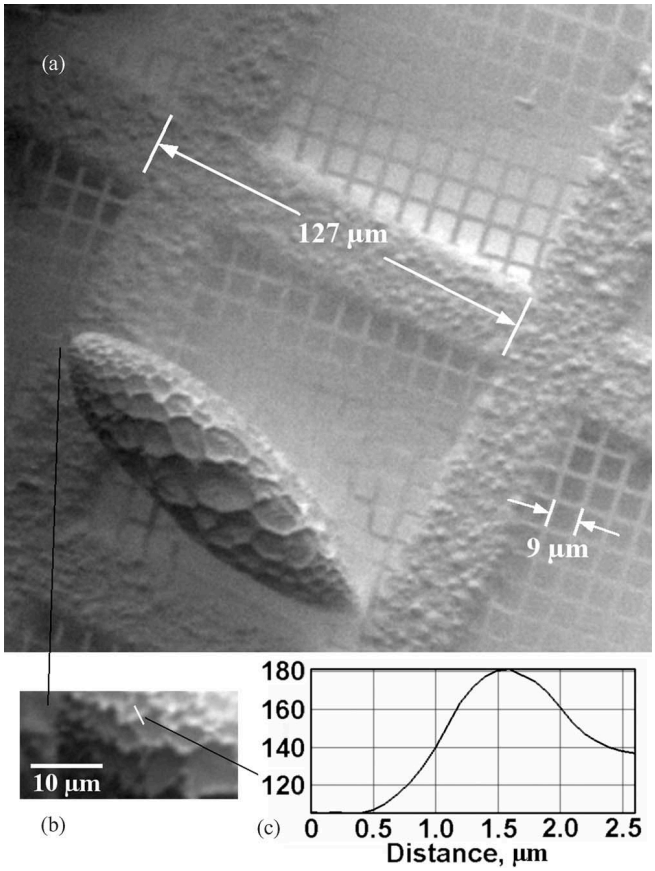

Figure 2.2: First image taken with a pinhole neutral helium microscope. The sample is an uncoated polen grain. Image from [110].

2.3 The atoms start moving - the Helium Source

In a Scanning Helium Microscope, atoms start their journey in the source. A typical SHeM source follows the design established for helium scattering [6, 7, 39]: helium is accelerated in a supersonic expansion from a high-pressure reservoir through a de Laval nozzle[2], into a vacuum chamber, known as the expansion chamber [10]. There, the central part of the beam is selected by a conically shaped aperture, called the skimmer [3].

[2]Often the nozzle is cut in the sonic plane, and is referred to as a *sonic nozzle* [10].

[3]As mentioned in the introduction, some designs skip the skimmer altogether and use a single collimated aperture far downstream [110].

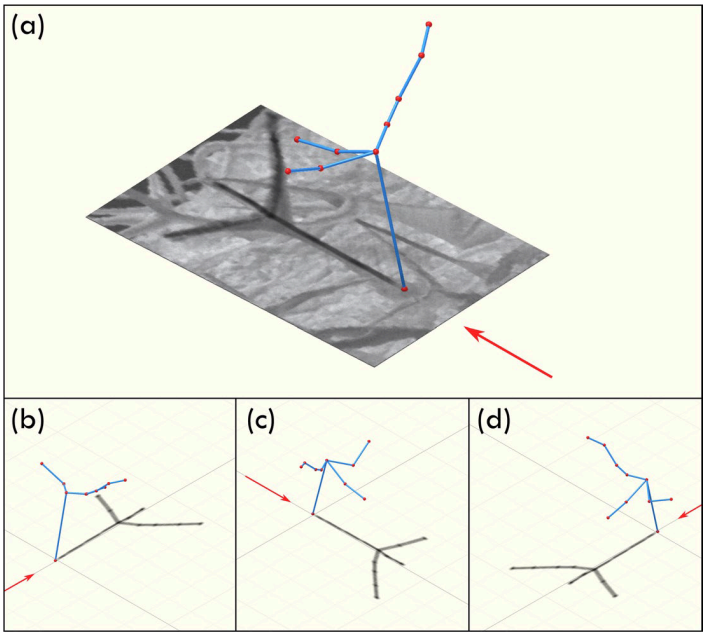

Figure 2.3: One of the first 3D images (wireframe model) taken with a neutral helium microscope. The image corresponds to a trichome on a plant leave (Arabidopsis thaliana) and demostrates the utility of the technique for non-destructive taxonomy. Image from [81].

When designing a Helium Source, one can essentially choose five parameters: temperature, pressure, nozzle radius[4], skimmer diameter and distance between skimmer and nozzle. In general, small nozzles and high pressures produce brighter[5] sources and therefore are more efficient in reducing undesired effects such as back-scattering interference (as the beam is more focused, if the same flow is assumed, fewer particles are emitted at undesired angles) [30, 54]. Similarly, cold sources are more intense than warm sources and produce higher parallel speed ratios (see section 2.3.2) [39, 86], which allows them to reach higher centre-line intensities. The absolute differences between a cold and a warm source at the same pressure can easily be on the order of $1 \cdot 10^{13}$ counts$/s \cdot m^2$ [86].

Once the nozzle size and temperature have been chosen, obtaining the beam properties corresponds to (i) solving the supersonic expansion of the Helium gas into a vacuum, and (2) calculating the beam intensity after the initial expansion. This section is structured with these two steps in mind: first, we describe the work done regarding the understanding of the beam's supersonic expansion, and then we revise the different models that give the beam intensity downstream.

[4]The issue of nozzle design is left as outside of the scope of this introduction. For a discussion of this topic see, for example, [10, 23].

[5]Count rate per steradian and unit area of the source.

2.3.1 The supersonic or free-jet expansion

The first component of a helium source is the nozzle, where atoms are accelerated to supersonic speeds in a physical phenomenon known as a supersonic expansion.

The theory describing supersonic expansions was developed in the 1970s and 1980s, and is based on splitting the expansion into two regimes: the first regime, within the nozzle, follows a Navier-Stokes flow and is solved through the isentropic nozzle model [87, 99]. The second regime, from close to the nozzle exit onward, is modelled through the Boltzmann equation. The flow is obtained either by solving the corresponding integrals under simplifying assumptions [22, 100] or using DSMC Montecarlo simulations [17, 18, 20].

The isentropic nozzle model

Within the nozzle, the helium atom is part of a gas: here, the density is high and Navier Stokes equations determine its dynamics. The isentropic nozzle model gives the total flux per unit time (from now on, centre line intensity) stemming from a de Laval nozzle (assuming that the nozzle is cut-off in the sonic plane). This derivation considers an ideal gas in which the flow can be assumed to be a reversible and adiabatic process. Therefore the gas can be considered isentropic - which means that the following analytical equation of the intensity can be obtained [87]:

$$I_0 = \frac{P_0}{k_{\mathrm{B}} T_0} \sqrt{\frac{2 k_{\mathrm{B}} T_0}{m}} \left(\frac{\pi}{4} d_{\mathrm{N}}^2\right) \sqrt{\frac{\gamma}{\gamma+1}} \left(\frac{2}{\gamma+1}\right)^{1/(\gamma-1)}. \tag{2.1}$$

One can also obtain the terminal velocity (which can be used to provide an approximation to the beam's de-Broglie wavelength) [87]:

$$v = \sqrt{\frac{5 k_B T_0}{m}}. \tag{2.2}$$

This model is used in the field to calculate the total flow stemming from the nozzle - as it is well known that helium is the closest we get to an ideal gas [107]. Some groups also choose to add a correction given by the thickness of the boundary layer in a real gas, for which Beijerink and Verster provide a correction factor for a monoatomic gas [10]. T_0, P_0 are the temperature and the pressure in the source. d_N is the diameter of the nozzle and m is the mass of a helium atom. γ is the heat capacity ratio ($\gamma = 5/3$ for helium), and k_B is the Boltzmann constant. To our knowledge, all helium microscopy

papers modelling the intensity of the helium beam use an initial intensity derived from the isentropic nozzle model (see section 2.3.2 for a breakdown).

Post-nozzle flow

Once the helium atom has left the nozzle, its flow is governed by the Boltzmann equation - as the Navier Stokes equations cease to apply. There are two main methods to solve the flow: either by numerically solving the Boltzmann equation under stringent assumptions that allow us to skip Montecarlo methods [5, 52, 87] or by simulating the particle flow using the Direct Simulation Monte Carlo method. The latter method is more computationally intensive, but also more accurate than the former as it relies on fewer assumptions.

In the first method, one typically assumes that the nozzle is a point source [100]. This assumption is grounded on work from Sherman and Ashkenas, which showed that a few nozzle diameters downstream, free jet streamlines become straight and could be extrapolated to a single point of origin close to the nozzle [5, 52]. The flow then can be solved using the collision integral for particles following Bose-Einstein statistics. The isentropic nozzle model at a short distance from the nozzle is used to obtain the initial conditions to start the integration[6]. To solve this equation, a velocity distribution, and an interaction potential have to be assumed. The equations needed to solve the expansion are included in [86, 87].

The velocity distribution of the atoms is taken to be an ellipsoidal Maxwellian:

$$f_{\text{ell}}\left(\vec{v}\right) = n\left(\frac{m}{2\pi k_{\text{B}} T_{||}}\right)^{\frac{1}{2}}\left(\frac{m}{2\pi k_{\text{B}} T_{\perp}}\right)\cdot \exp\left(-\frac{m}{2k_{\text{B}} T_{||}}(v_{||}-\bar{v})^2 - \frac{m}{2k_{\text{B}} T_{\perp}} v_{\perp}^2\right). \tag{2.3}$$

The choice of an ellipsoidal Maxwellian velocity distribution forms the basis to solve the spherically symmetrical Boltzmann equation [50]. In these models, the expansion's macroscopic properties are expressed in a spherical coordinate system. The temperature is split into two terms, modelling the velocity distributions of the radial and angular component of the velocity in spherical coordinates $v_{||}$ and $v_{\perp}$: $T_{||}$ and $T_{\perp}$. n is the number density.

On top of the assumption regarding the velocity distribution of the atoms, an interaction potential must be assumed. There are several options for this potential: the Lennard-Jones potential [62], the Tang, Toennies and Yu (TTY), and the Hurly Moldover (HM)

[6] This is a rather arbitrary distance that must be large enough to guarantee spherical symmetry and small enough to satisfy equilibrium conditions, typically a few nozzle diameters.

potentials [60, 103] being amongst the best known. Results of previous calculations show that the Lennard-Jones potential is accurate for source temperatures as low as 80 K [88, 89]. Therefore, this is often the preferred choice by practitioners in the field as the Helium source is rarely cooled below this temperature [88, 89, 91]. A detailed description of the Lennard-Jones potential and its implementation in the Boltzmann equation can be found in [90].

The numerical solution of the Boltzmann equation in its spherical approximation provides the evolution of the average gas velocity, and the temperatures $T_{||}$ and $T_{\perp}$ with respect to the distance from the nozzle. This solution can then be used to determine the intensity of the beam at the sample plane by means of the so-called quitting surface model - see section 2.3.2. This solution can also be used to obtain the velocity distribution and speed ratio of the beam, these are shown to be in **good agreement with experimental data in the paper number 3 in this thesis** [39].

An alternative way of solving the Boltzmann equation, requiring fewer assumptions, is to directly simulate particle-to-particle interactions using a method known as Direct Simulation Montecarlo [17, 20]. This method addresses the numerical infeasibility of simulating the flow particle by particle by grouping those particles onto pseudo-molecules that are taken to represent a larger group of real molecules. DSMC requires assumptions on the interaction of the pseudo-molecules with the surface and with each other. These are normally phenomenological models such as the hard-sphere model [20], the variable hard sphere model [83] and others [19]. DSMC is truer to nature than solving the Boltzmann equation under stringent assumptions but is also much more computationally expensive. Several papers have used this method to understand the behaviour of the helium expansion [18, 75, 77].

2.3.2 Intensity after the initial expansion

As the helium atom travels further away from the nozzle, it interacts less and less with neighbouring atoms. This means that modelling the supersonic expansion across the skimmer all the way until the sample plane is numerically inefficient.

Therefore, physicists often chose to use the fact that the Knudsen number of the flow increases with distance to the source, and that quasi-molecular flow is often reached before the first optical element -normally, the skimmer- to build simplified models of the intensity. Quasi-molecular flow allows for the recovery of analytical expressions of the centre-line intensity, as particles can be assumed to travel in a straight line without further interactions.

Over the years, several intensity models have been proposed for helium microscopes (and generally for helium sources). A combination of arbitrary variable labelling, numerical simplifications and empirical formulae has left researchers with no unified intensity models. The landscape is confusing, and in this introduction I attempt to unify and simplify the different intensity models and explain how they compare with each other.

To bring some clarity to this discussion, I propose the following geometrical conventions: consider always an expansion stemming from a nozzle, followed by a skimmer. The skimmer is placed at a distance x_S from the source of the supersonic expansion with no other apertures in between. Take a as the distance between the skimmer and the axial point in which the intensity is measured. The distance between the nozzle and the measuring point is then $(x_S + a)$ - see Fig. 2.4. All the rest of the physical variables correspond to those presented in section 2.3.2.

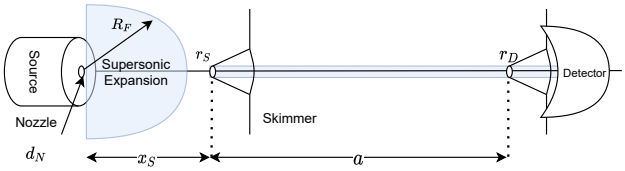

Figure 2.4: Main geometrical variables present in the quitting surface model.

I propose that the intensity should always be given as particles per second per unit area[7]. On top of this, the intensity can be assumed to be slowly-varying enough that to obtain a total intensity hitting a detector it is enough by multiplying the center-line intensity by the detector's area. The medley of analytical formulas found in literature can be confusing, but following this convention, one sees that they all have a common factor: the thermal-geometrical term, from now on referred to as I_{TG}. Overall, there are three families of intensity models: those that treat the nozzle as a source of a spherically symmetric flux, and account for any excess intensity by using an empirical factor [10], those that on top of this consider the thermal properties of the supersonic expansion through a dependency on the beam's speed ratio, and those that explicitly integrate the quitting surface[8] under some assumptions (as shown in the previous section). All three families of intensity models are faulty as they rely on overly simplistic assumptions, but they are also useful in that they provide an analytical expression for the intensity.

[7]I chose unit area over steradians to signify the departure from spherical symmetry typical of supersonic beams.

[8]Or an equivalent concept - known as the virtual source [30].

The quitting surface model

One of the most popular intensity models relies on the quitting surface model [86, 95, 100]. A quitting surface[9] is a useful theoretical construct that assumes that at a given point in the beam's supersonic expansion, particles start travelling in straight lines. This point is defined through asymptotical conditions on the properties of the expansion; either as the point in which the Mach number[10] of the expansion approaches its predicted terminal Mach number [3, 110] or as the point in which the parallel and perpendicular temperature of the Maxwellian distribution used to model the expansion decouple [104].

Regardless of the method used to define the quitting surface, the main utility of this model is that the intensity and velocity distribution of the beam can be obtained by integrating this spherical particle-emitting surface. The difficulties associated with this method are the relative arbitrarity of the definition of the quitting surface that depending on the condition chosen can be placed before or after the skimmer aperture.

As mentioned above, the quitting surface can be integrated to obtain a useful analytical model for the beam intensity: the Sikora approximation [100]. This expression was initially calculated for a quitting surface placed exactly at the skimmer aperture and was later generalised by Bossel to incorporate a quitting surface placed before the skimmer [22]. This is the formula that is now commonly used [86].

$$I_{\mathrm{S}} = I_{TG}\left\{1 - \exp\left[-S_i^2\left(\frac{r_{\mathrm{S}}(R_{\mathrm{F}}+a)}{R_{\mathrm{F}}(R_{\mathrm{F}}-x_{\mathrm{S}}+a)}\right)^2\right]\right\}, \tag{2.4}$$

where x_S is the distance between the nozzle and the skimmer and a is the distance between the skimmer and the point where the intensity is measured. R_F is the radius of the quitting surface. The first term of the Sikora approximation I_{TG} is the intensity corresponding to a naive spherically-symmetric model of the supersonic expansion, taken as if the atoms would travel in straight lines from the nozzle with equal probability at any angle and no thermal effects[11]. The total flow stemming from this ideal point source corresponds to the intensity resulting from the isentropic source model I_0. We name this factor the thermal-geometrical component, I_{TG}. The thermal-geometrical intensity measured at a detector of radius r_D is then:

$$I_{TG} = \pi I_0 \frac{r_D^2}{(x_S+a)^2}. \tag{2.5}$$

[9] Also referred to as "last collision surface" [10, 51].

[10] Ratio of flow velocity past to the local speed of sound, see [52] for a discussion in the context of atom beams.

[11] The density at the skimmer can also be used, if the point source assumption is dropped [86].

This component suffices to understand a basic design principle of neutral helium microscopy: reducing the axial length of the microscope is often beneficial, as the intensity will decrease with distance.

The second term of the Sikora equation, the exponential term is more interesting as it models the thermality of the beam. The S_i there indicates that depending on the microscope design both the perpendicular ($\perp$) and parallel ($||$) speed ratios are good choices for that parameter:

$$S_i = \sqrt{\frac{m\bar{v}^2}{2kT_i}}, \qquad i = ||, \perp. \tag{2.6}$$

In general, for small skimmers close to the quitting surface, the parallel speed ratio is the right choice (as the perpendicular spread is not a big contributor given that very little of the quitting surface is seen at the detector). However, for larger skimmers seeing a thermalised portion of the expansion (for example, when the expansion is not assumed to end until significantly after the skimmer) the perpendicular speed ratio is a better choice [86].

Further approximations

Parting from the quitting surface model, or similar approximations such as the virtual source model one can obtain further approximations by taking the limit at very small skimmers or considering a simpler flow pattern (such as an isotropic spherically symmetric expansion). Researchers often use these simplified expressions to determine the beam's intensity. Over the years, amongst several existing models, often the simpler ones have been favoured, (see, for example, [12, 65]) despite them not being backed by strong empirical measurements nor by strong theoretical support. In the following paragraphs, we review a few popular intensity models from the different families described in section 2.3.2 and show how they compare to the thermal geometrical term.

First, let's take a look at the expression used by Witham and Sanchez [110] to estimate the signal in their microscope. They use Miller derivation [99] for the isentropic intensity [12]. From the three families mentioned above, this corresponds to the first family of models that correct for the excess intensity from the supersonic expansion by using a peaking

[12]The intensity they use differs by one half to the derivation published by Pauly [87], we think this is due to a typo - but we keep their formulation.

factor κ.

$$I = \kappa \frac{P_0 \pi r_{nz}^2 (\frac{\gamma-1}{2}+1)^{\gamma/(\gamma-1)} \sqrt{\frac{\gamma k_B T_0}{m}}}{k T_0} \pi \frac{r_D^2}{(x_S+a)^2} \approx 0.4871 * 2\kappa\sqrt{\gamma/2} \frac{I_0}{f(\gamma)} \frac{r_D^2}{(x_S+a)^2} \approx 1.1026 I_{TG} \quad (2.7)$$

Where $f(\gamma) = \sqrt{\frac{\gamma}{\gamma+1}} \left(\frac{2}{\gamma+1}\right)^{1/(\gamma-1)} \approx 0.5135$. Here κ is the peaking factor, a value that is obtained numerically by calculating the flow after the aperture and comparing it with the equation above. This has been empirically measured to be approximately 2 for monoatonic gases. $\gamma = c_p/c_v$ is the heat capacity ratio, which is 5/3 for monoatomic gases.

Compare this model with another popular intensity model used by several researchers in the Bergen group, among others in their theoretical papers on helium microscope optimisation - to model the flow stemming from the nozzle [85, 86, 95]. This model stems directly from Pauly's ideal intensity equation [87] and barred some numerical accuracy lost in the author's approximations - and on the empirical measurement of the peaking factor - corresponds to eq. (2.7) divided by the peaking factor.

$$I = 0.155 \frac{P_0}{k_B T_0} (\frac{2 r_{nz}}{x_S+a})^2 \pi r_D^2 \sqrt{\frac{5 k_B T_0}{m}} = 0.62\sqrt{5/2} \frac{I_0}{f(\gamma)} \frac{r_D^2}{(x_S+a)^2} = 0.6077 I_{TG} \quad (2.8)$$

Where r_D is the radius of the detector downstream. Third, the intensity used by Bergin in his helium microscope optimisation paper, published after the Bergen optimisation papers. This intensity uses DePonte et al's center-line beam intensity (with a correction) [12, 30]. This is a model of the second type, in which an empirical formula for the dependency between the virtual source radius and the speed ratio of the beam is used (and therefore an inverse dependency on the speed ratio is introduced). In Bergin's derivation, the radius of the nozzle is not used, but instead the radius of the skimmer placed in front of the virtual source. Thus, he arrives at a similar quadratic dependency with the skimmer radius as Sikora does in the limit of small skimmers[13]:

$$I = \frac{0.18\pi^2 P_0 r_S^2}{\sqrt{m k_B T_0}} \frac{r_D^2}{S_{||}(x_S+a)^2} = \frac{1}{S_{||}} \frac{0.18\pi}{\sqrt{2} f(\gamma)} \frac{I_0}{r_{nz}^2} \frac{r_s^2 r_D^2}{(x_S+a)^2} \approx \frac{0.247866}{S_{||}} \left(\frac{r_s}{r_{nz}}\right)^2 I_{TG} \quad (2.9)$$

Note how all three empirical models have the same geometrical dependencies stemming from a spherically symmetrical expansion: the I_{TG} term. The intensity is then corrected

[13] In fact, both models are equivalent - barring the inverse the speed radius multiplying the formula [12].

upwards or downwards depending on further assumptions on the isentropic expansion and on the model used to explain the non-ideal behaviour of the beam.

The thermal-geometrical term I_{TG} gives a false image of reality as supersonically expanded atom beams decrease in intensity at a slower rate than a spherically symmetrical expansion. This is why corrections such as the full Sikora equation used by the Bergen group give a truer sense of the phenomena at play, let's revisit this equation at the limit of small skimmers (and generally of small exponents). This is a model of the third type, as Sikora's expression comes directly from integrating the beam's quitting surface. The model reads:

$$I_S = I_{TG}\left\{ S_i^2 \left(\frac{r_{\mathrm{S}}(R_{\mathrm{F}} + a)}{R_{\mathrm{F}}(R_{\mathrm{F}} - x_{\mathrm{S}} + a)} \right)^2 \right\}. \tag{2.10}$$

For a quitting surface at the skimmer $R_F = x_S$ we get:

$$I_S = I_{TG}\left\{ S_i^2 \left(\frac{r_{\mathrm{S}}(x_S + a)}{a x_S} \right)^2 \right\} = I_{TG}\left\{ S_i^2 \left(\frac{r_{\mathrm{S}}}{a} + \frac{r_{\mathrm{S}}}{x_S} \right)^2 \right\} \tag{2.11}$$

This equation adds three important (and physical) corrections: (i) the beam will be more intense the wider the skimmer is - which accounts for thermal components of the quitting surface. (ii) Higher speed ratios mean more intense beams - which is a measure of the quality of the supersonic expansion and its departure from a spherically symmetric expansion. (iii) Still, the closer you are to the beam source, the more intense the beam will be. Note that (i) is still an approximation and only holds for small skimmers - if the skimmer size is on the order of the size of the quitting surface increasing it further does not result in important intensity changes. Corrections such as the ones given by eq. (2.11) also have design implications: the beam intensity decreases slower than in the spherical case, which allows for larger technologically feasible microscopes. Optimising microscope designs disregarding this would correspond to ditching some of the benefits of a supersonic source in exchange for analytical simplicity. Therefore, it is important to be aware of these assumptions when facing microscope design (see section 2.6).

Skimmer effect

The intensity models discussed in the last section disregard any effect produced by the skimmer besides acting as an aperture. However, the reality is that skimmer interference is often a significant contributor to the beam's centre-line intensity - **see publication number 4 in this thesis** [86]. In its journey, a helium atom can see its trajectory perturbed by atoms backscattered from the skimmer, or more generally a perturbation of the flow caused by it.

Modelling the effect of the skimmer is a well-known challenge in helium beam experiments [23, 54, 107]. One of the most successful approximations to the problem is the one provided by Bird in the 1970s [18]. In this paper, Bird proposed the modified Knudsen number, and showed it to be a better predictor for skimmer interference than the Knudsen number. When designing a microscope, one should always aim for a modified Knudsen number larger than 1, as skimmer effects can decrease intensity by a factor of as much as 10 times [86]. The modified Knudsen number for a Lennard-Jones potential reads:

$$Kn^* = Kn\left(\frac{2}{5}S_{||}^2\right)^{-1/6} = \frac{1}{r_S\sigma\sqrt{2}n}\left(\frac{2}{5}S_{||}^2\right)^{-1/6}. \tag{2.12}$$

In here, the speed ratio term does not have any other effect than reducing the effective Knudsen number with respect to the normal Knudsen number. For a skimmer placed at a given distance x_S from the expansion, the true dominant factor is the skimmer radius r_S - smaller skimmers give larger Knudsen numbers. The Knudsen number can be easily approximated by the expression above and one can obtain the conditions in which the skimmer is well conditioned. In general, if one wants to control the optical properties of the beam, one must place the skimmer as close to the quitting surface as possible whilst having a radius that leads to a large enough modified Knudsen number. See [86] for a full data set and discussion on centre-line intensities.

Other effects

In addition to skimmer interference, helium atoms can interact with atoms scattered from any other element of the expansion chamber (also known as the background gas). Such interactions depend on the vacuum quality (pump capacity and in the case of a pulsed beam, size of the vacuum chamber) and can be modelled either through DSMC or through free molecular scattering. The latter is often preferred as it corresponds to a simple exponential law [54, 86, 107]:

$$\frac{I}{I_S} = \exp\left(-\sigma^2 n_{B_E} x_S - \sigma^2 n_{B_C} a\right). \tag{2.13}$$

Where σ is the scattering cross-section of the atoms and n_{B_E} and n_{B_C} are the background number densities in the expansion chamber and subsequent chamber. These background densities should be measured by a pressure gauge far away from the beam centre line. This contribution is often overlooked in microscope design as its both unavoidable and inconsequential.

2.4 Helium optics / Resolution limits

Once the supersonic expansion has been selected by a skimmer, the accelerated atoms continue to travel in straight lines through vacuum until they interact with the microscope optical elements.

In this regime, the behaviour of helium atoms can be modelled by atom optics through the wave-particle duality. This means that when compared to light or less massive corpuscles such as electrons, the theoretical resolution limit of helium atoms at the same energy is much higher [63]. This follows directly from the de Broglie wavelength equation: $\lambda_B = \frac{h}{p} = \frac{h}{\sqrt{2Em}}$. The mass of helium is about four orders of magnitude higher than the electron mass. Thus, at the same energy, the de-Broglie wavelength of neutral helium atoms will be two orders of magnitude smaller that of electrons. According to eq. (2.2) a room temperature helium beam has a wavelength of around 0.05 nm and an energy of 50 meV [16]. A beam cooled to 120 K (liquid nitrogen temperature) has a wavelength of around 0.1 nm and an energy of around 20 meV. However, the practical resolution limit of a helium microscope configuration is not given by the theoretical wavelength limit, but by aberration and diffraction (airy disk) broadening by the optical elements. As discussed in the introduction, two types of optical elements have been used, so far to successfully produce SHeM images: Fresnel zone plates and pinholes. Fresnel zone plates are a type of diffraction lens that focuses an incoming atomic or light beam into a small focal spot [27]. Pinholes are circular openings that restrict the size of the atom beam [110].

When referring to resolution, it is important to distinguish between the lateral resolution, determined by the size of the helium beam, and the "angular resolution", given by the solid angle covered by the detector opening. The lateral resolution is what impacts the minimum feature size that can be observed and therefore is referred in the field as "resolution". Diffraction with detecting apertures does not degrade the lateral resolution as in light optics, because helium microscopes image by measuring the flux through the aperture and not by projecting the image onto a sensor plane. Angular resolution determines the intensity of scattered helium in a particular direction. This is mainly of relevance for contrast, in particular for 3D imaging as multiple scattering makes it difficult to image high aspect ratio structures [8, 73].

The Newcastle group introduced the concepts supra- and sub-resolution to helium microscopy [44]. Supra resolution is the same as the lateral resolution, determined by the size of the helium beam. Sub-resolution refers to the fact that the wavelength of the helium atoms may introduce a contrast effect.

The difference between the resolutions of Fresnel zone plates and pinhole microscopes is given by the contributions of diffraction (airy disk) and aberration terms [80]. The square of the Full Width at Half Maximum[14] for the zone plate and the pinhole microscope can be written as:

$$\Phi_{\mathrm{PH}}^2 = O_{\mathrm{S}}^2 + \sigma_A^2 \tag{2.14}$$

$$\Phi_{\mathrm{ZP}}^2 = O_{\mathrm{S}}^2 + \sigma_A^2 + \sigma_{\mathrm{cm}}^2. \tag{2.15}$$

Where O_{S}^2 indicates the geometric optics contribution to the full width half maximum. That is to say, O_{S}^2 is the image of the source at the sample. For the zone plate microscope it is the demagnified image of the skimmer or a collimation aperture placed in front of the skimmer [48]. σ_A is the Airy disk contribution from edge diffraction from the zone plate or pinhole and σ_{cm} is a chromatic aberration term that appears for the case of the zone plate. The first equation holds under the assumption the Fresnel number is smaller than 1, which is the case for the limit of small pinholes. For Fresnel larger than 1 only the geometric optics term plays a role [85].

Besides the de-Broglie wavelength, there is no theoretical limit as to how small O_S can get. However, for the case of a pinhole, σ_A grows inversely with the pinhole radius: $1/r_{ph} \propto 1/O_S$ [85], thus the Airy term grows higher when one tries to decrease O_S. For the case of a zone plate, the resolution limit can be decreased by decreasing the zone plate radius r_{ZP} and the zone plate smallest zone width Δr. This is because the chromatic aberrations in a zone plate are proportional to its radius, while its Airy term depends linearly with Δr: $\sigma_A \propto \Delta r \propto O_S$. [95]. In other words, for a fixed zone plate radius, both the beam width and the Airy contribution decrease linearly with the same factor. This allows zone plates to reach significantly higher resolution (smaller spot size) than pinholes [12, 95].

The resolution limits for both instruments can be, in fact, explicitly obtained (see [12, 85, 95]). For a pinhole microscope:

$$\Phi_{PH}^{min} = K\sqrt{0.42\lambda W_{\mathrm{D}}\sqrt{3}}. \tag{2.16}$$

Where $K = 2\sqrt{2\ln 2/3}$ and W_{D} is the working distance. The 0.42 factor comes from the Airy disk standard deviation [78]. In a zone plate microscope the highest possible resolution is given by the width of the smallest zone (as the optical and Airy terms both

[14] The full width at half maximum of the beam's intensity profile [85].

linearly depend on Δr).

$$\Phi_{ZP}^{min} = K\sigma_A \approx \Delta r. \tag{2.17}$$

This is a well-known result obtained first for light optics [80]. In practice, this means that the resolution is limited by nanofabrication. It is difficult to make very small free-standing zones. For this reason, experiments have been done on a so-called Atom Sieve zone plate configuration. The atom sieve is a zone plate superimposed with a hole pattern. The fabrication limit is now determined by how small free-standing holes can be made, rather than how small free-standing zones. In fact, the resolution limit will be slightly smaller than the smallest free-standing hole, because the design can be made so that a hole covers two zones and the limiting factor remains the width of a zone Δr. The idea is adapted from photonics [68]. **See paper number 6 in this thesis for an implementation of this idea in neutral helium microscopy [37]**. The first focusing of helium atoms using an atom sieve was done in 2015 [36]. **See also [47], paper number 7 in this thesis, where the challenges associated with the construction of an atom sieve for SHeM are discussed.**

2.5 Detection technology

Detection remains the single biggest challenge in neutral helium microscopy. The big advantage of the technique - the inertness, low energy and surface sensitivity of the helium probe is its biggest disadvantage when it comes to detection. Up till now four types of neutral helium detectors have been reported in the literature: electron bombardment detectors [53], bolometers [106], Pitot tubes [38] and field ionisation detectors [84, 94] - including those that use resonance to improve the signal [28, 61]. So far, only electron bombardment detectors have been used in microscope design. This appears to be more a coincidence based on historical circumstances than anything else. Bolometers have traditionally been favoured in America since bolometers have been reported to be of equal efficiency when it comes to helium detection.

A key component of electron bombardment and field ionisation detectors is the ioniser. A substantial amount of work in this area has been performed by researchers in the University of Cambridge and elsewhere [2, 26, 29, 33, 53, 64, 67, 69]. Over time, successive iterations on the ioniser design have enabled ioniser efficiencies to routinely surpass $1{\cdot}10^{-3}$ - three orders of magnitude higher of what had been initially achieved [11]. We refer to Alderwick and Bergin's Ph.D. theses for a more detailed discussion of different ioniser designs [2, 11].

Once the helium atoms have been ionised, they need to be detected. To do so, they go

through an initial filtering step known as mass separation: designed to select only those ions that interest us (helium ions coming from the beam). In helium microscopy this is done through magnetic sectors [56] rather than quadruple mass filters [32], because they yield higher recorded intensities. Typically, helium atoms are directed from the ioniser to the mass separation stage and from the mass separation stage to the signal multiplier using ion optics [11, 102].

The signal multipliers used in SHeM are electron multipliers, typically tube-based multipliers known as channeltrons [98, 105]. In helium microscopy, electron multipliers must be used after the positively-charged helium ions have been "converted" to an equivalent amount of electrons. This is done through a conversion dynode, a mechanism that upon the impact of a charged ion emits secondary electrons [79]. For a comment on the dynode-multiplier design and set up the reader can check [11].

A lot of time and energy is being spent in order to increase the efficiency of neutral helium detectors. Especially promising are detector systems based on solenoidal ionisers, with recent work reaching a detector efficiency of as much as 0.5% - the highest obtained to date [14]. Another promising development is a recent framework aimed at optimising the balance between signal and temporal response in neutral helium detectors, with a reported signal improvement of 27% [82].

High-efficiency helium detectors may open the door for SHeM to resolve the scattering properties of the sample, akin to Helium Atom Scattering experiments. This would mean having an instrument able to resolve both the surface profile and its local structure from diffraction [8].

2.6 Optimal microscope configurations

The difficulties associated with detecting neutral helium atoms have prompted several researchers to try to optimise the design of helium microscopes. Most of these configurations aim to obtain a maximum beam intensity within a given resolution while satisfying reasonable technological constraints.

To date, there are four papers that aim to optimise the microscope design using a theoretical framework for the intensity. The first paper, written by Thomas Kaltenbacher [65] proposes a multi-objective optimisation approach to optimise a microscope composed of a pinhole and two zone plates. Unfortunately, Kaltenbacher does not consider the dependency of the intensity with the skimmer radius which is known to be crucial in the case of zone plate microscopes, rendering his approach unphysical in terms of the

intensity. The next two papers [85, 86], **corresponding to papers 1 and 2 in this thesis**, present analytical approximations to the optical configurations of a helium microscope, and the last paper by Bergin et al reiterate equivalent derivations with some small differences [12].

In Bergin's paper, a different equation for the chromatic aberration is used by fitting two parameters that produces smaller aberrations. Additionally, Sikora's intensity model for small skimmers is assumed throughout. The differences between Bergin's solution and ours stem from a small difference in the intensity model used, and in the way that the resolution of the microscope is modelled. Concretely, Bergin assumes that the skimmer is modelled by a Gaussian distribution placed *after the collimator* while we assume that the support of this distribution is limited by the skimmer as in geometric optics. This means that our approach produces a top-hat beam profile at high Fresnel numbers (no diffraction) while Bergin's produces a Gaussian profile. Experimental measurements of the profile of the beam in the pinhole set up by the Bergen group indicate that the beam is indeed more similar to a top hat than to a Gaussian (see Fig. 2.5). However, both approaches are similar and lead to the same qualitative conclusions on beam design. Note also that our work produces solutions valid for any value of W_D, while Bergin implicitly assumes $W_D \gg a$.

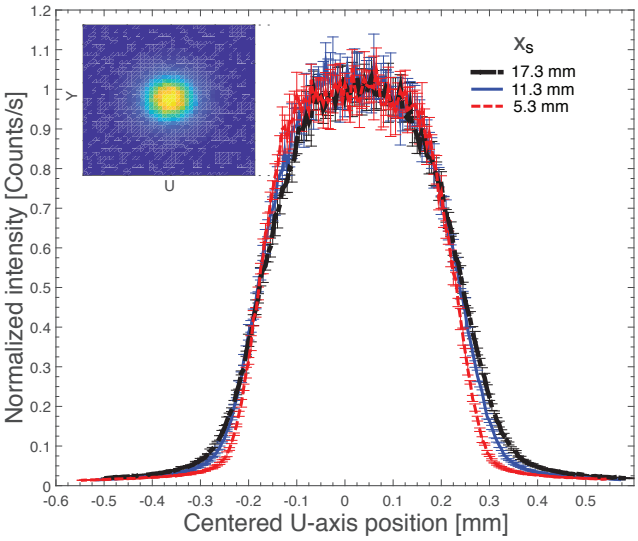

Figure 2.5: Measurements on the beam profile, here done for a cold source at 60 bar and a 390 µm diameter skimmer for three values of x_S. The complete intensity plot of the beam is shown in the upper left corner. Note how the flat top of the beam contrasts with the profile that one would expect from a Gaussian distribution. This image is obtained by moving the nozzle relative to the skimmer in 50 nanometer steps for three values of x_S. This image is reproduced from [86].

Figure 2.6: Simplified sketch of Witham and Sanchez pinhole set up [110]

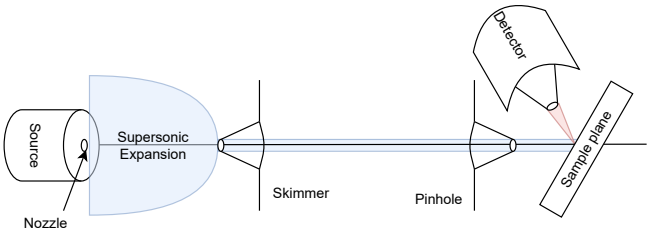

Figure 2.7: Simplified sketch of the microscope set up in Dastoor's group [42] .

We reproduce here our analytical solutions to this problem, as they are more general, and refer to chapter 4 for a complete analysis. For a pinhole configuration and $r_S \ll 1$, the radius of the pinhole and the skimmer at the intensity maximum are:

$$r_{\mathrm{ph}}^{\max} = \frac{\Phi a}{2K(a+W_{\mathrm{D}})} \approx \frac{\Phi}{2K}, \qquad a \gg W_{\mathrm{D}}. \tag{2.18}$$

$$r_{\mathrm{S}}^{\max} = \frac{\Phi a}{2W_{\mathrm{D}}K}. \tag{2.19}$$

Where Φ is the FWHM of the beam and $K = 2\sqrt{2\ln 2/3}$.

For a zone plate configuration analytical solutions are harder to obtain. So far, only one has been published: the optimal distance between the skimmer and the zone plate a, which corresponds to the solution of the following cubic equation:

$$a^3 + 2a^2\left(R_{\mathrm{F}} - \sqrt{3\Gamma}r_{\mathrm{zp}}\right) + aR_{\mathrm{F}}(R_{\mathrm{F}} - 4r_{\mathrm{zp}}\sqrt{3\Gamma}) = r_{\mathrm{zp}}\sqrt{3\Gamma}R_{\mathrm{F}}^2\left[\frac{2S^2\Phi'^2 + r_{\mathrm{zp}}^2(\Gamma-1)}{S^2\Phi'^2 - 0.5r_{\mathrm{zp}}^2}\right]. \tag{2.20}$$

Where $\Gamma \equiv \frac{1}{3}\left(\frac{2\Delta r}{\lambda}\right)^2$ is a constant of the problem which gives the relative size of the

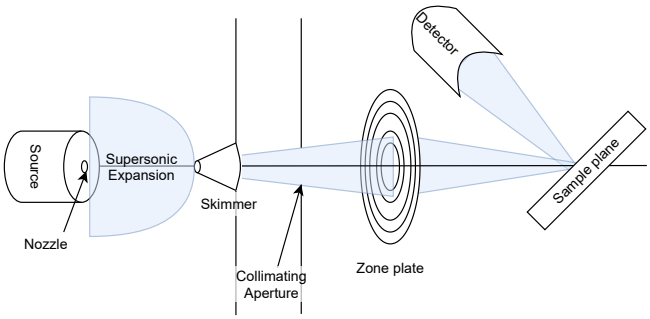

Figure 2.8: Simplified sketch of the zone plate set up showing how a Fresnel zone plate can be used to focus a helium beam .

smallest aperture of the zone plate compared with the average wavelength of the beam, usually $\Gamma \gg 1$. This approximation has been obtained under several assumptions listed in [95].

The work done in recent years on the issue of finding optimal configurations for helium microscopes has had two major impacts. First, it has shown that the designs used to that point were sub-optimal. In the case of the zone plate microscope the intensity could be increased by a factor of 7 compared to previous designs [95], and in the case of the pinhole microscope by 75% [85]. It has also led to a trend of designs using bigger skimmers and smaller pinhole-skimmer distances. The first was motivated by the realisation that increasing the skimmer distance had a significant effect on the centre line intensity, and the second was by the fact that in general smaller microscopes are more performant.

2.6.1 Microscopes with micro-skimmers

Initial designs of helium microscopes focused on using skimmers as small as technically feasible (below 1 µm) [38]. This was motivated by several reasons: first, research groups tried to obtain focal spots as small as possible, and micro-skimmers seemed the best way to go in the zone plate set up (see, for example, [35]). Second, central beam intensity models were misunderstood as independent on the skimmer radius (see, for example, [65]).

Partly due to these design mistakes, it became clear that centre-line intensities were a limiting factor. This triggered the work on microscope set up optimisation mentioned above. This work noted the important dependency of the centre-line intensity with the skimmer radius [12, 95], and cleared any confusion with regards to this issue.

Since then, new microscope designs use skimmers as big as possible within the desired resolution and taking into account skimmer interference at large Knudsen numbers as mentioned in section 2.3.2. This has the additional benefit that micro-skimmers are hard to produce, while larger micro-skimmers (with a diameter larger than 100 μm) can be easily machined [86].

2.7 Outlook: 3D imaging and beyond

Perhaps the most interesting perspective for helium microscopy is the potential to become a true nano-stereo microscope The success demonstrated by neutral helium microscopes in taking 2D images of microscopic samples has helped to increase the interest for imaging in three dimensions. In its simplest form, this can be done by measuring the displacement of particular points of an image when the sample is rotated by a given known angle. This technique has been demonstrated by Myles et al and has produced some basic three-dimensional reconstructions from neutral helium microscopy images [81].

To avoid the cumbersome point-by-point selection of this basic technique, Lambrick and Salvador developed Heliometric Stereo, an extension of Photometric stereo to helium microscopy [73] (**paper 5 in this thesis**). Due to helium microscopy images taken in an orthographic projection and constructed by imaging the sample point by point, photometric stereo can be easily translated to helium and it has an even easier practical implementation as the image acquisition conditions are highly controlled.

Heliometric stereo is based on the fact that the intensity signal measured in detectors placed in different angles will be different and depend on the tilting angle of the imaged surface. This dependency with the scattering distribution is both a curse and a blessing: on the one hand, for heliometric stereo to be implemented straightforwardly one must know the distribution. On the other hand, heliometric stereo sets the perfect conditions for estimating this distribution when it is unknown as it samples it for a variety of scattering angles. On top of this, there is increasing evidence that the scattering distribution of helium atoms from a broad arrange of samples is cosine, which makes the method straightforward to implement [43, 71, 72, 74].

This insight, added to the increased efficiency of neutral helium detectors, will allow scientists to design a highly multimodal SHeM. That is, a microscope that is able to resolve the 3D surface of any vacuum-compatible sample, and the scattering distribution of the beam.

Chapter 3

Conclusion

The work presented in this thesis focuses on addressing two research questions: what is the optimal configuration for a Scanning Helium Microscope, and whether a stereo-nanomicroscope can be designed using neutral helium atoms as the probing sample. These questions are then placed in the context of the broader research field, that spans several disciplines: from detector optimisation to beam measurement experiments.

Besides these two main research questions, some additional topics are addressed within their corresponding research papers. For example, the issue of building the focusing elements of the microscope, concretely an atom sieve, and whether theoretical models based on approximated solutions of the Boltzmann equation reproduce experimental findings.

When it comes to the two main research questions, both are addressed from a theoretical standing. The first two papers included in this thesis were the first to provide analytical solutions to the optimal optical configurations of SHeMs, and pave the way for smaller, more intense microscopes. Together with coetaneous improvements in detector efficiency (of more than two orders of magnitude), this will be used by the SHeM community to design the third generation of SHeMs.

The fifth paper included in this thesis demonstrates the possibility of designing a stereo helium microscope by adapting the technique of photometric stereo to helium. Besides its theoretical interest, the paper also includes design recommendations for a stereo-SHeM. In short: the introduction of at least four co-planar detectors - or, if that is not possible, the ability to rotate the sample about the beam axis. These findings will likely also enter the design consideration for next-generation SHeMs, and bring us closer to the realisation of a true non-destructive nano-stereomicroscope.

The remaining papers establish support for the theoretical models used for the beam's intensity and speed ratio (papers 3 and 4), and study several aspects of the zone plate microscope set up (papers 6 and 7). Accurately predicting the speed ratio is especially important for this set-up as this parameter determines the chromatic aberration of the beam. Similarly, the papers related to the construction of an atom sieve and the use of a zero-order filter propose significant improvements to helium zone plate microscopes. Atom sieves can be built with a smaller limit resolution than Fresnel zone plates because they are fully formed by pinholes. Similarly, the zero-order filtering approach provides a much narrower beam intensity profile at the sample plane, potentially improving imaging quality and resolution.

3.1 Future work

The success of Scanning Helium Microscopes as standard experimental and industrial tools largely depends on whether the theoretical findings presented in this thesis are successfully applied in microscope design. This work significantly impacts all three main microscope configurations - namely the pinhole, zone plate and stereo set ups. The pinhole set up is the less impacted, as current designs would just have to be slightly corrected by shortening the microscope length and adapting the pinhole size.

Besides correcting the pinhole design, future work will largely consist of implementing the proposed modifications in zone plate and stereo microscopes. For the zone plate set up, a design based on an atom sieve and a zero-order filter blocker with the parameters carefully adjusted as predicted theoretically would produce the highest resolution microscope to date. For the stereo microscope, an initial corroboration could be done by obtaining a 3D profile using a one-detector pinhole microscope and sample rotation. Once the principle is demonstrated, the proposed set up with multiple detectors should be built using recent advancements in detector technology to enhance its reconstruction accuracy.

Chapter 4

Publications

Article I

4.1 Theoretical model of the helium pinhole microscope

Adrià Salvador Palau, Gianangelo Bracco, Bodil Holst

Physical Review A, **94**, 6 (2016)

Theoretical model of the helium pinhole microscope

Adrià Salvador Palau,[1] Gianangelo Bracco,[1,2] and Bodil Holst[1,*]

[1] *Department of Physics and Technology, University of Bergen, Allégaten 55, 5007 Bergen, Norway*
[2] *CNR-IMEM, Department of Physics, University of Genova, V Dodecaneso 33, 16146 Genova, Italy*

(Dated: June 24, 2021)

In recent years, the development of neutral helium microscopes has gained increasing interest. The low energy, charge neutrality and inertness of the helium atoms makes helium microscopy an attractive candidate for the imaging of a range of samples. The simplest neutral helium microscope is the so called pinhole microscope. It consists of a supersonic expansion helium beam collimated by two consecutive apertures (skimmer and pinhole), which together determine the beam spot size and hence the resolution at a given working distance to the sample. Due to the high ionization potential of neutral helium atoms, it is difficult to build efficient helium detectors. Therefore, it is crucial to optimize the microscope design to maximize the intensity for a given resolution and working distance. So far this has not been addressed in the literature. Here we present an optimisation model for the helium pinhole microscope system. We show that for a given resolution and working distance there is a single intensity maximum. Further we show that with present day state of the art detector technology (ionisation efficiency $1 \cdot 10^{-3}$), a resolution of the order of 600 nm at a working distance of 3 mm is possible. In order to make this quantification we have assumed a Lambertian reflecting surface and calculated the beam spot size that gives a signal 100 cts/s within a solid angle of 0.02π sr, following an existing design. Reducing the working distance to the micron range leads to an improved resolution of around 40 nm.

I. INTRODUCTION

Neutral helium microscopy, short Nemi or SHem (scanning helium microscopy), refers to the use of a beam of neutral helium atoms as an imaging probe. The neutral helium beam is created by a supersonic expansion and has a very low energy (typically less than 0.1 eV), which means that the atoms map the outermost electron density distribution of the sample and do not penetrate into solid material [1, 2]. This makes neutral helium microscopy particularly suited for the investigation of fragile and/or insulating materials, nano-coatings and surfaces with high aspect ratios. By using two detectors it should even be possible to create a stereo microscope on the nano scale. Alternatively a small working distance helium microscope can be used to investigate all samples presently examined with scanning probe techniques.

The first neutral helium microscope images were published in 2008 [3]. They were transmission, shadow images of a porous structure. The images were obtained by using a Fresnel zone plate to focus a beam down to 3 µm and later to less than 1 µm, scan the beam across the sample and record the transmitted intensity [4]. Early focussing experiments using neutral helium atoms were carried out by O.Carnal et al, Holst and Allison and Doak et al. in the 1990's [5–7]. Since then two other research groups have managed to obtain helium microscope images in reflection with micron range resolution using pinhole microscopes [8–11]. The first reflection images were published in 2011 by Withman and Sanchez using a setup with just a pinhole and no skimmer [8]. This setup still claims the best resolution achieved so far with a helium microscope: 350 nm [12]. Mathematically the Witham-Sanchez setup can be seen as a special case of the two aperture microscope model we present in this paper, with the skimmer being very big. We therefore do not discuss it further.

A diagram of a helium pinhole microscope can be found in Fig. 1. The basic idea is simple: the supersonic expansion beam is collimated by two consecutive apertures, which we refer to as skimmer and pinhole. The pinhole is placed after the skimmer and is kept at a certain working distance from the sample plane. The resolution of the microscope is then determined by the spot size of the beam on the sample plane. In this work we define the resolution as the full width at half maximum intensity of the beam spot. The beam scattered off the sample is then collected at a given solid angle using a detector, and the variation in this signal, while the sample is scanned, is used to create an image.

The aim of this paper is to determine the geometry of the pinhole system which gives the maximum signal intensity in the beam spot on the sample for a given resolution. Our basic assumption is that the beam is created in a supersonic expansion. In such an expansion, the helium gas expands into vacuum through a nozzle that must have a diameter much bigger than the mean free path of the gas particles. The atoms then collide with each other until eventually collisions cease and the atoms are travelling in free molecular flow without interacting. The central part of the beam is selected by a collimating aperture (skimmer), which is conically-shaped to reduce backscattering of atoms into the beam. The supersonic expansion is chosen over for example an effusive source because it gives the highest centre line intensity [13].

A common way to describe a supersonic expansion the-

* Corresponding author, Bodil.Holst@uib.no

oretically is the quitting surface model. Here, the spherical quitting surface represents the distance from the nozzle where the atoms have reached molecular flow and are no longer interacting [14]. The velocity distribution of the atoms along the surface can be described by the most probable velocity $\bar{v}$ along the parallel direction (meaning the radial direction from the centre of propagation). This velocity is given together with either a single parallel temperature or, in a more detailed description, by a pair of temperatures $T_{||}, T_{\perp}$ associated to the orthogonal components of the velocity in spherical coordinates. At the quitting surface, the perpendicular temperature, $T_{\perp}$ must be much smaller than the parallel temperature $T_{||}$. In this paper, the conditions at the quitting surface are calculated solving Boltzmann equation [15–17]. Negligible collisional coupling is assumed at a distance where the temperatures of the beam fulfil $T_{\perp}/T_{||} \leq 0.01$. Stopping the integration at $T_{\perp}/T_{||} = 0.005$ was shown to affect the flow parameters by less than 0.1% with respect to the proposed setting $T_{\perp}/T_{||} \leq 0.01$ [18].

For a single temperature and constant density along the quitting surface, an analytical approximation for the intensity exists, obtained by Sikora in 1973 [14]. For a pair of temperatures, a numerical integral must be implemented [19]. From now on, we will name the single temperature solution *Sikora's approximation* and, following the convention in literature, the dual temperature model *ellipsoidal quitting surface model*. Both models are explained in detail in Section II.

In practise, one will often measure a reduction in the signal intensity compared to the theoretical model due to backscattering of atoms into the beam. For the most efficient microscope, an optimization of the expansion parameters (distance between nozzle and skimmer, beam pressure and temperature etc.) is therefore important. This has been studied for example in [20–22], and is not a topic of this paper. Hence, in this work all the parameters relative to the expansion enter as constants in the equations: most probable velocity and perpendicular and parallel temperatures of the beam, distance between the skimmer and the nozzle and the position of the quitting surface relative to the skimmer.

To simplify the calculations we consider not only the resolution but also the working distance as a constant of the optimization; The behaviour of the system with respect to the working distance is monotone and easy to calculate if need be. From an experimental point of view the working distance is an important parameter. The larger the working distance the more flexible the microscope will be with respect to what kind of samples can be investigated.

This leaves us with three variable parameters as can be seen from Fig. 1: The aperture openings, r_{S} and r_{ph}, and the distance between them, a. Once the desired resolution and working distance have been chosen, the system is reduced to a two variable optimization problem using the optical equations of the system, which we describe in the next section. The intensity can then be calculated over a wide span of combinations and plotted in a single graph. A single clear maximum is found that gives the best theoretical design of a pinhole helium microscope. In praxis it may be necessary to configure the microscope away from the maximum due to technical constraints. The calculations clearly show how much signal is lost compared to the maximum and provide the best choice from the subset of realisable microscopes.

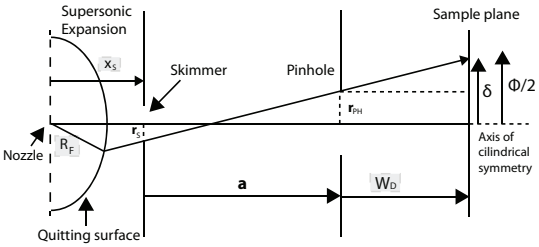

FIG. 1. Simplified illustration of a pinhole microscope setup. The constants of the problem are marked in grey boxes. W_{D} is the working distance, δ is the geometrical spread of the beam, Φ is the focal spot size. Due to diffraction effects 2δ is not always equal to Φ. r_{S} and r_{ph} are the radius of the skimmer and the radius of the pinhole respectively and a is the distance between the skimmer and the pinhole. Note that the system is cylindrically symmetric about the main axis.

II. THEORETICAL FOUNDATION

A. The optical system

The expression for the spread of the beam depends on the optical regime of the system, determined by the Fresnel number, F [23]:

$$\mathrm{F} = \frac{r_{\mathrm{ph}}^2}{W_D \lambda}. \tag{1}$$

Where r_{ph} is the radius of the pinhole and W_{D} is the working distance (see Fig. 1). λ is the average de Broglie wavelength of the beam, given by $\lambda = h/m\bar{v}$. m is the mass of a helium atom and $\bar{v}$ is the most probable velocity of helium atoms along the radial direction.

An analytical expression can be easily found that incorporates the two extreme optical cases: Geometrical optics (F»1) and Fraunhofer diffraction (F«1). We will see that for most real designs this expression suffices to determine the dynamics of the system. Using simple ray-optics, the geometrical image of the aperture projected onto the sample plane can be found to be:

$$\delta = r_{\mathrm{ph}} \left(1 + \frac{W_{\mathrm{D}}}{a}\right) + \frac{W_{\mathrm{D}} r_{\mathrm{S}}}{a}, \tag{2}$$

where a is the distance between the skimmer and the pinhole and r_{S} is the radius of the skimmer. To obtain

the standard deviation, σ, of the beam intensity profile we must convolute the geometrical image of the aperture with the Point Spread Function (PSF) of the diffraction trough the aperture. We know that the PSF of the Fraunhofer diffraction across a circular aperture can be approximated by a Gaussian with the following standard deviation [24]:

$$\sigma_{\mathrm{A}} = \frac{0.42\lambda W_{\mathrm{D}}}{2r_{\mathrm{ph}}}. \tag{3}$$

This convolution has a well-known result (from any treaty on Gaussian error propagation combining Gaussians with top-hat uncertainty distributions):

$$\sigma^2 = \frac{1}{3}\left(\delta^2 + 3\sigma_A^2(1-\theta(\mathrm{F}))\right). \tag{4}$$

$\theta(\mathrm{F})$ is the Heaviside step function, which ensures that the diffraction effect only appears for $\mathrm{F} < 1$.

Additionally, there will be an effect on the standard deviation stemming from the inhomogeneity of the intensity profile along the perpendicular direction. The intensity value, at big enough distances from the axis of symmetry, decreases significantly. However, if the nozzle-pinhole distance is much bigger than the pinhole radius, the intensity profile at the pinhole is approximately constant. This is often used in literature, where a center line intensity is calculated and then multiplied by the surface of the detector [14]. For the case of helium microscopes, where the nozzle-pinhole distance is typically of the order of several centimetres and the pinhole radius is of the order of a few micrometres, this approximation can always be used and eq. (4) suffices.

We define the focal spot size of the beam as the full width at half maximum associated to the standard deviation of the beam's intensity profile:

$$\begin{aligned}\Phi &= 2\sqrt{2\ln 2/3}\sqrt{\delta^2 + 3\sigma_A^2(1-\theta(\mathrm{F}))} \\ &\equiv K\sqrt{\delta^2 + 3\sigma_A^2(1-\theta(\mathrm{F}))}.\end{aligned} \tag{5}$$

For micrometer resolutions, we will see that due to the small wavelength of a helium beam, the Fresnel number is typically bigger than one (see Appendix A for a detailed description of the focal spot formula choice). This allows a purely geometrical optics treatment of the focal spot size. However, we choose to develop a formula that covers both extreme cases because sometimes the optimization procedure involves a wide span of Fresnel numbers.

From eq. (5) one can find three relations between r_{S}, a and r_{ph} (see Appendix B for the derivation). We consider two of these expressions, $r_{\mathrm{ph}} \to r_{\mathrm{ph}}(a, r_{\mathrm{S}})$ and $a \to a(r_{\mathrm{ph}}, r_{\mathrm{S}})$:

$$\begin{aligned}K^2(1+\gamma)^2 r_{\mathrm{ph}}^4 + 2K^2 r_{\mathrm{S}}\gamma(1+\gamma)r_{\mathrm{ph}}^3 + (K^2\gamma^2 r_{\mathrm{S}}^2 - \Phi^2)r_{\mathrm{ph}}^2 \\ + K^2(1-\theta(\mathrm{F}))\epsilon = 0.\end{aligned} \tag{6}$$

Where $\gamma = \frac{W_{\mathrm{D}}}{a}$ and $\epsilon = 3W_{\mathrm{D}}^2(0.42\lambda/2)^2$. And:

$$\begin{aligned}a^2\left(\frac{\Phi^2}{K^2} - r_{\mathrm{ph}}^2 - 3\sigma_A^2(1-\theta(\mathrm{F}))\right) - a\cdot 2r_{\mathrm{ph}}W_{\mathrm{D}}(r_{\mathrm{ph}}+r_{\mathrm{S}}) \\ - W_{\mathrm{D}}^2(r_{\mathrm{ph}}+r_{\mathrm{S}})^2 = 0.\end{aligned} \tag{7}$$

The equation (6) for the pinhole radius is a quartic equation in the Fraunhofer regime because the same focal spot size can be obtained when the diffraction term dominates over the geometrical term and vice-versa. In practice, the equation gives two real, positive solutions for which the one with maximum pinhole radius and therefore maximum intensity is chosen.

For the case of a (eq. (7)), the solution is uni-evaluated because there exist only one positive root:

$$a = \frac{r_{\mathrm{ph}}W_{\mathrm{D}}}{A}\left(r_{\mathrm{ph}} + r_{\mathrm{S}} \pm \sqrt{(r_{\mathrm{ph}}+r_{\mathrm{S}})^2 + A(1 + 2\frac{r_{\mathrm{S}}}{r_{\mathrm{ph}}} + \frac{r_{\mathrm{S}}^2}{r_{\mathrm{ph}}^2})}\right). \tag{8}$$

Where $A = \frac{\Phi^2}{K^2} - r_{\mathrm{ph}}^2 - 3\sigma_A^2(1-\theta(\mathrm{F}))$, if A is negative, a is also negative or non-real (except the case when the square root is 0) and if A is positive, we must take the positive root to ensure a positive value of a.

Using eq. (6) or (7), the system can be reduced to a two-variable optimization system.

B. The intensity models

As discussed in the introduction, the most general model of the intensity field of a supersonic helium beam is the ellipsoidal quitting surface model, with an elliptical velocity distribution:

$$\begin{aligned}f_{\mathrm{ell}}(\vec{v}) = n\left(\frac{m}{2\pi k_{\mathrm{B}}T_{||}}\right)^{\frac{1}{2}}\left(\frac{m}{2\pi k_{\mathrm{B}}T_{\perp}}\right)\cdot \\ \exp\left(-\frac{m}{2k_{\mathrm{B}}T_{||}}(v_{||}-\bar{v})^2 - \frac{m}{2k_{\mathrm{B}}T_{\perp}}v_{\perp}^2\right).\end{aligned} \tag{9}$$

Where m is the mass of a helium atom, k_{B} is Boltzmann's constant and $T_{||}$ and $T_{\perp}$ are the parallel and perpendicular temperatures. $\bar{v}$ is the most probable velocity of the beam along the radial direction and $v_{||}$ and $v_{\perp}$ are the parallel and perpendicular components of the velocity, corresponding to the radial and angular components in spherical coordinates.

Integrating eq. (9) over the quitting surface, across the skimmer and over the pinhole surface, one obtains the following intensity equation:

$$\begin{aligned}I_{\mathrm{D}} = \frac{\tau I_0}{2\pi a^2 R_{\mathrm{F}}^2 \mathrm{L}}\int_0^{r_{\mathrm{ph}}}\int_0^{r_{\mathrm{S}}}\int_0^{\pi} g(\delta) r\cdot\rho\cos^3\beta\cdot\epsilon^3 \\ e^{-S^2(1-\epsilon^2\cos^2\theta)}D(b)d\rho dr d\alpha.\end{aligned} \tag{10}$$

Where R_F is the radius of the quitting surface and $S = \bar{v}/\sqrt{2k_B T_{||}/m}$ is the parallel speed ratio. I_0 is the total intensity stemming from a nozzle of diameter d_n [13]:

$$I_0 = \kappa \frac{P_0}{k_B T_0} \sqrt{\frac{2k_B T_0}{m}} \left(\frac{\pi}{4} d_n^2\right) \sqrt{\frac{\gamma}{\gamma+1}} \left(\frac{2}{\gamma+1}\right)^{1/(\gamma-1)}. \tag{11}$$

Where P_0 and T_0 are the thermodynamic pressure and temperature of the helium gas before it undergoes the expansion. $\gamma = C_P/C_V = 5/3$ for helium. $\kappa = 2$ is a peak factor as defined in [13]. All other parameters are defined in detail in Appendix C. Unfortunately, the ellipsoidal quitting surface model has no simple analytical solutions and is often slow to compute over a wide space of solutions.

Using the quitting surface model with a single radial velocity distribution it can be shown that for $S \geq 5$, $r_S \ll R_F - x_S$, the intensity arriving at a small pinhole reads [14]:

$$I_S = \frac{I_0 \pi r_{ph}^2}{(R_F + a)^2} \left(1 - \exp\left[-S^2 \left(\frac{r_S (R_F + a)}{R_F (R_F - x_S + a)}\right)^2\right]\right). \tag{12}$$

Where $R_F - x_S$ is the axial distance between the quitting surface and the tip of the skimmer. This equation was obtained independently by Sikora and Andersen [14] and thus we refer to it as Sikora's approximation as mentioned in the introduction.

We can use this equation together with eq. (6) for F»1 to obtain a simple analytical equation for the position of the intensity maximum, given either a or r_S is taken to be constant.

$$\nabla I_S(r_S, a) = (0, 0), \qquad \partial_a^2 I < 0, \qquad \partial_{r_S}^2 I < 0. \tag{13}$$

Which corresponds to a subset of the solutions of the following equation:

$$\nabla \frac{r_{ph}^2}{(R_F + a)^2} \left(1 - \exp\left[-S^2 \left(\frac{r_S (R_F + a)}{R_F (R_F - x_S + a)}\right)^2\right]\right) = 0. \tag{14}$$

Where the radius of the pinhole, for $F \gg 1$ can be obtained from eq. (6), which reduces to a quadratic equation with a single physical solution:

$$r_{ph} = \frac{\frac{\Phi a}{K} - W_D r_S}{a + W_D}. \tag{15}$$

From eq. (14), it can be shown that the maximum of intensity is at (see Appendix D):

$$r_S^{max} = \frac{\Phi a}{2 W_D K}, \tag{16}$$

as long as the following condition holds:

$$\left(S \frac{R_F + a}{R_F (R_F - x_S + a)}\right)^2 \left(\frac{\Phi a}{W_D K} r_S - r_S^2\right) \ll 1. \tag{17}$$

The radius of the pinhole at the intensity maximum is then:

$$r_{ph}^{max} = \frac{\Phi a}{2K(a + W_D)} \approx \frac{\Phi}{2K}, \qquad a \gg W_D. \tag{18}$$

Comparing with eq. (15) one sees the importance of condition (17), because if $W_D r_S \ll \frac{\Phi a}{K}$ and $a \gg W_D$ is imposed, from eq. (15) one obtains:

$$r_{ph} \approx \frac{\Phi}{K}. \tag{19}$$

Which corresponds to the case where the beam does not widen after the pinhole.

Unfortunately, no analytical solution has been found for a^{max}, neither in this limit nor in the general case. However, the value can be easily obtained numerically (see Section III). The triplet $(a^{max}, r_{ph}^{max}, r_S^{max})$ is the optimal solution for the design of a helium microscope of a given resolution Φ, given working distance, W_D, and given conditions at the supersonic expansion P_0, T_0.

III. RESULTS AND DISCUSSION

A. An example: $\Phi = 5\mu m$, $W_D = 3$ mm.

To illustrate the optimization method we consider the pinhole helium microscope presented by Barr et al [22]. This microscope has been successfully built and has produced some of the best helium microscopy images at a resolution of 5μm. We evaluate how the microscope could be optimized using the same resolution and working distance as in the original setup.

By means of eq. (6), the problem is restricted to two variables: the skimmer-pinhole distance a and the skimmer aperture r_S. The intensity is then calculated by means of the ellipsoidal quitting surface model, eq. (10). A clear maximum of intensity can be observed which smoothly decreases along the line described by eq. (16) (see Fig. 2), giving the subset of maximums of intensity for each fixed a value. The Fresnel number is plotted at Fig. 3 . We see that in this case, the maximum is situated at F=19.42 , reasonably within the geometrical approximation.

It is also interesting to compare the intensity given by the ellipsoidal quitting surface model to the intensity given by Sikora's approximation. Both models peak at slightly different intensities, therefore it is useful to plot the fraction of the normalized intensities.

$$\zeta = \frac{I_S \cdot \max(I_D)}{I_D \cdot \max(I_S)}. \tag{20}$$

From Fig. 4 we see that Sikora's approximation fits well the behaviour of the quitting surface model near the intensity peak. Sikora's approximation diverges from the ellipsoidal quitting surface model at larger skimmers as expected theoretically, as it is in this regime that the component of the perpendicular temperature starts being important.

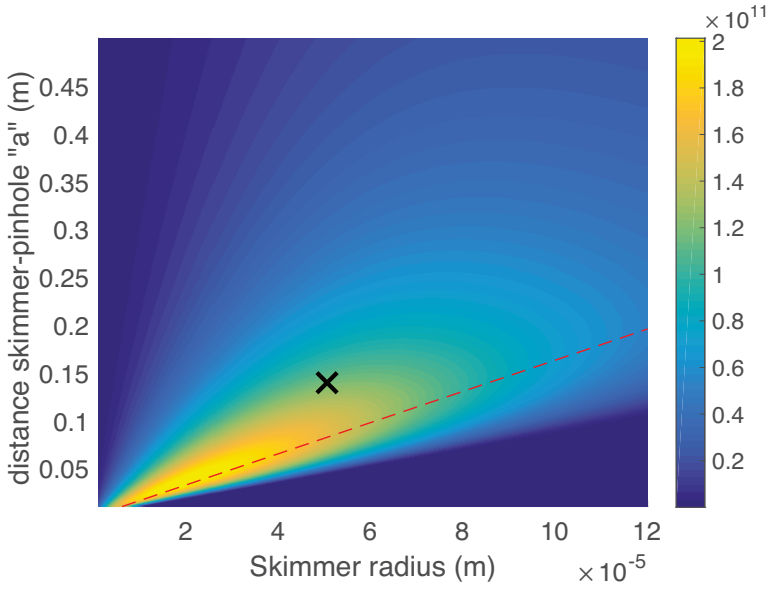

FIG. 2. Intensity (part/s) crossing a focal spot ($\Phi = 5\,\mu$m) of a pinhole helium microscope for a span of values of r_S and a. The dashed line shows the subset of maximal solutions given by eq. (16). The intensity was calculated using the ellipsoidal quitting surface model with the following parameters: $T_{||} = 0.00802$ K, $T_\perp = 0.00209$ K, $R_F = 0.0112$ m, $x_S = 0.0113$ m, $T_0 = 309$ K, $P_0 = 161$ Bar. The working distance of the microscope is set at 0.003 m, and the nozzle diameter d_n at 10µm. The maximum lies at $(a^{\max}, r_{ph}^{\max}, r_S^{\max}) = (0.035\,\text{m}, 1.7886 \cdot 10^{-6}\,\text{m}, 2.0250 \cdot 10^{-5}\,\text{m})$. The black cross indicates the configuration corresponding to the microscope designed by Barr et al [22]. The optimized design would increase the intensity by 75%. However, a distance of only 35 mm between the two pinholes would not be so easy to realize experimentally with a good pumping speed.

B. Parametric dependences

The optimisation presented in Fig. 2 was performed for a room temperature supersonic expansion beam, as in the original experiment. We compare now with a *cold* beam, which can be obtained by cooling the nozzle. Cooling the beam increases the flow and changes the velocity distribution. For the cold beam calculation we choose the temperature 150 K because this is a temperature which can easily be kept stable using for example liquid nitrogen cooling. The position of the maximum changes significantly. The optimized $a^{\max}$ value decreases from 0.035 m to 0.026 m, and the optimized skimmer radius decreases from 20.2 µm to 14.7 µm. The pinhole radius at the maximum remains nearly constant (see Fig. 5).

The pinhole microscope system shows a clear maximum for a particularly defined supersonic expansion. However, the position of the intensity maximum varies with the expansion parameters. Such dependences can be easily evaluated using Sikora's approximation.

The dependence of the intensity maxima with the speed ratio follows the expected trend. Higher speed ratios favour smaller microscopes and skimmer openings (see Fig. 6) due to the weaker divergence of the beam. This also yields higher maximum intensity values. One sees that the pinhole size depends very weakly of the speed ratio as predicted by eq. (18). The radius of the skimmer depends on the speed ratio through the value of a (see eq. (16)).

The intensity decreases and the skimmer-pinhole distance increases strongly with the working distance, W_D. In other words, the working distance should always be chosen as small as possible (see Fig. 7). The optimum pinhole radius decreases with the working distance, because it is the main contributor to the widening of the beam. The skimmer radius shows a more complicated dependence, reaching a minimum at low working distances and then increasing smoothly. This must be understood in combination with the skimmer-pinhole distance a, which at small working distances is very small and favours a small skimmer radius to lower the divergence of the beam (see Fig. 7).

Regarding the dependences with the focal spot size Φ, the intensity shows the expected quadratic dependence, similar to the area of a disk. This quadratic relation makes it hard to design high resolution microscopes with

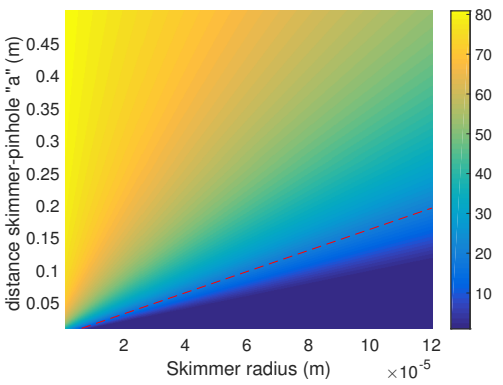

FIG. 3. Fresnel number for a span of values of r_S and a. The Fresnel number was calculated assuming an average wavelength of $\bar{\lambda} = 8.2535 \cdot 10^{-11}$ m. Note that the line of maximal intensity given by eq. (16) spans a region where $F \gtrsim 10$. The working distance of the microscope is set to 3 mm, and the resolution to 5 µm.

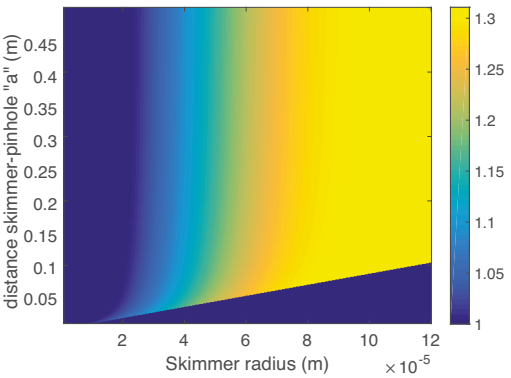

FIG. 4. Sikora's approximation intensity divided by the ellipsoidal model, ζ for a span of values of r_S and a (eq. (20)). Note how both models diverge at high apertures due to the omission of the perpendicular temperature effect in Sikora's approximation. At the intensity maximum both models behave similarly with $\zeta = 0.9722$.

enough intensity (see Fig. 8). Both aperture radii increase with the focal spot, the pinhole does it quasi linearly following eq. (16) while the skimmer shows a more complicated dependence. The skimmer-pinhole distance a peaks at small focal spot sizes and then decreases monotonically as the influence of the airy diffraction disappears (see Fig. 8).

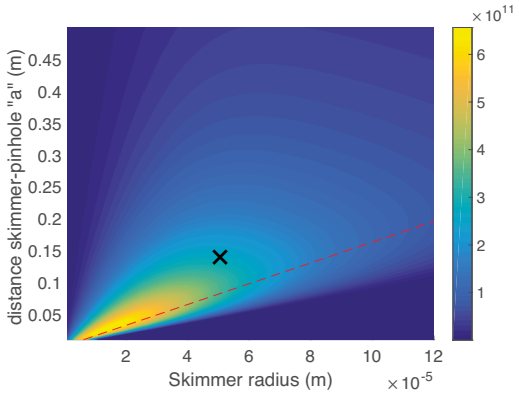

FIG. 5. Intensity (part/s) crossing the focal spot of a pinhole helium microscope for a span of values of r_S and a. The dashed line shows the subset of maximal solutions given by eq. (16). The intensity was calculated using the ellipsoidal quitting surface model with the following parameters: $T_{||} = 0.0054$ K, $T_\perp = 0.0039$ K, $R_F = 0.0112$ m, $x_s = 0.0113$ m, $T_0 = 131.3$ K, $P_0 = 161$ Bar. The working distance of the microscope is set to 3 mm, and the resolution to 5 µm. The maximum lies at $(a^{\max}, r_{\text{ph}}^{\max}, r_S^{\max}) = (0.0260, 1.7714 \cdot 10^{-6}, 1.4750 \cdot 10^{-5})$ m. The black cross indicates the configuration corresponding to the microscope designed by Barr et al [22].

C. Realistic resolution limits

Using Sikora's approximation, one can easily obtain the resolution limit of a realisable pinhole helium microscope. A minimal count rate of 100 counts per second is chosen and compared with the expected signal for the optimal microscope at each resolution. Lambertian reflection [25] at $\pi/4$ radians relative to the sample normal is assumed with the detector opening area perpendicular to the reflected direction. The intensity seen at a given solid angle is given by Lambert cosine law:

$$I_\Omega = I_{\text{inc}} \cos(\pi/4)\Omega_D = I_{\text{inc}} \cos^2(\pi/4)\frac{\pi R^2}{d^2}. \qquad (21)$$

Where I_{inc} is the incident intensity per solid angle, which corresponds to I_s/π. Ω_D is the solid angle seen by a detector with a circular opening of radius R at a distance d, oriented as described above. By considering the efficiency of the detector, the formula giving the expected count-rate reads:

$$N = \frac{I_s^{optim} R^2}{d^2}\eta \cos(\frac{\pi}{4})^2 \approx 1.4 \cdot 10^{-7} I_s^{optim}. \qquad (22)$$

Where R is the detector radius, chosen to be 0.5 mm. d is the distance between the sample surface and the detector, set at 3 mm. This corresponds to the solid angle of 0.02 π sr mentioned in the abstract. I_s^{optim} is the optimized

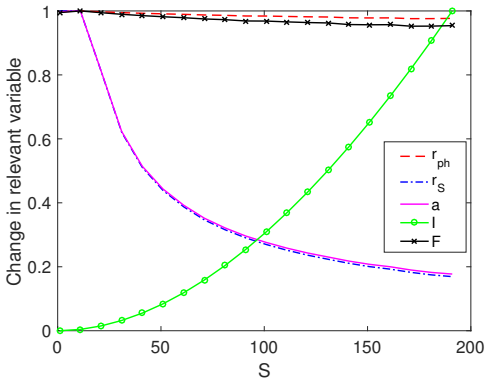

FIG. 6. Normalised optimized parameters of a pinhole helium microscope for a span of values of the speed ratio S. The intensity was calculated using Sikora's approximation with the following parameters: $T_0 = 131.3$ K, $P_0 = 161$ Bar. The working distance of the microscope is set at 0.003 m.

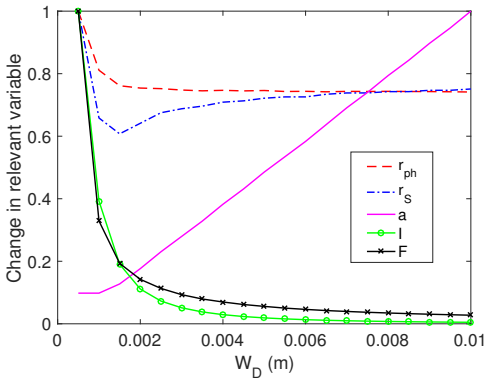

FIG. 7. Normalised optimized parameters of a pinhole helium microscope for a span of values of the working distance W_{D}. The intensity was calculated using Sikora's approximation with the following parameters: $T_0 = 131.3$ K, $P_0 = 161$ Bar. The working distance of the microscope is set at 0.003 m.

intensity using Sikora's approximation. η is the efficiency of the detector, chosen to be between 10^{-3} [26–29] and 10^{-5} (an upper limit estimate for a typical, commercial mass spectrometer). Note that all parameters are set as in the paper by Barr et al. [22]. As we can see in Fig. 9, sub-micrometer resolutions are achievable with a reasonable count rate.

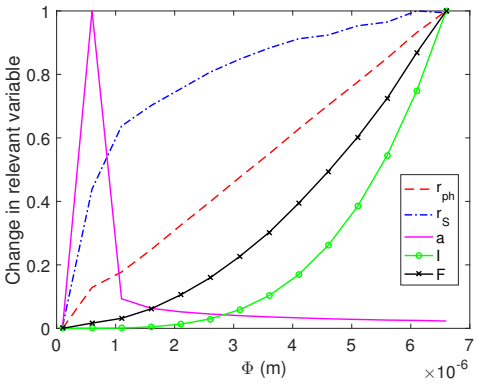

FIG. 8. Normalised optimized parameters of a pinhole helium microscope for a span of values of the focal spot Φ. The intensity was calculated using Sikora's approximation with the following parameters: $T_0 = 131.3$ K, $P_0 = 161$ Bar. The working distance of the microscope is set at 0.003 m.

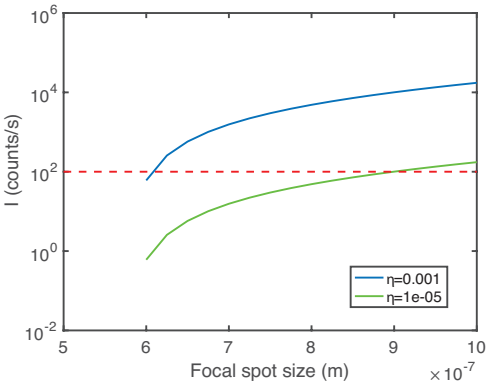

FIG. 9. Optimized count rate for different focal spot sizes. The intensity was calculated using Sikora's approximation with the following parameters: $T_0 = 131.3$ K, $P_0 = 161$ Bar. The working distance of the microscope is set at 0.003 m. The efficiency of the detector, placed at $\pi/4$ radians is $\eta = 1 \cdot 10^{-5}$ (lower line) or $\eta = 1 \cdot 10^{-3}$ (upper line).

D. The small working distance limit

A small W_{D} helium microscope would be suitable for the investigation of all samples currently investigated with scanning probe techniques as discussed in the introduction. In the limit $W_{\mathrm{D}} r_{\mathrm{S}}/a \ll r_{\mathrm{ph}}$, for $\eta = 0.001$, the maximum of intensity is always higher than 100 counts per second for a collection solid angle of 0.02π sr. Therefore, the minimal achievable resolution is determined by

the theoretical trade-off between Airy diffraction and beam widening in eq. (5). The smallest achievable Φ is given by the point where decreasing further the pinhole radius does not improve the resolution any more, because the diffraction term dominates. For a working distance of 10 µm, this point corresponds to (see Appendix E):

$$\Phi = K\sqrt{0.42\lambda W_{\mathrm{D}}\sqrt{3}} \approx 33\,\mathrm{nm}. \tag{23}$$

With $\lambda = 8.25 \cdot 10^{-11}$ m, corresponding to $T_0 = 131.3$ K. This equation is derived under the assumption $W_{\mathrm{D}} r_{\mathrm{S}}/a \ll r_{\mathrm{ph}}$, which for the case of $W_{\mathrm{D}} = 10$ µm only holds weakly, the real resolution is a bit higher, 40 nm. This has been calculated setting a lower bound for a of 5 cm, chosen as a technical constraint for the placement of a pump in the skimmer-pinhole chamber. A helium pinhole microscope with a working distance of 10 µm has already been demonstrated by Witham and Sanchez in their 350 nm resolution configuration [12].

IV. CONCLUSION

We present a theoretical model of a neutral helium pinhole microscope using the quitting surface approach to model the source intensity. We show that for a given microscope resolution, working distance, and constant source characteristics, there is a unique optimized solution. This optimized solution gives the sizes of the two apertures of the system and their separation. Our pinhole microscope model can easily be adapted to other source models considering attenuation of the beam or describing the flow of other atoms or molecules. The adaptation is done simply by changing the intensity equation whilst using the same optical expressions. We show that with the quitting surface intensity source model, high intensity, helium pinhole microscopes with a resolution down to around 40 nm are realisable. Further we suggest that an intensity improvement of up to 75% for existing helium pinhole microscopes is theoretically possible (although a practical realisation can be challenging).

APPENDIX A: THE FOCAL SPOT SIZE AT HIGH FRESNEL NUMBERS

If the Fresnel number is sufficiently high, a ray-optics treatment is sufficient to describe the focal spot size. In such a treatment, no convolution with a diffraction function is needed and the beam has the form of a top-hat function. Therefore, in such cases the resolution of the microscope is best understood by redefining the constant K in a way that the FWHM of the beam is simply the width of the top-hat function. This corresponds to $K \equiv 2$ so that eq. (5) reduces to:

$$\Phi = 2\delta. \tag{A1}$$

APPENDIX B: DERIVATION OF EQ. (6) AND (7)

Deriving eq. (6) and (7) is a simple algebra problem consisting of extracting $a \to a(r_{\mathrm{ph}}, r_{\mathrm{S}})$ and $r_{\mathrm{ph}} \to r_{\mathrm{ph}}(a, r_{\mathrm{S}})$ from eq. (5). We shall begin by obtaining $r_{\mathrm{ph}} \to r_{\mathrm{ph}}(a, r_{\mathrm{S}})$. Squaring eq. (5) one obtains:

$$\begin{aligned}\frac{\Phi^2}{K^2} &= \delta^2 + 3\sigma_{\mathrm{A}}^2(1-\theta(F)) \\ &= r_{\mathrm{ph}}^2\left(1+\frac{W_{\mathrm{D}}}{a}\right)^2 + 2r_{\mathrm{ph}}\left(1+\frac{W_{\mathrm{D}}}{a}\right)\frac{W_{\mathrm{D}} r_{\mathrm{S}}}{a} \\ &+ \left(\frac{W_{\mathrm{D}} r_{\mathrm{S}}}{a}\right)^2 + 3\left(\frac{0.42\lambda}{2}\right)^2 \frac{W_{\mathrm{D}}^2}{r_{\mathrm{ph}}^2}(1-\theta(F)).\end{aligned} \tag{B1}$$

Defining $\gamma = \frac{W_{\mathrm{D}}}{a}$ and $\epsilon = 3W_{\mathrm{D}}^2(0.42\lambda/2)^2$, multiplying by r_{ph}^2 and grouping by powers of r_{ph}, one obtains eq. (6). To obtain eq. (7) we can use eq. (B1), and multiply by a^2:

$$\begin{aligned}&\frac{\Phi^2}{K^2}a^2 \\ &= a^2 r_{\mathrm{ph}}^2\left(1+\frac{W_{\mathrm{D}}}{a}\right)^2 + 2a^2 r_{\mathrm{ph}}\left(1+\frac{W_{\mathrm{D}}}{a}\right)\frac{W_{\mathrm{D}} r_{\mathrm{S}}}{a} \\ &+ a^2\left(\frac{W_{\mathrm{D}} r_{\mathrm{S}}}{a}\right)^2 + 3a^2\left(\frac{0.42\lambda}{2}\right)^2 \frac{W_{\mathrm{D}}^2}{r_{\mathrm{ph}}^2}(1-\theta(F)).\end{aligned} \tag{B2}$$

Expanding the quadratic sums and grouping by powers of a, eq. (7) is recovered.

APPENDIX C: THE ELLIPSOIDAL QUITTING SURFACE MODEL

The ellipsoidal quitting surface model used in this paper is an extension of Sikora's ellipsoidal quitting surface model with the difference that the skimmer is allowed to be in a different position than the quitting surface. Such a model was published by U. Bossel in 1974 [19]. Unfortunately the original paper has a couple of typos so we describe here the corrected equations in detail. The main intensity equation arriving at the pinhole is eq. (10):

$$\begin{aligned}I_{\mathrm{D}} = \frac{\tau I_0}{2\pi a^2 R_{\mathrm{F}}^2 \mathrm{L}} \int_0^{r_{\mathrm{ph}}} \int_0^{r_{\mathrm{S}}} \int_0^{\pi} g(\delta) r \cdot \rho \cos^3\beta \cdot \epsilon^3 \\ e^{-S^2(1-\epsilon^2\cos^2\theta)} D(b) d\rho dr d\alpha.\end{aligned} \tag{C1}$$

Where R_{F} is the radius of the quitting surface and $S = \bar{v}/\sqrt{2k_{\mathrm{B}}T_{||}/m}$ is the parallel speed ratio. $\epsilon \equiv \left(\left(\tau\sin^2\theta + \cos^2\theta\right)^{-1/2}\right.$, $\tau \equiv \frac{T_{\parallel}}{T_{\perp}}$ are auxiliary functions. The function D(b) is defined as follows:

$$D(b) \equiv \frac{2}{\sqrt{\pi}} b e^{-b^2} + \left(2b^2+1\right)\left[1 + erf(b)\right], \quad b \equiv S\epsilon\cos\theta. \tag{C2}$$

Where I_0 is defined in eq. (11). $g(\delta)$ is obtained from the angular term in eq. (12) of Beijerinck and Verster paper [13] (in Bossel's work a $\cos^2$ function is chosen instead [19]):

$$g(\delta) = \cos^3\left(\frac{\pi\theta}{2\theta_0}\right), \qquad \theta_0 = \frac{\pi}{2}\sqrt{\frac{\gamma+1}{\gamma-1}-1} = \frac{\pi}{2}. \tag{C3}$$

Where $\gamma = C_P/C_V = 5/3$ for helium has been used. L corresponds to the integration of $g(\delta)$ along the half sphere (all the intensity emitted by the source is set to be contained in $g(\delta)$).

$$L \equiv \int_0^{\frac{\pi}{2}} g(\delta)\sin\delta d\delta = \frac{1}{4}. \tag{C4}$$

ρ is the radial coordinate at the pinhole plane and r is the radial coordinate at the skimmer plane. The angles β, α and θ are shown in Fig. 10. The analytical expressions that relate them to the radial coordinates of the system follow:

$$\cos\beta = \frac{a}{\sqrt{a^2+(r\sin\alpha)^2+(\rho-r\cos\alpha)^2}}, \quad a = x_D - x_S. \tag{C5}$$

$$\cos\theta = \frac{x_R(x_D-x_R)-y_R^2+z_R(\rho-z_R)}{R_F\sqrt{(x_D-x_R)^2+y_R^2+(\rho-z_R)^2}}. \tag{C6}$$

Where:

$$x_R = x_D - \xi(x_D-x_S), \qquad y_R = r\sin\alpha\left(\frac{x_D-x_R}{x_D-x_S}\right),$$

$$z_R = r\cos\alpha\left(\frac{x_D-x_R}{x_D-x_S}\right) - \rho\left(\frac{x_D-x_R}{x_D-x_S}\right) + \rho, \tag{C7}$$

are the Cartesian coordinates of a point **P** on the quitting surface (see Fig. 10).

$$\xi = \frac{B-\sqrt{B^2-AC}}{A}. \tag{C8}$$

$$A \equiv (x_D-x_S)^2 + (r\sin\alpha)^2 + (\rho-r\cos\alpha)^2, \tag{C9}$$

$$B = x_D(x_D-x_S) + \rho(\rho-r\cos\alpha), \tag{C10}$$

$$C = x_D^2 + \rho^2 - R_F^2. \tag{C11}$$

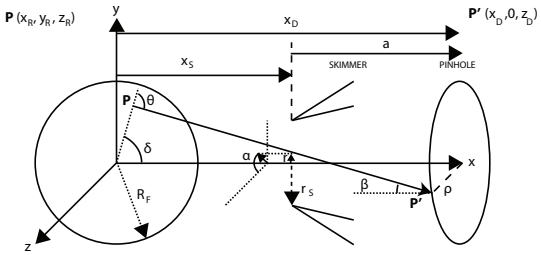

FIG. 10. Illustration of all variables used in the ellipsoidal quitting surface model. **P** is a point on the quitting surface from which a particle leaves in a straight trajectory until **P'**, a point placed on the pinhole plane. The point on the quitting surface is given by the set of Cartesian coordinates (x_R, y_R, z_R), which can be related to the polar coordinates r, α, ρ for further integration. x_S is the distance from the nozzle to the skimmer and x_D is the distance from the nozzle to the pinhole. Therefore $a = x_D - x_S$. The angles β and θ can also be expressed in terms of r, α and ρ.

APPENDIX D: DERIVATION OF EQ. (16)

To obtain eq. (16) we must differentiate I_S with respect to the skimmer radius and set it equal to 0 (eq. (12)). To do so we will first need to introduce eq. (15) in eq. (12) in order to obtain $I_S \to I_S(a, r_S)$. Once this is done, defining $D^2 \equiv \left(\frac{S(R_F+a)}{R_F(R_F-x_S+a)}\right)^2$ and taking the derivative, we obtain:

$$2D^2 r_S e^{-D^2 r_S^2}\left(\frac{\Phi a}{K} - W_D r_S\right)^2 - 2W_D(1-e^{-D^2 r_S^2})\left(\frac{\Phi a}{K} - W_D r_S\right) = 0, \tag{D1}$$

which reduces to:

$$e^{-D^2 r_S^2}\left(2D^2 r_S\left(\frac{\Phi a}{K} - W_D r_S\right) + 2W_D\right) = 2W_D. \tag{D2}$$

Taking the natural logarithm we get:

$$D^2 r_S^2 = \ln\left(1 + D^2\left[\frac{\Phi a}{W_D K} r_S - r_S^2\right]\right). \tag{D3}$$

Now, if $D^2\left[\frac{\Phi a}{W_D K} r_S - r_S^2\right] \ll 1$, we can expand the logarithm at first order using Taylor series. Thanks to eq. (15) we know that this condition corresponds to the case of small pinholes (or of small D^2).

$$r_S^2 \approx \frac{\Phi a}{W_D K} r_S - r_S^2 \to r_S \approx \frac{\Phi a}{2W_D K}. \tag{D4}$$

To proof that this corresponds to a maximum of the intensity function, we must show that the second derivative of eq. (12) respect the skimmer radius is negative. The

second derivative evaluated at eq. (D4) reads (out of a positive constant C^2):

$$C^2\frac{d^2}{dr_{\rm S}^2}I_{\rm S} = -\left(\frac{\Phi a D}{2K}\right)^2 e^{-D^2 r_{\rm S}^2}\left[\frac{D^2\Phi^2 a^2}{W_{\rm D}^2 K^2}+6\right]+2W_{\rm D}^2\left(1-e^{-D^2 r_{\rm S}^2}\right) \tag{D5}$$

Where we have not evaluated $r_{\rm S}$ in the exponentials in purpose, because we want to use $D^2\left[\frac{\Phi a}{W_{\rm D}K}r_{\rm S}-r_{\rm S}^2\right]\approx D^2 r_{\rm s}^2 \ll 1$. By combining this condition with eq. (D5), one obtains:

$$C^2\frac{d^2}{dr_{\rm S}^2}I_{\rm S} \approx -\left(\frac{\Phi a D}{2K}\right)^2\left[\frac{D^2\Phi^2 a^2}{W_{\rm D}^2 K^2}+6\right] < 0. \tag{D6}$$

V. APPENDIX E: DERIVATION OF EQ. (23)

One can derive the low limit working distance resolution limit directly from eq. (5):

$$\Phi = K\sqrt{\delta^2+3\sigma_A^2(1-\theta(\mathrm{F}))}. \tag{E1}$$

At the low resolution limit (very small pinholes), F is smaller than 1 and diffraction terms are present. The working distance is assumed to be very small, i.e.:

$$\frac{W_{\rm D}r_{\rm S}}{a} \ll r_{\rm ph}, \qquad \frac{W_{\rm D}}{a} \ll 1. \tag{E2}$$

Eq. (E1) is then reduced to:

$$\Phi = K\sqrt{r_{\rm ph}^2+3\sigma_A^2} = \sqrt{r_{\rm ph}^2+3\left(\frac{0.42\lambda W_{\rm D}}{2r_{\rm ph}}\right)^2}. \tag{E3}$$

One can find that $\frac{\partial}{\partial r_{\rm ph}}\Phi^2=0$, $\frac{\partial^2}{\partial^2 r_{\rm ph}}\Phi^2>0$ if:

$$r_{\rm ph} = \sqrt{\sqrt{3}\frac{0.42\lambda W_{\rm D}}{2}}. \tag{E4}$$

Which gives, the minimum resolution limit:

$$\Phi = K\sqrt{0.42\lambda W_{\rm D}\sqrt{3}}. \tag{E5}$$

[1] G. Bracco and B. Holst, "Surface Science Techniques," (Springer, 2013).
[2] D. Farias, G.H Rieder Rep. Prog. Phys. **61**, 1575-1664 (1998).
[3] M. Koch, S. Rehbein, G. Schmahl, T. Reisinger, G. Bracco, W. E. Ernst, and B. Holst, J. Microsc. **229**, 1 (2008).
[4] S. D. Eder, T. Reisinger, M. M. Greve, G. Bracco, and B. Holst, New. J. Phys. **14**, 73014 (2012).
[5] O. Carnal, M. Sigel, T. Sleator, H. Takuma, and J. Mlynek, Phys. Rev. Lett. **67**, 3231 (1991).
[6] B. Holst and W. Allison, Nature **390**, 244 (1997).
[7] R. B. Doak, R. E. Grisenti, S. Rehbein, G. Schmahl, J. P. Toennies, and C. Wöll, Phys. Rev. Lett. **83**, 4229 (1999).
[8] P. Witham and E. Sanchez, Rev. Sci. Instrum. **82**, 103705 (2011).
[9] P. Witham and E. Sanchez, Cryst. Res. Technol. **29**, 690 (2014).
[10] A. Fahy, M. Barr, J. Martens, and P. Dastoor, Rev. Sci. Instrum **86**, 023704 (2015).
[11] M. Barr, A. Fahy, J. Martens, A. P. Jardine, D. J. Ward, J. Ellis, W. Allison, and P. C. Dastoor, Nat. Commun. **7**, 10189 (2016).
[12] P. Witham and E. Sanchez, J. Microsc. **248**, 223 (2012).
[13] H. C. W. Beijerinck and N. F. Verster, Physica C **111**, 327 (1981).
[14] G. S. Sikora, *Analysis of asymptotic behavior of free jets: Prediction of Molecular Beam Instensity and Velocity Distributions*, Ph.D. thesis, Princeton (1973).
[15] J. Toennies and K. Winkelmann, J. Chem. Phys. **66**, 3965 (1977).
[16] T. Reisinger, G. Bracco, S. Rehbein, G. Schmahl, W. E. Ernst, and B. Holst, J. Phys. Chem A **111**, 12620 (2007).
[17] L. Pedemonte and G. Bracco, J. Chem. Phys. **119**, 1433 (2003).
[18] S. D. Eder, G. Bracco, T. Kaltenbacher, and B. Holst, J. Phys. Chem A **118**, 4 (2014).
[19] U. Bossel, *Skimming of Molecular Beams from Diverging Non-equilibrium Gas Jets*, Deutsche Luft- und Raumfahrt. Forschungsbericht (Deutsche Forschungs-und Versuchsanstalt für Luft-und Raumfahrt, 1974).
[20] H. C. W. Beijerinck, R. J. F. V. Gerwen, E. R. T. Kerstel, J. F. M. Martens, E. J. W. V. Vliembergen, M. Smits, and G. H. Kaashoek, Chem. Phys. **96**, 153 (1985).
[21] H. Hedgeland, A. P. Jardine, W. Allison, and J. Ellis, Rev. Sci. Instrum. **76**, 123111 (2005).
[22] M. Barr, A. Fahy, A. Jardine, J. Ellis, D. Ward, D. A. Maclaren, W. Allison, and P. C. Dastoor, Nucl. Instrum. Methods **B 340**, 76 (2014).
[23] E. Hecht, *Optics*, edited by A. Black, Vol. 4 (Addison Wesley, 2002).
[24] T. Stewart McKechnie, *General Theory of Light Propagation and Imaging Through the Atmosphere*, 1st ed.

(Springer, 2016) p. 624.
[25] J. H. Lambert, *Photometria, sive De mensura et gradibus luminus, colorum et umbrae* (1760).
[26] M. Matsuki, *Company MB Scientific, Private communication, detector available on a commercial basis upon request*.
[27] M. DeKieviet, D. Dubbers, M. Klein, U. Pieles, and C. Schmidt, Rev. Sci. Instrum. **71**, 123301 (2000).
[28] A. R. Alderwick, A. P. Jardine, H. Hedgeland, D. A. MacLaren, W. Allison, and J. Ellis, Rev. Sci. Instrum. **79** (2008), 10.1063/1.3030858.
[29] W. Allison, *Private Communication*
.

Article 2

4.2 Theoretical model of the helium zone plate microscope

Adrià Salvador Palau, Gianangelo Bracco, Bodil Holst

Physical Review A, **95**, 1 (2017)

A theoretical model of the helium zone plate microscope

Adrià Salvador Palau,[1] Gianangelo Bracco,[1,2] and Bodil Holst[1]

[1] *Department of Physics and Technology, University of Bergen, Allégaten 55, 5007 Bergen, Norway*
[2] *CNR-IMEM, Department of Physics, University of Genova, V Dodecaneso 33, 16146 Genova, Italy*

(Dated: September 21, 2016)

Neutral helium microscopy is a new technique currently under development. Its advantages are the low energy, charge neutrality and inertness of the helium atoms, a potential large depth of field and the fact that the helium atoms do not penetrate into any solid material. This opens, among others, for the creation of an instrument that can measure surface topology on the nano scale even on surfaces with high aspect ratios. One of the most promising designs for helium microscopy is the zone plate microscope. It consists of a supersonic expansion helium beam collimated by an aperture (skimmer) focused by a Fresnel zone plate onto a sample. The resolution is determined by the focal spot size, Φ, which depends on the size of the skimmer, the optics of the system and on the velocity spread of the beam through the chromatic aberrations of the zone plate. An important factor for the optics of the zone plate is the width of the outermost zone, Δr, which is fabrication limited to around 10 nm with present day state of the art technology. Due to the high ionization potential of neutral helium atoms, it is difficult to build efficient helium detectors. Therefore it is crucial to optimize the microscope design to maximize the intensity for a given resolution and width of the outermost zone. So far this has not been addressed in the literature. Here we present an optimization model for the helium zone plate microscope. Assuming constant Δr and Φ, we are able to reduce the problem to a two variable problem (zone plate radius and object distance) and we show that for a given beam temperature and pressure there is always a single intensity maximum. We compare our model with the highest resolution zone plate focussing images published and show that the intensity can be increased 7 times. Changing Δr to 10 nm leads to a further increase in intensity of more than 8000 times. Finally we show that with present day state of the art detector technology (ionisation efficiency 1×10^{-3}), a resolution of the order of 10 nm is possible. In order to make this quantification we have assumed a Lambertian reflecting surface and calculated the beam spot size that gives a signal 100 cts/s within a solid angle of 0.02 sr, following an existing helium microscope design.

I. INTRODUCTION

In a neutral helium microscope, short Nemi or SHeM (scanning helium microscope) a beam of neutral helium atoms is created by a supersonic expansion. An image is obtained by measuring either a reflected or transmitted signal as the helium beam is scanned across the sample. The energy of the beam is very low (less than 0.1 eV for a wavelength of 0.1 nm), which means that the atoms map the outermost electron density distribution of the sample and do not penetrate into solid material [1]. These properties make neutral helium microscopy suited for the investigation of nano-coatings, fragile and/or insulating surfaces and surface structures with high aspect ratios. By using for example a two detector setup it should even be possible to create a nano stereo microscope which can measure surface topography on the nano scale. If a small working distance is applied, the helium microscope can be used to investigate samples presently examined with scanning probe techniques, with the advantage that the helium beam offers completely standardised imaging properties.

The first neutral helium microscope images were published in 2008 [2]. They were transmission, shadow images of porous structures, obtained by scanning a beam focussed down to 2 µm using a Fresnel zone plate. Since then, two other research groups have managed to obtain helium microscope images in reflection with micron range resolution using pinhole microscopes [3–6]. The first reflection images were published in 2011 by Withman and Sanchez using a setup with just a pinhole and no skimmer [3]. This setup still claims the best resolution achieved so far with a helium microscope: 350 nm [7]. The theoretical resolution limit of a pinhole microscope is discussed in detail in [8].

The first helium atom focussing with a Fresnel zone plate was carried out by Carnal et al. using a beam of metastable helium [9]. Because the helium atoms do not penetrate into any solids, any transmission optical element used must be of the binary type with either completely transparent or completely opaque areas. The first focussing of a neutral, ground state helium beam with a zone plate was carried out by Doak et al. [10]. Both of these experiments used the classical Fresnel-Soret zone plate with alternating transparent and opaque zones. The Beynon-Gabor zone plate, which is also binary, has been suggested as an alternative attractive candidate for focusing of helium atoms [11]. The main advantage of the Beynon-Gabor zone plate is that it has no higher order foci. Unfortunately it is very challenging to fabricate. In 2015 a new optical diffraction element "the atom sieve" was introduced and focussing down to 3.6 µm diameter was demonstrated. The atom sieve was inspired by the photon sieve, which was invented in 2001 and originally intended for applications with soft X-rays [12]. It is a structure consisting of pinholes of varying size arranged

across the Fresnel zones in such a manner that it is possible to focus to a spot with a diameter smaller than the smallest pinhole. In addition, higher order diffraction and secondary maxima can be suppressed by several orders of magnitude. The original photon sieve as well as the first atom sieve are based on Fresnel-Soret zone plates. Other configurations have been suggested, for example, a Beynon-Gabor zone plate based photon sieve [13]. The great advantage of the atom sieve is that it is much easier to fabricate free standing holes than free standing rods, such as they are needed in a standard binary Fresnel zone plate. This is particularly important because the width of the outermost zone is a critical factor for the achievable resolution as will be discussed in the next section. It is reasonable to assume that fabrication of holes down to 10 nm should be possible [14].

A drawback of all zone plates is that only a fraction of the incident beam intensity goes into the first order focus. For the Fresnel-Soret zone plate as well as for the Beynon-Gabor zone plate the fraction is around 10% (zone plate efficiency). This is discussed in detail in [11]. The transmission window for the atom sieve can be adjusted to yield an intensity which is at least half the intensity of a standard Fresnel-Soret zone plate [12]. Alternative zone plate designs, where the first zones are blocked to facilitate zone plate stability and filtering of the zero order diffraction term, typically have a transmitted intensity higher than the atom sieve but lower than the Fresnel-Soret zone plate [15]. A further drawback is the presence of chromatic aberrations. This is particularly an issue for helium microscopy because the beam has a pressure dependent velocity spread. This is discussed in detail in the paper.

It should be mentioned that there is an alternative class of focussing element for neutral helium optics, namely mirrors [16–18]. The advantage of mirrors is that they have no chromatic aberrations so that the velocity spread of the beam does not play a role, though there will be a certain signal loss through diffraction and scattering from steps and point defects as well as inelastic scattering. The fabrication limit induced by the width of the outermost zone is also not an issue, so that the mirrors can in principle be made much larger. The use of graphene as a mirror coating gives an inert and very stable surface [19]. Quantum reflection for focusing has also been demonstrated [20]. Unfortunately, until now, it has not been possible to control the curvature of mirrors with high enough precision, so that Fresnel zone plate based optical elements remain the most promising approach for the focusing of neutral atom and molecular beams.

A diagram of a helium zone plate microscope can be found in Fig. 1. The basic idea is simple: the supersonic expansion helium beam is collimated by a conically shaped aperture, which we refer to as skimmer. An image of the skimmer opening is focussed onto a sample plane by a Fresnel zone plate. The resolution of the microscope is then determined by the focal spot size of the beam on the sample plane. In this work we define the resolution as the full width at half maximum intensity of the beam spot. The beam scattered off the sample is then collected at a given solid angle using a detector, and the variation in this signal, while the sample is scanned, is used to create an image. Alternatively the transmitted beam is detected by a detector placed behind a porous sample.

The aim of this paper is to determine the geometry of the zone plate system which gives the maximum signal intensity in the beam spot on the sample for a given resolution and given width of the outermost zone of the zone plate. Our basic assumption is that the beam is created in a supersonic expansion. For completeness we cite here the detailed description of how we model the source. The description is taken from [8]. In a supersonic expansion, the helium gas expands into vacuum through a nozzle that must have a diameter much bigger than the mean free path of the gas particles. The atoms then collide with each other until eventually collisions cease and the atoms are travelling in free molecular flow without interacting. The supersonic expansion is chosen over for example an effusive source because it gives the highest centre line intensity [21].

A common way to describe a supersonic expansion theoretically is the quitting surface model. Here, the spherical quitting surface represents the distance from the nozzle where the atoms have reached molecular flow and are no longer interacting [22]. The velocity distribution of the atoms along the surface can be described by the most probable velocity $\bar{v}$ along the parallel direction (meaning the radial direction from the centre of propagation). This velocity is given together with either a single parallel temperature or, in a more detailed description, by a pair of temperatures $T_{||}, T_{\perp}$ associated to the orthogonal components of the velocity in spherical coordinates. At the quitting surface, the perpendicular temperature, $T_{\perp}$ must be much smaller than the parallel temperature $T_{||}$. In this paper, the conditions at the quitting surface are calculated solving Boltzmann equation [23–25]. Negligible collisional coupling is assumed at a distance where the temperatures of the beam fulfill $T_{\perp}/T_{||} \leq 0.01$. Stopping the integration at $T_{\perp}/T_{||} = 0.005$ has shown to affect the flow parameters by less than 0.1% [26]. For a single temperature and constant density along the quitting surface, an analytical approximation for the intensity exists, obtained by Sikora in 1973 [22]. For a pair of temperatures, a numerical integral must be implemented [27]. From now on, we will name the single temperature solution *Sikora's approximation* and, following the convention in literature, the dual temperature model *ellipsoidal quitting surface model*. Both models are explained in detail in Section II.

Apart from the intensity contributions from the quitting surface model, one often measures an intensity reduction due to backscattering of atoms into the beam line. For a complete analysis, an optimization of the expansion parameters (nozzle-skimmer distance, beam pressure and temperature etc.) is therefore important.

This is not a topic of this paper and has been studied for example in [28–30]. Therefore, all the parameters relative to the expansion are considered constant in the equations. These correspond to the most probable velocity, the perpendicular and parallel temperatures of the beam, the skimmer-nozzle distance and the position of the quitting surface relative to the skimmer.

We choose two further parameters to be constant: the resolution and the width of the outermost zone. The behaviour of the system with respect to the width of the outermost zone is monotone and easy to calculate if need be. This leaves us with four variables as can be seen from Fig. 1: The skimmer opening, r_{S}, the zone plate radius r_{zp} the object distance, a, and the image distance, b. We show that this reduces to a two variable optimization problem using the optical equations of the system, which we describe in the next section. The intensity can then be calculated over a wide span of combinations and plotted in a single graph.

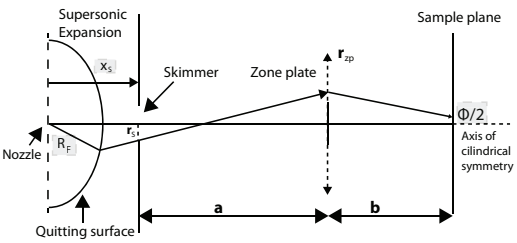

FIG. 1. Diagram of a zone plate microscope setup. The constants of the problem are marked in grey boxes. b is the working distance, Φ is the focal spot size. r_{S} and r_{zp} are the radius of the skimmer and the radius of the zone plate respectively and a is the distance between the skimmer and the zone plate. Note that the system is cylindrically symmetric about the main axis.

II. THEORETICAL FOUNDATION

A. The optical system

The size of the focal spot generated by a Fresnel zone plate by imaging an aperture of radius r_{S} is given by a convolution of the chromatic aberration term of the zone plate, σ_{cm}, the aperture (here, the skimmer), and the Airy diffraction term σ_{A} [15]. Both σ_{cm} and σ_{A} can be assumed to be Gaussian contributions, because the nature of the velocity spread from where the aberrations stem is Gaussian (eq. (13)) and the first ring of the Airy term approximates well to a Gaussian [31]. The skimmer is assumed to approximate to a step function and thus carries a $1/\sqrt{3}$ term in the convolution [8, 15].

The assumption that the skimmer approximates to a step function gives a maximum bound to the focal spot size. In reality, the intensity distribution decreases significantly along the skimmer radius for large skimmers placed close to the quitting surface. This has been experimentally investigated in [24, 26]. In this paper, we assume that the quitting surface is close enough to the skimmer so that the skimmer directly determines the object of the optical system. In general, for resolutions on the order of less than 1 µm, the skimmers needed for optimal design are sufficiently small compared to the radius of the quitting surface to justify such an assumption, regardless of how close the quitting surface is to the skimmer. It must be noted that the step function assumption is only used when determining the optic equations of the system. For the intensity model used in Sec. III to calculate the intensity of the focal spot, the real intensity profile and angular spread of the beam is considered with no further assumptions.

The standard deviation resulting from the convolution is multiplied by $2\sqrt{2\ln(2)}$ to obtain its Full Width at Half Maximum (FWHM):

$$\Phi = 2\sqrt{2\ln(2)}\sqrt{\sigma_{\mathrm{cm}}^2 + \sigma_{\mathrm{A}}^2 + \left(\frac{M r_{\mathrm{S}}}{\sqrt{3}}\right)^2} \equiv K\sqrt{\sigma_{\mathrm{cm}}^2 + \sigma_{\mathrm{A}}^2 + \left(\frac{M r_{\mathrm{S}}}{\sqrt{3}}\right)^2}. \quad (1)$$

Where σ_{cm} is the chromatic aberration, and σ_{A} is the Airy diffraction term limiting the resolution of the microscope. The magnification factor, M, of the optical system greatly influences the focal spot size. It is given by the following equation [15]:

$$M = \frac{b}{a} = \frac{f}{a - f}. \quad (2)$$

Where f is the focal length of the Fresnel zone plate which depends on its radius and Δr as follows [15]

$$f = \frac{2 r_{\mathrm{zp}} \Delta r}{\lambda}. \quad (3)$$

Where λ is the average de Broglie wavelength of the beam given by $\lambda = h/m\bar{v}$, m is the mass of a helium atom, h is the Planck constant and $\bar{v}$ is the most probable velocity of helium atoms along the radial direction. b corresponds to the distance of the focused image from the zone plate (Fig. 1). This is also the working distance of the microscope. From combining eq. (2) and (3) while assuming constant Δr and λ, one obtains $b \to b(a, r_{\mathrm{zp}})$, reducing the system from four to three variables. The chromatic aberration term stems from the dependence of the focal length on the wavelength. It can be proven to be [15, 32]:

$$\sigma_{\mathrm{cm}} = \frac{r_{\mathrm{zp}}}{S\sqrt{2}}. \quad (4)$$

Where $S = \bar{v}/\sqrt{2k_{\mathrm{B}}T_{||}/m}$ is the parallel speed ratio, which is used as a measure of the velocity spread of the beam. The Airy term stems from the diffraction of helium atoms with the Fresnel zone plate. It can be expressed in terms of the width of the smallest zone Δr

[15]:

$$\sigma_{\mathrm{A}} = \frac{0.42\Delta r a}{a - f}. \tag{5}$$

Where a is the distance between the aperture and the zone plate. If $a \gg f$ the equation reduces to:

$$\sigma_{\mathrm{A}} = 0.42\Delta r. \tag{6}$$

For the strong demagnification ($M \ll 1$) desired in a zone plate microscope, this is the case (see eq. 2), and therefore eq. (6) will be used throughout the paper. This diffraction term will have a constant influence on the focal spot size. Therefore, it is convenient to define a constant corrected focal spot size Φ', obtained by squaring eq. (1), subtracting σ_{A}^2 and redefining the left hand side of the equation:

$$\Phi' = \sqrt{\frac{\Phi^2}{K^2} - \sigma_{\mathrm{A}}^2}. \tag{7}$$

Eq. (1) now simplifies to:

$$\Phi'^2 = \sigma_{\mathrm{cm}}^2 + \left(\frac{M r_{\mathrm{S}}}{\sqrt{3}}\right)^2. \tag{8}$$

The optical system has three variables, the distance between the skimmer and the zone plate a, the radius of the skimmer r_{S} and the radius of the zone plate, r_{zp}. For a given focal spot size Φ, the variables are interrelated through eq. (1). In this paper we will mostly use the expression $r_{\mathrm{S}} \rightarrow r_{\mathrm{S}}(a, r_{\mathrm{ZP}})$:

$$r_{\mathrm{S}}^2 = \frac{3\lambda^2}{4\Delta r^2}\left(a - \frac{2 r_{\mathrm{zp}}\Delta r}{\lambda}\right)^2\left[\frac{\Phi'^2}{r_{\mathrm{zp}}^2} - \frac{1}{2S^2}\right]. \tag{9}$$

It is also interesting to obtain $a \rightarrow a(r_{\mathrm{S}}, r_{\mathrm{zp}})$.

$$a = f\left(r_{\mathrm{S}}\sqrt{\frac{1}{3\left(\Phi'^2 - (\frac{r_{\mathrm{zp}}}{S\sqrt{2}})^2\right)}} + 1\right). \tag{10}$$

This equation gives the expected limitations for a zone plate microscope. If the chromatic aberration and the Airy diffraction term add up to more than the desired focal spot, the solution is non-real and therefore the setup is non physical. Therefore eq. (10) sets a limit to the maximum physical zone plate radius for a given focal spot size. By imposing a real square root one obtains:

$$r_{\mathrm{zp}} \leq \sqrt{2} S \Phi'. \tag{11}$$

Eq. (11) also gives the theoretical minimum resolution of a zone plate microscope. By imposing that Φ' is real one obtains [15]:

$$\frac{\Phi^2}{K^2} \geq \sigma_{\mathrm{A}}^2, \qquad \Phi \gtrsim K\sigma_{\mathrm{A}} \approx \Delta r. \tag{12}$$

Which means that the minimum resolution of a zone plate microscope is given by the smallest achievable pattern on a zone plate.

B. The intensity models

As discussed in the introduction, the most general model of the intensity field of a supersonic helium beam is the ellipsoidal quitting surface model. Quoting from [8], a description of the model follows. The velocity distribution over the quitting surface is assumed to be elliptical Maxwell-Boltzmann:

$$f_{\mathrm{ell}}(\vec{v}) = n\left(\frac{m}{2\pi k_{\mathrm{B}} T_{||}}\right)^{\frac{1}{2}}\left(\frac{m}{2\pi k_{\mathrm{B}} T_{\perp}}\right)\cdot \exp\left(-\frac{m}{2k_{\mathrm{B}}T_{||}}(v_{||} - \bar{v})^2 - \frac{m}{2k_{\mathrm{B}}T_{\perp}}v_{\perp}^2\right). \tag{13}$$

Where m is the mass of a helium atom, k_{B} is Boltzmann's constant and $T_{||}$ and $T_{\perp}$ are the parallel and perpendicular temperatures. $\bar{v}$ is the most probable velocity of the beam along the radial direction and $v_{||}$ and $v_{\perp}$ are the parallel and perpendicular components of the velocity, corresponding to the radial and angular components in spherical coordinates.

Integrating eq. (13) over the quitting surface, across the skimmer and over the zone plate surface, one obtains the following intensity equation:

$$I_{\mathrm{E}} = \frac{\tau\eta I_0}{2\pi a^2 R_{\mathrm{F}}^2 \mathrm{L}}\int_0^{r_{\mathrm{zp}}}\int_0^{r_{\mathrm{S}}}\int_0^{\pi} g(\delta) r\cdot\rho\cos^3\beta\cdot\epsilon^3 e^{-S^2(1-\epsilon^2\cos^2\theta)} D(b) d\rho dr d\alpha. \tag{14}$$

Where R_{F} is the radius of the quitting surface. $\eta = 1/\pi^2$ is the geometrical efficiency of the zone plate for the first diffraction order, corresponding to about 10% of the incoming signal [15]. I_0 is the total intensity stemming from a nozzle of diameter d_{N} [21]:

$$I_0 = \kappa\frac{P_0}{k_{\mathrm{B}}T_0}\sqrt{\frac{2k_{\mathrm{B}}T_0}{m}}\left(\frac{\pi}{4}d_{\mathrm{N}}^2\right)\sqrt{\frac{\gamma}{\gamma+1}}\left(\frac{2}{\gamma+1}\right)^{1/(\gamma-1)}. \tag{15}$$

Where P_0 and T_0 are the thermodynamic pressure and temperature of the helium gas before it undergoes the expansion. $\gamma = \mathrm{C_P}/\mathrm{C_V} = 5/3$ for helium. $\kappa = 2$ is a peak factor as defined in [21]. All other parameters are defined in detail in Appendix B. Unfortunately, the ellipsoidal quitting surface model has no simple analytical solutions and is often slow to compute over a wide space of solutions.

Using the quitting surface model with a single radial velocity distribution it can be shown that for $S \geq 5$, $r_{\mathrm{S}} \ll R_{\mathrm{F}} - x_{\mathrm{S}}$, the intensity arriving at a zone plate small enough to justify a constant radial intensity distribution reads [22]:

$$I_{\mathrm{S}} = \frac{I_0\eta\pi r_{\mathrm{zp}}^2}{(R_{\mathrm{F}}+a)^2}\left\{1 - \exp\left[-S^2\left(\frac{r_{\mathrm{S}}(R_{\mathrm{F}}+a)}{R_{\mathrm{F}}(R_{\mathrm{F}} - x_{\mathrm{S}} + a)}\right)^2\right]\right\}. \tag{16}$$

Where $R_F - x_S$ is the axial distance between the quitting surface and the tip of the skimmer. This equation was obtained independently by Sikora and Andersen [22] and thus we refer to it as Sikora's approximation as mentioned in the introduction. The radius of the skimmer, can be obtained from eq. (9), reducing the intensity equation to two independent variables:

$$I_S(r_{zp}, a) = \frac{I_0 \eta \pi r_{zp}^2}{(R_F + a)^2} - \frac{I_0 \eta \pi r_{zp}^2}{(R_F + a)^2} \exp\left\{ -\frac{3\lambda^2}{4\Delta r^2}\left(a - \frac{2 r_{zp}\Delta r}{\lambda}\right)^2 \left[\frac{\Phi'^2 S^2}{r_{zp}^2} - \frac{1}{2}\right] \left(\frac{(R_F + a)}{R_F(R_F - x_S + a)}\right)^2 \right\}. \quad (17)$$

Assuming that a is generally much bigger than the focal length as previously discussed, $f = \frac{2 r_{zp}\Delta r}{\lambda}$, the maximum intensity of a helium beam monotonically increases with $1/\Delta r$. Therefore, to obtain the maximum intensity, Δr is chosen to be constant and equal to the smallest realisable value.

We can use this equation together with eq. (9) to obtain an analytical equation for the position of the intensity maxima given either a or r_{zp} is taken to be constant.

$$\nabla I_S(r_{zp}, a) = (0, 0), \qquad \partial_a^2 I < 0, \qquad \partial_{r_{zp}}^2 I < 0. \quad (18)$$

Which corresponds to a subset of the solutions of the following equation:

$$\nabla \frac{r_{zp}^2}{(R_F + a)^2}\left\{1 - \exp\left[-S^2\left(\frac{r_S(R_F + a)}{R_F(R_F - x_S + a)}\right)^2\right]\right\} = 0. \quad (19)$$

The derivatives with respect to the zone plate radius and the skimmer-zone plate distance a can both be solved analytically. The derivative of eq. (17) with respect to the skimmer-zone plate distance, a, is a simple cubic equation giving the a corresponding to the maximum intensity at a given zone plate radius.

$$a^3 + 2a^2\left(R_F - \sqrt{3\Gamma} r_{zp}\right) + a R_F (R_F - 4 r_{zp}\sqrt{3\Gamma}) = r_{zp}\sqrt{3\Gamma} R_F^2 \left[\frac{2S^2\Phi'^2 + r_{zp}^2(\Gamma - 1)}{S^2\Phi'^2 - 0.5 r_{zp}^2}\right]. \quad (20)$$

Where $\Gamma \equiv \frac{1}{3}\left(\frac{2\Delta r}{\lambda}\right)^2$ is a constant of the problem which gives the relative size of the smallest aperture of the zone plate compared with the average wavelength of the beam, usually $\Gamma \gg 1$. a^{max} is obtained by solving the cubic equality for a, which gives a single real positive solution.

This approximation has been obtained under the following assumptions, all of them justified in Appendix A.

$$\frac{(R_F + a)^2 (a - \sqrt{3\Gamma} r_{zp})\left[\frac{S^2\Phi'^2}{r_{zp}^2} - \frac{1}{2}\right]\left(a + \frac{R_F}{a}\sqrt{3\Gamma} r_{zp}\right)}{\Gamma R_F^2 a^2} \ll 1, \quad (21)$$

$$a^2 + R_F r_{zp}\sqrt{3\Gamma} \approx a^2, \quad (22)$$

$$(a - \sqrt{3\Gamma} r_{zp})^2 \approx a(a - 2\sqrt{3\Gamma} r_{zp}), \quad (23)$$

$$R_F - x_S \ll a. \quad (24)$$

III. RESULTS AND DISCUSSION

A. An example: $\Phi = 0.9$ μm, $\Delta r = 323$ nm

To illustrate the presented model we consider some of the best results published so far of focussing helium with a zone plate [33]. In the published 0.9 μm experiment, a was set to 1.528 m and Δr to approximately 323 nm (from the two zone plates that were used, we choose to study the one referred as "the MIT zone plate"). We compare it to the best setup achievable for the same focal spot size and Δr. Additionally, we find the best setup and best achievable intensity with the smallest realistic value of Δr (10 nm). The intensity is computed using the ellipsoidal quitting surface model (eq. (14)) and plotted with respect to two variables: r_{zp} and a. The skimmer radius r_S is a hidden variable related to r_{zp} and a by eq. (9). A clear intensity peak can be observed which for small zone plate radii follows well the approximation given by eq. (20) (see Fig. 2). In Fig. 2 and 3 the approximation is shown together with the real line of zero gradient of the ellipsoidal quitting surface model.

If Δr is set at a minimal construction limit of 10 nm, the intensity increases significantly: 8000 times with respect to the original setup (see Fig. 3). In this case, eq. (20) gives a value very close to the position of the intensity peak calculated numerically.

The literature has so far featured relatively large zone plates ($r_{zp} > 90$ μm), a regime where Sikora's approximation can perform badly [8]. Therefore it is important to compare Sikora's approximation with the ellipsoidal quitting surface model. To do so, it is useful to plot the fraction of the normalised intensities:

$$\zeta = \frac{I_S \cdot \max(I_E)}{I_E \cdot \max(I_S)}. \quad (25)$$

It can be seen that for zone plate microscopes, Sikora's approximation can be implemented broadly (Fig. 4). Interestingly, for the studied case ζ is significantly bigger than 1 only for very small zone plates. This is the opposite behaviour than one would expect, but it can be

understood when the skimmer radius is plotted. From the values of the skimmer radius one sees that the Sikora approximation fails for large radii, showing that the size of the aperture closer to the quitting surface (skimmer) is more important than the aperture further away (zone plate) (Fig. 5). This is due to the off-axis intensity decreasing faster the closer the quitting surface is to the plane of interest.

B. Parametric dependences

In this paper, we reduce a multi-variable multi-parametric system to a two variable equation, giving a single optimal configuration for a zone plate microscope. In this section, we discuss the dependence of the system on some of the parameters considered constant. Particularly, we plot the dependence of the optimized system geometry ($(a^{\max}, r_{\mathrm{zp}}^{\max}, r_{\mathrm{S}}^{\max})$) and intensity I, as function of the focal spot size Φ, the speed ratio S and the width of the outermost zone Δr.

To do so, we use Sikora's approximation (eq. (17)), which approximates well the intensity maxima and requires much lower computation times than the ellipsoidal quitting surface model.

From Fig. 6 we see that, as expected, a higher speed ratio yields a smaller optimal skimmer radius. This is because with higher speed ratios the beam is more collimated and thus increasing the skimmer radius affects the intensity less. Additionally, we see an expected increase of the intensity of the beam and an increase of both the zone plate radius and the distance a (also a result of a more collimated beam). We interpret the increase of the optimal zone plate radius as a consequence of smaller chromatic aberrations: bigger zone plates are expected to capture more particles but also to cause higher aberrations, the increase in the speed ratio compensates the increase of the aberration term (see eq. (4)).

The dependence of the studied variables on the focal spot size, Φ, is monotonous and increasing in all cases. A microscope with a larger resolution involves an optimal setup with larger components: both aperture sizes and the distance a increase with the resolution. Additionally, as expected, when the focal spot increases, the maximum intensity increases as well (see Fig. 7).

As explained in Sec. III A, the maximum intensity increases dramatically with a small Δr. This increase of intensity stems from a combination of a smaller microscope length with a larger zone plate radius. Therefore, the theoretical best helium microscope design is a compact microscope with a relatively large zone plate, combining the closeness to the atom source with a large angle of collection (see Fig. 8).

C. Realistic resolution limits

We calculate the resolution limits of a zone plate microscope by setting feasible constraints to all present variables and assuming Lambertian reflection with the sample surface, similar to what has been done in [8].

Concretely, the constraints we choose are a minimal working distance b of 10 µm (value that has been claimed in literature [7]), and a minimal skimmer radius of 100 nm. Δr is set at 10 nm and the radius of the zone plate is limited to a minimum of $10\Delta r$. a is set to a minimum of 1 mm.

A minimal count rate of 100 counts per second is chosen, considered to set the limit for a good signal to noise ratio. This is then compared with the beam intensity calculated using Sikora's approximation and deflected by a Lambertian surface [8]:

$$N = \frac{I_{\mathrm{s}}^{optim} R^2}{d^2} \eta_{\mathrm{D}} \cos(\frac{\pi}{4})^2 \approx 1.4 \cdot 10^{-7} I_{\mathrm{s}}^{optim}. \qquad (26)$$

Where $d = 3$ mm is the distance between the sample surface and the detector, $R = 0.5$ mm is the detector radius. This corresponds to the solid angle of $0.02\ \pi$ sr mentioned in the abstract. I_{s}^{optim} is the optimized intensity using Sikora's approximation. η_{D} is the efficiency of the detector, chosen to be between 10^{-3} [34–37] and 10^{-5} (an upper limit estimate for a commercial mass spectrometer). All parameters are set as in the pinhole microscope setup by Barr et al. [8, 30].

As we can see by comparing Fig. 7 and Fig. 9, resolutions close to the diffraction limit (10 nm) are possible for a very small working distance and the most efficient detector. Such a configuration usually requires a small number of zones. Even for a small number of zones (more than five) the resolution has been shown to approximate well to the optic lens limit and thus the result should be correct to within few nanometers [38]. For a detector of $\eta_{\mathrm{D}} = 10^{-5}$, a microscope with a resolution of 30 nm is possible. In this case, the number of zones used in practical setups is already large enough to be in the lens approximation regime.

The considered construction limits can be argued to be not stringent enough. Although a separation of 1 mm between the skimmer and the zone plate is possible, placing a vacuum pump within that distance is difficult. Similarly, a working distance of only 10 µm, although demonstrated, is technically challenging to implement in the reflection mode, and limits the samples that can be imaged. Therefore, we have also calculated the resolution limit with a minimum $a = 5$ mm and a minimum working distance, b, of 3 mm to set a limit which is not only realistic but also reasonably simple to implement. With both values of η_{D}, such a microscope has the same resolution limit of 100 nm, this limit is set by eq. (10) and not by the 100 counts/s limitation. For λ=0.088 nm, the associated skimmer radius is 0.33 µm, which is close to the fabrication limit [39]. The zone plate radius is 16 µm, a is 2 cm and b is 3 mm, Δr is 10 nm.

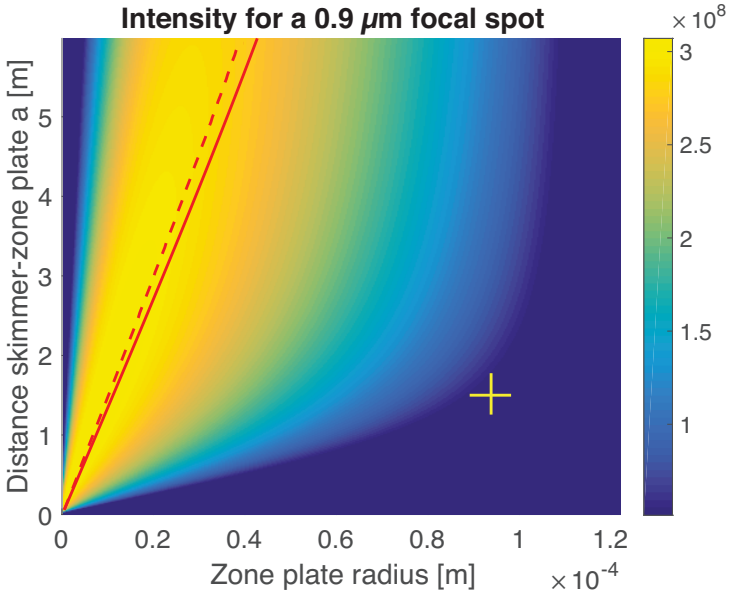

FIG. 2. Intensity [atoms/s] in the focal spot of a zone plate helium microscope for a span of values of r_{zp} and a. The solid line shows the subset of maximum solutions given by eq. (20), and the dashed line shows the numerical solution using the ellipsoidal quitting surface model. The intensity was calculated using the ellipsoidal quitting surface model with the following parameters: $T_{||} = 0.0052$ K, $T_{\perp} = 0.0035$ K, $R_{\mathrm{F}} = 0.01129$ m, $x_{\mathrm{S}} = 0.0113$ m, $T_0 = 115$ K, $P_0 = 101$ Bar, $\lambda = 0.089$ nm. The nozzle diameter d_{n} is set at 10 μm. The maximum lies at $(a^{\max}, r_{\mathrm{zp}}^{\max}, r_{\mathrm{S}}^{\max}) = (0.555\,\mathrm{m}, 3.763 \cdot 10^{-6}\,\mathrm{m}, 1.195 \cdot 10^{-5}\,\mathrm{m})$. The yellow cross indicates the configuration corresponding to the original setup used in [33]. The optimized design would increase the intensity by 7 times. An intensity increase of as much as 8000 times can be achieved by reducing Δr to 10 nm (see Fig. 3).

IV. CONCLUSION

In this paper, we present a theoretical model of the neutral helium zone plate microscope. Using the optical equations of the system and the quitting surface approach, we are able to obtain a two variable intensity function for a given microscope resolution and width of the outermost zone of the zone plate. This function shows a clear intensity peak from which the best zone plate microscope design can be recovered. By imposing realistic design constraints, we find that zone plate microscopes with a resolution as low as 10 nm are realisable. The implementation of the proposed model is shown to increase the intensity of a published setup by as much as 8000 times. The approach followed in this paper can easily be implemented for different intensity models, such as models describing other types of molecular beams and/or considering backscattering from the skimmer, by simply adapting the intensity equation.

ACKNOWLEDGMENTS

The work presented here was sponsored by the European Union: Theme NMP.2012.1.4-3 Grant no. 309672, project NEMI (Neutral Microscopy).

We thank Arnau Jiménez Castany and Kristoffer Johansen for their useful insights in the definition of eq. (18).

APPENDIX A: DERIVATION OF EQ. (20)

To obtain eq. (20), one must derive eq. (17) with respect to the skimmer-zone plate distance a and set it equal to 0. One then obtains (assuming $R_{\mathrm{F}} - x_{\mathrm{S}} \ll a$):

$$1 = \exp(-F) \cdot \left(1 + \frac{(\frac{S^2\Phi'^2}{r_{\mathrm{zp}}^2} - \frac{1}{2})(R_{\mathrm{F}} + a)^2 (a - \sqrt{3\Gamma} r_{\mathrm{z}}) \left[a^2 + R_{\mathrm{F}} r_{\mathrm{zp}} \sqrt{3\Gamma} \right]}{\Gamma R_{\mathrm{F}}^2 a^3} \right) \tag{A1}$$

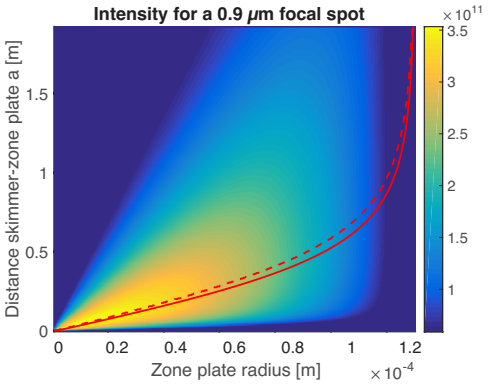

FIG. 3. Intensity [atoms/s] in a 0.9 μm focal spot of a zone plate helium microscope for a span of values of r_{zp} and a. The red line shows the subset of maximum solutions given by eq. (20) and the dashed line shows the real line of zero derivative in the ellipsoidal quitting surface model. The intensity was calculated using the ellipsoidal quitting surface model with the following parameters: $T_{||} = 0.0052$ K, $T_{\perp} = 0.0035$ K, $R_{\mathrm{F}} = 0.01129$ m, $x_{\mathrm{S}} = 0.0113$ m, $T_0 = 115$ K, $P_0 = 101$ Bar, $\lambda = 0.089$ nm. The nozzle diameter d_{n} is set at 10 μm. The maximum lies at $(a^{\max}, r_{\mathrm{zp}}^{\max}, r_{\mathrm{S}}^{\max}) = (0.06\ \mathrm{m}, 12.22 \cdot 10^{-6}\ \mathrm{m}, 1.173 \cdot 10^{-5}\ \mathrm{m})$. Note how the intensity peak is at $3.5 \cdot 10^{11}$ [atoms/s], corresponding to an intensity of about 8000 times the configuration used in [33]

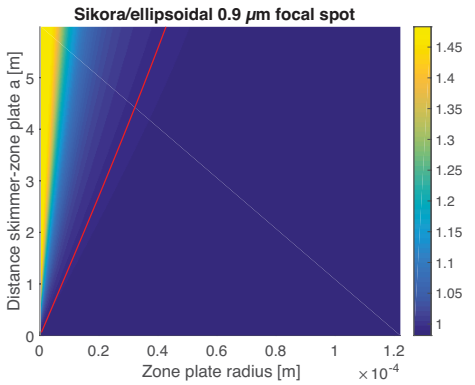

FIG. 4. Normalised fraction of Sikora's model divided by the ellipsoidal quitting surface model, ζ, for a span of values of r_{zp} and a. The solution was calculated for a zone plate helium microscope with a resolution of 0.9 μm and a Δr of 323 nm. The red line shows the subset of maximum solutions given by eq. (20). Both models were computed using the following parameters: $T_{||} = 0.0052$ K, $T_{\perp} = 0.0035$ K, $R_{\mathrm{F}} = 0.01129$ m, $x_{\mathrm{S}} = 0.0113$ m, $T_0 = 115$ K, $P_0 = 101$ Bar, $\lambda = 0.089$ nm.

With

$$F \equiv \frac{(\frac{S^2\Phi'^2}{r_{\mathrm{zp}}^2} - \frac{1}{2})(R_{\mathrm{F}} + a)^2(a - \sqrt{3\Gamma}r_{\mathrm{zp}})^2}{\Gamma R_{\mathrm{F}}^2 a^2}. \tag{A2}$$

Eq. (A1) can be written as follows:

$$\exp(-F) = \frac{1}{1+A} = 1 + \varpi, \qquad \varpi \equiv \frac{-A}{1+A}. \tag{A3}$$

with

$$A = \frac{(\frac{S^2\Phi'^2}{r_{\mathrm{zp}}^2} - \frac{1}{2})(R_{\mathrm{F}} + a)^2(a - \sqrt{3\Gamma}r_{\mathrm{zp}})\left[a^2 + R_{\mathrm{F}}r_{\mathrm{zp}}\sqrt{3\Gamma}\right]}{\Gamma R_{\mathrm{F}}^2 a^3}. \tag{A4}$$

By plotting A along a wide range of parameters one can see that for the conditions of interest along the intensity maxima $A \ll 1$. By taking the logarithm in eq. (A3) and expanding using Taylor series $\log(1 - A) \approx -A$, one obtains:

$$F \approx \frac{A}{1+A}. \tag{A5}$$

Which reduces to:

$$(a - \sqrt{3\Gamma}r_{\mathrm{zp}})(1 + A) = \frac{a^2 + R_{\mathrm{F}}r_{\mathrm{zp}}\sqrt{3\Gamma}}{a}. \tag{A6}$$

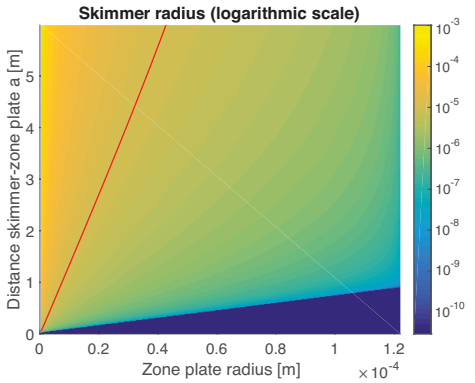

FIG. 5. Skimmer radius r_{S} [m], for a zone plate helium microscope with a resolution of 0.9 μm and a Δr of 323 nm. The radius is plotted with a logarithm scale due to the high variations in its magnitude. Note how in the areas where Sikora's approximation fails (see Fig. 4), the skimmer radius is largest. The red line indicates the subset of maximum solutions given by eq. (20). The radius was calculated using the following parameters: $S = 241.68$, $\lambda = 8.9 \cdot 10^{-11}$ m.

In general, the radius of the quitting surface, R_{F}, is of the order of millimetres (for the example shown in Sec. III C it corresponds to around 10 mm). For microscopes with low resolution and realistic speed ratios of the order of 100, the radius of the zone plate is as much as hundreds of times the focal spot size (see eq. (11)). Conservatively,

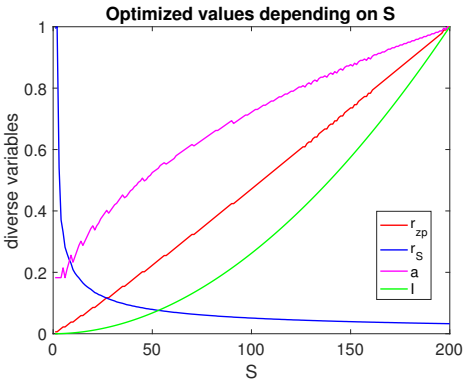

FIG. 6. Normalised optimized parameters of a zone plate helium microscope for a span of values of the speed ratio S. The intensity was calculated using Sikora's approximation with the following parameters: $T_0 = 115$ K, $P_0 = 101$ Bar at a fix resolution, $\Phi = 0.9$ µm. The maximum values of the parameters, used for normalization are: $r_{zp} = 10.2$ µm, $r_S = 458.6$ µm, $a = 0.05$ m, $I = 2.65 \cdot 10^{11}$ atoms/s. The small fluctuation of the data are due to numerical effects.

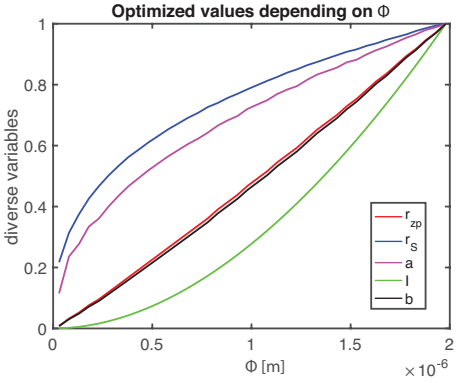

FIG. 7. Normalised optimized parameters of a zone plate helium microscope for a span of values of the focal spot size Φ. The intensity was calculated using Sikora's approximation with the following parameters: $T_0 = 115$ K, $P_0 = 101$ Bar, which corresponds to $S = 241.7$. The maximum values of the parameters, used for normalization are: $r_{zp} = 29.7$ µm, $r_S = 17.4$ µm, $a = 0.09$ m, $I = 1.68 \cdot 10^{12}$ atoms/s, $b = 0.007$ m. The small fluctuation of the data are due to numerical effects.

this means $O(r_{zp}) \approx 1 \cdot 10^{-4}$. The product of the zone plate radius and the radius of the quitting surface is then of the order of $R_F r_{zp} < 1 \cdot 10^{-6}$. $\sqrt{\Gamma}$ scales as $\Delta r/\lambda$, which for high Δr is on the order of a few thousand. When compared with the order of a^2, $O(a^2) \approx 1 \cdot 10^{-2}$,

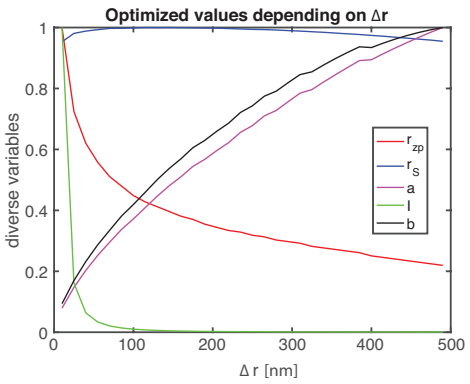

FIG. 8. Normalised optimized parameters of a zone plate helium microscope for a span of values of the width of the outermost zone Δr. The intensity was calculated using Sikora's approximation with the following parameters: $T_0 = 115$ K, $P_0 = 101$ Bar at a fix resolution $\Phi = 0.9$ µm. This corresponds to a speed ratio of $S = 241.7$. In this case, b has also been included to emphasize the reduction of the microscope length at high intensity setups. The maximum values of the parameters, used for normalization are: $r_{zp} = 12.5$ µm, $r_S = 13.9$ µm, $a = 0.7515$ m, $I = 3.81 \cdot 10^{11}$ atoms/s, $b = 0.0316$ m. The small fluctuation of the data are due to numerical effects.

the product $R_F r_{zp}\sqrt{3\Gamma}$ is at least one order of magnitude smaller (in practise in the studied cases, it was at least two orders of magnitude smaller). Therefore we can make the following approximation:

$$a^2 + R_F r_{zp}\sqrt{3\Gamma} \approx a^2. \tag{A7}$$

When developing eq. (A5), we will encounter $(a - \sqrt{3\Gamma} r_{zp})$ at first and second exponent. It will be helpful to find some approximation to it. $\sqrt{3\Gamma} r_{zp}$ is smaller than a such that the following approximation holds:

$$(a - \sqrt{3\Gamma} r_{zp})^2 = a^2 - 2\sqrt{3\Gamma} r_{zp} a + 3\Gamma r_{zp}^2 \approx a^2 - 2\sqrt{3\Gamma} r_{zp} a = a(a - 2\sqrt{3\Gamma} r_{zp}). \tag{A8}$$

Implementing these approximations in eq. (A5) one obtains:

$$\frac{(\frac{S^2\Phi'^2}{r_{zp}^2} - \frac{1}{2})(R_F + a)^2 (a - 2\sqrt{3\Gamma} r_{zp})}{\Gamma R_F^2} = \sqrt{3\Gamma} r_{zp}. \tag{A9}$$

By multiplying by r_{zp}^3 and grouping for powers of a, one recovers eq. (20):

$$a^3 + 2a^2\left(R_F - \sqrt{3\Gamma} r_{zp}\right) + a R_F (R_F - 4 r_{zp}\sqrt{3\Gamma}) = r_{zp}\sqrt{3\Gamma} R_F^2 \left[\frac{2S^2\Phi'^2 + r_{zp}^2(\Gamma - 1)}{S^2\Phi'^2 - 0.5 r_{zp}^2}\right]. \tag{A10}$$

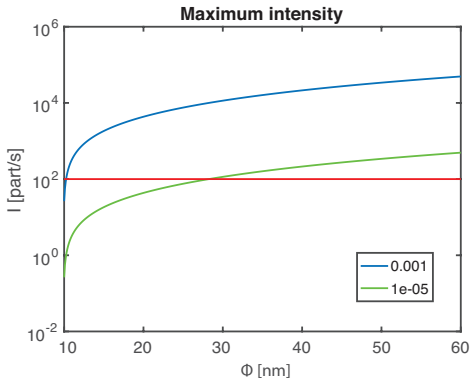

FIG. 9. Optimized count rate for different focal spot sizes. The intensity was calculated using Sikora's approximation with the following parameters: $T_0 = 115$ K, $P_0 = 161$ Bar. The efficiency of the detector, placed at $\pi/4$ radians is $\eta = 1 \cdot 10^{-5}$ (green line) or $\eta = 1 \cdot 10^{-3}$ (blue line). The red line indicates the 100 atoms/s intensity limit. The constraints on the calculation are a minimum working distance of 10 µm, a minimum skimmer radius of 100 nm and a minimum a of 1 mm. Δr is set at 10 nm.

Both, the explicit solutions of these equations and the second derivative of eq. (17) with respect to a are too lengthy to justify an analytical proof of the negative value of the second derivative at the intensity maximum. Instead, we follow a more practical numerical approach, which confirmed that the only real positive solution of eq. (A10) evaluates to a negative second derivative of eq. (17).

APPENDIX B: THE ELLIPSOIDAL QUITTING SURFACE MODEL

The ellipsoidal quitting surface model used in this paper is an extension of Sikora's ellipsoidal quitting surface model with the difference that the skimmer is allowed to be in a different position than the quitting surface. Such a model was published by U. Bossel in 1974 [27]. Unfortunately the original paper has a couple of typos so we describe here the corrected equations in detail. The main intensity equation arriving at the zone plate is eq. (14):

$$I_{\mathrm{E}} = \frac{\tau I_0}{2\pi a^2 R_{\mathrm{F}}^2 \mathrm{L}} \int_0^{r_{z_{\mathrm{P}}}} \int_0^{r_{\mathrm{S}}} \int_0^{\pi} g(\delta) r \cdot \rho \cos^3\beta \cdot \epsilon^3 \, e^{-S^2(1-\epsilon^2\cos^2\theta)} D(b) d\rho dr d\alpha. \quad \text{(B1)}$$

Where R_{F} is the radius of the quitting surface and $S = \bar{v}/\sqrt{2k_{\mathrm{B}}T_{||}/m}$ is the parallel speed ratio. $\epsilon \equiv \left(\left(\tau \sin^2\theta + \cos^2\theta\right)\right)^{-1/2}$, $\tau \equiv \frac{T_{||}}{T_{\perp}}$ are auxiliary functions.

The function D(b) is defined as follows:

$$D(b) \equiv \frac{2}{\sqrt{\pi}} b e^{-b^2} + \left(2b^2+1\right)\left[1 + erf(b)\right], \quad b \equiv S\epsilon\cos\theta. \quad \text{(B2)}$$

Where I_0 is defined in eq. (15). $g(\delta)$ is obtained from the angular term in eq. (12) of Beijerinck and Verster paper [21] (in Bossel's work a $\cos^2$ function is chosen instead [27]):

$$g(\delta) = \cos^3\left(\frac{\pi\theta}{2\theta_0}\right), \qquad \theta_0 = \frac{\pi}{2}\sqrt{\frac{\gamma+1}{\gamma-1}-1} = \frac{\pi}{2}. \quad \text{(B3)}$$

Where $\gamma = C_{\mathrm{P}}/C_{\mathrm{V}} = 5/3$ for helium has been used. L corresponds to the integration of $g(\delta)$ along the half sphere (all the intensity emitted by the source is set to be contained in $g(\delta)$).

$$L \equiv \int_0^{\frac{\pi}{2}} g(\delta)\sin\delta d\delta = \frac{1}{4}. \quad \text{(B4)}$$

ρ is the radial coordinate at the zone plate plane and r is the radial coordinate at the skimmer plane. The angles β, α and θ are shown in Fig. 10. The analytical expressions that relate them to the radial coordinates of the system follow:

$$\cos\beta = \frac{a}{\sqrt{a^2 + (r\sin\alpha)^2 + (\rho - r\cos\alpha)^2}}, \quad a = x_{\mathrm{D}} - x_{\mathrm{S}}. \quad \text{(B5)}$$

$$\cos\theta = \frac{x_{\mathrm{R}}(x_{\mathrm{D}} - x_{\mathrm{R}}) - y_{\mathrm{R}}^2 + z_{\mathrm{R}}(\rho - z_{\mathrm{R}})}{R_{\mathrm{F}}\sqrt{(x_{\mathrm{D}} - x_{\mathrm{R}})^2 + y_{\mathrm{R}}^2 + (\rho - z_{\mathrm{R}})^2}}. \quad \text{(B6)}$$

Where:

$$x_{\mathrm{R}} = x_{\mathrm{D}} - \xi(x_{\mathrm{D}} - x_{\mathrm{S}}), \qquad y_{\mathrm{R}} = r\sin\alpha\left(\frac{x_{\mathrm{D}} - x_{\mathrm{R}}}{x_{\mathrm{D}} - x_{\mathrm{S}}}\right),$$

$$z_{\mathrm{R}} = r\cos\alpha\left(\frac{x_{\mathrm{D}} - x_{\mathrm{R}}}{x_{\mathrm{D}} - x_{\mathrm{S}}}\right) - \rho\left(\frac{x_{\mathrm{D}} - x_{\mathrm{R}}}{x_{\mathrm{D}} - x_{\mathrm{S}}}\right) + \rho, \quad \text{(B7)}$$

are the Cartesian coordinates of a point **P** on the quitting surface (see Fig. 10).

$$\xi = \frac{B - \sqrt{B^2 - AC}}{A}. \quad \text{(B8)}$$

$$A \equiv (x_{\mathrm{D}} - x_{\mathrm{S}})^2 + (r\sin\alpha)^2 + (\rho - r\cos\alpha)^2, \quad \text{(B9)}$$

$$B = x_{\mathrm{D}}(x_{\mathrm{D}} - x_{\mathrm{S}}) + \rho(\rho - r\cos\alpha), \quad \text{(B10)}$$

$$C = x_{\mathrm{D}}^2 + \rho^2 - R_{\mathrm{F}}^2. \quad \text{(B11)}$$

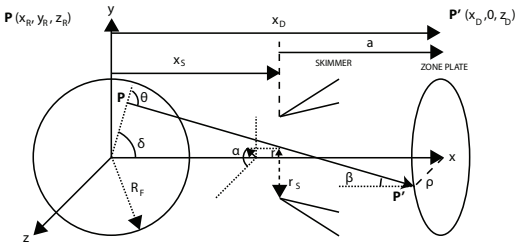

FIG. 10. Illustration of all variables used in the ellipsoidal quitting surface model. **P** is a point on the quitting surface from which a particle leaves in a straight trajectory until **P'**, a point placed on the zone plate plane. The point on the quitting surface is given by the set of Cartesian coordinates $(x_{\mathrm{R}}, y_{\mathrm{R}}, z_{\mathrm{R}})$, which can be related to the polar coordinates r, α, ρ for further integration. x_{S} is the distance from the nozzle to the skimmer and x_{D} is the distance from the nozzle to the zone plate. Therefore $a = x_{\mathrm{D}} - x_{\mathrm{S}}$. The angles β and θ can also be expressed in terms of r, α and ρ.

[1] G. Bracco and B. Holst, "Surface Science Techniques," (Springer, 2013).

[2] M. Koch, S. Rehbein, G. Schmahl, T. Reisinger, G. Bracco, W. E. Ernst, and B. Holst, J. Microsc. **229**, 1 (2008).

[3] P. Witham and E. Sanchez, Rev. Sci. Instrum. **82**, 103705 (2011).

[4] P. Witham and E. Sanchez, Cryst. Res. Technol. **29**, 690 (2014).

[5] A. Fahy, M. Barr, J. Martens, and P. Dastoor, Rev. Sci. Instrum **86**, 023704 (2015).

[6] M. Barr, A. Fahy, J. Martens, A. P. Jardine, D. J. Ward, J. Ellis, W. Allison, and P. C. Dastoor, Nat. Commun. **7**, 10189 (2016).

[7] P. Witham and E. Sanchez, J. Microsc. **248**, 223 (2012).

[8] A. Salvador Palau, G. Bracco, and B. Holst, Phys. Rev. A (Submitted) (2016).

[9] O. Carnal, M. Sigel, T. Sleator, H. Takuma, and J. Mlynek, Phys. Rev. Lett. **67**, 3231 (1991).

[10] R. B. Doak, R. E. Grisenti, S. Rehbein, G. Schmahl, J. P. Toennies, and C. Wöll, Phys. Rev. Lett. **83**, 4229 (1999).

[11] M. Greve, A. Vial, J. Stamnes, and B. Holst, Opt. Express **21**, 28483 (2013).

[12] L. Kipp, M. Skibowski, R. L. Johnson, R. Berndt, R. Adelung, S. Harm, and R. Seemann, Nature **414**, 184 (2001).

[13] W. Fan, L. Wei, H. Zang, L. Cao, B. Zhu, X. Zhu, C. Xie, Y. Gao, Z. Zhao, and Y. Gu, Opt. Express **21**, 1473 (2013).

[14] R. G. Hobbs, V. R. Manfrinato, Y. Yang, S. A. Goodman, L. Zhang, E. A. Stach, and K. K. Berggren, Nano Letters **16**, 4149 (2016).

[15] A. G. Michette, *Optical Systems for Soft X Rays*, edited by A. G. Michette (Plenum Press, New York, 1968).

[16] R. B. Doak, in *Helium Atom Scattering from Surfaces*, edited by E. Hulpke (Springer Berlin / Heidelberg, 1992).

[17] B. Holst and W. Allison, Nature **390**, 244 (1997).

[18] K. Fladischer and E. al., New. J. Phys. **12**, 33018 (2010).

[19] P. Sutter, M. Minniti, P. Albrecht, D. Farias, R. Miranda, and E. Sutter, Appl. Phys. Lett. **99**, 211907 (2011).

[20] H. C. Schewe, B. S. Zhao, G. Meijer, and W. Schöllkopf, New. J. Phys. **11**, 113030 (2009).

[21] H. C. W. Beijerinck and N. F. Verster, Physica C **111**, 327 (1981).

[22] G. S. Sikora, *Analysis of asymptotic behavior of free jets: Prediction of Molecular Beam Instensity and Velocity Distributions*, Ph.D. thesis, Princeton (1973).

[23] J. Toennies and K. Winkelmann, J. Chem. Phys. **66**, 3965 (1977).

[24] T. Reisinger, G. Bracco, S. Rehbein, G. Schmahl, W. E. Ernst, and B. Holst, J. Phys. Chem A **111**, 12620 (2007).

[25] L. Pedemonte and G. Bracco, J. Chem. Phys. **119**, 1433 (2003).

[26] S. D. Eder, G. Bracco, T. Kaltenbacher, and B. Holst, J. Phys. Chem A **118**, 4 (2014).

[27] U. Bossel, *Skimming of Molecular Beams from Diverging Non-equilibrium Gas Jets*, Deutsche Luft- und Raumfahrt. Forschungsbericht (Deutsche Forschungs-und Versuchsanstalt für Luft-und Raumfahrt, 1974).

[28] H. C. W. Beijerinck, R. J. F. V. Gerwen, E. R. T. Kerstel, J. F. M. Martens, E. J. W. V. Vliembergen, M. Smits, and G. H. Kaashoek, Chem. Phys. **96**, 153 (1985).

[29] H. Hedgeland, A. P. Jardine, W. Allison, and J. Ellis, Rev. Sci. Instrum. **76**, 123111 (2005).

[30] M. Barr, A. Fahy, A. Jardine, J. Ellis, D. Ward, D. A. Maclaren, W. Allison, and P. C. Dastoor, Nucl. Instrum. Methods **B 340**, 76 (2014).

[31] T. Stewart McKechnie, *General Theory of Light Propagation and Imaging Through the Atmosphere*, 1st ed. (Springer, 2016) p. 624.

[32] M. Young, Josa **62**, 972 (1972).

[33] S. D. Eder, T. Reisinger, M. M. Greve, G. Bracco, and B. Holst, New. J. Phys. **14**, 73014 (2012).
[34] M. Matsuki, *Company MB Scientific, Private communication, detector available on a commercial basis upon request*.
[35] M. DeKieviet, D. Dubbers, M. Klein, U. Pieles, and C. Schmidt, Rev. Sci. Instrum. **71**, 123301 (2000).
[36] A. R. Alderwick, A. P. Jardine, H. Hedgeland, D. A. MacLaren, W. Allison, and J. Ellis, Rev. Sci. Instrum. **79** (2008).
[37] W. Allison, *Private Communication*.
[38] J. Daniel, J. R. Stigliani, R. Mittra, and R. G. Semoni, J. Opt. Soc. Am. **57**, 610 (1967).
[39] J. Braun, P. K. Day, J. P. Toennies, G. Witte, and E. Neher, Rev. Sci. Instrum. **68**, 3001 (1997).

Article 3

4.3 Velocity distributions in microskimmer supersonic expansion helium beams: High precision measurements and modeling

SD Eder, Adrià Salvador Palau, T. Kaltenbacher, Gianangelo Bracco, Bodil Holst

Review of Scientific Instruments, **89**, 11 (2018)

Velocity distributions in microskimmer supersonic expansion helium beams: High precision measurements and modeling

S. D. Eder, A. Salvador Palau, T. Kaltenbacher, G. Bracco, and B. Holst

Citation: Review of Scientific Instruments **89**, 113301 (2018); doi: 10.1063/1.5044203
View online: https://doi.org/10.1063/1.5044203
View Table of Contents: http://aip.scitation.org/toc/rsi/89/11
Published by the American Institute of Physics

REVIEW OF SCIENTIFIC INSTRUMENTS **89**, 113301 (2018)

Velocity distributions in microskimmer supersonic expansion helium beams: High precision measurements and modeling

S. D. Eder,[1,a),b)] A. Salvador Palau,[2,a)] T. Kaltenbacher,[1,a)] G. Bracco,[1,3] and B. Holst[1]
[1]*Department of Physics and Technology, University of Bergen, Allégaten 55, 5007 Bergen, Norway*
[2]*Department of Engineering, Institute for Manufacturing, University of Cambridge, Cambridge CB3 0FS, United Kingdom*
[3]*CNR-IMEM, Department of Physics, University of Genova, V Dodecaneso 33, 16146 Genova, Italy*

(Received 11 June 2018; accepted 9 October 2018; published online 1 November 2018)

Supersonic molecular beams are used in many applications ranging from spectroscopy and matter wave optics to surface science. The experimental setup typically includes a conically shaped, collimating aperture, the skimmer. It has been reported that microskimmers with diameters below 10 μm produce beams with significantly broader velocity distributions (smaller speed ratios) than larger skimmers. Various explanations for this phenomenon have been proposed, but up till now, only a limited amount of data has been available. Here we present a systematic study of the velocity distribution in microskimmer supersonic expansion helium beams. We compare a 4 μm diameter skimmer with a 390 μm diameter skimmer for room temperature and cooled beams in the pressure range 11-181 bars. Our measurements show that for properly aligned skimmers, the only difference is that the most probable velocity for a given pressure and temperature is slightly lower for a microskimmed beam. We ascribed this to the comparatively narrow and long geometry of the microskimmers which can lead to local pressure variations along the skimmer channel. We compare our measurements to a model for the supersonic expansion and obtain good agreement between the experiments and simulations. *Published by AIP Publishing.* https://doi.org/10.1063/1.5044203

I. INTRODUCTION

Supersonic molecular beams are used in a range of scientific disciplines. Helium beams, in particular, are an established tool in surface science used in diffraction experiments and dynamics studies (diffusion and surface vibrations) and for monitoring thin film growth and thermal evaporation.[1,2] Work is ongoing to extend the use of helium beams toward direct imaging in neutral helium microscopes.[3–7] Molecular beams can also be employed as a carrier gas for deposition of other molecules.[8]

A supersonic molecular beam is created by a supersonic (free jet) expansion: atoms or molecules from a high pressure reservoir (typically up to 200 bars or more) expand into vacuum through a nozzle with a diameter larger than the mean free path of the gas particles in the reservoir. The expansion is adiabatic. As the atoms or molecules expand into vacuum, they collide until free molecular flow is reached. The advantage of the supersonic expansion compared to an effusive beam is the high beam density and narrow velocity distribution that can be achieved.[9] The central part of the beam is selected by a conically shaped, circular aperture, popularly referred to as the skimmer.

For most experiments, the skimmer has a diameter between 200 μm and a few mm. The first experiments using a microskimmer were presented by Braun *et al.*[10] This paper introduces the method of glass pulling for the creation of microskimmers which is used to this day. Measurements were obtained using a source pressure of 120 bars and a 10 μm diameter nozzle. In the paper, it is reported that speed ratios for 3 μm and 5 μm skimmers are considerably lower than those for a standard 1.6 mm diameter skimmer: 65 and 24, respectively, compared to 78 for the standard skimmer. The speed ratio is a standard way to express the quality of a molecular beam and is defined as $2\sqrt{\ln 2}\, u/\Delta u$ where u is the most probable (mean) velocity and Δu is the full width at half maximum (FWHM) of the velocity distribution.[11,12]

Braun *et al.* proposed geometrical imperfections and/or imperfections of the lip edge of the skimmer as well as difficulties in aligning the skimmer and nozzle as possible explanations for the reduced speed ratios. In their paper, they suggested that microskimmers can be used for atom optics experiments and indeed up till now, this has been the main application. The first experiment using a microskimmer to focus a neutral helium beam was carried out by Doak *et al.*[13] Focusing measurements were carried out using skimmers between 1 μm and 14 μm in diameter with a source pressure up to 150 bars and a 5 μm diameter nozzle. The expected focused spot diameter was not achieved. The relative deviation between expected and measured focus increases from 1.1 for a 14 μm skimmer (5.6 μm expected, 6.2 μm measured) to 5 (0.4 μm expected, 2 μm measured) for the 1 μm skimmer. It is suggested in the paper that this is due to the supersonic expansion continuing after the beam has passed through the skimmer aperture. It is stated that measurements were carried out for velocity distributions $\Delta u/u$ between ~1% FWHM and up to ~10% FWHM (corresponding to speed ratios between around 140 and 14). These speed ratios are not compared explicitly to standard

[a)]S. D. Eder, A. Salvador Palau, and T. Kaltenbacher contributed equally to this work.
[b)]Author to whom correspondence should be addressed: sabrina.eder@uib.no

skimmer measurements. The first neutral helium microscopy images were obtained a few years later. The resolution was around 2 μm, using a 1.2 μm diameter skimmer.[3] Experiments were also carried out with a 2.4 μm diameter skimmer. The paper states that speed ratios between 16 ± 1 and 140 ± 3 were obtained with source pressures between 11 bars and 191 bars using a 10 μm diameter nozzle. The paper also states that chromatic aberrations caused by the velocity distribution of the beam are the resolution limiting factor and that no signs of further expansion after the beam has passed through the skimmer could be observed. The first sub-micrometer focusing was obtained by Eder *et al.*[4] A microskimmer 1.1 μm in diameter was used. The measurements were performed at a source pressure of 81 bars and 110 bars using a 10 μm nozzle. However, the velocity distributions were not measured explicitly; instead, theoretical values were used to calculate the expected focus size. The agreement between the theoretically expected (calculated) and measured focus spot diameters was good, but the measurements had large error bars (up to ±34% of the measured focus spot diameter).

The importance of the speed ratio for the microscope resolution is discussed in Ref. 14. As described in detail in Ref. 14, the diffractive beam focusing elements used in some helium microscopes have chromatic aberrations. In order to achieve high resolution (small focus diameters) with such microscopes, the source, i.e., the skimmer diameter, needs to be as small as possible and at the same time the beam as monochromatic as possible. A lower speed ratio will lead to a lower resolution. This together with the discussion above illustrates how important it is to determine the true, best obtainable velocity distribution from microskimmers. In this paper, we present such a detailed study. Of particular importance is the use of our molecular beam source which allows the skimmer to be positioned with sub-micrometer precision relative to the nozzle.[15] Microskimmer measurements are compared with measurements using a standard skimmer. To ensure accurate measurements of high speed ratios, we employ our improved time-of-flight (TOF) method presented in Ref. 16. Further we use our theoretical model for the supersonic expansion described in Refs. 17 and 18 to model the experimental data. The model is described in Sec. III.

II. EXPERIMENTAL SETUP

The experiments presented here were carried out in the molecular beam apparatus at the University of Bergen, popularly referred to as MAGIE.[19] A drawing of the experimental setup can be seen in Fig. 1.

The neutral helium beam was created by a free jet expansion from a source reservoir through a 10 ± 1 μm diameter nozzle (Plano GmbH, A0300P). The central part of the beam was selected by either a standard skimmer (Beam Dynamics, Inc.) with a diameter of 390 μm or with a self-made glass microskimmer with a diameter of 4 μm. The microskimmer was made using a commercial micropipette puller (Narishige, PP-830) and lead glass tubes (Corning 8161) with an outer diameter of 1.5 mm and an inner diameter of 1.1 mm. The

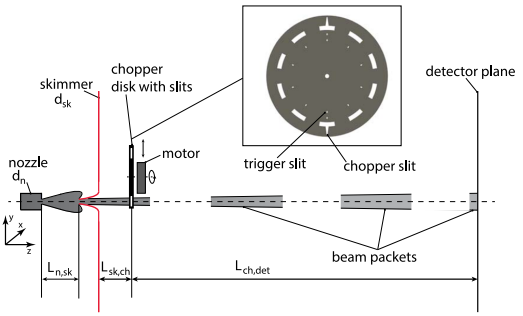

FIG. 1. Schematic representation of the TOF measurement setup. Inset: Detailed drawing of the chopper disk with its two trapezoidal shaped slits placed 180° apart. The trigger slits are used to tag each beam packet. Further details are given in the text.

key challenge when pulling microskimmers is to achieve the right skimmer opening angle even for small apertures. Bird described the expected quality differences between the flow in slender or wide angle skimmers.[20] Slender skimmers with opening angles below ~35° are predicted to give better skimming performance than wide angle skimmers. But as the skimmer becomes more slender, beam attenuation will occur due to collisions with molecules reflected from the skimmers' internal wall. Eventually this will lead to a break down of the beam. A break down of the beam is a rapid transition from supersonic to subsonic beam flow which is often described as a sudden blocking of the skimmer. Due to the somewhat manual nature of the skimmer pulling procedure, it is difficult to reproduce exactly the same openings and angles for individual skimmers. Generally the best skimmers were obtained by using a relatively high heating setting (70), high pulling force (about 100 g), and several heating steps (6). Decreasing the temperature or decreasing the number of heating steps made the taper of the skimmer longer and hence the opening angle smaller. Figure 2 shows a stereo microscope image (a) and a scanning electron microscope (SEM) image (b) of our self-made skimmer. The outer skimmer opening angle was determined from the stereo microscope image in Fig. 2(a) and found to be ~32.5° for the first ca. 200 μm followed by a more narrow section of ~12.5° opening angle. The microskimmer opening is circular [see Fig. 2(b)] with the opening lips having an estimated thickness of less than ~200 nm. After pulling, the glass tube was glued onto a copper holder using a two component glue (UHU PLUS ENDFEST 300). The length of the skimmer's glass tip protruding out of the copper holder was approximately 2.5 mm. After the glue had hardened, the glass tube was cut as short as possible to the inner rim of the copper holder using a diamond knife to just leave the top part. The mounting was performed using a stereo microscope. Care was taken to ensure that the skimmer opening was parallel to the mounting base so that the beam and skimmer opening were perpendicular to each other.

For all experiments, the skimmer was placed 11.5 ± 0.5 mm in front of the nozzle ($L_{n,sk}$). The distance from skimmer to chopper was 525 ± 1 mm ($L_{sk,ch}$), and the distance from chopper to detector was 1905 ± 5 mm ($L_{ch,det}$).

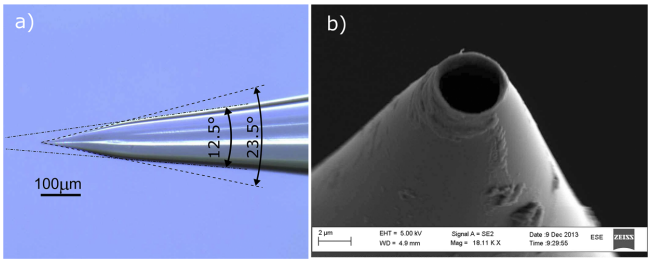

FIG. 2. (a) Stereo microscope image of the ∅4 μm microskimmer (glass). (b) SEM image of the ∅4 μm microskimmer (glass).

The beam source in MAGIE has been specifically designed for microskimmer experiments and is to our knowledge the only molecular beam source which allows positioning of the skimmer relative to the nozzle with sub-micrometer precision.[15] The source was operated at pressures in the range 11-181 bars at two different source temperatures, nominally 300 K and 125 K, obtained by cooling the nozzle with liquid nitrogen. For the alignment of the nozzle relative to the microskimmer, the nozzle is moved in the x and y directions across the skimmer opening (see Fig. 1). The optimum nozzle to skimmer position is found when the detected beam signal reaches a maximum. The detailed alignment procedure can be found in Ref. 15. It should be noted that the effective ionization area of the MAGIE detector is large: 4.6 × 6.6 mm. Thus, even though a skimmer exchange might slightly vary the detector entrance position of the investigated He beam, the described alignment procedure in combination with the relatively big size of the detector entrance ensures a sampling of the beams' centerline. The fixed skimmer to detector position for each investigated skimmer also ensures that the angle of the beam within the

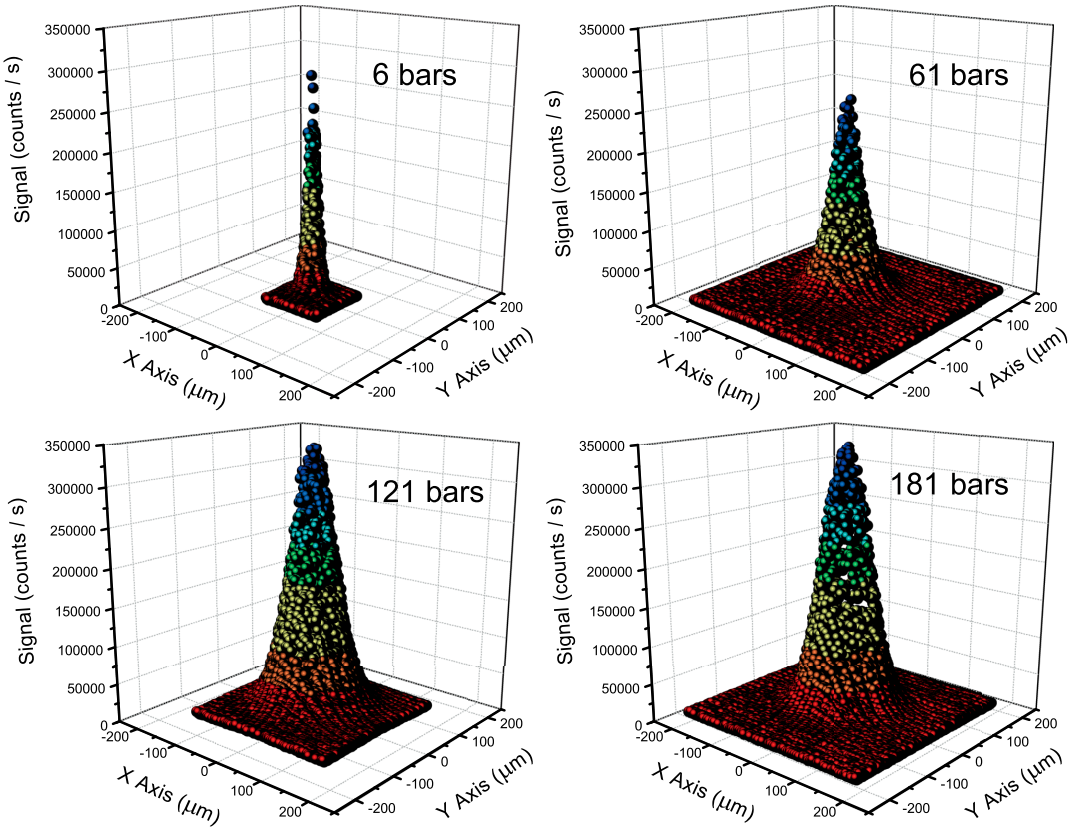

FIG. 3. 2D intensity maps recorded by scanning the 10 μm nozzle over the 4 μm glass skimmer (RT beam). Since the glass skimmer diameter is small compared to the spatial extension of the supersonic expansion, this 2D intensity maps can be seen as an approximate image of the expansion itself.

skimmer is constant for all different skimmers since the nozzle position is optimized for each measurement set. Possible small variations of the detector efficiency depending on where the beam enters the detector are not an issue for the presented measurements since the detector efficiency only affects the count rate not the TOF distribution. Figure 3 shows a recorded 2D x/y scan intensity map for the alignment of the nozzle with the 4 μm diameter microskimmer for 4 different source pressure values at 300 K. As can be seen in Fig. 3, the spatial extension of the 2D source profile increases with increasing source pressure values. This corresponds well to the theoretically expected and experimentally verified behavior of a spatial increase in the free jet expansion with pressure.[17,18,21,22] A higher source pressure leads to an increase in the detected source intensity likewise agreeing well with theoretical considerations.

The most probable beam velocity and the beam velocity distribution were obtained by time of flight measurements (TOF). The beam was chopped by a mechanical chopper operated at frequencies of 230 Hz, 310 Hz, and 320 Hz. The chopper is linked to a light emitting diode (LED)-photodetector system which sends a trigger signal to the detector electronics so that the arrival time for the atoms in each beam pulse is recorded. The TOF signal is determined by the actual velocity distribution of the beam convoluted with the chopper slit and the detector function. When the velocity distribution is narrow (speed ratio high), it cannot be determined accurately using the standard deconvolution procedure described in Ref. 12. We therefore used a new method recently developed in our group which allows the velocity distribution to be extracted with high accuracy.[16] The improved method is based on a systematic variation of the chopper convolution parameters providing a set of independent measurements that can be fitted to obtain the helium beams speed ratio.

III. THEORETICAL MODEL

Our theoretical model for the supersonic helium expansion is based on a theory proposed by Toennies and Winkelmann[23] in which the solution of the Boltzmann equation is obtained by means of the method of moments and assuming a Lennard-Jones (LJ) potential for the He-He interaction. The model was extended by Pedemonte *et al.*[24] to include other analytical He-He potentials, in particular the Hurly Moldover (HM) potential.[25] As in a previous study,[18] the calculations presented were performed treating helium as a real gas and employing the equation of state obtained by McCarty.[26]

The first assumption is to treat the expansion as spherically symmetric. Then an ellipsoidal velocity distribution (f_{ell}), which consists of two Maxwell distributions parameterized by two different temperatures (denoted by $T_\parallel$ and $T_\perp$ for the parallel and the perpendicular velocity components with respect to streamlines) is introduced,

$$f_{ell}(\vec{v}) = n\Big(\frac{m}{2\pi k_b T_{||}}\Big)^{\frac{1}{2}}\Big(\frac{m}{2\pi k_b T_\perp}\Big) \times \exp\Big(-\frac{m}{2k_b T_{||}}(v_{||}-u)^2 - \frac{m}{2k_b T_\perp}v_\perp^2\Big),$$

where m is the mass, n is the number density, $v_\parallel$ and $v_\perp$ are the radial and perpendicular components of the velocity, and u is the most probable velocity of the expanding gas. The evolution of the parameters n, u, $T_\parallel$, and $T_\perp$ with the distance from the source (z) is obtained by solving numerically the equations which contain the collision integral (2, 1),

$$\Omega^{(2,1)}(T_{eff}) = \Big(\frac{k_b T_{eff}}{\pi m}\Big)^{(1/2)}\int_0^\infty Q^{(2)}(E)\gamma^5 \exp(-\gamma^2)d\gamma,$$
$$\gamma = \sqrt{\frac{E}{k_b T_{eff}}}, \quad (1)$$

where T_{eff} is an effective average temperature varying between $T_\perp$ and $T_\parallel$, $Q^{(2)}$ is the viscosity cross section, and E is the collision energy of two atoms in the center-of-mass system. For collisions between Bose-Einstein particles, the viscosity cross section is defined as

$$Q^{(2)}(E) = \frac{8\pi\hbar^2}{mE}\sum_{l=0,2,4,\ldots}\frac{(l+1)(l+2)}{(2l+3)}\sin^2(\eta_{l+2}-\eta_l),$$

where η_l is the phase shift of the partial wave with orbital angular momentum l. For the present article, calculations were performed for LJ and HM potentials. Moreover, we have also considered the Pirani *et al.* (PI) potential[27,28] which modifies and improves the LJ potential ($V(r)$) retaining a simple expression

$$V(r) = \varepsilon\Big(\frac{\mu}{n(r)-\mu}\Big(\frac{r_m}{r}\Big)^{n(r)} - \frac{n(r)}{n(r)-\mu}\Big(\frac{r_m}{r}\Big)^{\mu}\Big),$$

where for He, $\mu = 6$, r is the distance, and $n(r)$ is given by

$$n(r) = \beta + 4\Big(\frac{r}{r_m}\Big)^2,$$

with parameters $r_m = 2.974$ Å, $\beta = 8$, and $\varepsilon = 2.974$ meV.[29]

IV. RESULTS AND ANALYSIS

Figures 4(a) and 4(b) show measurements of the most probable velocity (maximum velocity of the distribution) for different pressures for a cold and a room temperature beam. As can be seen, the theory reproduces the general trend of the experiments although there is a systematic deviation at lower pressures (the nozzle size d_n was kept constant throughout the experiment). It is not quite clear what causes this deviation. From an instrument design point of view, the high pressure range, which gives the highest speed ratio, is the most important. We also note that the velocities for the microskimmed beams are slightly lower (up to around 1%) for a given pressure for both temperatures. The reason for this is not quite clear. However, even though a smaller skimmer has a higher Knudsen number K_n and thus is assumed to show less skimmer interferences (see Ref. 20), the comparatively long and narrow geometries of microskimmers can possibly cause local pressure variations along the skimmer channel and this may slow the beam down, i.e., through a funnelling effect. It is surprising though that the effect does not increase with the source pressure.

Figures 5(a) and 5(b) show the corresponding speed ratio plots for the two temperatures. The first thing to note is the

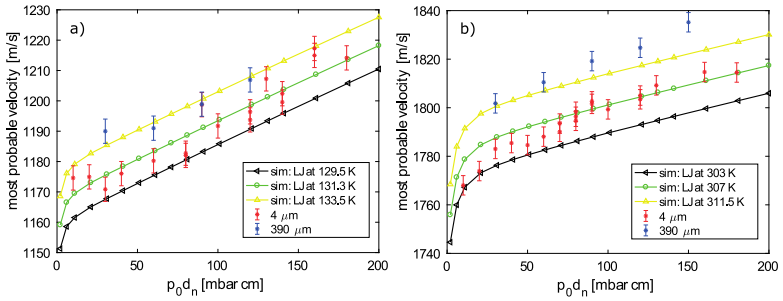

FIG. 4. Experimental results and simulations for the most probable velocity for cold beams (a) and for room temperature beams (b) as a function of $p_0 d_n$, where p_0 is the source reservoir pressure and d_n is the nozzle diameter. Note the slightly lower velocity for the microskimmer beam. This is discussed in the main text.

near to perfect overlap between the microskimmer and standard skimmer measurements. These results agree well with the prediction of Bird *et al.* stating that as long as the internal skimmer angle is greater than the effective angle of the thermal spreading of the beam, no significant collisions of molecules with the internal skimmer surface occur. Thus as long as the speed ratio is sufficiently high to attain this condition, no major internal skimmer interferences are expected. Furthermore, there is a reasonable agreement between theory and experiments although it is interesting to see that for higher pressures, the simulations seem to predict too high speed ratios for the cold beam and too low speed ratios for

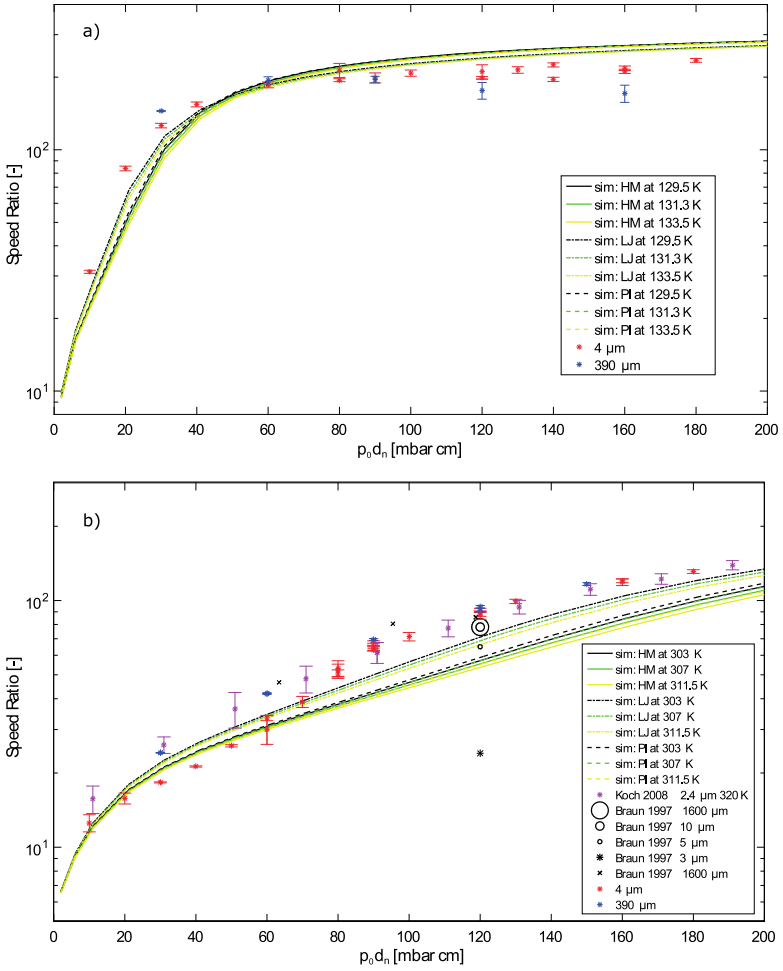

FIG. 5. Experimental results and simulations for the speed ratio of cold temperature beams (a) and room temperature beams (b) plotted together with simulations. For comparison, the speed ratio data from Braun *et al.*[10] and Koch *et al.*[3] are added to the room temperature plot in (b). Note the very similar behavior of microskimmer and standard skimmer as well as the very little variations in the results for the different simulations at different temperatures.

the warm beam. Comparing the three different potentials used for the simulation (LJ, HM, and PI), the LJ potential gives the best agreement for the present experimental conditions [most prominent for the room temperature beam, see Fig. 5(b)]. This better agreement of LJ potential was also observed in Ref. 25 for temperatures above 50 K or in Refs. 17 and 18. Finally, the strong disagreement between the presented 4 μm microskimmer measurements and the 3 μm microskimmer results from Braun *et al.* should be noted. Braun *et al.* proposed geometrical imperfections and/or imperfections of the lip edge of the skimmer as well as difficulties in aligning the skimmer and nozzle as possible explanations for the reduced speed ratios. A comparison between the skimmer images in Ref. 10 and Fig. 2 suggests that the skimmer geometries of both skimmers are similar. This leads us to the conclusion that most likely the mentioned misalignment is the reason for the reduced speed ratio experienced by Braun *et al.*

V. CONCLUSION

In this paper, we have presented a systematic study of velocity distributions of helium beams collimated by a microskimmer for a room temperature beam and a cooled beam. The measurements were carried out in the pressure range 11 bars–181 bars. Our results show that when the microskimmer is properly aligned with the nozzle, the speed ratio for the microskimmer does not differ from that of a standard skimmer. The most probable velocities for microskimmers appear to be slightly smaller than for standard skimmers. We measured a difference of up to around 1%. We attribute this to variations in the local pressure caused by the internal microskimmer geometry, i.e., a funnelling effect and/or scattering from the entrance interior lip, although the effect is not fully understood. Furthermore, we show that the experimental data fit well to the theoretical model we have developed.

ACKNOWLEDGMENTS

We gratefully acknowledge support from Bergen Research Foundation with Trond Mohn. S.D.E. gratefully acknowledges funding from the Research Council of Norway through a FRIPRO Mobility Grant (Contract No. 250018/F20). The FRIPRO Mobility grant scheme (FRICON) is co-funded by the European Union's Seventh Framework Programme for research, technological development, and demonstration under Marie Curie Grant Agreement (No. 608695). The work presented here was also sponsored by the European Union: Theme NMP.2012.1.4-3, Grant No. 309672, project NEMI (Neutral Microscopy).

[1] D. Farías and K.-H. Rieder, Rep. Prog. Phys. **61**, 1575 (1998).
[2] G. Bracco and B. Holst, *Surface Science Techniques* (Springer, 2013).
[3] M. Koch, S. Rehbein, G. Schmahl, T. Reisinger, G. Bracco, W. E. Ernst, and B. Holst, J. Microsc. **229**, 1 (2008).
[4] S. D. Eder, T. Reisinger, M. M. Greve, G. Bracco, and B. Holst, New J. Phys. **14**, 073014 (2012).
[5] P. Witham and E. Sanchez, Rev. Sci. Instrum. **82**, 103705 (2011).
[6] A. Fahy, M. Barr, J. Martens, and P. C. Dastoor, Rev. Sci. Instrum. **86**, 023704 (2015).
[7] M. Barr, A. Fahy, J. Martens, A. P. Jardine, D. J. Ward, J. Ellis, W. Allison, and P. C. Dastoor, Nat. Commun. **7**, 10189 (2016).
[8] L. Vattuone, G. Bracco, M. Smerieri, L. Savio, and M. Rocca, *Dynamics of Gas-Surface Interactions: Atomic-Level Understanding of Scattering Processes at Surfaces* (Springer, Heidelberg, New York, Dordrecht, London, 2013).
[9] G. Scoles, *Atomic and Molecular Beam Methods* (Oxford University Press, New York, Oxford, 1988).
[10] J. Braun, P. K. Day, J. P. Toennies, G. Witte, and E. Neher, Rev. Sci. Instrum. **68**, 3001 (1997).
[11] D. J. Auerbach, *Atomic and Molecular Beam Methods* (Oxford University Press, 1988).
[12] H. Pauly, *Atom, Molecule, and Cluster Beams 2* (Springer, 2000).
[13] R. B. Doak, R. E. Grisenti, S. Rehbein, G. Schmahl, J. P. Toennies, and C. Wöll, Phys. Rev. Lett. **83**, 4229 (1999).
[14] T. Reisinger and B. Holst, J. Vac. Sci. Technol., B: Microelectron. Nanometer Struct.–Process., Meas., Phenom. **26**(6), 2374 (2008).
[15] S. D. Eder, B. Samelin, G. Bracco, K. Ansperger, and B. Holst, Rev. Sci. Instrum. **84**, 093303 (2013).
[16] A. S. Palau, S. D. Eder, T. Kaltenbacher, B. Samelin, G. Bracco, and B. Holst, Rev. Sci. Instrum. **87**, 023102 (2016).
[17] T. Reisinger, G. Bracco, S. Rehbein, G. Schmahl, W. E. Ernst, and B. Holst, J. Phys. Chem. A **111**, 12620 (2007).
[18] S. D. Eder, G. Bracco, T. Kaltenbacher, and B. Holst, J. Phys. Chem. A **118**, 4 (2014).
[19] A. Apfolter, "Wiederaufbau und test einer He-streuapparatur und erste streuexperimente an amorpher sowie kristalliner SiO_2-oberflche," M.Sc. thesis, Graz University of Technology, 2005.
[20] G. A. Bird, Phys. Fluids **19**, 1486 (1976).
[21] T. Reisinger, M. M. Greve, S. D. Eder, G. Bracco, and B. Holst, Phys. Rev. A **86**, 043804 (2012).
[22] T. Nesse, S. D. Eder, T. Kaltenbacher, J. O. Grepstad, I. Simonsen, and B. Holst, Phys. Rev. A **95**, 063618 (2017).
[23] J. Toennies and K. Winkelmann, J. Chem. Phys. **66**, 3965 (1977).
[24] L. Pedemonte, G. Bracco, and R. Tatarek, Phys. Rev. A **59**, 3084 (1999).
[25] L. Pedemonte and G. Bracco, J. Chem. Phys. **119**, 1433 (2003).
[26] R. D. McCarty and V. D. Arp, "A new wide range equation of state for helium," in *Advances in Cryogenic Engineering* (Springer, Boston, MA, 1990).
[27] F. Pirani, M. Albertí, A. Castro, M. M. Teixidor, and D. Cappelletti, Chem. Phys. Lett. **394**, 37 (2004).
[28] F. Pirani, S. Brizi, L. F. Roncaratti, P. Casavecchia, D. Cappelletti, and F. Vecchiocattivi, Phys. Chem. Chem. Phys. **10**, 5489 (2008).
[29] S. Longo, P. Diomede, A. Laricchiuta, G. Colonna, M. Capitelli, D. Ascenzi, M. Scotoni, P. Tosi, and F. Pirani, in *Computational Science and Its Applications—ICCSA 2008*, edited by O. Gervasi, B. Murgante, A. Laganà, D. Taniar, Y. Mun, and M. L. Gavrilova (Springer, Berlin, Heidelberg, 2008).

Article 4

4.4 Center-line intensity of a supersonic helium beam

Adrià Salvador Palau, Sabrina D Eder, Truls Andersen, Anders Komr Ravn, Gianangelo Bracco, Bodil Holst

Physical Review A, **98**, 6 (2018)

Centre line intensity of a supersonic helium beam

Adrià Salvador Palau,[1] Sabrina D. Eder,[2] Truls Andersen,[2]
Anders Komár Ravn,[2] Gianangelo Bracco,[2,3] and Bodil Holst[2]

[1] *Department of Engineering, Institute for Manufacturing, University of Cambridge, Cambridge, CB3 0FS, UK*
[2] *Department of Physics and Technology, University of Bergen, Allégaten 55, 5007 Bergen, Norway*
[3] *CNR-IMEM, Department of Physics, University of Genova, V Dodecaneso 33, 16146 Genova, Italy*

(Dated: October 9, 2018)

Supersonic helium beams are used in a wide range of applications, for example surface scattering experiments and, most recently, microscopy. The high ionization potential of neutral helium atoms makes it difficult to build efficient detectors. Therefore, it is important to develop beam sources with a high centre line intensity. Several approaches for predicting the centre line intensity exist, with the so-called quitting surface model incorporating the largest amount of physical dependencies in a single analytical equation. However, until now only a limited amount of experimental data has been available. Here we present a comprehensive study where we compare the quitting surface model with an extensive set of experimental data. In the quitting surface model the source is described as a spherical surface from where the particles leave in a molecular flow determined by Maxwell-Boltzmann statistics. We use numerical solutions of the Boltzmann equation to determine the properties of the expansion. The centre line intensity is then calculated using an analytical integral. This integral can be reduced to two cases, one which assumes a continuously expanding beam until the skimmer aperture, and another which assumes a quitting surface placed before the aperture. We compare the two cases to experimental data with a nozzle diameter of 10 µm, skimmer diameters ranging from 4 µm to 390 µm, a source pressure range from 2 to 190 bar, and nozzle-skimmer distances between 17.3 mm and 5.3 mm. To further support the two analytical approaches, we have also performed equivalent ray tracing simulations. We conclude that the quitting surface model predicts the centre line intensity of helium beams well for skimmers with a diameter larger than 120 µm when using a continuously expanding beam until the skimmer aperture. For the case of smaller skimmers the trend is correct, but the absolute agreement not as good. We propose several explanations for this, and test the ones that can be implemented analytically.

I. INTRODUCTION

The supersonic expansion of a gas into vacuum can be used to obtain a molecular beam with high centre line intensities with narrow speed distributions [1–6]. Such beams are used in different applications, for example surface scattering experiments and atom beam microscopy [7–10]. Noble gas atoms are very hard to detect due to their high ionization potential [2]. Therefore, precise prediction of the beam centre line intensity plays an important role in designing instruments and experiments with a sufficient signal to noise ratio.

In a standard supersonic expansion source used in scattering experiments, a pressurised gas expands from a small aperture called a nozzle into a vacuum. The expansion is then collimated using an aperture placed at the end of a conical structure that points towards the nozzle, forming a beam. This conical structure is commonly known as a skimmer (see Fig. 1). The problem of precisely determining particle intensities after the skimmer attains different levels of complexity depending on the modified Knudsen number, Kn^* at the skimmer position, which determines the flow regime close to the skimmer [11]. The modified Knudsen number was introduced by Bird [11] to describe the changes in the flow due to backscattering of atoms from the skimmer.

$$\mathrm{Kn}^* = \mathrm{Kn}\left(\frac{2}{5}S_\parallel^2\right)^{-2/(\eta_p-1)}. \tag{1}$$

Where $S_\parallel$ is the parallel speed ratio, a measure of the velocity spread of the beam defined in Sec. II B. η_p is the term leading the inverse power law of the repulsive collision model. For a hard sphere gas $\eta_p \to \infty$, and for the Lennard-Jones potential $\eta_p = 13$ [12]. Kn is the Knudsen number:

$$\mathrm{Kn} = \frac{\lambda_0}{r_\mathrm{S}} = \frac{1}{r_\mathrm{S}\sigma\sqrt{2}n}, \tag{2}$$

where λ_0 is the mean free path of the gas particles and r_S is the radius of the skimmer. n is the number density at the skimmer and σ is the temperature dependent collision cross section of the gas atoms. In this case, σ can be calculated either according to the stagnation temperature, or according to the maximum between the stagnation temperature and the skimmer temperature. For the case of a cold source the collision velocity will be dominated by the warmer skimmer. The need for the modified Knudsen number is justified by the change in the mean free path due to backscattering of atoms from the skimmer; In eq. (2) λ_0 is the mean free path for particles unaffected by the skimmer presence.

The Knudsen number is used to estimate the validity of different flow regimes. Navier-Stokes flow can be assumed

for $\mathrm{Kn} < 0.2$, and free molecular flow for $\mathrm{Kn} > 1$ [11]. As the gas moves away from the nozzle, the mean free path of the particles increases and therefore the nature of the flow dynamics of the problem changes [11]. As explained before, we use here the modified Knudsen number, but the discussion of different flow regimes remains the same. The Knudsen number can only be assumed to be smaller than 0.2 in the space very close to the expansion origin (the nozzle), and hence the Navier-Stokes equations can't be generally used to model the flow of the beam close to, and after, the skimmer. Here, Direct Simulation Monte Carlo methods (DSMC), or direct numerical integration of the differential equation (under simplifying assumptions of the physics of the system), can be used to solve the Boltzmann equation [12, 13].

At $\mathrm{Kn}^* \lesssim 1$, the centre line intensity of the beam is known to be strongly affected by interaction between the beam and particles reflected from the skimmer [11]. Considering the reflection of particles from the skimmer wall makes solving the Boltzmann equation difficult, as DSMC methods are often computationally heavy. Some work has been done regarding the effect of skimmer geometries [11, 14–16]. However, much of this work lacks extensive validation due to the lack of experimental data. This, together with the complexity of some of the proposed approaches, has caused some authors to avoid skimmer attenuation by designing experiments where it is not present.

Another relevant contribution to the beam centre line intensity is the exponential decrease of intensity due to free molecular scattering of the beam's atoms with a background gas in the vacuum chambers [14, 16]. The importance of this contribution will depend on the quality of the pumping system in the experimental set-up and the flux from the nozzle into the expansion chamber.

Intensity calculations disregarding both the interaction between the beam and particles reflected from the skimmer, and collisions with background gas were presented in a range of analytical models published in the 1970's and 1980's, based on a Maxwellian velocity distribution of the supersonic expansion [17–20]. These models coexist with simpler treatments, disregarding the Maxwellian nature of the beam's velocity distribution (usually compensated by including a peak factor), for example [5, 13, 14, 21]. Others use Beijerinck and Verster 1981 model that incorporates cluster formation and uses the concept of a virtual source [8, 18, 22]. Analytical models have the advantage of requiring only relatively simple numerical solutions of the Boltzmann equation and of directly showing the dependencies with the different variables in the system. Among the most prolific analytical models are various adaptations of the quitting surface model [20].

In the quitting surface model, the spherical quitting surface is assumed to be located at the distance from the nozzle at which the atoms reach molecular flow [20]. The atoms then leave the quitting surface following straight trajectories determined by Maxwell-Bolzmann statistics. The ellipsoidal Maxwellian velocity distribution over the surface is given by three parameters: the most probable velocity $\bar{v}$ along the parallel direction (corresponding to the radial direction from the centre of propagation), and the parallel and perpendicular temperatures, respectively $T_{||}$ and $T_{\perp}$. These two temperatures are associated with the velocity spread of the beam in spherical coordinates [23], and in some models are reduced to a simpler description with only a radial temperature $T_{||}$ [20].

There are two popular ways to estimate the position of the quitting surface: i) calculating the terminal Mach number using the continuum assumption and taking the position of the quitting surface to be the distance from the nozzle where the terminal Mach number is close to being reached (see for example [21, 24]), or ii) directly computing the expansion's temperatures and observing the point where these temperatures de-couple. De-coupling is defined as the point where the perpendicular temperature is much smaller than the parallel temperature. Decoupling is typically assumed at a distance where the temperatures of the expansion fulfil $T_{\perp}/T_{||} \leq 0.01$, thus determining the position of the quitting surface. Alternative cutoff values have also been proposed [13], providing a certain degree of freedom to the choice of the quitting surface position. Typically, such temperatures are calculated through a numerical solution of the Boltzmann equation. Previous studies already used such an approach to predict the velocity distribution and intensity in the beam expansion [13, 25–27]. Given that (ii) is more general than (i), we use (ii) in this paper.

The quitting surface position can either be placed before the skimmer, at the skimmer or after the skimmer. If the quitting surface is taken to be before the skimmer, the parallel temperature $T_{\parallel}$ dominates. This means that the condition $T_{\perp}/T_{||} \leq 0.01$ is reached close to the expansion source, and that the perpendicular temperature of the beam quickly approaches 0. If the quitting surface is calculated to be at or after the skimmer it means that $T_{\perp}$ tends to 0 slowly. In this case, the perpendicular temperature $T_{\perp}$ is mostly used in the calculations, and the expansion is assumed to stop at the skimmer, even in the case that its calculation gives a position further away than the skimmer [20]. Regardless of where the expansion is assumed to stop, the centre line intensity is then calculated by integrating over the section of the quitting surface seen by the detector through the skimmer.

In this paper, we present a dataset of centre line intensity measurements for a helium atom beam, using several different skimmer apertures and designs, source temperatures, and skimmer to nozzle distances. We benchmark these intensity measurements with the quitting surface model, and discuss its shortcomings. Additionally, we present a ray tracing simulation of the quitting surface model. This is done using a modification of the ray tracing software known as McStas described in detail in [28]. This paper contains a large number of variables, many of which are used in several formulas. All formulas are introduced with definitions as they appear in the text. In

addition, to make it a bit easier for the reader to keep an overview, we have included an Appendix E with a table listing all the variables with definitions.

II. THEORETICAL FOUNDATION

A. The supersonic expansion

The expansion of gas through a small nozzle undergoes two different physical regimes: an initial continuum flow, governed by the Navier Stokes equations, followed by a molecular flow regime. In a sonic nozzle (a Laval tube cut-off in the sonic plane), the total flux per unit time (from now on, centre line intensity) stemming from the nozzle is typically calculated using the isentropic nozzle model [18]. The sonic plane corresponds to the plane where the Mach number $M = v/c = 1$ where v is the average velocity of the gas and c the local speed of sound [29]. The equation for the total intensity stemming from a nozzle then reads [18]:

$$I_0 = \frac{P_0}{k_B T_0}\sqrt{\frac{2k_B T_0}{m}}\left(\frac{\pi}{4}d_N^2\right)\sqrt{\frac{\gamma}{\gamma+1}}\left(\frac{2}{\gamma+1}\right)^{1/(\gamma-1)}, \tag{3}$$

where γ is the ratio of heat capacities (5/3 for Helium), and d_N is the diameter of the nozzle. In theory, this diameter must be corrected with the size of the boundary layer at the nozzle throat. However, this correction can typically be neglected. k_B is the Boltzmann constant, T_0 and P_0 are the flow stagnation temperature and pressure inside the nozzle, m is the mass of a gas particle. In the second flow regime, the expansion of the gas is calculated using the Boltzmann equation, assuming the nozzle is a point source, and using the following collision integral $\Omega(T_{\text{eff}})$ (corresponding to the RHS of the Boltzmann equation, that gives the rate of change of molecules in a phase-space element caused by particles that have suffered a collision) [13, 25].

$$\Omega(T_{\text{eff}}) = \left(\frac{k_B T_{\text{eff}}}{\pi m}\right)^{\frac{1}{2}}\int_0^\infty Q^{(2)}(E)\,\zeta^5 \exp\left(-\zeta^2\right)d\zeta. \tag{4}$$

$$\zeta = \sqrt{\frac{E}{k_B T_{\text{eff}}}}. \tag{5}$$

Where T_{eff} is an effective average temperature intermediate to the values of the parallel and perpendicular temperatures, $Q^{(2)}$ is the viscosity cross section and E is the collision energy of two atoms in the centre-of-mass system. For collisions between particles following Bose-Einstein statistics, the viscosity cross section can be written as follows [13, 30]:

$$Q^{(2)}(E) = \frac{8\pi\hbar^2}{mE}\sum_{l=0,2,4\ldots}\frac{(l+1)(l+2)}{2l+3}\sin^2(\eta_{l+2}-\eta_l), \tag{6}$$

where η_l are the phase shifts for orbital angular momentum l, obtained solving the scattering of He atoms in the chosen two body potential.

An ellipsoidal Maxwellian velocity distribution is assumed along the whole expansion [13]. The velocity distribution of the atoms in the expansion, f_{ell}, is defined in spherical coordinates by the two independent temperatures, $T_{||}$ and $T_\perp$, and their two corresponding velocities $v_\parallel$ and $v_\perp$ as described in the introduction,

$$f_{\text{ell}}(\vec{v}) = n\left(\frac{m}{2\pi k_B T_{||}}\right)^{\frac{1}{2}}\left(\frac{m}{2\pi k_B T_\perp}\right)\cdot \exp\left(-\frac{m}{2k_B T_{||}}(v_{||}-\bar{v})^2 - \frac{m}{2k_B T_\perp}v_\perp^2\right). \tag{7}$$

The numerical solution of the Boltzmann equation has been implemented for the Lennard-Jones potential (LJ) [31], defined as follows:

$$V_{\text{LJ}}(r_{\text{LJ}}) = 4\epsilon\left[\left(\frac{r_m}{r_{\text{LJ}}}\right)^{12} - \left(\frac{r_m}{r_{\text{LJ}}}\right)^{6}\right], \tag{8}$$

where r_{LJ} is the distance between any two interacting particles. r_m is the distance at which the potential reaches its minimum, for the case of He corresponding to $r_m = 2.974$ Å, $\epsilon = 2.974$ meV [32]. A detailed description of the potential and its implementation in the Boltzmann equation can be found in [13]. The simple LJ potential can be replaced by more sophisticated potentials, such as the Tang, Toennies and Yu (TTY) or Hurly Moldover (HM) potentials [33, 34]. However, results of previous calculations showed that this is only necessary for source temperatures below 80 K [13, 26, 35]. In the present study, the source temperature is higher than 80 K and the LJ potential is adequate.

The numerical solution of the Boltzmann equation in spherical approximation presented here provides the evolution of the gas velocity, and the temperatures $T_{||}$ and $T_\perp$ with respect to the distance from the nozzle.

B. The quitting surface model

As mentioned in the introduction, the quitting surface model assumes that the particles leave in molecular flow from a spherical surface of radius R_F centred at the sonic point. The centre line intensity of the beam is calculated by integrating over all the particles leaving from the quitting surface and arriving at the detector. In 1973, Sikora separated the quitting surface model in two approaches: one corresponding to what he called the *quitting surface model*, and one which he called the *ellipsoidal distribution model*. The first approach assumes a quitting surface placed before the skimmer and a Maxwellian velocity distribution featuring only the radial component of the velocity: $v_\parallel$. The second approach, the ellipsoidal distribution model, assumes an ellipsoidal Maxwellian velocity

distribution featuring both $v_\parallel$ and $v_\perp$, together with a quitting surface placed exactly at the skimmer. For the rest of the paper we will refer to the two approaches as Sikora's quitting surface approach and Sikora's ellipsoidal distribution approach.

Sikora's ellipsoidal distribution approach was later adapted by Bossel to be used for expansions stopping before the skimmer. In other words, Sikora's quitting surface approach (assuming a quitting surface placed before the skimmer) was adapted to incorporate ellipsoidal distributions [19]. To avoid confusion, it is enough to consider the position of the quitting surface itself: in the case of Sikora's ellipsoidal distribution approach, the expansion is considered to stop at the skimmer. In the case of Bossel's approach, the expansion can be chosen to stop at the skimmer or before it. Expansions stopping after the skimmer have thus far not been treated using the quitting surface model. An attempt of doing so is presented in this paper (see Appendix A).

Bossel's approach is the most general approach described so far, as under the right assumptions it reduces to both approaches proposed by Sikora. Bossel's approach corresponds to integrating eq. (7) over the quitting surface area seen by the detector through the skimmer:

$$I_{\mathrm{D}} = \frac{\tau I_0}{2\pi a^2 R_{\mathrm{F}}^2 L} \int_0^{r_{\mathrm{D}}} \int_0^{r_{\mathrm{S}}} \int_0^{\pi} g(\delta) r \rho \cos^3\beta \epsilon^3 \, e^{-S^2(1-\epsilon^2\cos^2\theta)} D(b) d\rho dr d\alpha, \quad (9)$$

where r_{D} is the radius of the detector opening, r_{S} is the radius of the skimmer (see Fig. 1), and a is the distance between the skimmer and the detector. r, β, θ, δ, α and ρ are geometrical parameters defined in Fig. 1. $\tau = \frac{T_\parallel}{T_\perp}$ is the fraction between parallel and perpendicular temperatures, which is used to simplify the integral through $\epsilon = \left(\tau \sin^2\theta + \cos^2\theta\right)^{-1/2}$. $g(\delta)$ is the angular dependency of the supersonic expansion density at the quitting surface, and $L = \int_0^{\frac{\pi}{2}} g(\delta)\sin\delta d\delta$ corresponds to its integral along the quitting surface. $S = \sqrt{\frac{m\bar{v}^2}{2kT_\parallel}}$ is the parallel speed ratio at the quitting surface.

Unfortunately, Bossel's approach has no simple analytical solutions and is often slow to compute over a wide variable space. For $S_i > 5$ Sikora showed that both his ellipsoidal distribution approach and quitting surface approach can be approximated as [20]:

$$I = I_1 \int_0^{2\pi} \frac{d\Phi}{2\pi} [e^{-S_i^2 \sin^2\theta_1}]_{\theta_{1\max(\Phi)}}^{\theta_{1\min(\Phi)}}. \quad (10)$$

Here, Φ is the angle of rotation about the beam axis, and θ_1 is the angle between the vector normal to the quitting surface and the vector connecting a given point on the quitting surface with a point in the detector plane. $\theta_{1\min(\Phi)}$ and $\theta_{1\max(\Phi)}$ are the minimum and maximum angles that fulfil the condition that the line connecting a point in the quitting surface and a point in the detector plane must cross the skimmer aperture. In the case of Sikora's quitting surface approach, θ_1 is defined from a spherical surface of radius R_{F}, and $S_i = S_\parallel = \sqrt{\frac{m\bar{v}^2}{2kT_{\parallel\infty}}}$ is the parallel speed ratio at the end of the expansion. In the case of Sikora's ellipsoidal distribution approach, θ_1 is defined from the skimmer aperture (the radius of the quitting surface is then the distance between the nozzle and the skimmer x_{S}, $R_{\mathrm{F}} = x_{\mathrm{S}}$), and $S_i = S_\perp = \sqrt{\frac{m\bar{v}^2}{2kT_\perp}}$ is the perpendicular speed ratio at the skimmer (see Fig. 1 for a sketch featuring these geometrical terms).

I_1 is defined as the intensity arriving at the detector, assuming that there is no skimmer. This can be obtained in two ways:

$$I_1 = \begin{cases} I_0 \pi r_{\mathrm{D}}^2 \eta_{\mathrm{D}} \frac{1}{(x_{\mathrm{S}}+a)^2}. & \text{Using eq. (3) for } I_0 \\ \eta_{\mathrm{D}} \pi r_{\mathrm{D}}^2 n v_\infty \left(\frac{x_{\mathrm{S}}}{x_{\mathrm{S}}+a}\right)^2. & \text{Using density at skimmer.} \end{cases}$$

Here, η_{D} is the efficiency of the detector in counts/partice. Sometimes, one might be interested to obtain the intensity per area. In order to do so, it suffices to divide I_1 by πr_{D}^2.

From eq. (10) it can be shown that for $r_{\mathrm{S}} \ll x_{\mathrm{S}}$, $r_{\mathrm{S}} \ll a$, $\frac{a}{r_{\mathrm{S}}} >> S_i$, and $r_{\mathrm{D}} << a$, the intensity arriving at the detector reads [20]:

$$I_{\mathrm{S}} = I_1 \left\{ 1 - \exp\left[-S_i^2 \left(\frac{r_{\mathrm{S}}(R_{\mathrm{F}}+a)}{R_{\mathrm{F}}(R_{\mathrm{F}} - x_{\mathrm{S}} + a)} \right)^2 \right] \right\}, \quad (11)$$

x_{S} is the distance between the nozzle and the skimmer. This equation, with the assumption of $S_i = S_\parallel$, and the expansion stopping before the skimmer is usually preferred to using the perpendicular speed ratio, as measuring the parallel speed ratio of atoms is a well established technique [36]. The simplicity of the model has motivated its usage for example to optimize the intensity of helium microscopes [10, 37].

C. Scattering contributions

The atoms leaving the quitting surface do not travel in a perfect vacuum. Rather, they interact with the background gas and the particles scattered from the chamber and skimmer walls. Such interactions can become significant at high nozzle pressures. There have been various approaches for accounting for this, from DSMC simulations, to simpler numerical models based on assumptions on the scattering properties of the skimmer walls [14, 38]. Analytical models for the skimmer contributions are so far non-existent due to the difficulty of solving the Boltzmann equation analytically in a typical nozzle-skimmer geometry. The method that has provided a better understanding is the DSMC method (see, for example [11]). This method is not employed in this paper due to its complexity, but it can be assumed to be the preferable method when precise, localized predictions are desired.

Here, we choose to only model the interaction with the background gas via free molecular scattering, as it can be modelled by a simple exponential law [14, 16]:

$$\frac{I}{I_{\mathrm{S}}} = \exp\left(-\sigma^2 n_{\mathrm{B_E}} x_{\mathrm{S}} - \sigma^2 n_{\mathrm{B_C}} a\right). \qquad (12)$$

$\sigma = \frac{r_m}{2^{1/2}}$ is the scattering cross section of the atoms in the Lennard-Jones potential. $n_{\mathrm{B_E}}$ and $n_{\mathrm{B_C}}$ are the background number densities in the expansion chamber and the subsequent chambers respectively, measured by a pressure gauge placed far away from the beam centre line.

D. Overall trends

In this section we qualitatively describe important trends in the expected behaviour of the centre line intensities according to the theory presented above.

1. For skimmers large enough, the exponential term in the equation for centre line intensity becomes negligible, (eq. (11)). Thus, increasing the radius of the skimmer further will not lead to an increase in the centre line intensity.

2. Larger skimmers display a decrease in centre line intensity at high pressure. This is due to the fact that a larger skimmer gives a smaller modified Knudsen number (eq. (1)) for a given pressure. It is known that for smaller modified Knudsen numbers in the so called transition regime, wide angled shock waves can form, which compromise the flow of the beam [11]. Note that the shock wave behaviour is not modelled by the theory presented above.

3. The closer the skimmer is to the quitting surface ($(R_{\mathrm{F}} - x_{\mathrm{S}}) \to 0$); the higher the centre line intensity will be, as the denominator in the exponential in eq. (11) reaches its minimum. This effect is due to the fact that a larger portion of the quitting surface is captured and this gives a larger centre line intensity.

4. Colder sources produce more intense beams because the gas passing through the nozzle has a higher density, which ends up influencing the centre line intensity equation (see eq. (3)).

5. Numerical solutions of the Boltzmann equation as described in Sec. II A predict an intensity dip at low source pressures for small skimmers. This dip cannot be extracted from the equations in a simple manner and will be discussed further in the main text.

E. The ray tracing simulation

As an independent test of eqs. (9) and (10), a ray tracing simulation of the quitting surface expansion was implemented. The simulation was performed using a modification of the ray-trace software package known as McStas described in [28, 39, 40].

In order to replicate the dynamics assumed during the derivation of eq. (9), a spherical source with ellipsoidal Maxwellian velocity distributions and an anisotropic number density was programmed. The McStas software works with sources featuring uniform spatial ray probability distributions that are later corrected for their real probability weights determined by the physics of the system (in this case, the Maxwellian velocity distribution of the source, and the anisotropic number density). This poses a problem when simulating the quitting surface because most of the rays yield probabilities that are too low, bringing insufficient sampling at the detector. To avoid this effect, we only computed the particles stemming from the surface of the quitting surface seen by the detector through the skimmer (see Fig. 2). This reduces the computation power needed for each experiment and therefore allows for better statistics in the detector.

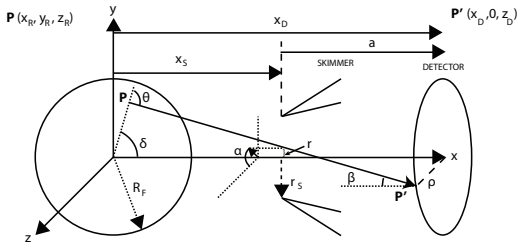

FIG. 1. Illustration of all variables used in the ellipsoidal quitting surface model. **P** is a point on the quitting surface from which a particle leaves in a straight trajectory until **P'**, a point placed on the detector plane. The point on the quitting surface is given by the set of Cartesian coordinates (x, y, z), which can be related to the polar coordinates r, α, ρ for integration. x_{S} is the distance from the nozzle to the skimmer and x_{D} is the distance from the nozzle to the detector. Therefore $a = x_{\mathrm{D}} - x_{\mathrm{S}}$. The angles β and θ can also be expressed in terms of r, α and ρ.

The simulation is performed as follows: first, a circular target or focus of interest is set, which determines the area of the detector, where the rays will hit. Then, the point P' is generated randomly over the area of the detector. Subsequently, a point P over the quitting surface is randomly generated and its connecting vector $\vec{r}$ is computed. Only the points visible by the detector through the skimmer are allowed (see Fig. 2). Therefore a maxi-

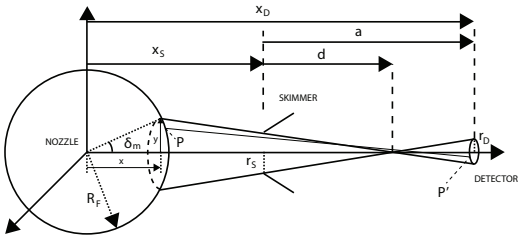

FIG. 2. Diagram of the section of the quitting surface considered in the ray tracing simulation, only the angle $\delta_{\rm m}$ seen by the detector through the skimmer contributes to the intensity at the detector. $R_{\rm F}$ is the radius of the quitting surface, y is the distance between the axis of symmetry and the projection of the maximum-angle ray on the quitting surface, $r_{\rm S}$ is the skimmer radius and $r_{\rm D}$ is the radius of the detector. a is the distance between the skimmer and the detector, d is the distance from the skimmer to the point where the maximum-angle ray crosses the symmetry axis. $x_{\rm D}$ is the distance between the nozzle and the detector and $x_{\rm S}$ is the distance between the nozzle and the skimmer. x is the distance from the point of emission of the maximum angle ray to the nozzle plane.

mal angle δ_m is set (see the derivation in Appendix C).

$$\begin{aligned}\delta_m &= \arcsin\frac{y}{R_{\rm F}} \\ &= \arcsin\left(\frac{\frac{d}{r_{\rm S}}(d+x_{\rm S}) - \sqrt{\frac{d^2}{r_{\rm S}^2}R_{\rm F}^2 + R_{\rm F}^2 - (d+x_{\rm S})^2}}{R_{\rm F}(\frac{d}{r_{\rm S}})^2 + R_{\rm F}}\right)\end{aligned} \tag{13}$$

With d corresponding to the distance from the skimmer to the point where the maximum-angle ray crosses the symmetry axis (see Fig. 2):

$$d = \frac{a r_{\rm S}}{r_{\rm D} + r_{\rm S}}. \tag{14}$$

Which means that the point P must be contained within the following angles:

$$\delta = (0, \delta_m),\ \phi = (0, 2\pi). \tag{15}$$

In Cartesian coordinates, P is:

$$P = R_{\rm F}\left(\sin\delta\cos\phi, \sin\delta\sin\phi, \cos\delta\right). \tag{16}$$

Following, a scalar velocity v is randomly generated between two limiting values along the direction of the vector $\vec{r}$. From its Cartesian components, the perpendicular and parallel velocities are obtained:

$$\begin{aligned} v_{||} &= \vec{v}\cdot\vec{u}_r = v_x\sin\delta\cos\phi + v_y\sin\delta\sin\phi + v_z\cos\delta, \\ v_{\perp} &= \vec{v}\cdot\vec{u}_\delta = v_x\cos\delta\cos\phi + v_y\cos\delta\sin\phi - v_z\sin\delta, \\ v_{\perp'} &= \vec{v}\cdot\vec{u}_\phi = -v_x\sin\phi + v_y\cos\phi. \end{aligned} \tag{17}$$

A probability weight factor given by the Maxwellian velocity distribution of the beam is set for the ray travelling from P to P' (see Figs. 2 and 1). The intensity recorded at the detector will be the sum of all probability weight factors. Therefore, we can recover eq. (23) (Appendix B) in angular coordinates to infer the intensity contributions:

$$dI = \frac{I_0 A_{\rm D}}{A_{\rm S} L} f_{\rm ell}(\vec{v}) g(\delta) v^2 d\Omega dv. \tag{18}$$

$A_{\rm D} = \pi r_{\rm D}^2$ is the area of the detector. For the experiments presented here, this corresponds to the area of the pinhole placed in front of the detector (see Fig. 3), $A_{\rm S} \approx \pi y^2$ is the area of the section of the sphere from which particles are simulated assuming $r_{\rm S} \ll R_{\rm F}$ (the computed section of the quitting surface is small enough relative to $R_{\rm F}$ that its area approximates to the area of a circle). L is defined as in eq. (29) (Appendix B) but taking care to integrate only between 0 and δ_m. $d\Omega$ is the solid angle seen through the skimmer from the centre of the detector, this is approximately the same as the solid angle seen from P' through the skimmer. This approximation is true for detectors placed sufficiently far away from the skimmer.

III. EXPERIMENTAL SETUP FOR INTENSITY MEASUREMENTS

The setup used to obtain the experimental measurements presented in this paper is shown in Fig. 3. All the measurements have been obtained using the molecular beam instrument at the University of Bergen, known as MAGIE. This instrument is equipped with a home-built source which enables the skimmer and nozzle to be positioned relative to each other with 50 nm precision [5]. This is particularly important to ensure proper alignment in centre line intensity experiments using small skimmers. A detailed description of the system can be found in [41]. In contrast to most other helium atom scattering instruments with time-of-flight detection, MAGIE has a movable detector arm, which allows us to measure the straight through intensity of the beam without any sample. A centre line intensity measurement is performed by setting the initial pressure in the inlet channel and measuring the inlet channel temperature. For the experiments presented here, the beam source is either "warm" (at ambient temperature) or "cold" (at roughly 125 K). The helium gas expands through a pinhole aperture nozzle, 10 µm in diameter to a lower pressure chamber where it undergoes a supersonic expansion. We use a Pt-Ir electron microscope aperture as nozzle (purchased from Plano GmbH, A0301P) [5]. The expansion is then collimated by a skimmer placed 5.3 ± 0.1 mm, or 11.3 ± 0.1 mm, or 17.3 ± 0.1 mm away from the nozzle. Figure 4 shows an example of the alignment procedure. The nozzle is moved across the skimmer opening in 50 nm steps in a 2D array and eventually moved to the position

of maximum intensity which is clearly visible. Note that a displacement of just 0.2 mm leads to a noticeable change in intensity.

Further downstream, at 973 mm from the nozzle, a 400 µm aperture is placed to further reduce the background pressure and thus minimize the beam attenuation. Finally, at 2441 mm from the nozzle an ionization detector is set. The detector has an efficiency of $\eta_{\mathrm{D}} = 2.1 \cdot 10^{-6}$ (provided by the manufacturer). Just in front of the detector another aperture is placed. Two different apertures with diameters 200 µm and 50 µm respectively, were used in the experiments. This allows us to measure the centre line intensity. A table with the diameter of the aperture for each intensity experiment is given in Appendix D.

Five skimmers were used to collimate the beam, two made of nickel, two made of glass and an additional metallic skimmer known as the Kurt skimmer. The nickel skimmers have apertures 120 and 390 µm in diameter. They are produced by Beam Dynamics (model 2) and have a streamlined profile [42] (see dimensions in Fig. 5). The glass skimmers are home made using a *Narishige* PP-830 glass pulling machine, using Corning 8161 Thin Wall capillaries with an outer diameter of 1.5 mm and an inner diameter of 1.1 mm. The glass skimmers are mounted on a Cu holder (see dimensions in Fig. 5). Their apertures are 18 and 4 µm respectively, measured using an electron beam microscope. Stereo microscope measurements on the glass skimmers showed an outer opening angle of $\approx 32.5°$ for the first 200µm, followed by a more narrow section of $\approx 12.5°$. The inner opening angle could not be determined, but due to the thin opening lip ($\approx$ 200nm), it is expected to be similar to the outer opening angle. This corresponds to what is known as a *slender* skimmer. Slender skimmers are known to produce better performance than wide angle skimmers, as long as the modified Knudsen number at the skimmer is kept large enough [11]. This condition is fulfilled in the experiments presented here due to the large values of $S_{||}$ and the small skimmer openings.

The Kurt skimmer is also home made. It is designed to be used with interchangeable apertures on 2 mm diameter discs. Two apertures are used in this study: 5 and 100 µm in diameter. The dimensions of the Kurt skimmer can be found in Fig. 5 (note the inverted cone shape before the aperture). The Kurt skimmer is made of stainless steel type 1.4301.

IV. RESULTS

Throughout Figs. 7-12 we use open circles for the nozzle-skimmer distance x_{S}= 5.3 mm, triangles for x_{S}= 11.3 mm, and asterisks for x_{S}= 17.3 mm. The labels are included in Fig. 7 only. Error bars are not included in the plots because they are too small to show.

A. Ray tracing benchmarking of the centre line intensity integral

A spherical quitting surface is simulated using the ellipsoidal quitting surface velocity distribution defined in eq. (7). The centre line intensity obtained through the ray tracing simulation is then compared with eqs. (9) and (11) for different spans of the different variables present in the equation. In all cases the result from the analytical models lies within the statistical margin of error of the simulation (see Fig. 6). In the further sections of this paper we will just show the results from eqs. (9) and (11).

B. 120 µm and 390 µm skimmers

In this section, the measured intensities for the large skimmers from Beam Dynamics (see Fig. 5) (120 and 390 µm diameters), are compared with the predictions from eq. (12) for the two variations of the model described in Sec. II A.

1. *Warm source, $T_0 \approx 300K$*

The results for a warm source are shown in Figs. 7 and 8. Fig. 7 shows the experimental results and eq. (12) with the expansion assumed to stop at the skimmer, and $S_i = S_{\perp}$. The experimental results are reproduced fairly well over the whole range, but with a trend towards too high theoretical values for higher pressures. To obtain $n_{\mathrm{B_E}} \rightarrow n_{\mathrm{B_E}}(P_0)$ for eq. (12), we use a set of measured background pressures in the expansion chamber. From observation this dependency is linear, and the equation obtained is:

$$n_{\mathrm{B_E}} = \frac{1}{k_{\mathrm{B}} T_0} \left(m_E \cdot P_0 + n_E \right). \tag{19}$$

m_E and n_E are the linear fit coefficients from fitting the measured background pressures P_B with respect to P_0. Concretely, for this set of measurements $m_E = 3.9 \cdot 10^{-4} \frac{Pa}{bar}$, $n_E = -5.8 \cdot 10^{-4} Pa$ if P_0 is given in bar and $n_{\mathrm{B_E}}$ in SI units (positive values of $n_{\mathrm{B_E}}$ are guaranteed by the experimental pressure range, $P_0 \geq 2$ bar). The number density after the skimmer, $n_{\mathrm{B_C}}$, was experimentally measured to be approximately 1/20 of $n_{\mathrm{B_E}}$, eq. (19) was used with the corresponding factor.

Fig. 8 shows the values of eq. (12) for the 120 µm and 390 µm skimmers, where the expansion is assumed to stop before the skimmer (in this case for $T_{\perp}/T_{\parallel} \leq 0.1$), and $S_i = S_{\parallel}$. At small source pressures there is good agreement between experiments and simulations, but the dependency on the nozzle-skimmer distance is lost. At high pressures the model becomes non-physical because the point at which $T_{\perp}/T_{\parallel} \leq 0.1$ is calculated to be positioned after the skimmer. One must note that the decrease in centre line intensity at high pressures is

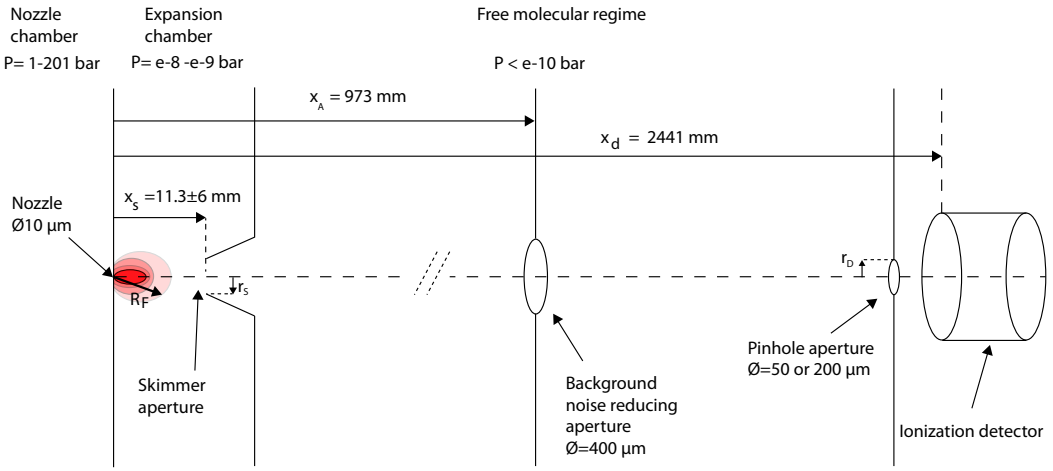

FIG. 3. Sketch of the experimental setup used for the centre line intensity measurements. A skimmer is used to select the supersonic beam, followed by two apertures. Vacuum pumps are placed in each chamber to reduce interactions of reflected particles with the beam. $R_{\rm F}$ is the radius of the quitting surface, from where the gas particles are assumed to leave following a mollecular flow.

not given by the model (eq. (11)) being un-physical, but instead by $S_\parallel^2 r_{\rm S}^2/R_{\rm F}^2 \to 0$ as P_0 increases. If the expansion is assumed to always stop at the skimmer ($R_{\rm F} = x_{\rm S}$) as in the case of Fig. 7, this condition does not hold any more and the predicted centre line intensity increases monotonically with P_0. In this case, eq. (12) is also used. The discrepancy at low pressures is discussed in Sec. V.

2. *Cold source $T_0 \approx 125K$*

We present the measured intensities for a beam with a source temperature of 125 ± 2 K and we compare them with the predictions from eq. (12). We obtain $n_{\rm B_E} \to n_{\rm B_E}(P_0)$ as in eq. (19): $m_E = 5 \cdot 10^{-4} \frac{Pa}{bar}$, $n_E = 48 \cdot 10^{-4} Pa$. In the case of cold sources, if one chooses to determine the quitting surface position by the ratio of temperatures $T_\perp/T_\parallel \leq 0.1$, the quitting surface is placed after the skimmer already at quite low pressures. Thus, computing the eq. (12) for the case of $S_i = S_\parallel$ and the expansion stopping before the skimmer is only valid for a few measurement points. Therefore, we only present the results for the case of the expansion stopping at the skimmer and $S_i = S_\perp$. In general, the prediction power of the model decreases for a cold source (see Fig. 9).

C. Micro skimmers

The centre line intensity plots for micro skimmers show marked dips in the intensity, especially for the cold source cases. Centre line intensity dips are also observed at higher pressures for a warm source (see Figs. 10 and 11). The model predicts the dips for a cold source, but in both cases fails to fit the experimental data well. The centre line intensity measured for both skimmers is in the same range, while the model predicts a more pronounced difference between the 18 µm skimmer and the 4 µm skimmer.

D. The Kurt skimmer

To experimentally determine the importance of Kn*-driven skimmer effects we use a skimmer designed in such a way that such effects are expected to clearly dominate over the centre line intensity trends. This is the case of the Kurt skimmer (see Sec. III), which due to its inverted-cone walls concentrates the reflecting particles along the beam center line, leading to a low Kn* (see eq. (1)). Comparing the Kurt skimmer intensities with the Beam dynamics skimmers, one sees that skimmer effects are not clearly observed until about 40 bar, for nozzle-skimmer distances corresponding to $x_{\rm S} > 11.3$ mm (see Fig 12). This means that the discrepancies at lower pressures between eq. (12) and the micro-skimmer

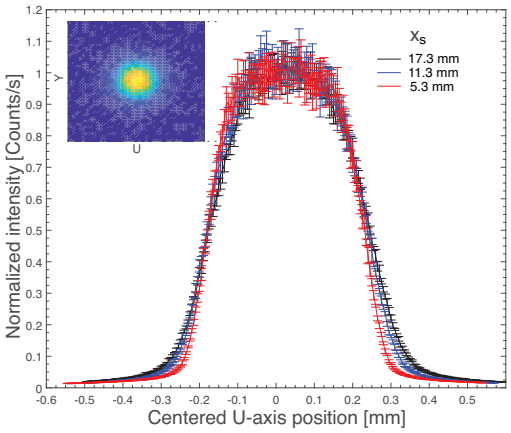

FIG. 4. Example of the alignment procedure, here done for a cold source at 60 bar and a 390 µm diameter skimmer. The nozzle is moved relative to the skimmer in 50 nanometer steps for three values of x_S . The optimum alignment position of the nozzle relative to the skimmer is obtained by finding the centre point of the maximum of intensity. The complete intensity plot of the beam is shown in the upper left corner.

measurements cannot be explained by skimmer interactions only. In fact, the modified Knudsen number in the case of micro-skimmers at 40 bar is expected to be larger than in the case of the Kurt skimmer due to the $1/r_S$ dependency (see eq. (1)).

Note how skimmer interference in the case of the Kurt skimmer is not significant until the nozzle-skimmer distance is set at 5.3 mm, (see Fig 12). A similar effect is seen, for a cold source, in the case of the 390 µm Beam Dynamics skimmer, where for $x_S = 5.3$ mm, skimmer interference becomes evident (see Fig. 9). The same effect is not clearly observed for the smaller, 120 µm Beam Dynamics skimmer. This can be seen as an experimental confirmation of the importance of the modified Knudsen number, which predicts stronger skimmer effects for larger skimmers.

E. Complete experimental data

In this section, we plot the complete dataset of measurements carried out during this study, with the exception of measurements corresponding to the Kurt skimmer, that are plotted separately. In order to preserve the relevant intensity magnitude, and thus make comparisons easier the intensities plotted have been normalized to the radius of the aperture in front of the detector used to perform each measurement. Therefore, in this section, the intensities are given in counts/s $\cdot$ m^2. The centre line intensity data for a warm source $T_0 \approx 300$ K is shown in Fig. 13, and for a cold source $T_0 \approx 125$ K in Fig. 14. Additionally, we plot the difference in centre line intensity per square meter between cold and warm sources for each experiment (Figs. 15 and 16).

From Fig. 15, one can observe that for large skimmers cold sources produce a higher centre line intensity than warm sources, especially for high source pressures. This is given by eq. (3) and by the larger speed ratios obtained in cold beams. For the case of the 120µm skimmer, this difference reduces the further away the skimmer is placed from the nozzle due to the evolution of $T_\perp$ along the beam axis.

For the case of micro skimmers, cold sources are generally *less* intense than warm sources, except for very large pressures. This is due to an intensity dip occurring for cold sources at low and medium pressures driven by the evolution of the beam's perpendicular speed (see Discussion). The smaller the collimating skimmer is the larger the influence of this dip on the measured centre line intensity. This is because larger skimmers collect particles with a larger perpendicular temperature range.

V. DISCUSSION

The analytical model based on Sikora's ellipsoidal distribution approach ($S_i = S_\perp$, expansion stopped at the skimmer) predicts the centre line intensity of a helium beam generated by a source at ambient temperature with reasonable accuracy. However, the model has several limitations, each of which will be discussed in detail in this section.

1. *Poor fit at high pressures*: for most skimmers, the model overshoots the measured intensities at high pressures ($P_0 \gtrsim 50$ bar). This phenomenon is likely due to a combination of two effects: skimmer interference, and a continuing expansion of the beam after the skimmer. By observing the data, we can see that in the case of a warm source this overshoot does not significantly vary when two skimmers with the same design but different diameter are used (in this case, the Beam Dynamics skimmers). This points towards the idea that skimmer interference can't be the main cause of the overshoot, as the influence of the particles reflected from the skimmer is expected to strongly depend on the skimmer radius. However, in the case of a cold source, the overshoot is more significant for the 120 µm Beam Dynamics skimmer than its 390 µm equivalent. What is likely happening is that the helium beam continues to expand significantly after the skimmer following different dynamics than before it, due to the removal of particles by the skimmer edges. According to the simulations of the expansion performed in this study, this is particularly relevant for the case of a cold source, where the quitting surface is often predicted to be several centimetres after the skimmer. This renders

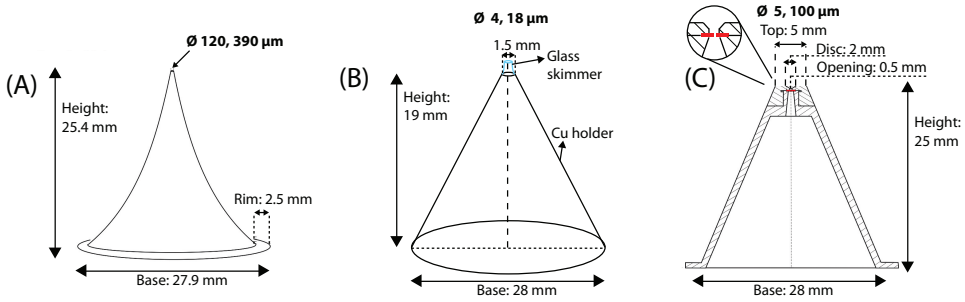

FIG. 5. Drawings of the skimmers used for the centre line intensity measurements. (A) corresponds to the Beam Dynamics skimmers, with diameters of 120 and 390 µm, (B) to glass micro-skimmers mounted on copper, with diameters of 4 and 18 µm and (C) corresponds to the Kurt skimmer, with inserted appertures of 5 and 100 µm .

Sikora's treatment of a beam that expands due to its non vanishing $T_\perp$ at the skimmer un-physical as it assumes no further collisions after the skimmer.

During the preparation of this paper, efforts were undertaken to adapt Sikora's model to a beam expanding after the skimmer using simple geometrical rules. This was motivated by the observations made by Doak et al, whom used micro-skimmers to perform focusing experiments and observed a deviation between expected and measure focal spot size. They suggested that this may have been due to the supersonic expansion continuing after the beam has passed through the skimmer aperture [43]. This adaptation can be found in Appendix A (Fig. 19) but did not produce very promising results. A treatment using a DSMC simulation of the whole system is most likely a more accurate approach in order to predict intensities at large pressure values. This approach is also much more complex than the analytical models presented here.

Another possible explanation of these discrepancies would be the non-physical nature of a "hard" quitting surface. Replacing it with a "soft" treatment may yield interesting results. The centre line intensity would be calculated then by integrating over a series of infinitesimally spaced successive quitting surfaces.

The higher overshoot at $P_0 \gtrsim 50$ bar for the smaller Beam Dynamics skimmer in the case of a cold source occurs in all cases except one: $x_S = 5.3$ mm (see Fig. 9). In order to understand this peculiarity, one must re-visit the modified Knudsen number. The case of $x_S = 5.3$ mm for a cold source and $r_S = 390$ µm, is the case expected to have the lowest modified Knudsen number (largest r_S and number density at the skimmer, see eq. (1)). Therefore, it is likely that this particular case is the only one showing skimmer interference governed by the interaction with reflected particles.

2. *Low predictability of micro-skimmer intensities*: on the one hand, skimmer interference and skimmer clogging are known to be determined by the modified Knudsen number Kn^*, which strongly depends on the skimmer diameter (eq. (1)). Micro-skimmers, are thus expected to show less interference than their larger counter-parts under the same conditions. This effect is clearly seen in Fig. 9, where skimmer effects are present only for the larger 390 µm skimmer.

   On the other hand, smaller skimmers sometimes have very thin and long geometries, causing a possible increase of pressure along the skimmer channel. This effect is likely what causes the bad fit between the model predictions and the observed micro-skimmer centre line intensities.

   Notwithstanding, it is important to note that Sikora's ellipsoidal quitting surface model is able to predict the *general trends* of micro skimmer intensities. This includes the centre line intensity dip at low pressure for small skimmers. This dip is driven by the behaviour of the perpendicular speed ratio at low pressures, that is predicted by the simulation of the supersonic expansion to decrease first and increase later (see Fig. 17).

   However, the experimental observability of this dip is actually determined by the radius of the skimmer and the distance between the nozzle and the skimmer. If $\frac{r_S}{x_S} S_\perp$ is small enough ($\lesssim 0.8$), then the term $\left[-S_\perp^2 \left(\frac{r_S(R_F+a)}{R_F(R_F-x_S+a)}\right)^2\right]$ in eq. (11) is small too. This makes the exponential term in eq. (11) dominate, and the effect of the dip in $S_\perp$ can be clearly observed in the beam centre line intensity. This explains why this dip is only experimentally observed for the case of micro-skimmers.

   This good trend replication is particularly relevant for purposes of optimization, where the value of

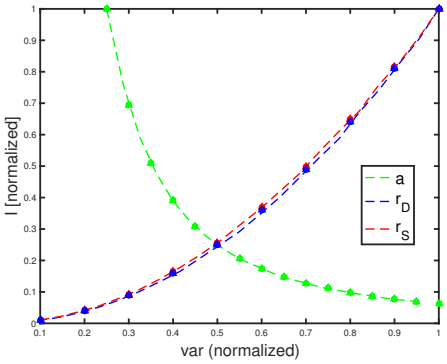

FIG. 6. Plot of the ray tracing simulation (dashed lines) compared with eq. (9) and (11) (respectively, circles, crosses for $S_i = S_\parallel$ and triangles for $S_i = S_\perp$, superposed). The green line show the effect on the centre line intensity of varying the distance between the skimmer and the detector, a. The blue and red lines show the intensity change when varying the radius of the pinhole in front of the detector, r_D, and the radius of the skimmer, r_S. The centre line intensity and the variable values have been normalized to 1 in order to show all dependences in a single plot. The calculations are done at a fixed skimmer position $x_\mathrm{S} = 11.3$ mm (the centre position). a is varied between 0.5 m and 2 m, r_D is varied between 10 µm and 100 µm, and the radius of the skimmer, r_S is varied between 1 µm and 10 µm. While a variable is varied, the others are kept fix at the maximum value of their span ($a = 2$ m, $r_\mathrm{D} = 100$ µm, $r_\mathrm{S} = 10$ µm. The source temperature is 115 K and the source pressure is 161 bar. Both the ray tracing simulation and the centre line intensity model assume a quitting surface placed just before the skimmer position ($R_\mathrm{F} = 11.2$ mm).

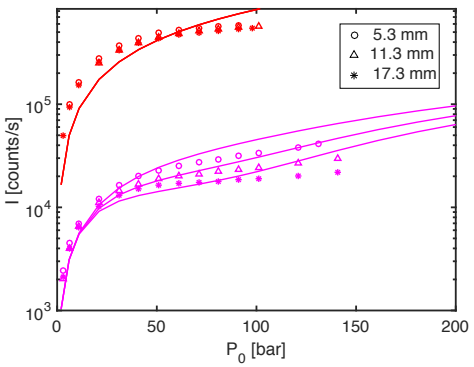

FIG. 7. Plot of measured and predicted intensities for a warm source (300 K), 120µm (pink) and 390µm (red) skimmers, and for three values of x_S: 5.3 mm (circles), 11.3 mm (upwards arrows) and 17.3 mm (asterisks). The intensities are computed assuming that the expansion stops at the skimmer with $S_i = S_\perp$. Note that, for the larger skimmer, the centre line intensity becomes independent of the distance between the skimmer and the nozzle, so that all the curves collapse in one simulated curve (in good agreement with what is observed experimentally). The difference in intensities between the two skimmers is due to the fact that they were obtained using different pinholes in front of the detector (see Appendix D and Fig. 3)

interest is not so much the centre line intensity but the combination of parameters maximizing it.

3. *Weak dependence on the nozzle-skimmer distance of the $S_i = S_\parallel$ variant*: only when the expansion is allowed to stop at the skimmer and the perpendicular speed ratio is used, does the predicted centre line intensity significantly depend on the nozzle-skimmer distance, x_S. This is expected, as in this case the thermal spread of the beam is caused by the value of the perpendicular temperature at the skimmer $T_\perp$, and this value varies strongly with x_S. Despite $S_\parallel << S_\perp$ causing a stronger exponential contribution in eq. (11), the variation on $S_\perp$ with the skimmer radius is much stronger than the fraction term in the exponential, making the $S_i = S_\parallel$ variant actually less dependent on x_S (as $S_\parallel$ remains constant).

VI. CONCLUSION

We present a dataset of centre line intensity measurements for a supersonic helium beam and compare it to various intensity models. We show that these models replicate the experimental data well for skimmers with diameters 120 and 390 µm. Particularly, we show that Sikora's ellipsoidal distribution approach, assuming a quitting surface placed at the skimmer position, with the expansion dominated by the supersonic expansion perpendicular temperature $T_\perp$ fits the experimental data best.

We present a ray tracing simulation approach, used to numerically replicate the introduced centre line intensity models. We show that the ray tracing approach and analytical models (Sikora's and Bossel's) follow very similar dependencies with the different geometrical variables of the experiment.

In the presented dataset, we observe Knudsen number dependent skimmer interference for a 390 µm skimmer, and a specially designed 100 µm skimmer placed 5.3 mm away from a cold source. We postulate that the rest of the discrepancies between the experimental data and the model may be due to either backscattering interferences at quasi-molecular flow regimes, or a continuation of the supersonic expansion after the beam has passed through the skimmer. Another explanation may be that the as-

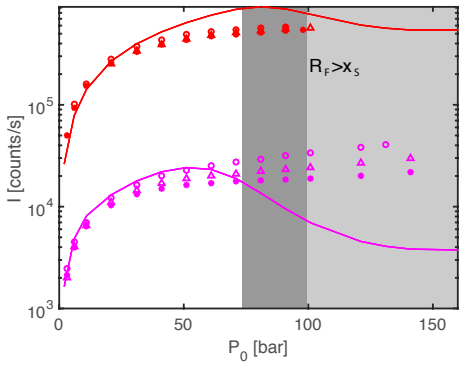

FIG. 8. Plot of measured intensities for a warm source (300 K), and 120µm (pink) and 390µm Beam Dynamics skimmers (red). The measured intensities are compared to eq. (12), with the expansion stopped before the skimmer and $S_i = S_\parallel$. Note how after the quitting surface has surpassed the skimmer, the model loses its predictability (light grey for x_S = 17.3 mm, dark grey indicates the whole span for the different values of x_S). The difference in intensities between the two skimmers is due to the fact that they were obtained using different pinholes in front of the detector (see Appendix D).

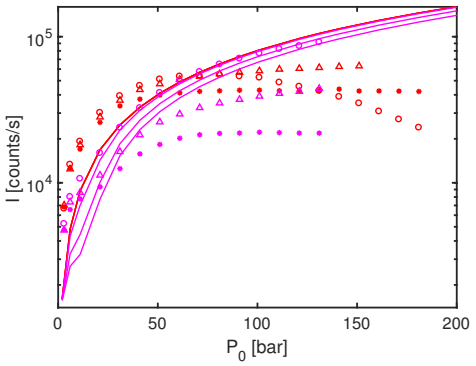

FIG. 9. Plot of measured and predicted intensities for a cold source (125 K) and the Beam Dynamics skimmers: 120 µm (pink) and 390 µm (red). The intensities are computed using eq. (12) and assuming that the expansion stops at the skimmer with $S_i = S_\perp$. The intensities are plotted for three values of x_S: 5.3 mm (circles), 11.3 mm (upwards arrows) and 17.3 mm (asterisks). Note how for $P_0 > 40$ bar and 390 µm skimmer (red), in the case of $x_S = 5.3$ mm, skimmer effects are clearly present and the centre line intensity is significantly lower than for the other two x_S positions. All measurements were taken with $r_D = 25$µm (see Appendix D and Fig. 3)

sumption of the quitting surface stopping abruptly at a given distance is is too simple to adequately describe the physics in this regime.

ACKNOWLEDGMENTS

The work presented here was sponsored by the European Union: Theme NMP.2012.1.4-3 Grant no. 309672, project NEMI (Neutral Microscopy). We thank Yair Segev from the the Weizmann Institute of Science (Israel) for his very useful and detailed comments, especially for his comments regarding theoretical background. We thank Kurt Ansperger Design, Entwicklung und Bau von Prototypen, Moserhofgasse 24 C / 1, 8010 Graz, Austria and Department of Physics/Experimental Physics, Finemechanical Laboratory and Workshop, Karl-Franzens-University Graz, Universitatsplatz 5, 8010 Graz, Austria for the design and production of the Kurt skimmer. We thank Jon Roozenbeek for his useful edits.

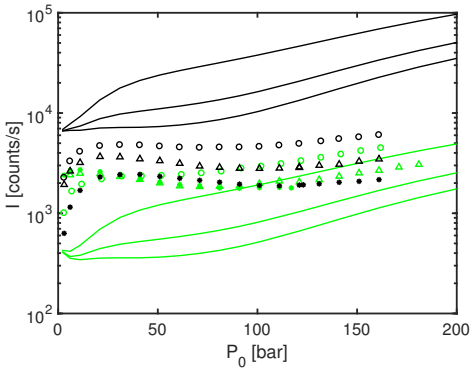

FIG. 10. Plot of measured and predicted intensities for a warm source and the glass skimmers: 18µm (black) and 4µm (green). The intensities are computed using eq. (12) and assuming that the expansion stops at the skimmer with $S_i = S_\perp$.

APPENDIX A: ADAPTATION TO AN EXPANSION AFTER THE SKIMMER

An untreated case in literature is when collisional expansion continues after the skimmer. A way to approach this problem is to assume that the expansion is unaffected by this interaction and simply project the quitting surface further ahead until its predicted radius R_F (see Fig. 18).

The centre line intensity must be calculated using eq. (12), with $a \to a'$, $r_S \to r'_S$, $x_S \to x'_S$:

$$a' = a - \left(R_F \cos(\arctan \frac{r_S}{x_S}) - x_S \right) \qquad (20)$$

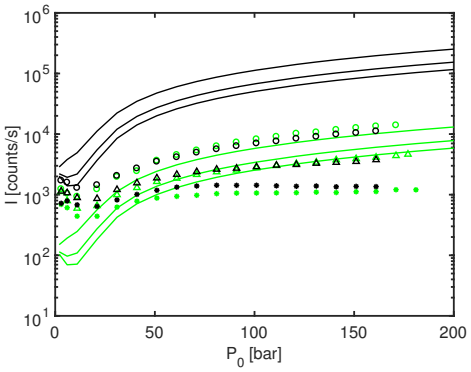

FIG. 11. Plot of measured and predicted intensities for a cold source and the glass skimmers: 18µm (black) and 4µm (green). The intensities are computed assuming that the expansion stops at the skimmer with $S_i = S_\perp$.

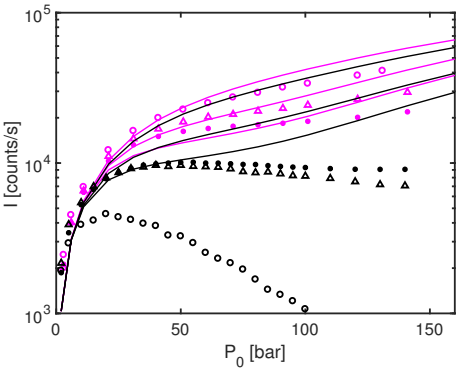

FIG. 12. Plot of measured and computed intensities for the 100 µm Kurt skimmer (black) and a 120 µm (pink) Beam dynamics skimmer for a warm source. The intensities are computed assuming that the expansion stops at the skimmer with $S_i = S_\perp$. Note how strong discrepancies are not observed except for the case of the 100 µm Kurt skimmer. Two discrepancy modes can be observed, a very significant one for x_S= 5.3 mm and a less significant one for the rest of nozzle-skimmer distances.

$$r'_S = R_F \sin\left(\arctan\frac{r_S}{x_S}\right) \tag{21}$$

$$x'_S = R_F \cos\left(\arctan\frac{r_S}{x_S}\right) \tag{22}$$

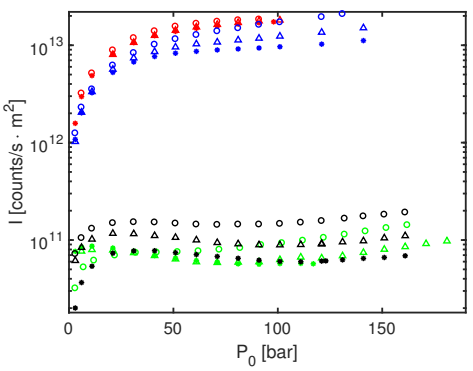

FIG. 13. Measured centre line intensities per area in counts/$s\cdot m^2$ for a warm source, and for the following skimmer apertures: 120 µm Beam Dynamics (blue), 390 µm Beam Dynamics (red), 18 µm glass skimmer (black), and 4 µm glass skimmer (green). The circle, triangle, and asterisk markers correspond to the nozzle-skimmer distances, x_S, of 5.3 mm, 11.3 mm, and 17.3 mm respectively.

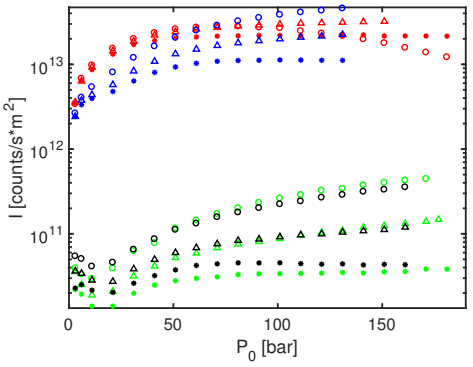

FIG. 14. Measured centre line intensities per area in counts/$s\cdot m^2$ for a cold source, and for the following skimmer apertures: 120 µm Beam Dynamics (blue), 390 µm Beam Dynamics (red), 18 µm glass skimmer (black), and 4µm glass skimmer (green). The round, triangle, and asterisk markers correspond to the nozzle-skimmer distances, x_S, of 5.3 mm, 11.3 mm, and 17.3 mm respectively.

APPENDIX B: DERIVATION OF THE QS MODEL

The contribution to the number density by a differential of the quitting surface dS placed at a point P to the point P' is [19]:

$$dN(x_D, 0, z_D) = n(R_F, \delta, \eta) f_{ell}(v, \theta) d^3v. \tag{23}$$

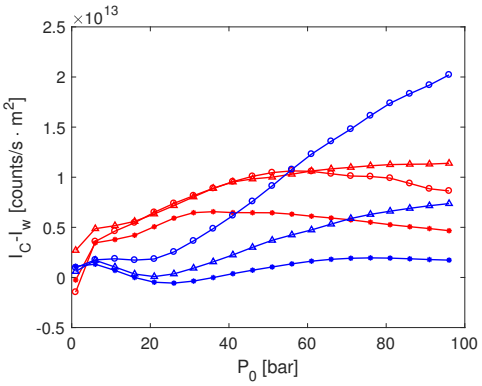

FIG. 15. Measured differences between cold source and warm source beam intensities per area in counts/$s \cdot m^2$ for the following skimmer apertures: 120 µm Beam Dynamics (blue), 390 µm Beam Dynamics (red).The circle, triangle, and asterisk markers correspond to the nozzle-skimmer distances, x_S, of 5.3 mm, 11.3 mm, and 17.3 mm respectively. The continuous line indicates that where experimental data was missing, data was extrapolated from the closest experimental points.

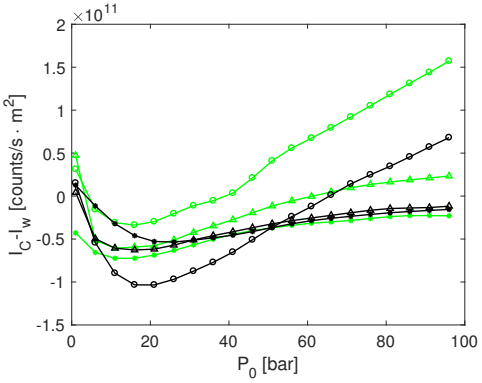

FIG. 16. Measured differences between cold source and warm source beam intensities per area in counts/$s \cdot m^2$ for the following skimmer apertures: 18 µm glass skimmer (black), and 4µm glass skimmer (green). The round, triangle, and asterisk markers correspond to the nozzle-skimmer distances, x_S, of 5.3 mm, 11.3 mm, and 17.3 mm respectively. The continuous line indicates that where experimental data was missing, data was extrapolated from the closest experimental points.

In this equation, $n(R_F, \delta, \eta) \equiv n(R_F)g(\delta)$ is the number density at the quitting surface, that is allowed to depend on the angle δ to account for the fact that the nozzle is not actually point-like. $f_{ell}(v, \theta)$ is the ellipsoidal Maxwellian distribution defined in eq. (7). v is the modulus of the speed vector and θ is the angle between the segment PP'

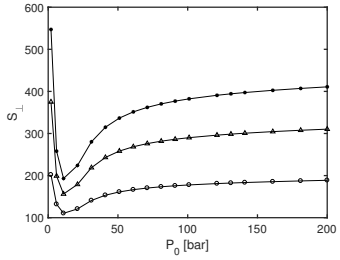

FIG. 17. Predicted value of $S_\perp$ for a cold source (125 K) according to the numerical calculation of the supersonic expansion presented in Sec. II A. The round, triangle, and asterisk markers correspond to the nozzle-skimmer distances, x_S, of 5.3 mm, 11.3 mm, and 17.3 mm respectively.

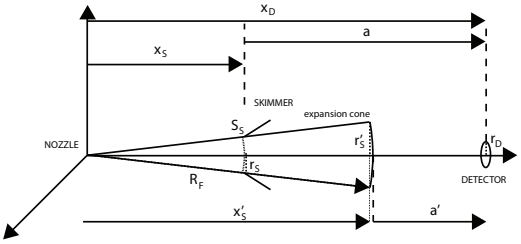

FIG. 18. Diagram of the supersonic expansion for the case of a radius of the quitting surface radius higher that the distance between the nozzle and the skimmer. The quitting surface is assumed to expand unaffected by the skimmer aperture, except by collimation. R_F is the radius of the quitting surface, y is the distance between the axis of symmetry and the projection of the maximum-angle ray on the quitting surface, r_S is the skimmer radius and r_D is the radius of the detector. a is the distance between the skimmer and the detector, d is the distance from the skimmer to the point where the maximum-angle ray crosses the symmetry axis. x_D is the distance between the nozzle and the detector and x_S is the distance between the nozzle and the skimmer.

and P (see Fig. 1). Following the derivation from [19], one obtains:

$$N(\mathrm{P}') = \frac{\tau n(R_F)}{2\pi a^2} \int_0^{r_S} \int_0^{\pi} g(\delta) r \cos^3\beta \cdot \epsilon^3 e^{-S_\parallel^2(1-\epsilon^2\cos^2\theta)} D(b) dr d\alpha, \tag{24}$$

where $S_\parallel = U/c_\parallel$ is the parallel speed ratio, $\epsilon = \left(\left(\tau \sin^2\theta + \cos^2\theta\right)^{-1/2}\right.$, $\tau = \frac{T_\parallel}{T_\perp}$. The function $D(b)$ is

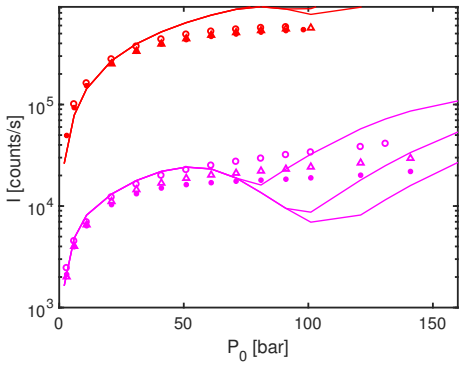

FIG. 19. Plot of measured intensities for a warm source and the Beam Dynamics skimmers: (300 K), and 120µm (pink) and 390µm Beam Dynamics skimmers (red). The measured intensities are compared to eq. (12), with the expansion stopped after the skimmer and $S_i = S_\parallel$.

defined as follows:

$$D(b) \equiv \frac{2}{\sqrt{\pi}} b e^{-b^2} + \left(2b^2+1\right)\left[1 + erf(b)\right], \qquad b \equiv S_\parallel \epsilon \cos\theta \tag{25}$$

The angle β is shown in Fig. 1. $N(P')$ corresponds to the number density at a radial position from the axis of symmetry, to obtain the number density at a circular detector we must integrate over the arriving differential volume:

$$N_{\text{total}} = \Delta x \int_{\text{S}} N(\text{P}') d\text{S} = 2\pi\Delta x \int_0^{r_{\text{D}}} N(x_{\text{D}}, \rho)\rho d\rho. \tag{26}$$

Imposing that the proportion of intensities must correspond to the proportion of number densities, we can obtain the expression for the centre line intensity arriving at a circular detector:

$$\frac{I_{\text{D}}}{I_0} = \frac{N_{\text{total}}}{2\pi \int_{R_{\text{F}}-\Delta x}^{R_{\text{F}}} \int_0^{\frac{\pi}{2}} n(r) r^2 g(\delta) \sin\delta d\delta dr}. \tag{27}$$

We obtain:

$$I_{\text{D}} = \frac{\tau I_0}{2\pi a^2 R_{\text{F}}^2 L} \int_0^{r_{\text{D}}} \int_0^{r_{\text{S}}} \int_0^{\pi} g(\delta) r \cdot \rho \cos^3\beta \cdot \epsilon^3 \, e^{-S_\parallel^2 (1-\epsilon^2\cos^2\theta)} D(b) d\rho dr d\alpha. \tag{28}$$

Where I_0 is defined in eq. (3). L corresponds to the integration of $g(\delta)$ along the half sphere (all the intensity emitted by the source is set to be contained in $g(\delta)$).

$$L \equiv \int_0^{\frac{\pi}{2}} g(\delta) \sin\delta d\delta. \tag{29}$$

.

APPENDIX C: EQUATIONS FOR THE RAY TRACING CODE

Using trigonometry, it is possible to determine exactly the maximum possible δ_m within a source-skimmer-detector geometry (see Fig. 2).

$$\delta_m = \arcsin\frac{y}{R_{\text{F}}}. \tag{30}$$

Now, we use the Pythagorean theorem to obtain y, the height of the triangle containing the angle δ_m, x is the basis of the triangle as shown in Fig. 2.

$$\frac{y}{d + (x_{\text{S}} - x)} = \frac{r_{\text{S}}}{d}, \qquad x = \sqrt{R_{\text{F}}^2 - y^2}. \tag{31}$$

Expanding eqs. (31) we obtain the following quadratic equation:

$$\left(\frac{yd}{r_{\text{S}}} - d - x_{\text{S}}\right)^2 = R_{\text{F}}^2 - y^2, \tag{32}$$

expanding in powers of y:

$$y^2\left((\frac{d}{r_{\text{S}}})^2 + 1\right) + y\left(-2\frac{d}{r_{\text{S}}}(d + x_{\text{S}})\right) + (d + x_{\text{S}})^2 - R_{\text{F}}^2 = 0 \tag{33}$$

Which can be solved using the quadratic formula:

$$y = \frac{2\frac{d(d+x_{\text{S}})}{r_{\text{S}}} \pm \sqrt{4\frac{d^2}{r_{\text{S}}^2}R_{\text{F}}^2 - 4(d+x_{\text{S}})^2 + 4R_{\text{F}}^2}}{2(\frac{d}{r_{\text{S}}})^2 + 2} = \frac{\frac{d}{r_{\text{S}}}(d + x_{\text{S}}) \pm \sqrt{\frac{d^2}{r_{\text{S}}^2}R_{\text{F}}^2 + R_{\text{F}}^2 - (d+x_{\text{S}})^2}}{(\frac{d}{r_{\text{S}}})^2 + 1}. \tag{34}$$

The distance d is also obtained using trigonometry (see Fig. 2).

$$\frac{r_{\text{S}}}{d} = \frac{r_{\text{D}}}{a - d} \rightarrow d = \frac{a r_{\text{S}}}{r_{\text{D}} + r_{\text{S}}}. \tag{35}$$

To determine whether to take the positive or negative square root in eq. 34, we can take the case $x = R_{\text{F}}$ (which corresponds to the case $R_{\text{F}} \rightarrow \infty$). In this case, from trigonometry it is easy to see that $y = \frac{r_{\text{S}}}{d}(d + x_{\text{s}} - R_{\text{F}})$. Thus, the geometrically-sound case corresponds to the negative square root.

VII. APPENDIX D: r_{D}-r_{S} TABLE

TABLE I. Table showing the values for the skimmer radius r_{S}, and the radius of the pinhole placed in front of the detector r_{D}, for the experiments presented in this paper.

Skimmer diameter	r_{S}	r_{D} (warm)	r_{D} (cold)
4 µm	2 µm	100 µm	100 µm
18 µm	9 µm	100 µm	100 µm
100 µm	50 µm	25 µm	not shown
120 µm	60 µm	25 µm	25 µm
390 µm	195 µm	100 µm	25 µm

VIII. APPENDIX E: GLOSSARY OF SYMBOLS

Symbol	Description
Kn^*	Modified Knudsen number
Kn	Knudsen number
$S_\parallel$	Parallel speed ratio
η_P	Power law parameter on the collision model
λ_0	Mean free path of gas particles
r_S	Skimmer radius
n	Number density of the gas at the skimmer
σ	Cross section of gas particles
$\bar{v}$	Most probable velocity along the radial direction
$T_\parallel$	Parallel temperature of the expansion
$T_\perp$	Perpendicular temperature of the expansion
$v_\parallel$	Parallel component of the velocity
$v_\perp$	Perpendicular component of the velocity
M	Mach number
v	Average velocity of the gas
c	Local speed of sound
I_0	Total intensity stemming from the nozzle
T_0	Stagnation temperature inside the nozzle
P_0	Stagnation pressure inside the nozzle
k_B	Boltzmann constant
γ	Ratio of heat capacities
d_N	Diameter of the nozzle
m	Mass of a gas particle
$\Omega(T_\mathrm{eff})$	Collision integral in the Boltzmann equation
T_eff	Effective average temperature of the gas
Q^2	Viscosity cross-section
E	Collision energy in the centre of mass system
$\hbar$	Reduced Planck constant
η_l	Phase shifts for orbital momentum l
f_ell	Velocity distribution in the expansion
V_LJ	Lennard-Jones potential
r_LJ	Distance between two interacting particles
r_m	Distance where V_LJ is minimum
ϵ	Depth of the potential well in V_LJ
R_F	Radius of the quitting surface
I_D	Centre-line intensity (ellipsoidal model)
τ	$T_\parallel/T_\perp$
a	Distance between the skimmer and the detector
r_D	Radius of detector opening
P	Point on the quitting surface
P'	Point on the detector
$\vec{r}$	Vector connecting P and P'
r	Distance from beam axis to where the skimmer plane intersects $\vec{r}$
x,y,z	Cartesian coordinates
β	Angle between $\vec{r}$ and the xz plane
θ	Angle between P and $\vec{r}$
α	Angle between r (note, not \vec{r}) and the xz plane
ρ	Distance between P' and the detector centre
$g(\delta)$	Angular dependency of the gas density on the quitting surface
L	Integral of $g(\delta)$ over the quitting surface
S_i	Speed ratio term in Sikora's model
I	Sikora's centre line intensity before approximation
Φ	Angle of rotation about the beam axis
$T_{\parallel\infty}$	Asymptotic value of the parallel temperature
η_D	Efficiency of the detector in counts/part
I_1	Intensity arriving at the detector assuming no skimmer presence
x_S	Distance between nozzle and skimmer
I_S	Sikora's centre line intensity assuming $r_\mathrm{S} \ll x_\mathrm{S}$, $r_\mathrm{S} \ll a$,$a/r_\mathrm{S} >> S_i$, $r_\mathrm{D} << a$
n_BE	Background number density in the expansion chamber
n_BC	Background number density in subsequent chambers
δ_m	Maximal angle on the quitting surface
d	Distance from the skimmer to the point where the maximum-angle ray crosses the beam axis
ϕ	Azimuthal angle in spherical coordinates
δ	Polar angle in spherical coordinates ($\delta = 0$ lays over x)
A_D	Area of the detector
A_S	Area of the skimmer
x_A	Distance between the nozzle and the noise-reducing aperture

[1] R. Campargue, Rev. Sci. Instrum. **35**, 111 (1964).

[2] H. Pauly, *Atom, Molecule, and Cluster Beams I*, 1st ed. (Springer-Verlag, Berlin, 2000).

[3] D. P. DePonte, S. D. Kevan, and F. S. Patton, Rev. Sci. Instrum. **77**, 55107 (2006).

[4] G. Scoles, B. D, and U. Buck, *Atomic and Molecular Beam Methods*, Vol. 1 (Oxford University Press, New York Oxford, 1988) p. 752.

[5] S. D. Eder, B. Samelin, G. Bracco, K. Ansperger, and B. Holst, Rev. Sci. Instrum **84** (2013).

[6] U. Even, EPJ Tech. Instrum. **2**, 17 (2015).

[7] M. Koch, S. Rehbein, G. Schmahl, T. Reisinger, G. Bracco, W. E. Ernst, and B. Holst, J. Microsc. **229**, 1 (2008).

[8] A. Fahy, M. Barr, J. Martens, and P. Dastoor, Rev. Sci. Instrum **86**, 023704 (2015).

[9] S. D. Eder, T. Reisinger, M. M. Greve, G. Bracco, and B. Holst, New. J. Phys. **14**, 73014 (2012).

[10] A. Salvador Palau, G. Bracco, and B. Holst, Phys. Rev. A (2016).

[11] G. A. Bird, Physics of Fluids **19**, 1486 (1976).

[12] G. a. Bird, *Molecular Gas Dynamics and Direct Simulation of Gas Flows*, 1st ed. (Oxford University Press, New York Oxford, 1994) p. 458.

[13] T. Reisinger, G. Bracco, S. Rehbein, G. Schmahl, W. E. Ernst, and B. Holst, J. Phys. Chem A **111**, 12620 (2007).

[14] H. Hedgeland, A. P. Jardine, W. Allison, and J. Ellis, Rev. Sci. Instrum. **76**, 123111 (2005).

[15] J. Braun, P. K. Day, J. P. Toennies, G. Witte, and E. Neher, Rev. Sci. Instrum. **68**, 3001 (1997).

[16] M. J. Verheijen, H. C. W. Beijerinck, W. A. Renes, and N. F. Verster, Chem. Phys. **85**, 63 (1984).

[17] J. B. Anderson and J. B. Fenn, Physics of Fluids **8**, 780 (1965).

[18] H. C. W. Beijerinck and N. F. Verster, Physica C **111**, 327 (1981).

[19] U. Bossel, *Skimming of Molecular Beams from Diverging Non-equilibrium Gas Jets*, Deutsche Luft- und Raumfahrt. Forschungsbericht (Deutsche Forschungs-und Versuchsanstalt für Luft-und Raumfahrt, 1974).

[20] G. S. Sikora, *Analysis of asymptotic behavior of free jets: Prediction of Molecular Beam Instensity and Velocity Distributions*, Ph.D. thesis, Princeton (1973).

[21] P. Witham and E. Sanchez, Rev. Sci. Instrum. **82**, 103705 (2011).

[22] M. Barr, A. Fahy, A. Jardine, J. Ellis, D. Ward, D. A. Maclaren, W. Allison, and P. C. Dastoor, Nucl. Instrum. Methods **B 340**, 76 (2014).

[23] G. A. Bird, AIAA Journal **8**, 1998 (1970).

[24] A. Amirav, U. Even, and J. Jortner, Chem. Phys. **51**, 31 (1980).

[25] J. Toennies and K. Winkelmann, J. Chem. Phys. **66**, 3965 (1977).

[26] L. Pedemonte and G. Bracco, J. Chem. Phys **119**, 1433 (2003).

[27] M. Usami and K. Teshima, JSME Int. J **42**, 369 (1999).

[28] B. Holst, Rev. Sci. Instrum. , 1 (2015).

[29] H. Pauly, *Atom, Molecule, and Cluster Beams I: Basic Theory, Production and Detection of Thermal Energy Beams*, Atom, Molecule, and Cluster Beams (Springer, 2000).

[30] B. Holst, S. Eder, A. Salvador Palau, and G. Bracco, Review of Scientific Instruments (under review).

[31] J. E. Jones, Proc. R. Soc. A **106**, 441 (1924).

[32] S. Longo, P. Diomede, A. Laricchiuta, G. Colonna, G. Capitelli, D. Ascenzi, M. Scoltoni, P. Tosi, and F. Pirani, in *Lecture Notes in Computer Science 2008*, edited by G. et al (Springer-Verlag, Berlin, 2008) p. 1131.

[33] K. T. Tang, J. P. Toennies, and C. L. Yiu, Phys. Rev. Lett. **74**, 1546 (1995).

[34] J. J. Hurly and M. R. Moldover, J. Res. Natl. Inst. Stand. Technol. **105**, 667 (2000).

[35] L. Pedemonte, G. Bracco, and R. Tatarek, Phys. Rev. A **59**, 3084 (1999).

[36] A. Salvador Palau, S. D. Eder, T. Kaltenbacher, B. Samelin, G. Bracco, and B. Holst, Rev. Sci. Instrum. (2015).

[37] A. Salvador Palau, G. Bracco, and B. Holst, Phys. Rev. A **95**, 13611 (2017).

[38] K. Luria, W. Christen, and U. Even, J. Phys. Chem A **115**, 7362 (2011).

[39] K. Lefmann and K. Nielsen, Neutron News **10**, 20 (1999).

[40] P. Willendrup, E. Farhi, and K. Lefmann, in *Physica. B. Condens. Matter*, Vol. 350 (2004).

[41] A. Apfolter, "Master Thesis," (2005).

[42] B. Dynamics, Beam Dynamics.

[43] R. B. Doak, R. E. Grisenti, S. Rehbein, G. Schmahl, J. P. Toennies, and C. Wöll, Phys. Rev. Lett. **83**, 4229 (1999).

Article 5

4.5 True-to-size surface mapping with neutral helium atoms

Sam M Lambrick, Adrià Salvador Palau, Poul Erik Hansen, Gianangelo Bracco, John Ellis, Andrew P Jardine, Bodil Holst

Physical Review A, **103**, 5 (2021)

True to size surface mapping with neutral helium atoms

Sam M. Lambrick,[1,*] Adrià Salvador Palau,[2,†] Poul Erik Hansen,[3]
Gianangelo Bracco,[4] John Ellis,[1] Andrew P. Jardine,[1] and Bodil Holst[2]

[1] *Department of Physics, Cavendish Laboratory, JJ Thomson Avenue, University of Cambridge, Cambridge, CB3 0HE, UK*
[2] *Department of Physics and Technology, University of Bergen, Allégaten 55, 5007 Bergen, Norway*
[3] *Danish Fundamental Metrology A/S Kogle Alle 5, 2970 Hørsholm, Denmark*
[4] *CNR-IMEM, Department of Physics, University of Genova, V Dodecaneso 33, 16146 Genova, Italy*

(Dated: April 15, 2021)

Three-dimensional mapping of microscopic surface structures is important in many applications of technology and research, including areas as diverse as microfluidics, MEMS and geoscience. However on the nanoscale, using established techniques for such imaging can be extremely challenging. Scanning helium microscopy (SHeM) is a new technique that uses neutral helium atoms as a probe, enabling completely non-destructive imaging. The technique is broadly applicable and ideal for many otherwise difficult to image materials such as insulators, ultra-thin nano-coatings and biological samples. Here we present a method for implementation and operation of a stereo helium microscope, by applying the photometric stereo method of surface reconstruction to helium microscopy. Four detectors around the sample are typically required, but we show how sample rotation can be used to perform stereo reconstruction with a single detector instrument, or to improve the quality of the reconstructed surface by increasing the number of independent measurements. We examine the quality of the reconstructed surface and show that for low aspect ratio good absolute height is recovered. For features with height/width ~ 1 the shape of the surface is still recovered well (8% error) despite multiple scattering and masking of the helium beam by surface topography. Therefore it is possible to perform accurate reconstruction of the shape of nanoscale structures with a height to width ratio of at least unity.

I. INTRODUCTION

Accurate measurements of surface topography are essential to many fields of modern research. However, applying established techniques on the micro- and nanoscale is often difficult; for example, electron microscopy is complicated by the local secondary electron emission properties of surfaces [1] and scanning probe methods are limited by the tip profile [2]. The emerging technique of scanning helium microscopy (SHeM) [3–5], which uses a beam of neutral atoms, provides a promising new opportunity. Thermal energy helium atoms have several advantages as imaging probes; they are inert and their energies are very low compared to other particle probes used for imaging, such as electrons or helium ions. Specifically, the energy of the atoms in a supersonic helium beam is approximately 50 meV, corresponding to a de Broglie wavelength of around 0.05 nm [6]. These energies are between three and six orders of magnitude lower than the energies typically used in electron and helium ion imaging [7]. Furthermore, thermal helium atoms scatter from the outermost electron density distribution of the surface without any penetration into the material [6] and propagate in straight-line trajectories that are unaffected by electromagnetic fields. Thus helium atoms are capable of providing information about the true geometrical structure of a surface [6, 8]. Together, these properties mean SHeM is ideal for probing the topography of samples that are difficult to measure otherwise, either because conventional probe-surface interactions limit the measurements, or because the sample can react or deteriorate during the process of imaging. In particular, helium is well suited to imaging insulators and biological samples, as well as ultra-thin coatings and other nano-materials that have a significant three dimensional structure.

3D structure determination has recently been reported using helium atoms [9] using the stereophotogrammetry technique, which was applied to taxonomic studies of the trichomes on a mouse eared cress leaf, and dorsal skin of a Port Jackson shark. The method works by triangulation; the sample was tilted by known angles and corresponding points on the surface were used to obtain a small number of 3D coordinates with a single-detector. The method is thus similar to observation using an optical stereomicroscope with a single source of illumination. The points used for triangulation were mapped manually between subsequent images; the difficulty being that each point in the image has to be carefully mapped to the corresponding point in each rotated image, and more importantly that several rotations about different axes are required to obtain a good three-dimensional reconstruction [10].

An alternative approach to 3d imaging with atoms has been made possible by the recent discovery that unlike highly prepared 'pristine' atomic surfaces, which scatter with an angular distribution containing strong specular and diffracted components [6, 8], many 'unprepared' technological surfaces scatter diffusely with an approximate cosine like distribution [11–14]. The cosine-like dis-

* Corresponding author, sml59@cam.ac.uk
† The two first authors contributed equally to this work

tribution appears and is centred on the surface normal, even when the sample is illuminated on a microscopic level. On a macroscopic scale, when averaging over a significant fraction of surface, such behaviour has long been known as Knudsen's cosine law [15–18]. However, identifying similar behaviour on a microscopic scale means that by sampling the scattered distribution in several different directions, the local surface orientation can in-principle be determined, and hence by integration the 3D surface profile. An exact cosine distribution does not even need to be assumed, providing sufficient independent angular measurements are obtained. In order to make use of this principle, the second generation of SHeM instrument that has been developed in Cambridge includes the capability to simultaneously acquire images from 4 detectors arranged around the incoming helium micro-probe.

In this article, we present a three-dimensional surface profile reconstruction technique which we refer to as 'heliometric stereo', an adaptation of the photometric stereo method to helium microscopy. Photometric stereo uses photographs of an object illuminated from different angles to reconstruct a 3D image of the object, by using differences in the light intensities due to the different angles of illumination [19]. Heliometric stereo works analogously, but, taking into account the differences of image formation, instead of changing the illumination angles, the observation angles are changed.

In photography or traditional light microscopy an object is illuminated with a number of light sources. An image of the object is produced by the light rays scattered from the object going through a series of lenses, and then being projected onto a light-sensitive detector/film with spatial resolution. In helium microscopy, and other scanning imaging techniques such as SEM, images are formed by illuminating the sample point by point with a focused or collimated beam and measuring the intensity collected by one or several detectors. By rastering the sample under the beam (equivalent to rastering the beam over the sample), an image viewed from the incident beam is generated through Helmholtz reciprocity; the same process that is used in scanning electron microscopes and in dual photography [20]. Fig. 1 shows the method of image production via scanning in comparison to image formation with broad illumination. In principle, helium microscopy could also use the same imaging principle as photography. However, it is not possible with present technology to build a helium detector with spatial resolution, though suggestions have been made that it could be done with field ionisation detection [21, 22].

The lateral resolution of SHeM images is determined by the size of the helium micro-probe incident on the sample, which in turn determines the minimum extent of each pixel in the image. The image contrast is governed by the angular size and position of the helium detectors, which sample the distribution of atoms scattered from the illuminated point on the surface. Practically, SHeM images are always limited by shot-noise, due to the finite flux of atoms. When using pinhole collimation to form

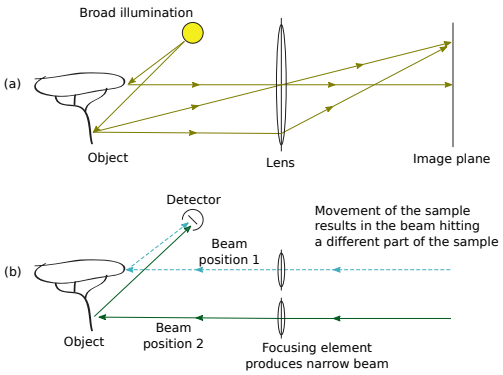

FIG. 1. (a) The process of image formation using a lens and broad illumination and (b) the alternative method of producing images by scanning a focused probe follows from inverting the direction of the light rays to give an image appearing as if it were formed behind the focusing element, in (b) the two beam positions would not happen simultaneously. Understanding the projection allows the right coordinate system to be used for heliometric stereo.

the microprobe the flux drops strongly with increasing resolution [23, 24]; consequently the smallest helium microprobe reported to date is 350 nm [4, 25, 26]. Fortunately, higher intensities can be achieved by focussing the beam with a Fresnel zone-plate; theoretical calculations [24, 27] have estimated that the helium microprobe can be reduced to a diameter of order 10nm.

In the design of a neutral helium microscope, it is important to distinguish between the lateral resolution, which is determined by the size of the helium beam and gives the ability to distinguish between features spatially separated on the sample, and the 'angular resolution' which is given by the solid angle covered by the detector opening. The smaller the solid angle, the more well defined the angle of detection is. Hence the 'angular resolution' determines the possibility of accurately knowing the intensity of scattered helium in a particular direction but does not have an impact on the minimum feature size observable. In order to achieve good angular resolution, detectors are designed to cover as small a solid angle as permitted by the signal to noise ratio of the instrument [28].

In the current work we show that photometric stereo applied to helium (heliometric stereo) is an ideal technique for 3D image reconstruction in helium microscopes, because the point-by-point illumination of the sample allows for a straightforward implementation of the reconstruction process. Only a few images are required for surface reconstruction, which is important as it typically takes much longer to acquire images in a SHeM instrument, compared to electron or He ion microscopy. Heliometric stereo requires detection at multiple angles, which

can be simultaneously achieved in a microscope with multiple helium detectors, but we also show how sample rotation can be used to obtain multiple independent intensity measurements in a single detector instrument. We discuss both normal and non-normal incidence helium beams; the latter which when combined with rotation allows reconstruction of otherwise inaccessible parts of the sample surface. Finally, we show how the quality of the reconstruction is affected by the presence of significant multiple scattering or regions of the surface which do not have direct line of sight to the helium source or detector.

The remainder of the paper is organised as follows. Section II begins with an overview of the photometric stereo method, which is then developed to establish heliometric stereo, and ends with an example 3D reconstruction. Then follows a discussion of possible extensions and additional considerations (section III). Results are presented on image reconstruction on two technological relevant shapes: a sample with modest topology, which is simulated with a microscope set up corresponding to existing SHeM instrumentation, and a sample with high aspect ratio. The former is used to examine the effects of SNR and the number of detectors while the latter is used to examine the role of multiple scattering and the limits of the technique (section IV). The paper finishes with a discussion of factors to consider when designing a helium microscope for use with heliometric stereo and an outlook for the technique (section V).

II. GENERAL METHOD: HELIOMETRIC STEREO

A. The photometric stereo technique

The established technique of photometric stereo relies on the assumption that a point on the surface of the image will scatter light with a given angular distribution, known as a bidirectional reflection distribution function (BRDF), which gives the scattered intensity as a function of the incoming and outgoing angles [29]. If the camera position is fixed, the intensities recorded in the camera will depend only on the local surface orientation and the scattering distribution; and for the same material and surface condition, all points on the sample can be assumed to have the same scattering distribution.

If the bidirectional scattering distribution function is known, a series of images obtained by illuminating the sample from a different directions can be used as intensity maps to infer the local surface orientation, and thus the local surface gradient. These gradients may then be integrated over the surface to give a 3D height map of the sample.

1. Obtaining the surface normals

Photometric stereo techniques generally assume Lambertian scattering, a type of scattering that corresponds to a surface which is a perfect diffuse light scatterer [19]. Lambertian scattering is also referred to as cosine scattering, as the light intensity values recorded at pixel (x', y') in the camera image is

$$I_{(x',y')} = \rho \cos\theta = \rho\, \hat{\boldsymbol{n}} \cdot \hat{\boldsymbol{d}}, \tag{1}$$

as illustrated in in Fig. 2 (a) for scattering from position (x, y) on the surface. In the current work we use (x, y) to refer to a spatial position in a coordinate system we are interested (could be arbitrary but usually that of the sample with the z axis parallel to the overall sample normal) while (x', y') refers to a position in the image. Here, θ is the angle between the surface normal and the incident light source, $\hat{\boldsymbol{n}}$ is the unit normal to the surface, $\hat{\boldsymbol{d}}$ is a unit vector from the surface to the light source, and ρ is the albedo or reflectance factor for that point on the surface. For light the outgoing angle, χ, does not appear in the intensity equation as the $\cos\chi$ dependence in the scattering is exactly compensated by the $(\cos\chi)^{-1}$ dependence from the projection of the surface area into the camera. Instead, the cosine term arises from the projection of the light source onto a surface at angle θ; the area of surface that the light hits is proportional to $(1/\cos\theta)^{-1}$.

Where there are multiple light sources we can write

$$\vec{I}_{(x',y')} = \rho \mathsf{D} \hat{\boldsymbol{n}}, \tag{2}$$

in which $\vec{I}$ is a m-dimensional vector of pixel intensities corresponding to m images taken from those different light sources. D is a $m \times 3$ matrix containing the normalized vectors connecting the light sources and the point (x', y') for each image. As there are three degrees of freedom in the system there have to be at least three non co-planar vectors in D for a unique solution to exist, corresponding to three distinct light sources. The surface normals, $\hat{\boldsymbol{n}}$, and reflectances, ρ, can be obtained from eq. (2) by solving the system of linear equations for each pixel in the image,

$$\rho_{(x',y')} = |\mathsf{D}^{-1} \vec{I}_{(x',y')}|, \tag{3}$$

$$\hat{\boldsymbol{n}}_{(x',y')} = \frac{1}{\rho} \mathsf{D}^{-1} \vec{I}_{(x',y')}. \tag{4}$$

If the height of the surface can be described by a function of the lateral position, *i.e.* $z = f(x, y)$, then

$$\hat{\boldsymbol{n}}(x, y) = \boldsymbol{\nabla} F(x, y, z) = \boldsymbol{\nabla}[z - f(x, y)]. \tag{5}$$

Thus once the surface normals are found, the gradient field given by eq. (5) may be integrated to obtain an equation of the surface, *i.e.* a topographic map of the sample.

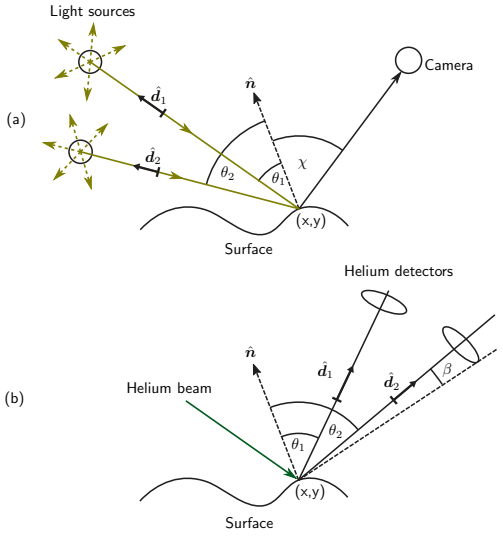

FIG. 2. Correspondence between photometric stereo, (a), and heliometric stereo, (b). $\hat{\boldsymbol{n}}$ is the local unit normal to the surface, $\hat{\boldsymbol{d}}_i$ are the directions to the light sources or detectors. In the case of photography multiple light sources are used to generate images with different $\hat{\boldsymbol{d}}$ vectors, in the case of helium microscopy multiple detectors are used with a single focused illumination to give different $\hat{\boldsymbol{d}}$ by the reciprocity of focused beam imaging.

2. *Surface reconstruction from normals*

The gradient field in eq. (5), can be integrated using established methods from the field of surface reconstruction. Here, we use Harker and O'Leary's MATLAB toolbox [30]. For a more detailed explanation and mathematical proofs their work should be referred to [31, 32] as only a brief outline is given below.

A least squares approach is used to find the matrix of heights Z that upon derivation with respect to x and y gives the least distance from the measured gradient field, given by the normals $\hat{\boldsymbol{n}}$. The discrete derivatives of Z can be written as $\mathsf{L}_x\mathsf{Z}$ and $\mathsf{Z}\mathsf{L}_y^{\mathsf{T}}$. The matrices $\hat{\mathsf{Z}}_x$ and $\hat{\mathsf{Z}}_y$ represent the *measured* gradient field given by $\hat{\mathsf{Z}}_x = n_x/n_z$, $\hat{\mathsf{Z}}_y = n_y/n_z$. Thus, the least squares minimization corresponds to minimizing ϵ:

$$\epsilon = \left\|\hat{\mathsf{Z}}_x - \mathsf{Z}\mathsf{L}_x^{\mathsf{T}}\right\|_F^2 + \left\|\hat{\mathsf{Z}}_y - \mathsf{L}_y\mathsf{Z}\right\|_F^2, \tag{6}$$

where $\|...\|_F$ represents the appropriate norm. Expanding and differentiating to minimize ϵ yields an equation with a unique solution [31].

3. *Image projection*

A complication of the photometric stereo technique is the way a physical object is projected onto an imaging plane so that pixel indices can be related to physical coordinates. In a camera (without the use of a telecentric lens) a perspective projection is formed, meaning that displacements on the image do not correspond directly to physical distances: the physical distance between two pixels changes across the image depending on the distance to the object and the focal length of the lens used. Helium microscopes, however, are pixel-by-pixel imaging instruments that necessarily produce images in an orthographic projection: the image is formed through the two-dimensional rastering of the sample by fixed distances between pixels. Thus there is a fixed correspondence between pixel locations in an image and physical locations on the sample.

In either photography or helium microscopy the sample is mapped onto a plane with a projection. In a photograph the object is projected through the lens onto the camera sensor, the axis of projection is then normal to the camera. The projection axis corresponds to the z axis in eqs. (1-5). Translating to helium microscopy the z axis in the heliometric stereo method is parallel to the beam and the points x', y' used in the method are defined by the direction of the beam, and not necessarily in the plane of the motion of the microscope's nanopositioning stages. The implications of the projection have to be considered carefully when sample rotations are used to acquire extra 3D information on the sample (see Section III).

4. *Applying photometric stereo to helium microscopy*

We are in the fortunate situation that cosine distributed scattering can also be used to model the scattering of neutral helium atoms from many surfaces, where it is known as Knudsen's cosine law [18]. Although helium scattering from highly prepared 'pristine' atomic surfaces shows complex scattering distributions [6, 8], many 'normal', 'unprepared' or 'technological' surfaces studied to date are consistent with an approximate cosine distribution [15–18] and recent SHeM image modelling shows excellent agreement with simulations that use a cosine model of scattering [12–14]. Under Knudsen's scattering law, the photometric stereo method may therefore be applied to helium microscopy and in fact requires very little modification. The scattering geometry is illustrated in Fig. 2(b), where each point on the sample is assumed to scatter with a cosine distribution about the local surface normal $\hat{\boldsymbol{n}}(x, y)$. (Deviations from a perfectly cosine distribution are mitigated by over-constraining the system, as discussed below.)

Assuming cosine scattering of helium atoms from the sample surface, the scattered intensity into an element of

solid angle $\mathrm{d}\Omega$ is

$$\mathrm{d}I_{(x',y')} \propto \cos\theta \, \mathrm{d}\Omega, \tag{7}$$

where θ is the angle between the detector and the surface normal at the point (x, y). The intensity reaching a particular detector is then

$$I_{(x',y')} \propto \int_{\Omega_D} \cos\theta \, \mathrm{d}\Omega, \tag{8}$$

where Ω_D is the solid angle of the detector entrance aperture. In certain existing helium microscopes the detector apertures occupy a significant fraction of solid angle, covering a wide range of detection angles [4] so the extent of the solid angle needs to be considered. However, providing the aperture is not too large, as is usually the case [3], since the cosine function varies slowly, the integral can be approximated by $\Omega_D \cos\theta$. For an aperture occupying a small circular region of the solid angle hemisphere ($\lesssim \%$ of the total hemisphere), with half-cone angle β and angle from the surface to the center of the aperture of θ, it can be shown that the signal becomes (see appendix A)

$$I_{(x',y')} \propto \frac{1}{2}\pi \cos\theta \, (1 - \cos 2\beta), \tag{9}$$

which also has a cosine dependency with θ. Thus, where detector apertures are small or occupy circular regions of equal solid angle then the intensity detected in a helium microscope can be written as

$$I_{(x',y')} \propto \cos\theta = \rho \, \hat{\boldsymbol{n}} \cdot \hat{\boldsymbol{d}} \tag{10}$$

which is the equivalent to eq. (1). The application of the basic photometric stereo method in helium microscopes follows with $\hat{\boldsymbol{d}}$ defined as the unit vector from the point (x, y) to the detector.

If, due to the practical considerations of design, the solid angles of the detector apertures are not all equal, or if the detectors do not have the same efficiency the modification of eq. (2) is

$$\vec{I}_{(x',y')} = \rho \hat{\Omega} \mathsf{D} \hat{\boldsymbol{n}}, \tag{11}$$

where $\hat{\Omega}$ is a constant diagonal matrix containing the solid angles and detection probability of the various detectors and D and ρ have the same meaning as in eq. (2). In practice the values in $\hat{\Omega}$ can be attained via a calibration of the detectors prior to the acquisition of the data, or by numerically solving the equation provided that there exist enough independent observations.

B. Simulated helium images

We use simulated helium micrographs to test the heliometric stereo method. These micrographs are generated by ray-tracing, with each ray representing a helium atom [13, 14, 33]. The method assumes straight line trajectories of atoms within a 3D space consisting of the sample and local environment within the microscope. The rays are traced, scattering off the surfaces, until they either intersect a detector surface or leave the simulation region, with both directly scattered rays and multiply scattered rays included. All images used in the current work are generated using a cosine model of the scattering events.

In the first set up, we use instrument dimensions which have already been realised experimentally, to demonstrate what can be achieved with present technology. We use a simulated beam-source and detector geometry comparable to the one used in the existing SHeM in Cambridge [3]. As shown in Fig. 3, our set up assumes a helium beam diverging from a circular virtual source, corresponding to a the skimmer in the supersonic nozzle expansion. The helium microprobe is then formed by collimation using a pinhole of 2 µm diameter [34]. The 'virtual source' is assumed to be a uniformly emitting disc of radius 50 µm at a distance 50 cm behind the pinhole (*i.e.* rays are emitted from all elements of the surface and at all angles with the same probability). The large distance between the virtual source and pinhole, compared to the distance between pinhole and sample (1 mm), means that the beam has only a small divergence. Thus the spot size of the beam is approximately 2 µm, with a depth of field of several millimetres.

To obtain simulated images, four detectors were placed at 90° from each other and at 35° from the sample normal, with a normal incidence beam ($z = z'$), as shown in Fig. 3. Given these source and detection geometries, only the number of rays to use and the sample itself need to be provided to complete the simulation set up. The number of simulated rays were chosen to provide a realistic level of signal to noise (SNR) to recent experiments. The data from Fig. 1 in Lambrick et. al [12] was used as a representative experimental SHeM image. The darkest pixel in the image was assumed to be representative of the background signal and was subtracted, then the standard deviation and mean intensity from pixels on a flat region of the sample were taken to be the noise and the signal level respectively, giving an SNR of ~ 30. All simulated images used below have equal or lower signal to noise ratios than that experimentally measured value.

C. Heliometric reconstruction

In order to test the heliometric stereo technique, we use a test sample containing a series of technologically inspired geometric structures: an octagonal pyramid with a depressed top, a rectangular pyramid, a cap of a sphere, a series of increasingly deep pyramidal depressions and a three-dimensional triangle. The feature sizes are all in the 5-100 micron range and have low aspect ratios ($\sim 0.1 - 0.4$), with detailed dimensions given in Fig. 18 of the appendix. These geometries were chosen for different reasons: The increasingly deep pyramidal depres-

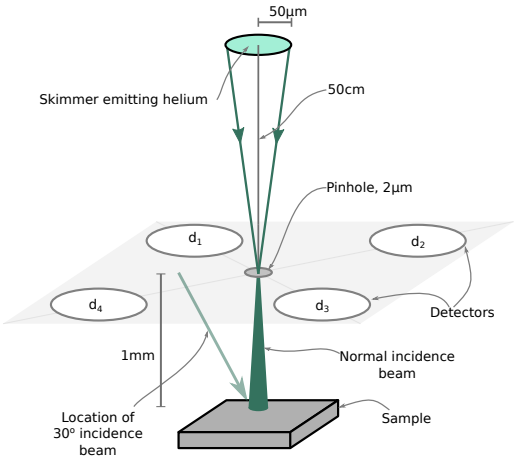

FIG. 3. The simulation set up that was used to generate the images of the test sample and the model of the source used. Four detectors were placed on a plane equidistant around the sample with an angle of 35° to the sample normal. The beam rays are generated in the virtual pinhole with a divergent distribution assuming a circular uniform virtual source shown at the top of the figure (skimmer), for the non-normal incidence simulations the beam source was moved but the detectors were kept the same locations.

sions tests of the quality of reconstruction with depth. The octagonal pyramid with a depressed top tests how the reconstruction handles complicated geometries with a a further depression. The rectangular pyramid has different slopes and is aimed to test the reconstruction precision with angle. The spherical cap is intended to test for the reconstruction of smooth geometries and continuously changing surface gradients. Finally, the three-dimensional triangle has vertical surfaces and tests reconstruction of geometries with abruptly varying heights. Due to their regular forms, these samples resemble artificial structures and we note that the sharp edges would make it very difficult to image them true to size using secondary electron emission based techniques.

Fig. 4 illustrates the stages of producing synthetic helium images from the known sample surface and using them to reconstruct the surface. 1. The original sample surface is input to the ray tracing simulations; 2. Four images are generated from the four detectors: it can be seen that the lightest areas in the images point towards the respective detector while the dark areas point away. 3. The four images are then used to calculate the surface normals, by solving equation 4, which represent the gradient field of the surface. 4. Finally, the gradient field is integrated to find a reconstructed surface. It can be seen that there is a good qualitative match between the original surface and the reconstructed surface in the first and fourth panels. The quantitative accuracy of the reconstruction is discussed in section IV.

1. *Accuracy of reconstruction*

Fig. 6 shows a normalised percentage error plot of the basic reconstruction shown in Fig. 4, while figure 5 shows selected line profiles of the original and reconstructed surface. The error has been normalised by the height of the tallest feature on the surface: the large pyramid structure on the bottom left. The overall RMS error was 2.4%, however we note that there are sections of significantly larger error within the plot. It should be noted that the 2.4% RMS error will be a combination of an intrinsic error to the method and errors resulting from the noisy initial data (simulated images). Noise in the images will result in noise in the gradient field, which will relate in a non-trivial way to errors in the reconstruction. The impact of SNR is discussed further in the next section. Noticeable are the sharp edges on the central pyramid and the deepest of the trenches on the top left side of Fig. 4. Therefore we may say that reconstruction works well with two identified caveats, the first being surfaces that are parallel to the beam (vertical in the case of normal incidence) and hence do not get illuminated; and second multiple scattering: the deepest trench causes a significant amount of multiple scattering, which results in a loss of the well defined relationship between signal and surface orientation.

In the next section we consider how increasing the number of detectors through the use of rotations, and how varying the image SNR affects the accuracy of the reconstruction.

III. EXTENSIONS AND FURTHER CONSIDERATIONS

A. Non-cosine and multiple scattering

As discussed in Section II A 4 cosine scattering is a good first approximation for the scattering of helium atoms from technological samples. However, this type of scattering does not always fully explain experimental data. For example, the existence of non-topographic forms of contrast where the scattering distribution is not fixed across the sample breaking one of the assumptions of heliometric stereo [28, 35] necessarily require deviation from cosine scattering. Heliometric stereo can be extended to more general forms of scattering by emulating preexisting photometric stereo methodologies, for example by using a parameterized scattering distribution that is fitted to the data (see, for example, [36–38]). In the current work, the albedo or reflectance factor is assumed to be sufficient.

An additional contrast feature of helium atom microscopy is multiple scattering which is taken here to

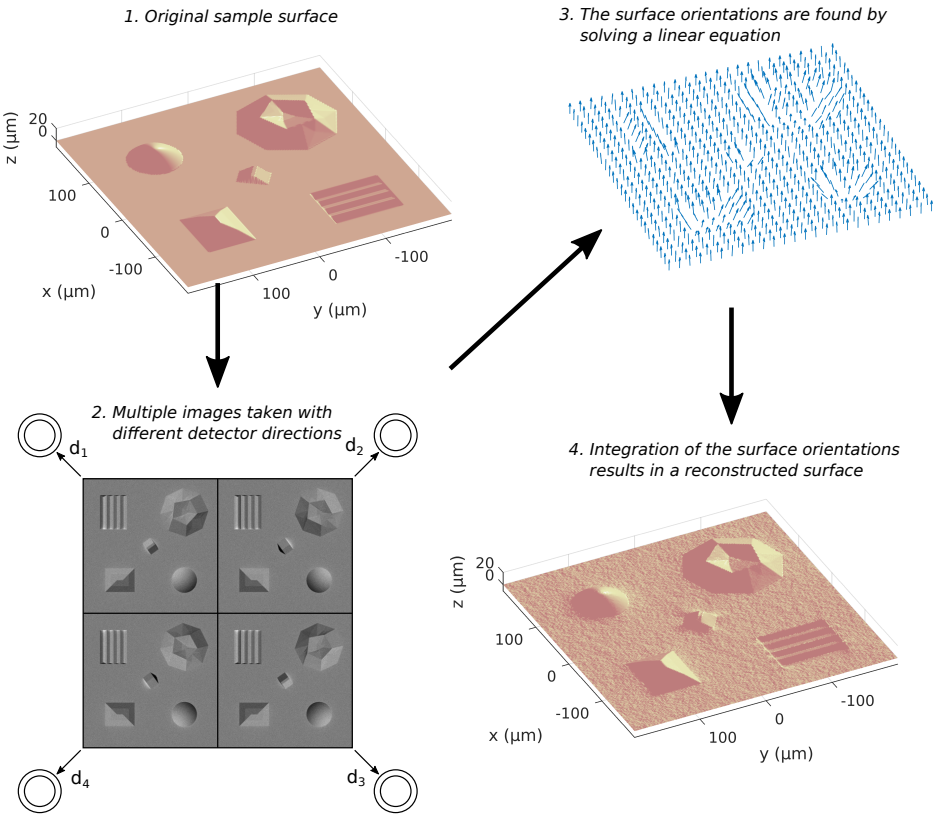

FIG. 4. Overview of the basic heliometric stereo method. 1. The original sample. 2. The sample is imaged using multiple detectors placed in different directions to yield a series of helium images, in the example shown here, the set up shown in Fig. 3 was used to generate the simulated helium images. 3. Those helium images are used as the terms $\vec{I}$ in equation 4 to acquire the surface normals. 4. Finally, as the normals to a surface are the gradient of that surface they may be integrated to give a reconstructed surface. The accuracy of the reconstruction presented here is discussed in section II C.

mean the situation when the helium atoms are 'bouncing' from one distinct area on the sample to another [12, 13, 26]. This can cause regions in images to appear brighter, in particular where there is significant topography in the form of deep or tall features (high aspect ratios). In the present work it is assumed that overconstraining the problem combined with the albedo factor can largely negate the issue of multiple scattering for samples with modest topography. The implications of multiple scattering are considered further in section IV D.

B. Masked regions

A significant contrast feature of helium microscopy is the presence of masking [13, 14, 26], where the direct line of sight between the beam-sample intersection and the detector is blocked by another part of the sample. Qualitatively, masks can be thought of as similar to conventional shadows (they are notably different in mechanism however, shadows are a lack of illumination rather than a lack of detection). As the line of sight is blocked, the detected signal has no bearing on the normal of the surface.

While 3D information is coded in the size and shape of the masks, directly including masked areas in the reconstruction of the normals leads to substantial error. Where the images contain significant masking the sim-

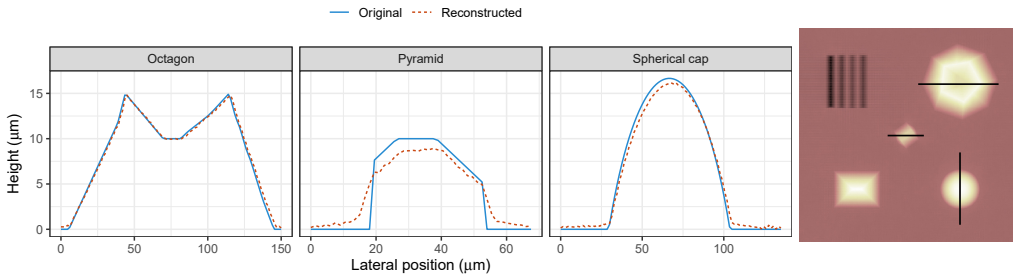

FIG. 5. Three lines profiles extracted from the reconstructions presented in figure 4. The location of the line profiles are shown on the height map of the original surface on the far right. The high quality of the reconstruction in the case of the octagonal and spherical cap features is evident, while the limitations near sharp edges can be seen in the case of the pyramidal feature.

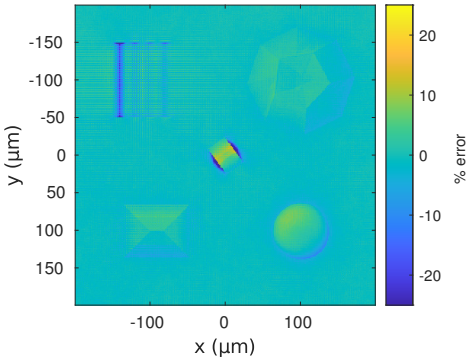

FIG. 6. The percentage error between the reconstructed surface using the 4 detector geometry shown in Fig. 3 and the original surface (surface plots of both are shown in Fig. 4). The error has been normalised by the height of the tallest of the large pyramid structure on the bottom left of the sample. The RMS percentage error was 2.4% overall.

plest approach is to exclude the masked regions, however care must be taken not to underconstrain parts of the reconstruction. If only a small fraction of the image is masked ($\sim 1-5\%$ of an image) it is possible that they need not be excluded—the low intensity recorded in the masks would render the normal to be perpendicular to the detection direction, not a bad approximation where the regions concerned are small.

In the current work, masking is addressed using an automatic threshold method: masked regions of images are excluded from the reconstruction by choosing an intensity level below which pixels are discarded. The upper bound that the threshold can be is obtained by imposing that for every point in the image the following system of equations has at least three independent linear equations:

$$W\vec{I}_{(x',y')} = W\rho\hat{\Omega}\mathsf{D}\boldsymbol{n}. \tag{12}$$

The masking threshold is chosen as a scalar smaller than the threshold value that visually captures the masking contributions, which can be seen in the intensity histogram of the images as peaks in small intensity values (see Appendix D).

An alternative to the threshold approach, a weighting strategy is possible in order to handle masked regions, or regions with low signal to noise ratio. For example, one can weight regions with lower intensities less so that when a value of $I_{(x',y')}$ is fed into the linear least squares minimisation algorithm used to solve eq. (11), that value contributes less [39]. A straightforward way to achieve a weighting would be to make the weighting of pixels to monotonically increase with the intensity. Note that in Poisson statistics the standard deviation of the count rate is inversely proportional to its square root (higher intensities mean that the quality of the signal is better [40]).

C. Sample rotation

Helium microscopes generally have a poor signal to noise ratio compared to modern photography which poses a problem when reconstructing 3D surfaces, as the data quality is lower than in the case of photography. Fortunately, we can obtain more independent observations of each point and improve the quality of the reconstruction by rotating the sample. The same 'trick' can also be used to allow helium microscopes that do not possess enough physical detectors to perform heliometric stereo. If the rotation is performed about the beam axis, for example azimuthal rotation of a sample with a normally incident beam, there is a straight-forward mathematical implementation of eq. (11) as the image plane, and hence coordinate system are the same throughout all images. If the sample is rotated about a different vector, the correspondence between points on rotated images becomes more complex, although there can be benefits of doing so.

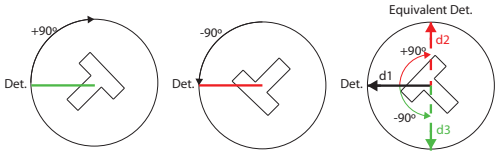

FIG. 7. Rotation in heliometric stereo. After collecting the first image (right) the sample is rotated by 90° and two further images are obtained (middle and left), these images may be rotated to lie ontop of the original image if the reverse rotations are applied to the detector vectors $\hat{\boldsymbol{d}}_2$ and $\hat{\boldsymbol{d}}_2$ as shown in the right panel.

1. *Rotation about the beam axis*

As helium microscopy produces images in an orthographic projection, rotating the sample about the beam axis mathematically corresponds to an inverse rotation of the detector position (see Fig. 7). By rotating the new images I so that each (x', y') coordinate in the image corresponds to the (x', y') coordinates of the rest of the images, the new data can be incorporated as an additional detector. Additionally, the corresponding vector $\vec{d}$ has to be rotated in the opposite direction to the sample by the same angle (see the equivalent detectors in Fig. 7).

Aligning two images of the same sample at different rotation angles can be done through image recognition software, or through a rotation of the scanning pattern. Image recognition software sometimes requires human input, which can lead to error in the reconstruction. Alternatively, rotating the scanning pattern with the sample so that each pixel of the image always corresponds to the same position on the sample produces images aligned down to the accuracy of the positioning stage. The latter method is chosen in this paper to remove human error from the results.

Applying rotations about the beam axis allows for i) the implementation of heliometric stereo with a single detector, and ii) a convenient method to obtain more data and reduce reconstruction error.

2. *Rotation about other axes*

For rotation about an axis other than the beam axis, the beam hits different regions of the sample at different angles, so that there is no complete bijective correspondence (no one-to-one correspondence) between the points of two images (see Fig. 8). On one hand, this makes it difficult to use sample rotation to get more independent data points for eq. (4). On the other hand, rotations about axes other than the beam axis allows to image parts of the sample that otherwise would never intersect the incident beam as a result of shadowing.

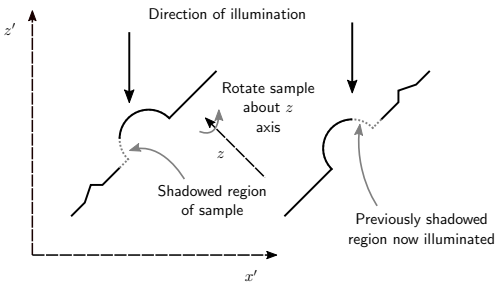

FIG. 8. Sketch of the lack of bijective correspondence between helium microscopy images in the case of rotation not about the beam axis. Regions of the sample that are shadowed can be imaged if we rotate about an axis other than the beam axis. The primed coordinates are the heliometric stereo coordinates with the z' axis parallel to the beam while the unprimed coordinates are those of the sample with z parallel to the overall sample normal.

The fact that shadowing prevents the beam from intersecting all sample points in every rotated image is not an impediment to recovering the 3D surface of a sample from a set of images taken at different rotation angles. To do so, several different sample surface reconstructions can be combined into a single surface after the application of heliometric stereo. Such an approach contrasts with rotating the sample about the beam axis, in which eq. (7) is over-determined.

IV. DETAILED RESULTS

A. Rotation to give more detectors

As discussed in section III C 1, rotations about the beam axis can provide a greater number of effective detectors beyond the number of physical detectors. A simulation was performed with the same detector set up as described in Fig. 3, but with the sample rotated about the beam axis in intervals of 72° to give a total of 5 sets of 4 images. Reconstructions were then performed using different levels of signal to noise and different numbers of rotations (and hence effective detectors).

Fig. 9 gives the root mean square error for different combinations of detectors and rotations for three different levels of signal to noise. It is noted that a similar improvement to the reconstruction is obtained both with an improvement of a factor of 2 in SNR or with an increase of the number of images by a factor 4. Since the noise in neutral helium microscopy is dominated by shot noise [41], both improvements require the same increase in acquisition time. There also seems to be a minimum level of error which is not improved by adding more information. That error is likely a result of failures of the

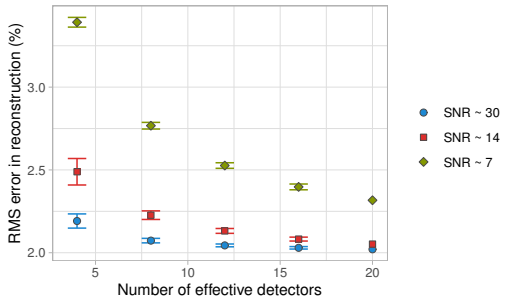

FIG. 9. The root mean squared error (RMS) for the reconstructed surfaces as a function of the number of effective detectors for three different levels of signal to noise ratio (SNR) in the simulated images. The error bars represent the standard deviation of the errors for the reconstructions: using different combinations of the rotations. The RMS error tends towards a lower limit of $\sim 2\%$. The limit on the overall RMS error is due to elements of the sample that heliometric stereo cannot recover well with the cosine model, i.e. the sharp walls on the side of the central feature and the deepest trench on the top left feature (in the error map in Fig. 4). It can be noted that improvements in SNR ratio have a similar impact as increasing the number of detectors by an equivalent amount: SNR improvement by a factor of 2 (and thus measuring time by $\sim$ 4) has a similar impact as increasing the number of detectors by 4.

method near vertical surfaces (such as around the central feature) or deep features that have a higher proportion of multiple scattering (such as the top left feature on the error map in Fig. 4). Reducing the number of detectors to 3 can result in good reconstructions, but can also cause the reconstruction to fail (if detectors 1, 2, & 3 are taken from Fig. 4 for example), demonstrating the importance of slightly overconstraining the problem to get reliable results.

B. Using a single detector

As discussed above heliometric stereo can also be applied to a microscope with only a single detector provided rotations about the beam axis can be performed. It must be note the all areas of a surface need to be covered by at least 3 and preferably 4 images and that due to the use of matrix-based techniques to reconstruct the surface from the gradient field rectangular images need to be used. This can be addressed either by i) padding the images with the downside of some parts of the sample being unconstrained, or ii) using a special scanning pattern rotated counter to the sample rotation. The latter approach is taken here.

Single-detector heliometric stereo was successfully tested using the images obtained by rotating the sample but only using the first detector, effectively creating a

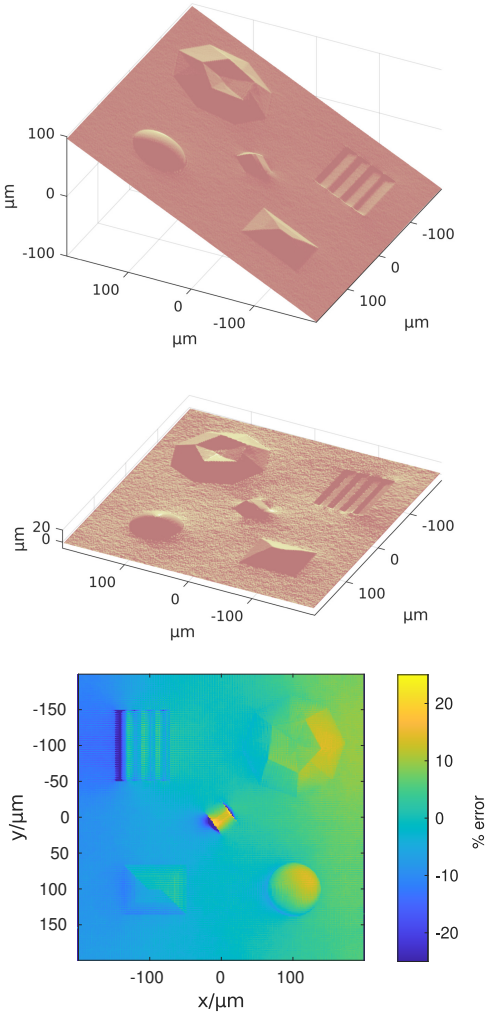

FIG. 10. For non-normal incidence the initial reconstruction is tilted due to the sample being 'viewed from an angle' (top) but may be rotated (middle) and then compared to the original surface. The root mean squared error (bottom) was 16.7%, the higher calculated error compared to the normal incidence case is due to a slight overall tilt, $\sim 0.4^\circ$ left on the sample after rotation which can be seen in the error image on the left. Correcting for the $\sim 0.4^\circ$ overall tilt by rotating the surface yeilds an overall RMS error of 3.4%, slightly greater but comparable to the error found in the normal incidence case.

reconstruction from 5 images with only a single detector. The images used for the reconstruction and the recon-

structed surface are shown in Fig. 20 in the appendix. The method of rotating the scanning pattern along with the sample can be seen in the simulated helium images there. The possibility of implementing heliometric stereo using a single detector is important because the current generation of helium microscopes operate in this configuration.

C. Non-normal incidence

As described in Section II, it is possible to reconstruct the height of a sample using a beam that is incident the sample at an angle. In general, the incidence direction of the beam defines the z axis of the reconstruction method, and thus the scanning pattern used by the sample manipulation in the microscope should take this into account.

Once the surface is reconstructed it will appear tilted, as the helium images are taken 'from an angle'. The surface can then be rotated to match the original sample. To demonstrate the process, heliometric stereo has been applied to simulated images with an incidence angle of 30° and the results are shown in Fig. 10.

Non-normal incidence can be combined with sample rotation as described in Section III C 2: multiple reconstructions are combined rather than using the additional images to over-constrain a single reconstruction. An advantage of using rotations in this manner is that parts of the sample that are not illuminated in one sample orientation are illuminated in another. Fig. 11 compares the errors in the reconstructed surface for i) non-normal incidence and rotations with ii) a single non-normal incidence data-set and iii) a normal incidence data set. The reconstruction from a set of 4 images with a single sample orientation manages to capture a vertical surface in the central feature on the sample better than the normal incidence reconstructions (due to the surface not being parallel to the beam in the non-normal case).

However as can be seen in the averaged image simply averaging the 5 sets of data does not produce a better reconstruction than the normal incidence case (effectively adding more detectors), thus a more complex averaging mechanism is needed. A form of weighted averaging could be employed, however it will not be simple to identify which reconstructions to give a high/low weight.

D. The impact of aspect ratio on reconstruction

The test sample considered in the previous section demonstrates the ability of the method to reconstruct surfaces with relatively low aspect ratios where there is little masking or multiple scattering. In order to understand how the method works with higher aspect ratios and where masking and multiple scattering start to affect the reconstruction accuracy, a simple sample was designed with 4 rods whose height and slope were varied. Fig. 12 shows an example with an aspect ratio of 0.6.

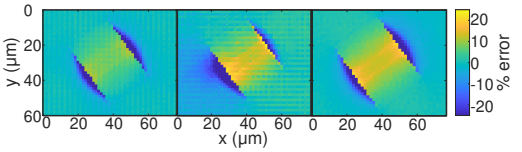

FIG. 11. The errors in the reconstructed surface for: normal incidence and rotations (left), a non-normal incidence set of images without rotations (middle), and non-normal incidence with rotations (right). Note that the single orientation non-normal incidence reconstruction captures well one vertical surface and the other very poorly, the high error region being 1-2 pixel rather than 3 pixels wide—the beam intersected the right-hand side of the sample here. However, when all the different orientations are averaged in a simple manner the reconstruction loses the sharp verticals: non-normal incidence rotations do give us more accurate information, but simple averaging does not fully make use of them.

The aspect ratio was quantified as the height over half the separation between the centres of two rods. For the simulated images used in this section the same virtual microscope set up was used as presented in Fig. 3.

Fig. 13 shows how the accuracy of the reconstructed height of the rods, measured as the difference between the height in the circular regions on the top and the four corners of the reconstruction, varies with the aspect ratio. To evaluate what proportion of the error was being introduced as a result of multiple scattering, reconstructions were also performed with only the single scattering contribution of the images as a comparison. Presented are the height accuracy both with and without multiple scattering and with and without applying thresholding. We note that the error introduced by multiple scattering is present at all but the smallest aspect ratios, red points, but remains less than 20% for aspect ratios less than 0.5. Using only single scattering, blue points, the reconstruction keeps a high accuracy until masking becomes a significant feature in the images. The application of thresholding does not appear to increase the accuracy of the reconstructed height, green points, though there is an effect on the shape as discussed in the next paragraph; however thresholding does improve the accuracy at high aspect ratios for the reconstruction where multiple scattering is excluded, purple points. It is notable that even where the multiple scattering is significant and is causing a quantitative error in the reconstructed the qualitative shape of the reconstructed surface is still recovered well, as can be seen in Fig. 12, which is for 'rods' of aspect ratio 0.6.

Observing Fig. 12 we note that while under conditions where the height is not reconstructed to a high accuracy, it does appear that the shape of the surface is still reconstructed well. In order to quantify the accuracy of the shape reconstruction we allow the reconstructed surface heights to vary: $z_2 = \alpha z + \beta$ and perform a least squares minimisation to find α, β that fit the original surface best.

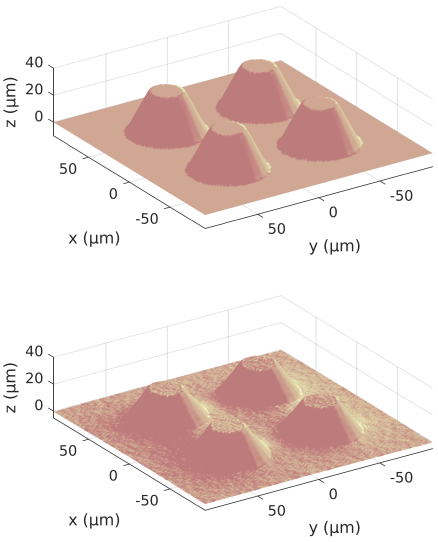

FIG. 12. The original surface with and aspect ratio of 0.6 and the reconstruction with the microscope set-up shown in Fig. 3. It can be seen that there is a good qualitative reconstruction despite the height only being reconstructed as 75% of the original height. The other samples used in the aspect ratio investigation have same footprint and cone top but with varying slopes of the sides.

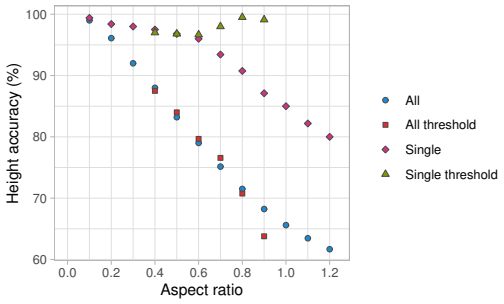

FIG. 13. Accuracy of the reconstructed height with respect to the aspect ratio of the sample. 100% represents the original height. Reconstructions were performed with and without multiple scattering (red and light blue), and with the thresholding method for removing masking introduced in Sec. III B (green for multiple scattering and the threshold method and purple for single scattering). The error bars represent the level of noise in the regions of reconstruction.

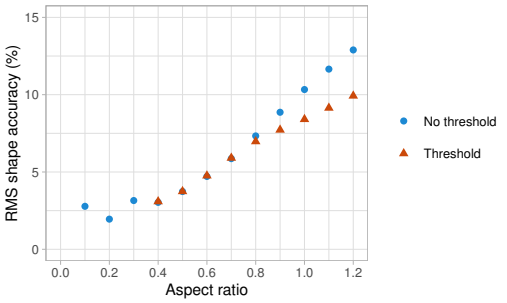

FIG. 14. RMS error between the original surface and the scaled reconstruction normalised relative to the height of the original sample. To consider the accuracy of the method in reconstructing the *shape* of the surface, the reconstructed surface is allowed to scale linearly to best fit the original surface. It can be seen that the errors remain below 10% for aspect ratios below 1 and below 5% for aspect ratio < 0.7. It can also be seen quantitatively that the application of thresholding to remove masked regions of the sample improves the accuracy of the shape reconstruction.

The RMS error is then calculated for the scaled surface and normalised by the height of the cone structure. The results are shown in Fig. 14, where we note that the overall accuracy in the shape of the reconstruction remains better than 10% for all the samples below aspect ratio 1 and that for aspect ratios < 0.7 the RMS error is less than 5%. Overall there is good reproduction of the shape of the surface for low to modest aspect ratios in the sample. It is also shown that the application of the thresholding method discussed in section III B improves the accuracy of the shape reconstruction where there is masking present. An example showing where the thresholding method improves the shape of the reconstructed surface is in Fig. 15 with the aspect ratio 0.8 sample. Here, without thresholding, masking distorts the footprint of the cone, but removing that masking from the reconstruction restores the footprint accurately.

E. The near future: high resolution, high aspect ratio features

The 3D imaging of samples with high aspect ratio features on the nanoscale presents a significant challenge to current technology. We note from the results in the previous section that good shape reproduction is found with the aspect ratio 1 sample, to about 8% error. Its height is reconstructed as 66% of the original height. Thus high aspect ratio features are reconstructed well qualitatively with the current formalism. However, multiple scattering limits the quantitative accuracy of the height, which represents the main obstacle to the application of the method to high aspect ratio features.

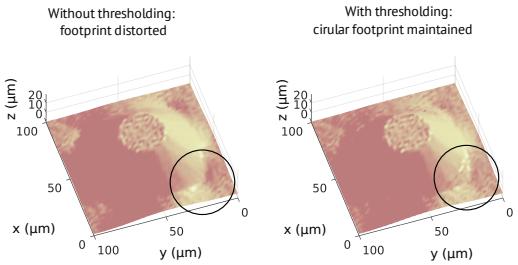

FIG. 15. The reconstructed surfaces with and without thresholding applied for the aspect ratio 0.8 sample. It can be seen that the circular footprint of the cone is distorted where the thresholding is not applied and thus masked regions are included in the reconstruction. By removing the masked regions, the circular footprint is restored (see black circle).

Due to the scale independent nature of the ray tracing simulation we may consider the interesting possibility of applying heliometric stereo to a helium microscope with the estimated best possible resolution of 10 nm [27]. At such resolutions reconstruction of samples with heights of $\sim$ 100 nm should be possible. A simulation was performed with the appropriate scale between beam width and rod height, it was chosen to change from the sample normal to the detectors from 35.3°, as in Fig. 3, to an angle of 19.5° in order to reduce any masking from the simulated images. A shape error of 7% was found and a height 60% of the original height was reconstructed. It is noted that the change of detector positions to minimise masking has slightly improved the shape reconstruction but made the absolute height error worse due to an increased detection of the multiple scattering signal.

V. DISCUSSION

A. Design recommendations

There are certain design principles that that should be considered when designing a neutral helium microscope that is intended to perform heliometric stereo reconstruction. These considerations are given below and while some of them are necessary for the application of heliometric stereo to be possible, it should be noted that some may also be counter to other scientific or practical considerations.

First, in order to perform heliometric stereo without rotating the sample then at least 4 not co-planar detectors are needed. If 4 physical detectors are not possible then the ability to rotate the sample about the beam axis is required, which is likely to be easier with a normal incidence microscope, and in that case at least 2 detectors are recommended so that only one rotation is needed per reconstruction. More than 4 detectors may have benefits for difficult samples by allowing more aggressive thresholding and may allow the application of more advanced adaptations to heliometric stereo, but they are not necessary.

If at least 4 detectors are present then a non-normal incidence microscope would be more flexible as it allows the sample to be imaged from different directions, giving more 3D information. It would also allow detection on the specular condition that may be desirable in other helium scattering experiments. The detectors should, as close as possible, occupy circular regions of solid angle to maintain the cosine assumption, and the solid angle of the detectors should be kept modest, as far as the signal level allows, in order to reduce the possibility of 'partial masking' where only part of the detector is within line of sight of the sample. In order to keep the amount of masking modest we suggest that detectors should be placed not-too-far from the incidence direction to keep the amount of masking modest: we suggest no greater than $30-40°$. All the above requirements are already met by the 2nd generation SHeM being developed in Cambridge.

An alternative, potentially ideal, design of a helium microscope may involve detectors that can be rotated around the sample instead of fixed detector positions. Such a configuration would have a high degree of flexibility for both heliometric stereo and other experiments. However, such an instrument would be a major technical challenge that so far has not been demonstrated experimentally.

For a single detector microscope to perform reconstructions it is necessary to include the ability to rotate the sample about the beam axis to obtain a vector of intensities $\vec{I}$ (see Fig. 20), which must be the key consideration if designing a microscope for heliometric stereo without multiple detectors. In practice enabling such rotations will likely mean designing a machine for normal incidence or one that can be adapted to operate at normal incidence.

B. Constraints

There are two notable constraints on the application of heliometric stereo. The most important, which applies to all scanning helium microscopes, is the difficulty in obtaining an adequate SNR in the underlying measurements, given the incident helium intensity and the limited efficiency of neutral helium detectors. The finite SNR, together with the effect of multiple scattering, degrades the quality of the images and therefore the quality the subsequent 3D reconstruction. However, a high level of robustness to noise has been demonstrated in section IV B; specifically, reconstruction is successful with SNR levels well below those in recently published SHeM images. In addition, by rotating the sample to acquire a greater number of virtual detectors, the effective SNR can be further improved, albeit at the expense of longer

measurement durations.

A less fundamental limitation on the presented method is the reliance on the diffuse scattering assumption. Although diffuse scattering is the predominant mode for neutral helium atoms scattering from technological samples, other scattering distributions are also to be expected, although such deviations are likely to be highly sample specific, making general comments difficult. However, it is possible to distinguish between cases where the scattering distribution remains constant across the sample, and where it varies with position. If the scattering distribution is expected to be constant but not diffuse, Eqs (1), (2) and their dependencies must be re-written as it cannot be generally expressed as a matrix multiplication. Assuming a known distribution or distribution family, one can still numerically solve for $\hat{\boldsymbol{n}}$ and the distribution parameters using well-established methods [36–38]. If the distribution family (its parametric expression) is not known, a non-parametric solver can be used, provided that there is enough experimental data [42]. Note that here the problem is to first find the function f so that $I = f(\hat{\boldsymbol{n}}, \hat{\boldsymbol{d}})$ where $\hat{\boldsymbol{d}}$ is known point-by-point and I is measured and then invert it. If the parametric distribution varies across the sample, the problem is still solvable but doing so is significantly harder as the regions must be established in which there is a distribution shift. Fortunately, such problems have already been addressed in light scattering using the technique of orientation-consistency, which requires the measurement of sections with known orientations and similar scattering distributions [36]. Similar techniques could be potentially implemented for helium, especially in the case of samples with known ordered regions or structures.

C. Outlook

We note that diffraction at the detector opening (i.e. airy disk diffraction for a circular entrance aperture) will not influence the lateral resolution of the microscope. This is because the wavelength of the helium atoms for all practical purposes will always be less than 0.1 nm (the wavelength of a liquid nitrogen cooled beam). Thus, the beam spread introduced through diffraction at the detector opening is negligible even for nm lateral resolution[4, 25, 26]

Masking and multiple scattering were highlighted as issues with heliometric stereo, however, it has been shown that where they are only present in small parts of a set of helium images the overall reconstruction is still good. The thresholding method has been shown to improve the reconstruction results by removing masked regions of the sample from the reconstruction where there is sufficient constraint of the linear problem. Cases of large amounts of masking and significant regions of multiple scattering will occur where higher aspect ratios are present in the sample and new methods will need to be applied to acquire accurate reconstructions. Given the ability of the ray tracing framework to model multiple scattering an iterative approach may be suggested as a route of further work where the initial reconstruction is simulated with ray tracing and the multiple scattering signal then removed from the original images. It may also be possible to combine heliometric stereo with triangulation-based photogrammetry where accurate heights of high aspect ratio features are needed.

We note that adaptations of photometric stereo could be also potentially be applied to stereo electron or stereo helium ion microscopes and that a considerable amount of work has already been done on stereo electron microscopy using techniques based around photogrammetry[43]. However, the challenge for the application of photometric stereo here is that for images generated by secondary electron imaging, the signal is strongly dependent on the geometry of the system - i.e. the signal is much stronger at edges, etc, - and, in general, there isn't a well defined angular selection of the detection. This makes true to size surface mapping difficult [1]. Some work has been done also on 3D helium ion microscopy imaging [44]. The problem with the secondary electron signal is similar here. For both stereo scanning electron microscopy and stereo helium ion microscopy the work done so far has relied on very many images being available for reconstructing the sample. In cases where beam damage is induced on the sample, the method presented here may be of particular interest.

VI. CONCLUSION

We present an adaptation of photometric stereo to neutral helium microscopy: heliometric stereo. The method takes advantage of the dependency of the scattered intensity of a helium beam on the local normals of the sample. Through ray-tracing simulations of a comparable helium microscope with a spot size of 2 micron, we show that the heliometric stereo method is able to resolve the three-dimensional surface of microscopic samples by using just a few images. The reconstructed surface displayed a root mean squared error of roughly 2% of the characteristic length scale of the sample with a signal to noise ratio of just 30 in the images used. We find good shape reconstruction with samples with aspect ratio up to 0.6, with the shape being recovered with less than 5% error. Up to aspect ratio 1.2 with the error is less than 10%. The success at recovering the shape of the sample, even at high aspect ratios, raises the possibility of accurate high resolution and high aspect ratio 3D reconstructions in the near future.

The only condition for the implementation of heliometric stereo is that sufficient images of the sample are obtained to resolve the equations of the normals. For simple geometries this can be done with just three images, that can be obtained in a single experiment in a multi-detector helium microscope, or by rotating the sample three times. The easiness of implementation means that existing he-

lium microscope configurations can be adapted, for example by rotating the sample holders so that the helium beam is normally incident.

Heliometric stereo is a convenient method for three-dimensional resolution of helium microscopy samples, as the slow acquisition times of helium microscopes and the difficulty of manual point selection and tracing make other methods, like triangulation-based photogrammetry, more cumbersome to implement.

SUPPORTING DATA

A supporting data pack is provided to accompany this publication: `doi:10.17863/CAM.65551`.

ACKNOWLEDGEMENTS

We are grateful for useful discussions with Dr. David Ward. The work was supported by EPSRC grants EP/R008272/1. SML acknowledges funding from Mathworks Ltd.

Appendix A: Integration of aperture

In the simple model of diffuse contrast the detected signal, I, is a function of the angle between the surface normal and the centre of the detector aperture, ψ, and the half cone angle of the aperture, β. An integral is performed over the aperture modified by a cosine term, $\cos\chi$, where the angle χ is the angle between the surface normal and a single point on the aperture. Fig. 16 demonstrates the geometry of the model and the *signal* is thus

$$I \propto \int \cos\chi \, \mathrm{d}\Omega. \tag{A1}$$

Defining θ to be the angle to the axis from the surface point to the centre of the detector aperture and φ to be the azimuthal angle around that axis the integral becomes

$$I(\psi,\beta) \propto 2\int_0^{\pi} \mathrm{d}\varphi \int_0^{\beta} \mathrm{d}\theta \, \sin\theta \, \cos\chi. \tag{A2}$$

The cosine term, $\cos\chi$, may be written as the dot product between the unit normal to the surface and the normalised vector from the surface to the infinitesimal point on the aperture being summed. Defining φ to be relative to the x axis the unit normal is

$$\hat{\boldsymbol{n}} = \begin{pmatrix} \sin\psi \\ 0 \\ \cos\psi \end{pmatrix} \tag{A3}$$

which is fixed as ψ is a constant. the normalised vector from the surface to a point on the aperture, $\hat{\boldsymbol{d}}$ can be found by considering a Cartesian coordinate system on the model. The aperture lies on the unit sphere directly above the surface along the z axis by a distance $\cos\beta$. Referring to Fig. 17 points on the plane of the aperture have positions given by the 2D polar coordinates of $(r = z\tan\theta, \varphi)$, thus the components of the vector are $x = z\tan\theta\cos\varphi$, $y = z\tan\theta\sin\varphi$. Thus the normalised vector to the infinitesimal point on the aperture is

$$\hat{\boldsymbol{d}} = \frac{\cos\beta}{\cos\beta\sqrt{(1+\tan^2\theta\,\cos^2\phi + \tan^2\theta\,\sin^2\varphi)}} \begin{pmatrix} \tan\theta\,\cos\varphi \\ \tan\theta\,\sin\varphi \\ \cos\beta \end{pmatrix} \tag{A4}$$

$$= cos\theta \begin{pmatrix} \tan\theta\,\cos\varphi \\ \tan\theta\,\sin\varphi \\ 1 \end{pmatrix}. \tag{A5}$$

and the dot product is then

$$\cos\chi = \hat{\boldsymbol{n}}\cdot\hat{\boldsymbol{d}} = \cos\theta\,(\sin\psi\,\tan\theta\,\cos\varphi + \cos\psi) \tag{A6}$$

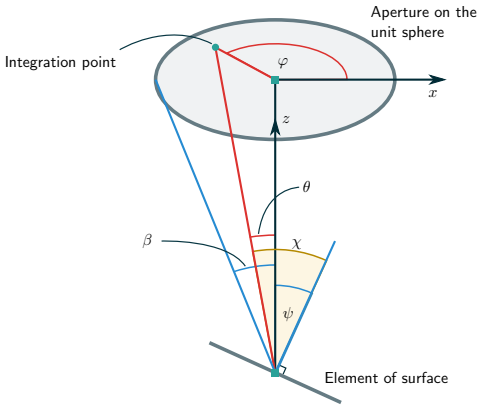

FIG. 16. The geometric set up of the contrast model. A circular aperture is on a unit sphere with an element of surface in the centre. The element of surface is at some angle ψ to the centre of the aperture and the extent of the aperture is defined by its half cone angle β. To calculate the signal intensity for a particular (ψ,β) half of the aperture is integrated over (by symmetry the intensity from the other half will be equal) through the angles (θ,φ). The integration variables and geometry are shown in red, and the variables of signal are shown in blue. The angle χ, in yellow, is between the normal to the surface element and the line from the surface element to the integration point, $cos\chi$ weights the integral according to the cosine model of diffuse scattering.

which allows the signal, from eq. (A2), to be written as

$$I(\psi,\beta) \propto 2\int_0^{\pi} \mathrm{d}\varphi \int_0^{\beta} \mathrm{d}\theta \, \sin\theta\,\cos\theta\,(\sin\psi\,\tan\theta\,\cos\varphi + \cos\psi). \tag{A7}$$

1. Analytic form

The integral in eq. (A7) can be evaluated analytically to give an explicit expression for the signal:

$$I \propto 2\sin\psi \int_0^{\pi} \cos\varphi\,\mathrm{d}\varphi \int_0^{\beta} \sin\theta\,\cos\theta\,\tan\theta\,\mathrm{d}\theta + 2\pi\cos\psi\int_0^{\beta}\sin\theta\,\cos\theta\,\mathrm{d}\theta \tag{A8}$$

$$= 0 + 2\pi\cos\psi\int_0^{\beta}\frac{1}{2}\sin 2\theta\,\mathrm{d}\theta \tag{A9}$$

$$= \frac{1}{2}\pi\cos\psi\,(1-\cos 2\beta). \tag{A10}$$

The above holds, however, only for a limited range of the (ψ,β) space—as the aperture gets larger and the angle

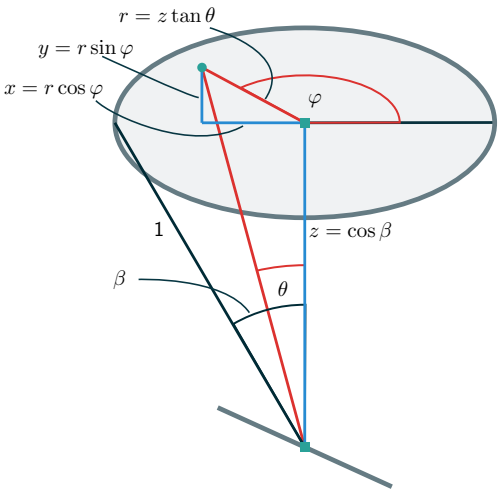

FIG. 17. The geometry deriving the vector to the infinitesimal point on the aperture via a Cartesian system. The three components of the vector from the surface element to an integration point on the detector aperture are shown in blue, x and y in terms of the intermediate variable r. As in Fig. 16 the integration variables are shown in red. Due to the symmetry of the system in the y axis the values of $-y$ and y are equivalent.

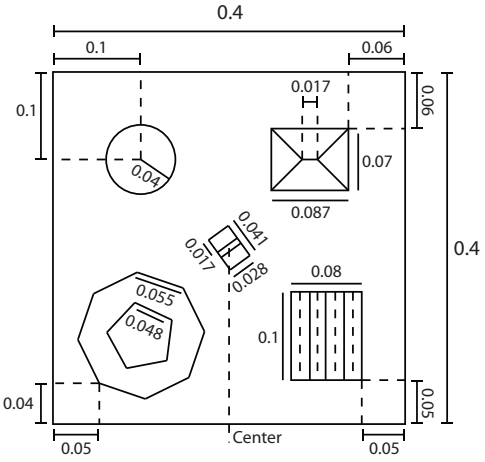

FIG. 18. Sample dimensions in µm. Note how the sphere protruding from the sample is only one third of a sphere of diameter 100 µm and therefore the measure shown is just its projection over the sample plane. The heights of each structure are: 16 µm for the sphere, 16 µm for the top right structure, -5 µm ,-4 µm, -5 µm, -8 µm from left to right for the four depressed structures at the bottom right of the sample, 15 µm for the pentagon at the bottom left and 10 µm for the central structure. Complete dimensions and code to generate the sample are included in the supplementary documentation.

of the surface gets larger part of the aperture is going to fall 'behind' the surface, thus would contribution 0 to the integral. Eq. (A10) may thus be applied when

$$\psi + \beta \leq \frac{\pi}{2}. \tag{A11}$$

When eq. (A11) does not hold the cosine approximation of macroscopic apertures does not hold. Where detector apertures are small (small β this can largely be ignored.

Appendix B: Least squares reconstruction

The appropriate norm used in the least squares Reconstruction is the Frobenius norm on a matrix, which may be defined as

$$\|\mathsf{A}\|_F = \sqrt{\mathrm{tr}(\mathsf{A}\mathsf{A}^\mathsf{T})}. \tag{B1}$$

Appendix C: Sample dimensions

Fig. 18 details all the relevant sample dimensions. The dimensions have been rounded to the third decimal. A full reconstruction and source code with the complete measures are included in the supplementary documentation.

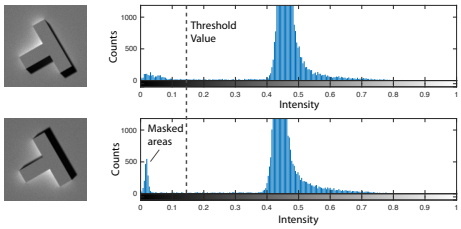

FIG. 19. Selection of uninformative masked regions by using the histogram of helium microscopy images.

Appendix D: Histogram-based threshold method

In order to select a masking threshold, a scalar is chosen so that it visually captures all masking contributions, while still ensuring that the reconstruction is fully determined at all points. These contributions can be seen in the intensity histogram of the images as peaks in small intensity values (see Fig. 19).

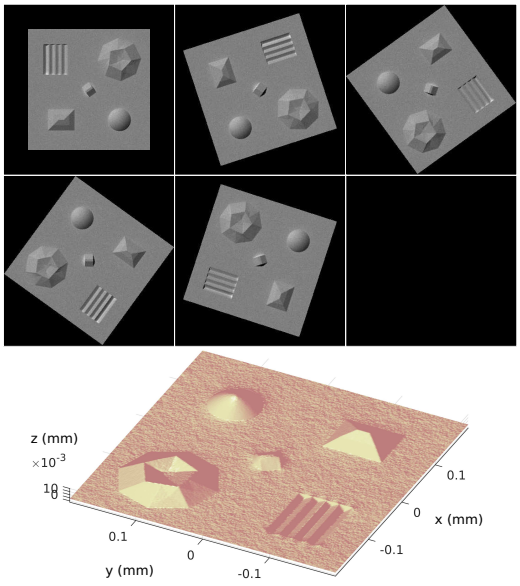

FIG. 20. 5 images taken with a single detector while rotating the sample—note the masks face in the same direction across the images indicating the detector direction. The scanning pattern was rotated along with the images to minimise under-constrained parts of the sample (parts that have fewer than 3 data points), thus the same region of the sample is imaged in each case.

Appendix E: One detector reconstruction

Figure 20 shows 5 images taken with a single fixed position detector while rotating the sample and the scanning pattern. Note the masks maintain their orientation while the sample topography rotates. The scanning pattern is modified such that the same area of sample is observed in each image.

[1] M. T. Postek and A. E. Vladár, Scanning **35**, 355 (2013).
[2] J. Shen, D. Zhang, F.-H. Zhang, and Y. Gan, Applied Surface Science **422**, 482 (2017).
[3] M. Barr, A. Fahy, A. Jardine, J. Ellis, D. Ward, D. MacLaren, W. Allison, and P. Dastoor, Nuclear Instruments and Methods in Physics Research Section B: Beam Interactions with Materials and Atoms **340**, 76 (2014).
[4] P. Witham and E. Sanchez, Review of Scientific Instruments **82**, 103705 (2011).
[5] M. Koch, S. Rehbein, G. Schmahl, T. Reisinger, G. Bracco, W. E. Ernst, and B. Holst, J. Microsc. **229**, 1 (2008).
[6] B.Holst and G.Bracco, "Surface Science Techniques," (Springer, 2013) Chap. 12, pp. 333–367.
[7] D. Joy, R. Ramachandra, and B. Griffin, Microscopy and Microanalysis **15** (2009), 10.1017/S1431927609092757.
[8] D. Farias and K.-H. Rieder, Rep. Prog. Phys. **61**, 1575 (1998).
[9] T. A. Myles, S. D. Eder, M. G. Barr, A. Fahy, J. Martens, , and P. C. Dastoor, Scientific Reports **9**, 2148 (2019).
[10] L. C. Gontard, R. Schierholz, S. Yu, J. Cintas, and R. E. Dunin-Borkowski, Ultramicroscopy **169**, 80 (2016).
[11] S. Lambrick et al., to be published.
[12] S. M. Lambrick, L. Vozdecky, M. Bergin, J. E. Halpin, D. A. MacLaren, P. C. Dastoor, S. A. Przyborski, A. P. Jardine, and D. J. Ward, Applied Physics Letters **116**, 061601 (2020).
[13] S. M. Lambrick, M. Bergin, A. P. Jardine, and D. J. Ward, Micron **113**, 61 (2018).
[14] A. Fahy, S. D. Eder, M. Barr, J. Martens, T. A. Myles, and P. C. Dastoor, Ultramicroscopy **192**, 7 (2018).
[15] M. Knudsen, *The kinetic theory of gases: some modern aspects*, 3rd ed. (London, London, 1950).
[16] D. R. O'Keefe and R. L. Palmer, Journal of Vacuum Science and Technology **8**, 27 (1971).
[17] F. Celestini and F. Mortessagne, Physical Review E **77**, 021202 (2008).
[18] R. Feres and G. Yablonsky, Chemical Engineering Science **59**, 1541 (2004).
[19] R. J. Woodham, Optical Engineering **19**, 191139 (1980).
[20] J.-J. Greffet and M. Nieto-Vesperinas, JOSA A **15**, 2735 (1998).
[21] D. J. Riley, M. Mann, D. A. MacLaren, P. C. Dastoor, W. Allison, K. B. Teo, G. A. Amaratunga, and W. Milne, Nano Letters **3**, 1455 (2003).
[22] R. Doak, Y. Ekinci, B. Holst, J. Toennies, T. Al-Kassab, and A. Heinrich, Review of scientific instruments **75**, 405

(2004).
[23] A. S. Palau, G. Bracco, and B. Holst, Physical Review A **94** (2016), 10.1103/PhysRevA.94.063624.
[24] M. Bergin, D. Ward, J. Ellis, and A. Jardine, Ultramicroscopy **207**, 112833 (2019).
[25] S. D. Eder, T. Reisinger, M. M. Greve, G. Bracco, and B. Holst, New. J. Phys. **14**, 73014 (2012).
[26] P. Witham and E. Sanchez, Crystal Research and Technology **49**, 690 (2014).
[27] A. Salvador Palau, G. Bracco, and B. Holst, Phys. Rev. A **95**, 13611 (2017).
[28] M. Barr, A. Fahy, J. Martens, A. P. Jardine, D. J. Ward, J. Ellis, W. Allison, and P. C. Dastoor, Nature Communications **7**, 10189 (2016).
[29] J. C. Stover (Society of Photo-Optical Instrumentation Engineers, 2012).
[30] `https://uk.mathworks.com/matlabcentral/fileexchange/43149`.
[31] M. Harker and P. O'Leary, in *2008 IEEE Conference on Computer Vision and Pattern Recognition* (2008) pp. 1–7.
[32] M. Harker and P. O'Leary, Journal of Mathematical Imaging and Vision **51**, 46 (2015).
[33] S. Lambrick, "slambrick/SHeM-Ray-Tracing-Simulation: SHeM Ray Tracing Simulation," (2018).
[34] T. Reisinger, G. Bracco, S. Rehbein, G. Schmahl, W. E. Ernst, and B. Holst, J. Phys. Chem A **111**, 12620 (2007).
[35] M. Bergin, S. M. Lambrick, H. Sleath, D. J. Ward, J. Ellis, and A. P. Jardine, Scientific Reports **10**, 1 (2020).
[36] A. Hertzmann and S. M. Seitz, IEEE Transactions on Pattern Analysis and Machine Intelligence **27**, 1254 (2005).
[37] S. Ikehata, D. Wipf, Y. Matsushita, and K. Aizawa, in *2012 IEEE Conference on Computer Vision and Pattern Recognition* (IEEE, 2012) pp. 318–325.
[38] D. B. Goldman, B. Curless, A. Hertzmann, and S. M. Seitz, IEEE Transactions on Pattern Analysis and Machine Intelligence **32**, 1060 (2009).
[39] T. Strutz, *Data fitting and uncertainty: A practical introduction to weighted least squares and beyond* (Vieweg and Teubner, 2010).
[40] J. Garnaes, P.-E. Hansen, N. Agersnap, J. Holm, F. Borsetto, and A. Kühle, Applied optics **45**, 3201 (2006).
[41] M. Bergin, *Instrumentation and contrast mechanisms in scanning helium microscopy*, Ph.D. thesis, Fitzwilliam College, University of Cambridge (2018).
[42] S. Ikehata and K. Aizawa, in *Proceedings of the IEEE Conference on Computer Vision and Pattern Recognition* (2014) pp. 2179–2186.
[43] L. A. Jácome, G. Eggeler, and A. Dlouhy, Ultramicroscopy **122**, 48 (2012).
[44] F. Vollnhals and T. Wirtz, Analytical Chemistry **90**, 11989 (2018).

Article 6

4.6 Zero-order filter for diffractive focusing of de Broglie matter waves

SD Eder, AK Ravn, B Samelin, G Bracco, Adrià Salvador Palau, T Reisinger, Erik Bergback Knudsen, K Lefmann, Bodil Holst

Physical Review A, **95**, 2 (2017)

Zero-order filter for diffractive focusing of de Broglie matter waves

Eder, S. D. ; Ravn, A. K. ; Samelin, B. ; Bracco, G.; Salvador Palau, A. ; Reisinger, T.; Bergbäck Knudsen, Erik

Published in:
Physical Review A

Link to article, DOI:
10.1103/PhysRevA.95.023618

Publication date:
2017

Document Version
Publisher's PDF, also known as Version of record

Zero-order filter for diffractive focusing of de Broglie matter waves

S. D. Eder,[1] A. K. Ravn,[2] B. Samelin,[1] G. Bracco,[3] A. Salvador Palau,[1] T. Reisinger,[1,*] E. B. Knudsen,[4] K. Lefmann,[2] and B. Holst[1,†]

[1]*Department of Physics and Technology, University of Bergen, Allégaten 55, 5007 Bergen, Norway*
[2]*Nanoscience Center, Niels Bohr Institute, University of Copenhagen, 2100 Copenhagen, Denmark*
[3]*Department of Physics, IMEM, CNR, University of Genova, Via Dodecaneso 33, 16146 Genova, Italy*
[4]*NEXMAP, Physics Department, Technical University of Denmark, 2800 Kongens Lyngby, Denmark*

(Received 4 August 2016; published 21 February 2017)

The manipulation of neutral atoms and molecules via their de Broglie wave properties, also referred to as de Broglie matter wave optics, is relevant for several fields ranging from fundamental quantum mechanics tests and quantum metrology to measurements of interaction potentials and new imaging techniques. However, there are several challenges. For example, for diffractive focusing elements, the zero-order beam provides a challenge because it decreases the signal contrast. Here we present the experimental realization of a zero-order filter, also referred to as an order-sorting aperture for de Broglie matter wave diffractive focusing elements. The zero-order filter makes it possible to measure even at low beam intensities. We present measurements of zero-order filtered, focused, neutral helium beams generated at source stagnation pressures between 11 and 81 bars. We show that for certain conditions the atom focusing at lower source stagnation pressures (broader velocity distributions) is better than what has previously been predicted. We present simulations with the software ray-tracing simulation package MCSTAS using a realistic helium source configuration, which gives very good agreement with our measurements.

DOI: 10.1103/PhysRevA.95.023618

I. INTRODUCTION

de Broglie matter wave optics has attracted much interest in recent years. For reviews related to quantum metrology and fundamental quantum mechanics tests, see [1–3]. de Broglie matter waves created by supersonic expansion, in particular neutral helium beams, are established tools in surface science [4,5]. Presently, helium beams are mainly used in studies of surface diffraction and dynamics, but the research is ongoing for applying them in microscopic imaging. The helium beam has a low energy (typically less than 100 meV) and does not penetrate solid material: The helium beam maps the electron density distribution of the surface. This makes neutral helium microscopy an attractive candidate for the imaging of insulating and/or fragile surface structures and nanocoatings. By using two detectors, recording the scattered beams at different angles, it should even be possible, in principle, to make a nanoscale stereo microscope. The first helium focusing experiments of neutral helium were carried out by Carnal *et al.* [6] using a metastable beam and later by Doak *et al.* [7] using a ground-state helium beam. The first neutral helium microscopy images were obtained using a diffractive focusing element: A Fresnel-Soret zone plate (zone plate with a square-wave amplitude transmission function) was used to focus a helium beam down to a few micrometers [8] and later even below 1 μm [9]. An alternative pinhole helium microscopy setup was subsequently introduced [10–13]. The first reflection microscopy images were obtained with this method [10]. Diffractive focusing elements have also been used to focus molecules [14] and to measure atom interaction potentials [15,16] and have been proposed as a method for investigation of the Casimir-Polder force [17].

Because of the low energy of the atoms or molecules in the beams used in de Broglie matter wave optics experiments, the beams cannot penetrate solid material as mentioned above and therefore the diffracting focusing elements have to work by reflection or for transmission must be free-standing suspended structures. This is a fabrication challenge and limits the number of possible elements. Fresnel-Soret zone plate focusing has been used on several occasions as described above (see also [7,18]). Recently, another diffracting focusing element, the atom sieve, was introduced [19]. The atom sieve is based on the photon sieve invented earlier [20]. It consists of pinholes of varying size arranged across the Fresnel zones in such a manner that it is possible to focus on a spot with a diameter smaller than the smallest pinhole. In addition, higher-order diffraction and secondary maxima can be suppressed by several orders of magnitude.

As an alternative to Fresnel zone plates, mirrors can be used as focusing elements [21–23]. The use of graphene as a mirror coating gives an inert and very stable surface [24]. In addition, one-dimensional focusing with quantum reflection from a curved substrate has been demonstrated [25].

Up until now it has not been possible to control the curvature of mirrors with high precision, so Fresnel-zone-based optical elements remain the most promising approach for the focusing of neutral-atom and molecular beams, but the zero-order contribution is a major issue. For a standard Fresnel-Soret zone plate, 25% of the incident beam (half of the transmitted intensity) goes into the zero-order focus and only about 10% into the first-order focus [26]. The standard procedure, also adopted in x-ray applications, is to block the central part of the zone plate with an opaque middle stop, but this does not prevent the zero-order beam from contributing through the open fraction of the focusing element and the larger the middle stop, the higher the intensity loss. To filter out the last fraction of the zero

*Present address: Institute of Nanotechnology, Karlsruhe Institute of Technology, Hermann-von-Helmholtz-Platz 1, 76344 Eggenstein-Leopoldshafen, Germany.
†bodil.holst@uib.no

order a so-called order-sorting aperture needs to be applied, as is done, for example, in nanoscale x-ray imaging [27].

In this paper we present the realization of an order-sorting aperture (zero-order filter) for de Broglie matter waves. An additional advantage apart from the zero-order filtering is that it is possible to reduce the size of the middle stop so that the intensity in the focus can be increased. This is particularly important for de Broglie matter waves, because they often have low intensity. The successful implementation of the zero-order filter has enabled us to test systematically the focus size of neutral helium beams at lower pressures and we present a Monte Carlo simulation model of the focusing for all pressure regimes based on the MCSTAS instrument simulation software for neutron instrumentation [28,29].

II. EXPERIMENTAL SETUP

The experiments presented here were carried out in the neutral helium microscope prototype instrument at the University of Bergen. The microscope is popularly referred to as NEMI, short for neutral microscope. We will adhere to this convention for the rest of the paper. The neutral helium beam was created by a free-jet expansion from a source reservoir through a (5 ± 1)-μm-diam nozzle. The central part of the beam was selected by a skimmer placed 11.5 ± 0.5 mm in front of the nozzle. Two different skimmers were used: a (10 ± 1)-μm-diam skimmer and a (50 ± 2)-μm-diam skimmer. The beam source in NEMI has been specifically designed for microskimmer experiments, allowing one to position the skimmer relative to the nozzle with submicrometer precision [30].

A drawing of NEMI can be seen in Fig. 1. The beam transmitted through the microskimmer is focused by a Fresnel-Soret zone plate 192 μm in diameter with a 50-μm-diam middle stop [31] onto a translation stage (PI miCos). For the experiments presented here, a 10-μm-wide slit was mounted on the translation stage and used to scan the beam. The beam fraction transmitted through the slit was detected in a pitot tube detector placed under the translation stage.

The Fresnel zone plate used for the experiments presented here is designed to have a focal length of 168.14 mm for a wavelength of $\lambda = 0.055$ nm, corresponding to a beam temperature of about 320 K (there is a small wavelength dependence also with the source reservoir pressure). The focal length is chosen to fit the geometry of the NEMI system with an object distance g (distance between the skimmer and Fresnel zone plate) of 935 mm and an image distance b (distance between Fresnel zone plate and slit plane) of 205 mm.

All experiments were carried out at source pressures between 11 and 81 bars. The corresponding most probable He beam wavelength varies slightly with pressure from $\lambda \approx 0.0555 \pm 0.0004$ nm to $\lambda \approx 0.0564 \pm 0.0004$ nm. The width of the velocity distribution, and thereby the width of the wavelength distribution, varies much more. Traditionally, this beam property is quantified using the parameter of speed ratio S, where S is defined as $S = 2\sqrt{\ln(2)}\, v/\Delta v$ [32], where Δv is the full width at half maximum (FWHM) of the velocity distribution and v the most probable beam velocity. Since NEMI does not have a time-of-flight system, theoretical values for the speed ratios were obtained by numerically solving the Boltzmann equation [15,33,34]. The speed ratio varied from 9.0 to 25.8.

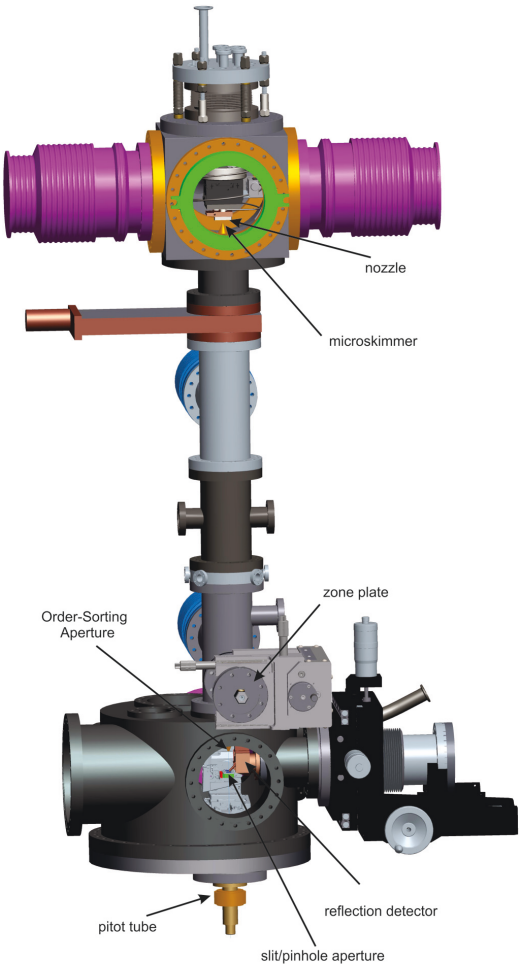

FIG. 1. Drawing of NEMI used to perform the measurements presented here. The focused helium atom spot profile is observed by moving a 10-μm slit aperture, mounted on a translation stage, across the focused spot and measuring the pressure increase in the Pitot tube detector. To the right the detector setup used for reflection imaging can be seen. It is not used for the experiments presented here.

III. THEORETICAL BACKGROUND

A. Analytical model

The size of the focused helium atom spot is determined by the geometry of the system, the size of the source, and the chromatic aberration caused by the velocity spread of the beam. The chromatic aberration for a Fresnel zone plate can be described by the transversal width of the chromatic point spread function [35]. Using a simple geometrical argument

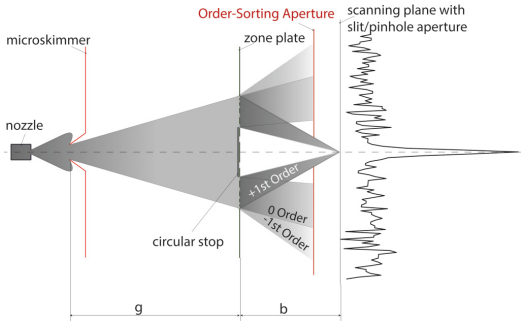

FIG. 2. Diagram of the zero-order filter setup. After the free-jet expansion through the nozzle, the central part of the helium beam is selected by the microskimmer. The beam hits the Fresnel zone plate. The central part of the zone plate has been blocked by a circular middle stop, which filters part of the zero-order beam. The rest of the zero-order beam (and most of the higher orders) is blocked by the order-sorting aperture with a diameter slightly smaller than the middle stop.

as described in [14], we get an expression for the transversal width w,

$$w = \sqrt{\ln(2)}\frac{D_{ZP}}{S}, \tag{1}$$

where D_{ZP} is the diameter of the Fresnel zone plate and S is the speed ratio of the beam. In the model it is assumed that the point spread function does not change significantly when slightly off axis and hence that each point on the source will contribute with a point spread function of the same size. The final focused spot size d_{focus} can thus be described as a convolution of the transversal width w with the geometrical image of the source. A simplified model for the final focused spot size is given by approximating the source image and w with Gaussian functions. The skimmer diameter d_{sk} is taken to be the FWHM of the object function [9]. We thus obtain for the theoretical final spot size d_{focus},

$$d_{\text{focus}} = \sqrt{w^2 + (M\, d_{\text{sk}})^2}, \tag{2}$$

where $M = b/g$ is the magnification factor given by the geometry of the system (see Fig. 2).

B. MCSTAS simulations

MCSTAS [36] is a ray-tracing simulation software package developed specifically with the purpose of simulating neutron scattering instruments and experiments [28,29], distributed using the GNU General Public License. The domain specific language (DSL) is built on ANSI-C. There are three levels of coding in MCSTAS. The bottom level is the MCSTAS kernel, where all low-level particle transportation routines, geometry engines, etc., are placed. It is written in ANSI-C and provides the basis for the MCSTAS DSL and compiler used on the other levels. The middle level is the component files. These files are the building blocks of the MCSTAS simulated instruments and here the Monte Carlo choices are taken. The top level is the instrument file. It consists of a number of calls to different components and a geometrical description of the instrument setup.

The assumption used throughout the simulations is that the helium atoms behave just like neutrons, only four times heavier. As long as we are only interested in the diffraction properties and set the material parameters so that the "neutrons" cannot penetrate any material, this is a valid assumption. MCSTAS does not take into account interaction between particles, which is appropriate for the description of the supersonic expansion beam used here.

In order to simulate NEMI in MCSTAS, four instrument components were implemented: (i) a beam source, (ii) a zone plate, 192 μm in diameter with a 50-μm middle stop, (iii) the corresponding zero-order filter with a 40-μm opening, and (iv) a detection plane. The beam source has been implemented as a ray-tracing version of the ellipsoidal quitting surface model with a $\cos^3$ density distribution over the quitting surface as described in [37]. The quitting surface represents the distance from the nozzle in any direction, where the atoms have reached molecular flow and are no longer interacting. The velocity distribution over the quitting surface is obtained by solving numerically the Boltzmann equation [15,33,34] (see also Ref. [38]).

The simulations were carried out by tracing around 10^8 rays, originating from the source. The starting position and velocity of each ray was selected at random, according to the source intensity and velocity distribution described above. MCSTAS in its present form does not include the phase in the simulations. Each ray was traced to the plane of the zone plate. Using the velocity (wavelength) associated with the ray, the standard formula for the wavelength-dependent focal length of a zone plate [35], the starting position of the ray at the quitting surface, and the position of the ray at the zone plate, the position of the ray in the image plane was determined. This position was then traced back or forward to the detector plane. To simulate the experiment, the rays were binned in 10-μm-wide slots at 0.3-μm distance, which corresponds to the readout positions of the 10-μm-wide detector slit. A ray would be binned into all the overlapping slots at its point of arrival.

IV. RESULTS AND ANALYSIS

A drawing of our zero-order filter setup can be seen in Fig. 2. The crucial idea is that the zero order can be filtered out completely by combining a middle stop with a collimating aperture (order-sorting aperture). We use a circular aperture, 40 μm in diameter, designed to be slightly smaller than the 50-μm-diam middle stop. This ensures that the zero-order beam is completely blocked regardless of where the aperture is placed in the beam line as long as the zone plate and aperture are aligned. To ensure maximum focused intensity transfer, the position of the aperture is adjusted so that the cone of the beam coming into focus matches the diameter of the aperture. Because the wavelength of the atoms is so small (less than 0.1 nm) compared to the diameter of the aperture (20–50 μm), the optimum position can be found through simple geometrical optics. For our system here, using a Fresnel zone plate with a diameter of 192 μm and an image distance of 205 mm, the optimum position of the 40-μm-diam aperture is 42.7 mm

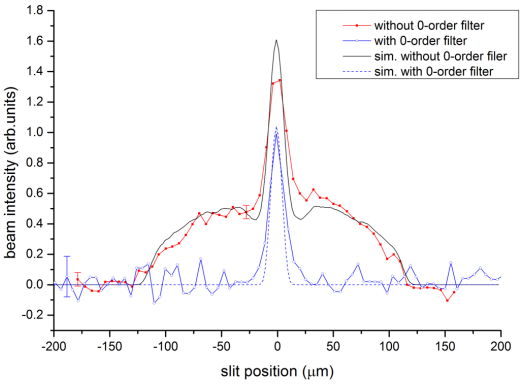

FIG. 3. Experimental focusing results showing two focused beams with and without zero-order filtering together with MCSTAS simulations. The two intensity curves have been normalized relative to the maximum intensity measured with zero-order filtering and the background has been subtracted for both curves. As can be seen, the zero-order background is completely removed by our zero-order filter. These experiments were carried out at a pressure of 76 bars, using a 10-μm diameter skimmer.

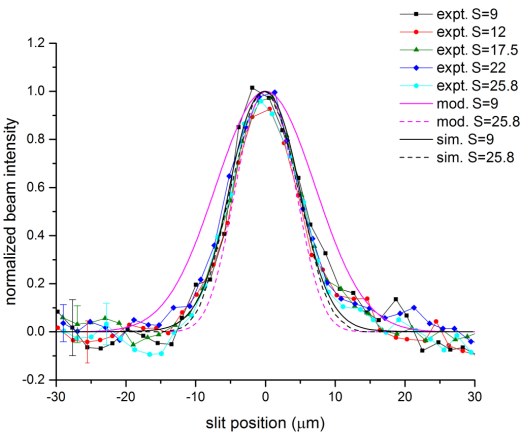

FIG. 4. Experimental focusing results for a 50-μm skimmer with pressures ranging from 11 to 81 bars, plotted together with simulations (sim.) and the analytical model (mod.); here S denotes the speed ratio.

from the image plane. For our measurements the distance was about 43 mm.

Figure 3 shows experimental results and simulations of focusing of a 76-bar helium beam down to about 3 μm. The results were obtained using the 10-μm-diam skimmer. The two graphs in the figure show focusing with and without the zero-order filter. Zero-order filtering is successfully demonstrated. There is good agreement between simulations and experimental data for both the filtered and unfiltered measurements. The measured intensity in the focus for the unfiltered beam is slightly lower than predicted by the simulations. Further, the footprint to the right is slightly raised compared to the simulations. Both of these effects can be explained as a slow response of the pressure gauge to a sudden pressure change. First, the gauge does not respond rapidly enough to the pressure increase, which leads to a slightly too low maximum intensity measurement. Then it does not respond rapidly enough to the pressure drop, which leads to a raised footprint. The slit was scanned from the left to the right quite fast. Each data point corresponds to about a 5-s measurement time.

Figure 4 shows focusing results for varying pressures from 11 to 81 bars corresponding to speed ratios between 9.0 and 25.8. The results were obtained using the 50-μm-diam skimmer. The predictions of the analytical models for speed ratios of 9.0 and 25.8 are plotted convoluted with a 10-μm slit function to match the experimental data. MCSTAS simulations for speed ratios 9.0 and 25.8 are also plotted. There is no change in focus size with speed ratio for the experimental data. It can clearly be seen that for the 50-μm-diam skimmer used here the analytical model overestimates the focus size for low-speed ratios and does not reproduce the footprint. The reason for this is that the analytical model corresponds to a situation where each point source illuminates uniformly in all directions. The model does not account for the change in angular distribution of the beam incident on the zone plate for off-axis points on the source. The larger the source (skimmer) and the smaller the speed ratio, the larger this effect will be. It has previously been shown that the analytical model provides good agreement for small skimmers in the micrometer range (see, for example, [9]). The MCSTAS simulations predict only a very small change in focus size with speed ratio and fit the data very well except for the footprint to the right, which is slightly raised. The reason for this is presumably the slow response of the pressure gauge to the pressure drop discussed already for Fig. 3. Further simulations (not shown) show that for skimmer sizes in the micrometer range, the two models converge.

V. CONCLUSION

In this paper we presented the experimental realization of a zero-order filter (order-sorting aperture) for diffractive de Broglie matter wave focusing elements. We used the zero-order filter to perform measurements of focusing of a neutral helium beam with source stagnation pressures between 11 and 81 bars. We showed that an analytical model previously used in the literature overestimates the focus size for low-speed ratios for the 50-μm-diam skimmer used in our experiments. We attributed this to the fact that the angular distribution of the beam incident on the zone plate changes as the source points move away from the axis. This effect was not accounted for in the analytical model. Simulations of the focusing results using the program package MCSTAS with an ellipsoidal quitting surface source model yielded very good agreement with the experimental results.

ACKNOWLEDGMENT

We acknowledge funding from the European Union through Theme NMP.2012.1.4-3, Grant No. 309672, Project NEMI.

[1] A. D. Cronin, J. Schmiedmayer, and D. E. Pritchard, Rev. Mod. Phys. **81**, 1051 (2009).
[2] M. Arndt, A. Ekers, W. von Klitzing, and H. Ulbricht, New J. Phys. **14**, 125006 (2012).
[3] T. Juffmann, H. Ulbricht, and M. Arndt, Rep. Prog. Phys. **76**, 086402 (2013).
[4] D. Farías and K.H. Rieder, Rep. Prog. Phys. **61**, 1575 (1998).
[5] G. Bracco and B. Holst, *Surface Science Techniques* (Springer Science & Business Media, New York, 2013).
[6] O. Carnal, M. Sigel, T. Sleator, H. Takuma, and J. Mlynek, Phys. Rev. Lett. **67**, 3231 (1991).
[7] R. B. Doak, R. E. Grisenti, S. Rehbein, G. Schmahl, J. P. Toennies, and C. Wöll, Phys. Rev. Lett. **83**, 4229 (1999).
[8] M. Koch, S. Rehbein, G. Schmahl, T. Reisinger, G. Bracco, W. E. Ernst, and B. Holst, J. Microsc. **229**, 1 (2008).
[9] S. D. Eder, T. Reisinger, M. M. Greve, G. Bracco, and B. Holst, New J. Phys. **14**, 073014 (2012).
[10] P. Witham and E. Sánchez, Rev. Sci. Instrum. **82**, 103705 (2011).
[11] P. J. Witham and E. J. Sánches, J. Microsc. **248**, 223 (2012).
[12] A. Fahy, M. Barr, J. Martens, and P. Dastoor, Rev. Sci. Instrum. **86**, 023704 (2015).
[13] M. Barr, A. Fahy, J. Martens, A. Jardine, D. Ward, J. Ellis, W. Allison, and P. Dastoor, Nat. Commun. **7**, 10189 (2016).
[14] T. Reisinger and B. Holst, J. Vac. Sci. Technol. B **26**, 2374 (2008).
[15] T. Reisinger, G. Bracco, S. Rehbein, G. Schmahl, W. E. Ernst, and B. Holst, J. Phys. Chem. A **111**, 12620 (2007).
[16] S. Eder, G. Bracco, T. Kaltenbacher, and B. Holst, J. Phys. Chem. A **118**, 4 (2013).
[17] T. Reisinger, G. Bracco, and B. Holst, New J. Phys. **13**, 065016 (2011).
[18] T. Judd, R. Scott, G. Sinuco, T. Montgomery, A. Martin, P. Krüger, and T. Fromhold, New J. Phys. **12**, 063033 (2010).
[19] S. D. Eder, X. Guo, T. Kaltenbacher, M. M. Greve, M. Kalläne, L. Kipp, and B. Holst, Phys. Rev. A **91**, 043608 (2015).
[20] L. Kipp, M. Skibowski, R. Johnson, R. Berndt, R. Adelung, S. Harm, and R. Seemann, Nature (London) **414**, 184 (2001).
[21] R. D. Doak, in *Helium Atom Scattering from Surfaces*, edited by E. Hulpke (Springer, Berlin, 1992), Vol. 27.
[22] B. Holst and W. Allison, Nature (London) **390**, 244 (1997).
[23] K. Fladischer, H. Reingruber, T. Reisinger, V. Mayrhofer, W. E. Ernst, A. E. Ross, D. A. MacLaren, W. Allison, D. Litwin, J. Galas, S. Sitarek, P. Nieto, D. Barredo, D. Farías, R. Miranda, B. Surma, A. Miros, B. Piatkowski, E. Søndergård, and B. Holst, New J. Phys. **12**, 033018 (2010).
[24] P. Sutter, M. Minniti, P. Albrecht, D. Farías, R. Miranda, and E. Sutter, Appl. Phys. Lett. **99**, 211907 (2011).
[25] H. C. Schewe, B. S. Zhao, G. Meijer, and W. Schöllkopf, New J. Phys. **11**, 113030 (2009).
[26] M. M. Greve, A. M. Vial, J. J. Stamnes, and B. Holst, Opt. Express **21**, 28483 (2013).
[27] A. Sakdinawat and D. Attwood, Nat. Photon. **4**, 840 (2010).
[28] K. Lefmann and K. Nielsen, Neutron News **10**, 20 (1999).
[29] P. Willendrup, E. Farhi, and K. Lefmann, Physica B **350**, E735 (2004).
[30] S. Eder, B. Samelin, G. Bracco, K. Ansperger, and B. Holst, Rev. Sci. Instrum. **84**, 093303 (2013).
[31] T. Reisinger, S. Eder, M. Greve, H. Smith, and B. Holst, Microelectron. Eng. **87**, 1011 (2010).
[32] H. Pauly, in *Atom, Molecule, and Cluster Beams I*, edited by H. Pauly (Springer, Berlin, 2000), Vol. 1.
[33] J. Toennies and K. Winkelmann, J. Chem. Phys. **66**, 3965 (1977).
[34] L. Pedemonte and G. Bracco, J. Chem. Phys. **119**, 1433 (2003).
[35] A. G. Michette, in *Optical Systems for Soft X Rays*, edited by A. Michette (Plenum, New York, 1968).
[36] MCSTAS, a ray-tracing simulation software package, available at www.mcstas.org.
[37] H. C. W. Beijernick and N. F. Verster, Physica C **111**, 327 (1981).
[38] A. S. Palau, G. Bracco, and B. Holst, Phys. Rev. A **94**, 063624 (2016).

Article 7

4.7 Atom sieve for nanometer resolution neutral helium microscopy

R. Flatabo, M. M Greve, SD Eder, M. Kallane, Adrià Salvador Palau, K. Berggren, Bodil Holst

Journal of Vacuum Science and Technology B, **35**, 6 (2017)

Atom sieve for nanometer resolution neutral helium microscopy

Running title: Atom sieve for nanometer resolution neutral helium microscopy
Running Authors: Flatabø et al.

Atom sieve for nanometer resolution neutral helium microscopy

Ranveig Flatabø,[1,2,a)] Martin M. Greve,[1] Sabrina D. Eder,[1] Matthias Kalläne,[3,4] Adrià Salvador Palau,[5] Karl K. Berggren,[2] and Bodil Holst[1,b)]

[1)] *Department of Physics and Technology, University of Bergen, Allegaten 55, 5007 Bergen, Norway*

[2)] *Research Laboratory of Electronics, Massachusetts Institute of Technology, MA 02139, USA*

[3)] *Institute for Experimental and Applied Physics, University of Kiel, Leibnizstrasse 19, 24098 Kiel, Germany*

[4)] *Ruprecht Haensel Laboratory, University of Kiel and DESY, Kiel, Germany*

[5)] *Department of Engineering, Institute for Manufacturing, University of Cambridge, CB30FS, UK*

Neutral helium microscopy is a new tool for imaging fragile and/or insulating structures as well as structures with large aspect ratios. In one configuration of the microscope, the neutral helium atoms are focused as de Broglie matter waves using a Fresnel zone plate. The ultimate resolution is determined by the width of the outermost zone. Due to the low-energy beam (typically less than 0.1 eV), the neutral helium atoms do not penetrate solid material and the Fresnel zone plate therefore has to be a free-standing structure. This creates particular fabrication challenges. The so-called Fresnel photon sieve structure is especially attractive in this context, as it consists merely of holes. Holes are easier to fabricate than the free-standing rings required in a standard Fresnel zone plate for helium microscopy, and the diameter of the outermost holes can be larger than the width of the zone that they cover. Recently, a photon sieve structure was used for the first time, as an atom sieve, to focus a beam of helium atoms down to a few μm. The holes were randomly distributed along the Fresnel zones to suppress higher order foci and side lobes. Here we present a new atom sieve design with holes distributed along the Fresnel zones with a fixed gap. This design gives higher transmission and higher intensity in the first order focus. We present an alternative electron beam lithography fabrication procedure that can be used for making such high transmission atom sieves with very high resolution, potentially smaller than 10 nm. The atom sieves were patterned on a 35 nm or a 50 nm thick silicon nitride membrane. The smallest hole is 35 nm, the largest 376 nm. In a separate experiment, patterning μm-scale areas with hole sizes down to 15 nm is demonstrated. The smallest gap between neighbouring holes in the atom sieves is 40 nm. They have 47011 holes each and are 23.58 μm in diameter. The opening ratio is 22.60 %, and the Fresnel zone coverage of the innermost zones is as high as 0.68. This high-density pattern comes with certain fabrication challenges, which we discuss.

[a)]Electronic mail: ranveig.flatabo@uib.no
[b)]Electronic mail: bodil.holst@uib.no

I. INTRODUCTION

The first neutral helium microscopy images were published in 2008[1]. Several groups have worked on the technique[2–6] . In a neutral helium microscope (NEMI), a beam of neutral helium atoms with narrow velocity (wavelength) distribution is used to image a sample. An image is obtained by measuring either the reflected or transmitted signal as the beam is scanned across the sample. The energy of the beam is less than 0.1 eV for a wavelength of 0.1 nm, which means that the atoms probe the outermost electron density distribution of the sample without penetrating into solid material[7]. These properties make neutral helium microscopy particularly suited for the investigation of fragile and/or insulating surfaces as well as high aspect ratio structures. Recently it was shown that helium microscopy can distinguish between different metal films on an insulating substrate[5]. However, the big challenge is to create a high-resolution microscope, partly because the focusing element must be of the binary type with either completely transparent or completely opaque areas.

Helium-atom focusing with a binary Fresnel zone plate was first carried out by Carnal et al. using a beam of metastable helium atoms[8]. The first focusing of a neutral, ground state helium beam with a zone plate was carried out by Doak et al[9,11]. Currently, the best zone plates made for helium microscopy have a nominal outermost zone width of 50 nm[10].

The Beynon-Gabor zone plate, which is also binary, has been suggested as an alternative candidate for focusing helium atoms[12]. The main advantage of the Beynon-Gabor zone plate is that it has no higher-order foci. Unfortunately, it is very challenging to fabricate. In 2015 a new optical diffraction element, the atom sieve, was introduced and used to focus helium atoms down to 3.6 μm[13]. The atom sieve is a direct analog to the photon sieve, which was invented in 2001 for applications with soft X-rays[14]. It consists of holes of varying diameter, arranged across the Fresnel zones in such a manner that it is possible to focus to a spot with a diameter smaller than the smallest hole. In addition, higher-order diffraction and secondary maxima can be suppressed. There are several advantages of the atom sieve. Firstly, it is easier to fabricate free-standing holes than free-standing ring segments as no support structure is needed. Moreover, the design can be tuned so that the diameter of the outermost hole is larger than the width of the outermost zone that it covers. In contrast,

the minimum structure size of a first order Fresnel zone plate is limited by the width of the outermost zone[27]. A higher resolution can be obtained by using higher order foci, but this comes with a significant reduction in intensity. For a standard Fresnel zone plate 10.1 % of the incident beam goes into the first order focus and only 1.1 % into the third order[17]. For an atom Fresnel zoneplate these numbers are further reduced due to the support rods needed to keep the zone plate ring structure together. Intensity is a big issue in helium microscopy[15,16], so this is a major limitation.

Here we present a new high-transmission atom sieve design. The paper begins with an experimental section, where we first present the design requirements followed by the fabrication procedure. There then follows a result and discussion section showing SEM images of the fabricated atom sieves and the first atom sieve transmission tests demonstrating that the structure is transparent to atoms. The paper finishes with a summary and conclusion.

II. EXPERIMENTAL

A. Atom Sieve Design Considerations

In the original photon sieve work, suppression of higher order foci and side lobes were particularly important, and a Weber transmission window was used, giving holes randomly distributed along the zones[14]. This limits the number of holes and hence the open area ratio (total transmissivity). The first atom sieve used the original photon sieve design and had an opening ratio (total transmissivity) of 9.22 % only, giving a transmissivity of 1.86 % of the incident beam into the first order focus[13]. For the neutral helium microscope it is crucial to ensure maximum intensity in the first order focus, as discussed in the introduction. For this reason we changed the design of the atom sieve, and used a transmission window similar to a rectangular shaped window, but with increasing transmission towards the center, to fit as many holes as possible in each zone based on a predefined minimum gap. The minimum gap is discussed below. By doing so, the opening ratio of the sieve (total transmissivity) increases to 22.60 % and the intensity in the first order focus is 4.57 %.

Another important decision was to determine hole sizes that could realistically be patterned. This is important for the resolution, but also for the transmissivity, as it determines how large a zone plate can be made for a given focal length. The focal length was chosen so

that it corresponds to a microscope that can be constructed and further so that the velocity spread of the beam does not cause chromatic abberations (see Ref. 15). The hole size varies from 376 nm to 35 nm. The smallest holes that have ever been made with direct-write lithography are around 1 nm in size. They were made using helium ion beam lithography[18]. Direct-write ion lithography is in principle an attractive technique for atom sieve patterns, as one can pattern directly on the membrane i.e. no resist is needed. This enables a one-step fabrication process where the result can be examined in-situ. Moreover, the backscattering contribution to the lithographic point spread function of light ions, such as helium and neon, is shown to be minimal, and hence dose modifications might not be needed[19,20]. However, these are relatively new techniques with low throughput, limited stability and, in the case of helium ions, low sputtering yields[21]. Electron beam lithography, followed by reactive ion etching, was chosen as the method of fabrication, and an atom sieve pattern with a minimum hole size of 35 nm was realized. To ensure maximum transmissivity the diameter of the holes was chosen to be the same as the zone widths. As discussed in the introduction, it is possible to design a transmission function enabling the hole diameter to be larger than its zone, but this comes at the cost of intensity.

The aim is eventually to install the atom sieve in a new helium microscope, currently being designed. This determined a focal length of approximately 10 mm for a helium atom de Broglie wavelength of approximately 0.1 nm for the sieve. With minimum hole size and focal length given, the sieve diameter could be calculated (the sieve diameter is 23.58 μm).

Finally, the gap between adjacent holes was selected. This is essential for the transmission of the device, since large values reduce the number of holes. The gap between neighbouring holes varies from 53 nm to 40 nm, depending on how many holes one can fit into one zone. Hence, the zones in the atom sieve have a very high zone coverage (i.e. exposed area in one Fresnel zone divided by the total area of the corresponding zone). The zone coverage of the innermost zone is 0.68 (corresponding to a hole diameter of 376 nm and a gap of 53 nm) and it slowly decreases to 0.39 for the outermost zone (for a 35 nm Fresnel zone overlaid with holes of 35 nm and a gap of 40 nm). The minimum gap of 40 nm was chosen as a safe value, making sure that it was possible to pattern separate holes with electron beam lithography and transfer the pattern into the membrane.

The atom sieve design is shown in Fig. 1. Note that it is not rotationally symmetrical. The stripe in the horizontal direction exists as the positioning of the holes start at the same

angle on each zone. Each zone is filled with as many holes as possible (with the given minimum hole distance).

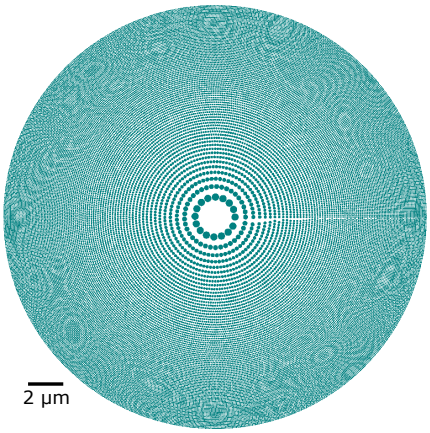

FIG. 1. Atom sieve design maximized for total transmissivity. The pattern is not symmetrical, which is discussed in the text. The central opaque area corresponds to the first zone, which is kept closed for stability reasons.

B. Fabrication Procedure

The fabrication process is illustrated in Fig. 2. It shares some steps with the fabrication procedure used in[22], but with some modifications. In this work we use 35 nm or 50 nm thick SiNx membranes with low stress (low stress membrane was chosen to prevent the membrane from cracking). The membrane thicknesses were chosen to keep the aspect ratio of the etched holes adequate. However, it comes with the obvious trade-off of being more fragile than thicker membranes, which we discuss in Sec. III.

First, photolithography was used to pattern membrane windows on the backside of the SiNx/Si/SiNx wafer. To open the membrane windows, a dry etch step was performed using 15 SCCM (gas flow rate: standard cubic centimeters per minute) CF_4, 150 W, 10 mTorr for 2 minutes. Then, the underlying silicon was etched using KOH (30% KOH in de-ionized water) at 80° C, creating SiNx membranes.

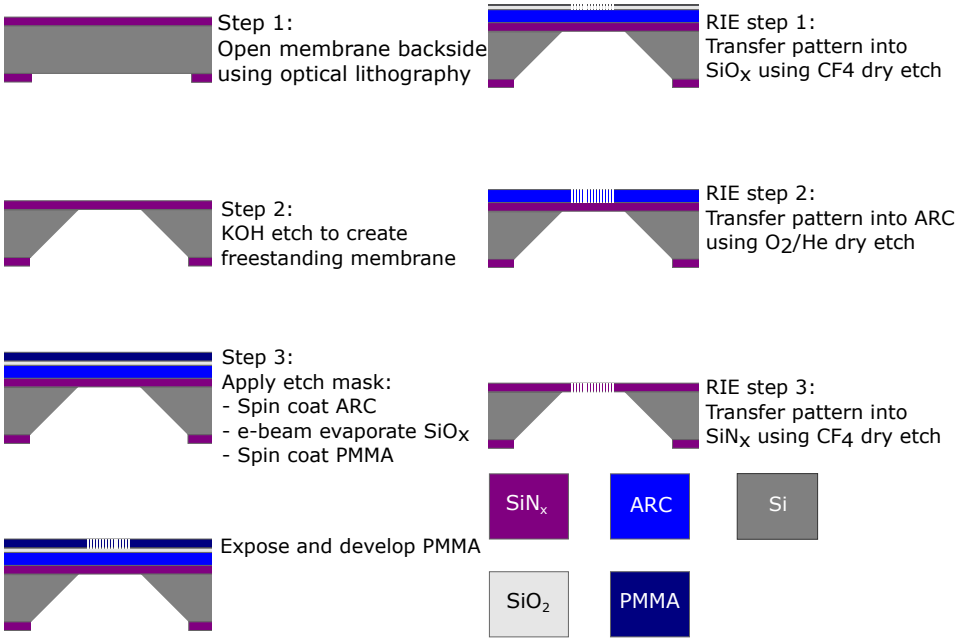

FIG. 2. (Color online)Step-by-step fabrication procedure for creating the free-standing membrane structure.

As the resist, poly(methylmethacrylate) (PMMA) alone cannot withstand the reactive ion etching that creates free-standing holes, the membrane was coated with an etch mask consisting of 110 nm antireflective coating (ARC), 10 nm SiO_x and 60 nm PMMA (2 % in anisole, 950 K). Firstly, ARC was spin-coated onto the chip at 3000 RPM for 1 minute and baked at 180° C for 3 minutes. 10 nm SiO_x was then deposited by the means of electron beam evaporation. Finally, PMMA was spin-coated onto the sample at 3000 RPM for 1 minute and baked at 180° C for 3 minutes.

The PMMA was exposed using 125 keV electrons (ELS-F125 Elionix), 1 nA current and 2.5 nm step size. As the beam enters the resist, the electrons interact with the resist and the substrate and causes energy to be delivered to points different from the point of incidence, commonly known as proximity effects. Due to the high zone coverage of the atom sieve design (0.68 to 0.39) it is extremely sensitive to such unintended exposure, especially as the final structure needs to be free-standing. To find the correct dose (i.e. areal dose density)

multiple atom sieves were patterned with a single exposure dose, analogous to the standard dose matrices. The innermost zones are receiving the largest dose per zone and get the largest amount of unintended exposure. This causes over-exposure. Therefore, the dose was linearly increased from 2.8 mC/cm^2 to 3.8 mC/cm^2 going from the innermost zone to the outermost zone (again using a 125 keV electron beam, 1 nA current and 2.5 nm step size). It should be noted that there are accurate and rigorous ways to calculate the correct dose needed in a pattern of high surface coverage[23,28,29]. However, as a crucial part in this work is to transfer the pattern into the membrane, which also causes a minor hole broadening (discussed below), the correct doses was found by iteration.

The sample was developed in 1:3 MIBK:IPA (methyl isobutyl ketone:2-propanol)at 0° C for 30 seconds, and dried using pressurized nitrogen. Cold development was chosen, as it has been found to improve feature quality and resolution[24,25].

The pattern was transferred to the SiO_x-layer using 15 SCCM of CF_4 at 150 W and 10 mTorr. Pattern transfer into the ARC was done using 20 SCCM He and 10 SCCM of O_2 at 10 mTorr and 200 W. Finally, pattern transfer into the SiNx was done using 15 SCCM of CF_4 at 150 W and 10 mTorr. Reactive ion etching produces anisotropic etch profiles. Nevertheless, a broadening of about 5 nm in the diameter is found when comparing circles in an atom sieve that was not etched (i.e. atom sieve in PMMA) with holes in an atom sieves.

III. RESULTS AND DISCUSSION

A. The Atom Sieve

Figure 3 shows an overview image of an atom sieve. The diameter of the sieve is 23.58 μm ± 0.01 μm and it contains 47011 holes. Close-up SEM images are given in Fig. 4. The holes of the innermost zone have a diameter of 378 nm ± 4 nm, and the holes of the outermost zone 38 nm ± 4 nm. Both slightly too large and slightly too small holes will lead to a reduction in transmissivity into the first order focus, because a too large hole will open up into the neighbouring zone and give destructive interference. The overall deviation, taken for all holes is so small that the reduction is likely to be negligible[30]. It is very important for the function of the atom sieve that the size of the holes and their position are correct

to within a fraction of the Fresnel zone they cover, since otherwise a hole will contribute with destructive interference[30]. In other words, the positioning of the small holes needs to be more accurate than the positioning of the big holes. In Fig. 5 a SEM image of the fabricated atom sieve (black holes) is superimposed with the design pattern (white "holes"). As can be seen, the positioning of even the smallest holes is accurate to within a fraction of the hole diameter.

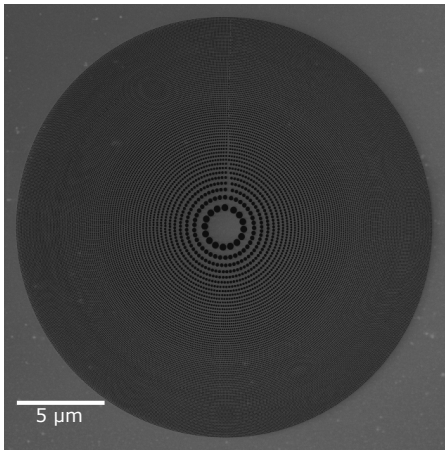

FIG. 3. Overview SEM image of the fabricated free-standing atom sieve.

The membrane thickness of 35 nm was chosen to keep the aspect ratio of the etched holes adequate. However, this comes with a trade-off of being more fragile than a thicker membrane. The 35-nm thick membranes easily broke due to handling or transport. An improvement in stability was seen when using a membrane thickness of 50 nm.

In a separate experiment it was desirable to investigate the smallest diameter hole-sizes. A lower hole density, and a random hole distribution was selected for these test experiments, as illustrated in Fig. 6. The diameter of the holes in the SEM image ranges from 25 nm to 15 nm.

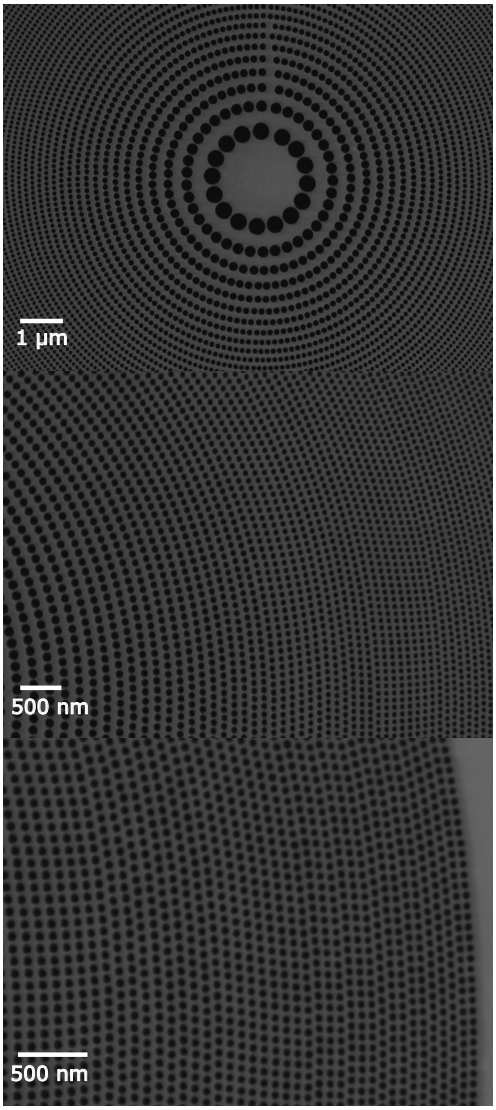

FIG. 4. Close-up SEM images of a free-standing atom sieve. The holes of the innermost zone have a diameter of 378 nm ± 4 nm, and the holes of the outermost zone are found to be 38 nm ± 4 nm.

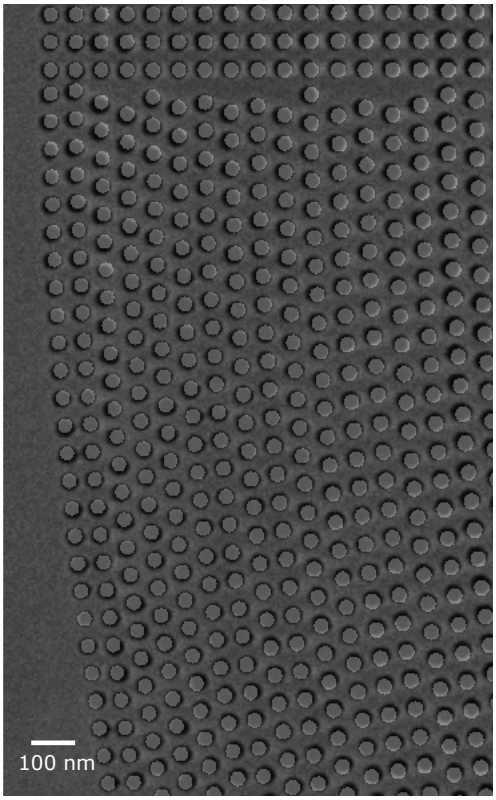

FIG. 5. Overview SEM image of the free-standing atom sieve where the design pattern is superimposed onto the image. The design-holes are white, while the underlying SEM image consists of black holes.

B. Atom Transmission Tests

Ultimately the atom sieve will be integrated in a new neutral helium atom microscope instrument. However, prior to that we wanted to check if it is transmissive to atoms. This is crucial, because in order to be a functional atom sieve, the holes must be free standing. It can be difficult to evaluate just by optical inspection or inspection in a SEM if all material has been removed. This is illustrated in Fig. 7, where a 20 μm circle on a SiNx membrane appears to be fully etched, but in fact is not. For this reason we installed the atom sieve as a sample in our existing helium microscope[26] and measured the overall transmissivity by

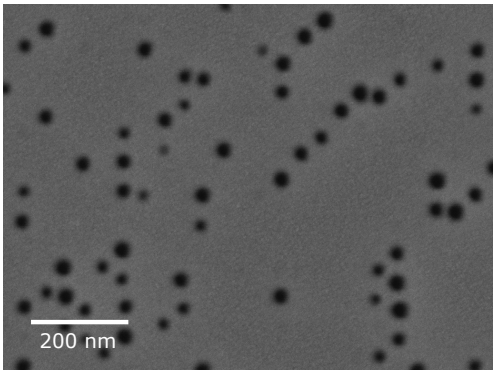

FIG. 6. Free-standing holes with a diameter ranging from 25 nm to 15 nm.

sending a 20 μm helium beam onto the sample. Presently the minimum resolution in our helium microscope is only around 5 μm, so it was not possible to do a detailed mapping. Figure 8 presents a line scan of the sieve. The transmissivity is normalized to the intensity measured when no sample is present (i.e. 100 % signal), and the background has been subtracted. The transmissivity of the sieve is found to be 23.8% ± 3%, in good agreement with the nominal transmissivity of 22.6 %.

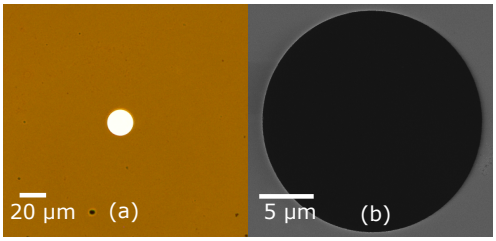

FIG. 7. (a) Transmission optical microscopy image and (b) SEM image of a 20 μm circle in a 200 nm thick SiNx membrane that appears to be free-standing. However, transmission helium atom microscopy measurements revealed that the structure was not etched through.

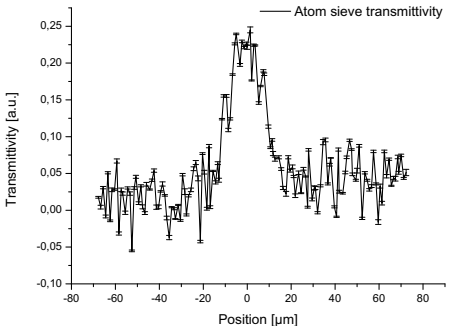

FIG. 8. Overall transmissivity of the atom sieve measured in the neutral helium microscope. The transmissivity of the sieve is found to be 23.8% ± 3%, in good agreement with the nominal transmissivity of 22.6 %.

IV. SUMMARY AND CONCLUSION

We have fabricated atom sieves, with a smallest hole diameter of 35 nm. The atom sieves were designed for maximum transmission so that the diameter of the smallest hole corresponds to the width of the outermost zone. This means that we have made a zone plate which can be used to do neutral helium microscopy with resolution in the range of 35 nm. In addition, we have demonstrated writing of µm-scale areas with holes down to 15 nm in diameter. By using a transmission window where the hole areas are reduced in the outer parts e.g. a Weber window, it is possible to design an atom sieve with a resolution larger than the hole diameter. In a recent paper Palau et al[16] shows that with the velocity spread and intensity of present day beam sources and present day detector technology, the limiting factor for a realistic helium microscope design is the resolution of the optical element, determined by the width of the outermost zone. Thus our work shows that helium microscopy with a resolution better than 15 nm should be possible.

V. ACKNOWLEDGEMENTS

The authors thank M. Mondol, T. Savas and J. Daley at MIT Nanostructure Laboratory, and B. Samelin at University of Bergen Nanophysics Laboratory. This work was done at the MIT Nanostructure Laboratory and the MIT Scanning-Electron-Beam Lithography

facility. The helium microscopy test was done at the University of Bergen, Nanophysics Laboratory. R. Flatabø gratefully acknowledges support from Bergen Research Foundation and the Norway-America Association through American-Scandinavian Foundation's The Stolt-Nilsen Fund for education.

REFERENCES

[1]M. Koch, S. Rehbein, G. Schmahl, T. Reisinger, G. Bracco, W.E. Ernst and B. Holst, J. Microscop, **229**, 1, 1, 2008

[2]P. Witham and E. Sánchez, Rev. Sci. Instrum., **82**, 103705, 2011

[3]P. Witham and E. Sánchez, Cryst. Res. Technol., **49**, 690, 2014

[4]A. Fahy, M. Barr, J. Martens, and P. Dastoor, Rev. Sci. Instrum. **86**, 023704, 2015

[5]M. Barr, A. Fahy, J. Martens, A.P. Jardine, D.J. Ward, J. Ellis, W. Allison, and P.C. Dastoor, Nat. Commun. **7**, 10189, 2016

[6]P. Witham and E. Sánchez, J. Microscop. **248**, 223, 2012

[7]G. Bracco and B. Holst, Surface Science Techniques, (Springer Science & Business Media), 2013

[8]O. Carnal, M. Sigel, T. Sleator, H. Takuma, and J. Mlynek, Phys. Rev. Lett. **67**, 3231, 991

[9]R.B. Doak, R.E. Grisenti, S. Rehbein, G. Schmahl, J.P. Toennies, and C. Wöll, Phys. Rev. Lett. **83**, 4229, 1999

[10]T. Reisinger, S. Eder, M.M. Greve, H.I. Smith, B. Holst, Microelectron. Eng., **87**, 1011, 2010

[11]R. Rehbein, J. Phys. IV France, **104**, 207, 2003

[12]M.M. Greve, A. Vial, J. Stamnes, and B. Holst, Opt. Express **21**, 28483, 2013

[13]S.D. Eder, X. Guo, T. Kaltenbacher, M.M. Greve, M. Kalläne, L. Kipp, and B. Holst, Phys. Rev. A, **91**, 043608, 2015

[14]L. Kipp, M. Skibowski, R.L. Johnson, R. Berndt, R. Adelung, S. Harm, and R. Seemann, Nature, **414**, 184, 2002

[15]A.S. Palau, G. Bracco and B. Holst, Phys. Rev A, **95**, 013611, 2017

[16]A.S. Palau, G. Bracco and B. Holst, Phys. Rev A, **94**, 063624, 2016

[17]A.G. Michette, Optical Systems for Soft X Rays, (Plenum Press, New York), 1986

[18]D.A. Oulianov, R.A. Crowell, D.J. Gosztola, I.A. Shkrob, O.J. Korovyanko, and R.C. Rey-de-Castro, J. Appl. Phys. **101**, 053102, 2007

[19]D. Winston, B.M. Cord, B. Ming, D.C. Bell, W.F. DiNatale, L.A. Stern, A.E. Vladar, M.T. Postek, M.K. Mondol, J.K.W. Yang, K.K. Berggren, J. Vac. Sci. Technol. B, **27**, 2702, 2009

[20]D. Winston, V.R. Manfrinato, S.M. Nicaise, L.L Cheong, H. Duan, D. Ferranti, J. Marshman, S. McVey, L.A. Stern, J. Notte, K.K. Berggren, Nano Lett., **11**, 4343, 2011

[21]M.M. Marshall, J. Yang, A.R Hall, Scanning, **34**, 101, 2012

[22]J.O. Grepstad, M.M. Greve, T. Reisinger and B. Holst, J. Vac. Sci. Technol. B, **31**, 06F402, 2013

[23]G. Owen, J. Vac. Sci. Technol. B, **8**, 1889, 1990

[24]W. Hu, K. Sarveswaran, M. Lieberman, G.H. Bernstein, J. Vac. Sci. Technol. B, **22**, 1711, 2004

[25]B. Cord, J. Lutkenhaus and K.K. Berggren, J. Vac. Sci. Technol. B, **25**, 2013, 2007

[26]S.D. Eder, A.K. Ravn, B. Samelin, G. Bracco, A.S. Palau, T. Reisinger, E.B. Knudsen, K. Lefmann and B. Holst, Phys. Rev. A, **95**, 023618, 2017

[27]G. Schmahl and D. Rudolph, Zone Plates for X-Ray Microscopy in X-Ray Microscopy. (Springer Series in Optical Sciences), **43**, 1984

[28]M. Peckerar, R. Bass, K.W. Rhee, J. Vac. Sci. Technol. B, **18**, 3143, 2000

[29]M. Parikh, Journ. Appl. Phys., **50**, 4371, 1979

[30]E. Hecht, Optics 4 Edition, (Addison-Wesley), 2001

Chapter 5

Bibliography

Bibliography

[1] W. Adams, M. Sadatgol, and D. Ö. Güney. Review of near-field optics and superlenses for sub-diffraction-limited nano-imaging. *AIP Advances*, 6(10):100701, 2016.

[2] A. R. Alderwick. *Instrumental and analysis tools for atom scattering from surfaces.* PhD thesis, University of Cambridge, 2010.

[3] A. Amirav, U. Even, and J. Jortner. Cooling of large and heavy molecules in seeded supersonic beams. *Chemical Physics*, 51(1-2):31–42, 1980.

[4] G. Anemone, A. Al Taleb, S. D. Eder, B. Holst, and D. Farías. Flexible thin metal crystals as focusing mirrors for neutral atomic beams. *Physical Review B*, 95(20): 205428, 2017.

[5] H. Ashkenas and F. Sherman. Proceedings of the 4th international symposium on rarefied gas dynamics. *Vol. II, edited by JH deLeeuw (Academic, New York, 1966) p*, 84(0), 1966.

[6] M. Barr, K. O'Donnell, A. Fahy, W. Allison, and P. Dastoor. A desktop supersonic free-jet beam source for a scanning helium microscope (shem). *Measurement Science and Technology*, 23(10):105901, 2012.

[7] M. Barr, A. Fahy, A. Jardine, J. Ellis, D. Ward, D. MacLaren, W. Allison, and P. Dastoor. A design for a pinhole scanning helium microscope. *Nuclear Instruments and Methods in Physics Research Section B: Beam Interactions with Materials and Atoms*, 340:76–80, 2014.

[8] M. Barr, A. Fahy, J. Martens, A. P. Jardine, D. J. Ward, J. Ellis, W. Allison, and P. C. Dastoor. Unlocking new contrast in a scanning helium microscope. *Nature Communications*, 7:10189, Jan. 2016. ISSN 2041-1723. doi: 10.1038/ncomms10189.

[9] D. Barredo, F. Calleja, P. Nieto, J. J. Hinarejos, G. Laurent, A. L. V. de Parga, D. Farías, and R. Miranda. A quantum-stabilized mirror for atoms. *Advanced materials*, 20(18):3492–3497, 2008.

[10] H. Beijerinck and N. Verster. Absolute intensities and perpendicular temperatures of supersonic beams of polyatomic gases. *Physica B+ C*, 111(2-3):327–352, 1981.

[11] M. Bergin. *Instrumentation and contrast mechanisms in scanning helium microscopy*. PhD thesis, Fitzwilliam College, University of Cambridge, Dec. 2018.

[12] M. Bergin, D. Ward, J. Ellis, and A. Jardine. A method for constrained optimisation of the design of a scanning helium microscope. *Ultramicroscopy*, 207:112833, 2019. ISSN 0304-3991. doi: https://doi.org/10.1016/j.ultramic.2019.112833.

[13] M. Bergin, S. M. Lambrick, H. Sleath, D. J. Ward, J. Ellis, and A. P. Jardine. Observation of diffraction contrast in scanning helium microscopy. *Scientific Reports*, 10(1):1–8, Feb. 2020. ISSN 2045-2322. doi: 10.1038/s41598-020-58704-1.

[14] M. Bergin, D. Ward, S. Lambrick, N. von Jeinsen, B. Holst, J. Ellis, A. Jardine, and W. Allison. Low-energy electron ionization mass spectrometer for efficient detection of low mass species. *Review of Scientific Instruments*, 92(7):073305, 2021.

[15] S. Berryman. Ancient Atomism. In E. N. Zalta, editor, *The Stanford Encyclopedia of Philosophy*. Metaphysics Research Lab, Stanford University, Winter 2016 edition, 2016.

[16] B.Holst and G.Bracco. *Surface Science Techniques*, volume 51 of *Springer Series in Surface Sciences*, chapter 12, pages 333–367. Springer, 2013.

[17] G. Bird. Direct simulation and the boltzmann equation. *The Physics of Fluids*, 13 (11):2676–2681, 1970.

[18] G. Bird. Transition regime behavior of supersonic beam skimmers. *The Physics of fluids*, 19(10):1486–1491, 1976.

[19] G. Bird. Recent advances and current challenges for dsmc. *Computers & Mathematics with Applications*, 35(1-2):1–14, 1998.

[20] G. A. Bird. Molecular gas dynamics and the direct simulation of gas flows. *Molecular gas dynamics and the direct simulation of gas flows*, 1994.

[21] S. Bize, P. Laurent, M. Abgrall, H. Marion, I. Maksimovic, L. Cacciapuoti, J. Grünert, C. Vian, F. P. Dos Santos, P. Rosenbusch, et al. Cold atom clocks and applications. *Journal of Physics B: Atomic, molecular and optical physics*, 38(9): S449, 2005.

[22] U. Bossel. Skimming of molecular beams from diverging non-equilibrium gas jets. In *Presented at the 11th Bien. Fluid Dyn. Symp. on Advanced Probl. and Method in Fluid Mech*, pages 3–8, 1974.

[23] J. Braun, P. Day, J. Toennies, G. Witte, and E. Neher. Micrometer-sized nozzles and skimmers for the production of supersonic he atom beams. *Review of scientific Instruments*, 68(8):3001–3009, 1997.

[24] J. G. Breman, D. L. Heymann, G. Lloyd, J. B. McCormick, M. Miatudila, F. A. Murphy, J.-J. Muyembé-Tamfun, P. Piot, J.-F. Ruppol, P. Sureau, et al. Discovery and description of ebola zaire virus in 1976 and relevance to the west african epidemic during 2013–2016. *The Journal of infectious diseases*, 214(suppl_3):S93–S101, 2016.

[25] G. Brusdeylins, R. B. Doak, and J. P. Toennies. Measurement of the dispersion relation for rayleigh surface phonons of lif (001) by inelastic scattering of he atoms. *Physical Review Letters*, 46(6):437, 1981.

[26] H. G. Bullman. *Development of a position sensitive atom detector for helium-surface scattering*. PhD thesis, University of Cambridge, 1998.

[27] O. Carnal, M. Sigel, T. Sleator, H. Takuma, and J. Mlynek. Imaging and focusing of atoms by a fresnel zone plate. *Physical review letters*, 67(23):3231, 1991.

[28] S. L. Chin. *Multiphoton Ionization of Atoms*. Elsevier, 2012.

[29] M. DeKieviet, D. Dubbers, M. Klein, U. Pieles, and C. Schmidt. Design and performance of a highly efficient mass spectrometer for molecular beams. *Review of Scientific Instruments*, 71(5):2015–2018, 2000.

[30] D. DePonte, S. Kevan, and F. Patton. Brightness of micronozzle helium source. *Review of scientific instruments*, 77(5):055107, 2006.

[31] R. Doak, R. Grisenti, S. Rehbein, G. Schmahl, J. Toennies, and C. Wöll. Towards realization of an atomic de broglie microscope: helium atom focusing using fresnel zone plates. *Physical review letters*, 83(21):4229, 1999.

[32] D. Douglas. Linear quadrupoles in mass spectrometry. *Mass spectrometry reviews*, 28(6):937–960, 2009.

[33] S. Dworski. *Atom optical methods for surface studies*. PhD thesis, University of Cambridge, 2004.

[34] L. A. Earl, J. D. Lifson, and S. Subramaniam. Catching hiv in the actwith 3d electron microscopy. *Trends in microbiology*, 21(8):397–404, 2013.

[35] S. Eder, T. Reisinger, M. Greve, G. Bracco, and B. Holst. Focusing of a neutral helium beam below one micron. *New Journal of Physics*, 14(7):073014, 2012.

[36] S. Eder, X. Guo, T. Kaltenbacher, M. Greve, M. Kalläne, L. Kipp, and B. Holst. Focusing of a neutral helium beam with a photon-sieve structure. *Physical Review A*, 91(4):043608, 2015.

[37] S. Eder, A. Ravn, B. Samelin, G. Bracco, A. S. Palau, T. Reisinger, E. B. Knudsen, K. Lefmann, and B. Holst. Zero-order filter for diffractive focusing of de broglie matter waves. *Physical Review A*, 95(2):023618, 2017.

[38] S. D. Eder. A neutral matter-wave microscope (nemi): Design and setup. 2012.

[39] S. D. Eder, A. Salvador Palau, T. Kaltenbacher, G. Bracco, and B. Holst. Velocity distributions in microskimmer supersonic expansion helium beams: High precision measurements and modeling. *Review of Scientific Instruments*, 89(11):113301, 2018.

[40] R. Erni, M. D. Rossell, C. Kisielowski, and U. Dahmen. Atomic-resolution imaging with a sub-50-pm electron probe. *Physical review letters*, 102(9):096101, 2009.

[41] I. Estermann and O. Stern. Beugung von molekularstrahlen. *Zeitschrift für Physik*, 61(1):95–125, 1930.

[42] A. Fahy, M. Barr, J. Martens, and P. Dastoor. A highly contrasting scanning helium microscope. *Review of Scientific Instruments*, 86(2):023704, 2015.

[43] A. Fahy, S. D. Eder, M. Barr, J. Martens, T. A. Myles, and P. C. Dastoor. Image formation in the scanning helium microscope. *Ultramicroscopy*, 192:7–13, Sept. 2018. ISSN 0304-3991.

[44] A. J. Fahy. A practical consideration of scanning helium microscopy. 2018.

[45] D. Farias and K.-H. Rieder. Atomic beam diffraction from solid surfaces. *Rep. Prog. Phys.*, 61(12):1575, 1998.

[46] K. Fladischer, H. Reingruber, T. Reisinger, V. Mayrhofer, W. Ernst, A. Ross, D. MacLaren, W. Allison, D. Litwin, J. Galas, et al. An ellipsoidal mirror for focusing neutral atomic and molecular beams. *New journal of Physics*, 12(3): 033018, 2010.

[47] R. Flatabø, M. M. Greve, S. D. Eder, M. Kalläne, A. S. Palau, K. K. Berggren, and B. Holst. Atom sieve for nanometer resolution neutral helium microscopy. *Journal of Vacuum Science & Technology B, Nanotechnology and Microelectronics: Materials, Processing, Measurement, and Phenomena*, 35(6):06G502, 2017.

[48] R. Flatabø, S. D. Eder, A. K. Ravn, B. Samelin, M. M. Greve, T. Reisinger, and B. Holst. Fast resolution change in neutral helium atom microscopy. *Review of Scientific Instruments*, 89(5):053702, 2018.

[49] J.-J. Greffet and M. Nieto-Vesperinas. Field theory for generalized bidirectional reflectivity: derivation of helmholtzs reciprocity principle and kirchhoffs law. *JOSA A*, 15(10):2735–2744, 1998.

[50] R. Grundy. Axially symmetric expansion of a monatomic gas from an orifice into a vacuum. *The Physics of Fluids*, 12(10):2011–2018, 1969.

[51] A. H. M. Habets. Supersonic expansion of argon into vacuum. 1977.

[52] B. B. Hamel and D. R. Willis. Kinetic theory of source flow expansion with application to the free jet. *The physics of Fluids*, 9(5):829–841, 1966.

[53] H. Hedgeland. *The development of quasi-elastic helium-3 spin-echo spectroscopy as a tool for the study of surface dynamics*. PhD thesis, University of Cambridge, 2007.

[54] H. Hedgeland, A. Jardine, W. Allison, and J. Ellis. Anomalous attenuation at low temperatures in high-intensity helium beam sources. *Review of scientific instruments*, 76(12):123111, 2005.

[55] S. W. Hell and J. Wichmann. Breaking the diffraction resolution limit by stimulated emission: stimulated-emission-depletion fluorescence microscopy. *Optics letters*, 19(11):780–782, 1994.

[56] C. G. Herbert and R. A. Johnstone. *Mass spectrometry basics*. CRC press, 2002.

[57] B. Holst and e. al. Material properties particularly suited to be measured with helium scattering: selected examples from 2d materials, van der waals heterostructures, glassy materials, catalytic substrates, topological insulators and superconducting radio frequency materials. *Phys Chem. Chem. Phys.*, 94:7653, 2021.

[58] B. Holst and W. Allison. An atom-focusing mirror. *Nature*, 390(6657):244–244, 1997.

[59] B. Holst, J. Huntley, R. Balsod, and W. Allison. Mechanical properties of ultrathin single crystals for atom-mirror applications: Au (001), si (001). *Journal of Physics D: Applied Physics*, 32(20):2666, 1999.

[60] J. J. Hurly and M. R. Moldover. Ab initio values of the thermophysical properties of helium as standards. *Journal of research of the National Institute of Standards and Technology*, 105(5):667, 2000.

[61] G. Hurst, M. Payne, M. Nayfeh, J. Judish, and E. Wagner. Saturated two-photon resonance ionization of he (2 s 1). *Physical Review Letters*, 35(2):82, 1975.

[62] J. E. Jones. On the determination of molecular fields.i. from the variation of the viscosity of a gas with temperature. *Proceedings of the Royal Society of London. Series A, Containing Papers of a Mathematical and Physical Character*, 106(738): 441–462, 1924.

[63] D. Joy, R. Ramachandra, and B. Griffin. Choosing a beam-electrons,protons, he or ga ions? *Microscopy and Microanalysis*, 15, 07 2009. doi: 10.1017/S1431927609092757.

[64] A. Kalinin, L. Y. Rusin, and J. Toennies. Ion source with longitudinal ionization of a molecular beam by an electron beam in a magnetic field. *Instruments and Experimental Techniques*, 49(5):709–713, 2006.

[65] T. Kaltenbacher. Optimization of a constrained linear monochromator design for neutral atom beams. *Ultramicroscopy*, 163:62–68, 2016.

[66] A. Kantrowitz and J. Grey. A high intensity source for the molecular beam. part i. theoretical. *Review of Scientific Instruments*, 22(5):328–332, 1951.

[67] E. Keppler, V. Afonin, C. Curtis, A. Dyachkov, J. Erö, C. Fan, K. Hsieh, D. Hunten, W.-H. Ip, A. Richter, et al. Neutral gas measurements of comet halley from vega 1. *Nature*, 321(6067):273–274, 1986.

[68] L. Kipp, M. Skibowski, R. Johnson, R. Berndt, R. Adelung, S. Harm, and R. Seemann. Sharper images by focusing soft x-rays with photon sieves. *Nature*, 414 (6860):184–188, 2001.

[69] J. R. B. Knowling. *Helium atom scattering: experiment and the interpretation of experiment.* PhD thesis, University of Cambridge, 2000.

[70] M. Koch, S. Rehbein, G. Schmahl, T. Reisinger, G. Bracco, W. E. Ernst, and B. Holst. Imaging with neutral atoms - a new matter-wave microscope. *J. Microsc.*, 229(1):1–5, 2008. ISSN 1365-2818. doi: 10.1111/j.1365-2818.2007.01874.x.

[71] S. M. Lambrick, M. Bergin, A. P. Jardine, and D. J. Ward. A ray tracing method for predicting contrast in neutral atom beam imaging. *Micron*, 113:61–68, Oct. 2018. ISSN 0968-4328. doi: 10.1016/j.micron.2018.06.014.

[72] S. M. Lambrick, L. Vozdecky, M. Bergin, J. E. Halpin, D. A. MacLaren, P. C. Dastoor, S. A. Przyborski, A. P. Jardine, and D. J. Ward. Multiple scattering in scanning helium microscopy. *Applied Physics Letters*, 116(6):061601, Feb. 2020. ISSN 0003-6951. doi: 10.1063/1.5143950.

[73] S. M. Lambrick, A. S. Palau, P. E. Hansen, G. Bracco, J. Ellis, A. P. Jardine, and B. Holst. True-to-size surface mapping with neutral helium atoms. *Physical Review A*, 103(5):053315, 2021.

[74] S. Lambrick et al. *to be published*.

[75] K. Luria, W. Christen, and U. Even. Generation and propagation of intense supersonic beams. *The Journal of Physical Chemistry A*, 115(25):7362–7367, 2011.

[76] D. MacLaren, W. Allison, and B. Holst. Single crystal optic elements for helium atom microscopy. *Review of Scientific Instruments*, 71(7):2625–2634, 2000.

[77] G. Markelov and M. Ivanov. A comparative analysis of 2d/3d micronozzle flows by the dsmc method. In *39th Aerospace Sciences Meeting and Exhibit*, page 1009, 2001.

[78] T. S. McKechnie. *General theory of light propagation and imaging through the atmosphere*. Springer, 2016.

[79] S. Medhe. Mass spectrometry: detectors review. *Chem Biomol Eng*, 3:51–58, 2018.

[80] A. G. Michette. *Optical systems for soft X rays*. Springer, 1884.

[81] T. A. Myles, S. D. Eder, M. G. Barr, A. Fahy, J. Martens, and P. C. Dastoor. Taxonomy through the lens of neutral helium microscopy. *Scientific reports*, 9(1): 1–10, 2019.

[82] T. A. Myles, A. Fahy, J. Martens, P. C. Dastoor, and M. G. Barr. Fast neutral atom microscopy: An optimisation framework for stagnation detectors. *Measurement*, 151:107263, 2020.

[83] K. Nanbu. Variable hard-sphere model for gas mixture. *Journal of the Physical Society of Japan*, 59(12):4331–4333, 1990.

[84] K. O'Donnell, A. Fahy, M. Barr, W. Allison, and P. Dastoor. Field ionization detection of helium using a planar array of carbon nanotubes. *Physical Review B*, 85(11):113404, 2012.

[85] A. S. Palau, G. Bracco, and B. Holst. Theoretical model of the helium pinhole microscope. *Physical Review A*, 94(6), Dec. 2016. ISSN 2469-9926, 2469-9934. doi: 10.1103/PhysRevA.94.063624.

[86] A. S. Palau, S. D. Eder, T. Andersen, A. K. Ravn, G. Bracco, and B. Holst. Centerline intensity of a supersonic helium beam. *Physical Review A*, 98(6):063611, 2018.

[87] H. Pauly. *Atom, Molecule, and Cluster Beams I: Basic Theory, Production and Detection of Thermal Energy Beams*, volume 28. Springer Science & Business Media, 2012.

[88] L. Pedemonte and G. Bracco. Study of he flow properties to test he dimer potentials. *The Journal of chemical physics*, 119(3):1433–1441, 2003.

[89] L. Pedemonte, G. Bracco, and R. Tatarek. Theoretical and experimental study of he free-jet expansions. *Physical Review A*, 59(4):3084, 1999.

[90] T. Reisinger, G. Bracco, S. Rehbein, G. Schmahl, W. E. Ernst, and B. Holst. Direct Images of the Virtual Source in a Supersonic Expansion. *J. Phys. Chem A*, 111(49):12620, 2007. doi: 10.1021/jp076102u.

[91] T. Reisinger, G. Bracco, S. Rehbein, G. Schmahl, W. E. Ernst, and B. Holst. Direct images of the virtual source in a supersonic expansion. *The Journal of Physical Chemistry A*, 111(49):12620–12628, 2007.

[92] T. Reisinger, M. M. Greve, S. D. Eder, G. Bracco, and B. Holst. Brightness and virtual source size of a supersonic deuterium beam. *Physical review a*, 86(4): 043804, 2012.

[93] R. Rhodes. *The making of the atomic bomb*. Simon and Schuster, 2012.

[94] D. J. Riley, M. Mann, D. A. MacLaren, P. C. Dastoor, W. Allison, K. B. Teo, G. A. Amaratunga, and W. Milne. Helium detection via field ionization from carbon nanotubes. *Nano Letters*, 3(10):1455–1458, 2003.

[95] A. Salvador Palau, G. Bracco, and B. Holst. Theoretical model of the helium zone plate microscope. *Phys. Rev. A*, 95(1):13611, 2017. doi: 10.1103/PhysRevA.95.013611.

[96] M. Sato and F. Mizuno. Depth of field at high magnifications of scanning electron microscopes. *Journal of Vacuum Science & Technology B: Microelectronics and Nanometer Structures Processing, Measurement, and Phenomena*, 18(6):3047–3051, 2000.

[97] L. Scipioni, L. Stern, J. Notte, S. Sijbrandij, and B. Griffin. Helium ion microscope. *Advanced Materials and Processes*, 166(6):27, 2008.

[98] G. Scoles, D. Bassi, U. Buck, D. Laine, and C. Braun. Atomic and molecular beam methods, vol. i. *Applied Optics*, 28(16):3258, 1989.

[99] G. Scoles, D. Miller, W. Gentry, H. Pauly, D. Bassi, H. Hefter, K. Bergman, M. Zen, J. Reuss, C. Meijdenberg, D. Abuerbach, M. Kappes, S. Leutwyler, U. Valbusa, U. Buck, Y. Lee, P. Dagdigian, S. Stolte, R. Dren, and S. Iannotta. *Atomic and Molecular Beam Methods: Vol. 1*. 01 1998. ISBN 0 -10-504280-8.

[100] G. S. Sikora. Analysis of asymptotic behavior of free-jets: prediction of molecular beam intensity and velocity distributions. 1974.

[101] E. H. Stelzer. Beyond the diffraction limit? *Nature*, 417(6891):806–807, 2002.

[102] M. Szilagyi. *Electron and ion optics*. Springer Science & Business Media, 2012.

[103] K. Tang, J. Toennies, and C. Yiu. Accurate analytical he-he van der waals potential based on perturbation theory. *Physical review letters*, 74(9):1546, 1995.

[104] J. P. Toennies and K. Winkelmann. Theoretical studies of highly expanded free jets: Influence of quantum effects and a realistic intermolecular potential. *The Journal of Chemical Physics*, 66(9):3965–3979, 1977.

[105] H. Tuithof, A. H. Boerboom, and H. Meuzelaar. Simultaneous detection of a mass spectrum using a channeltron electron multiplier array. *International Journal of Mass Spectrometry and Ion Physics*, 17(3):299–307, 1975.

[106] C. Van de Runstraat, R. W. Van Resandt, and J. Los. An absolute bolometer detector for energetic neutral particles. *Journal of Physics E: Scientific Instruments*, 3(7):575, 1970.

[107] M. Verheijen, H. Beijerinck, W. Renes, and N. Verster. A quantitative description of skimmer interaction in supersonic secondary beams: Calibration of absolute intensities. *Chemical physics*, 85(1):63–71, 1984.

[108] K. Vernon-Parry. Scanning electron microscopy: an introduction. *III-Vs Review*, 13(4):40–44, 2000.

[109] R. Wilson, B. Holst, and W. Allison. Optical properties of mirrors for focusing of non-normal incidence atom beams. *Review of scientific instruments*, 70(7):2960–2967, 1999.

[110] P. Witham and E. Sanchez. A simple approach to neutral atom microscopy. *Review of Scientific Instruments*, 82(10):103705, Oct. 2011. ISSN 0034-6748. doi: 10.1063/1.3650719.

[111] P. Witham and E. Sánchez. Increased resolution in neutral atom microscopy. *Journal of microscopy*, 248(3):223–227, 2012.

[112] P. Witham and E. Sanchez. Exploring neutral atom microscopy. *Crystal Research and Technology*, 49(9):690–698, Sept. 2014. ISSN 02321300. doi: 10.1002/crat.201300401.

Graphic design: Communication Division, UiB / Print: Skipnes Kommunikasjon AS

uib.no

ISBN: 9788230845233 (print)
9788230862483 (PDF)